Ion Pairing in Aqueous Metal Sulfates and Platinum Group Metal Ammonium Solutions

Thesis presented to the

UNIVERSITY OF CAPE TOWN

In fulfilment of the requirements for the degree of

DOCTOR OF PHILOSOPHY

By

RICHARD P. MATTHEWS

MSc (Chemistry)

Supervisor: Assoc. Professor Kevin J. Naidoo

Scientific Computing Research Unit and

Department of Chemistry

University of Cape Town

March 2010

ABSTRACT

The structure and dynamics of ions and ion pairs in solution play an integral part in several biological and chemical processes. Historically the calculation of ion pair association constants from computer simulations has been complicated due to the difficulty in validating metal ion force fields for solution simulations. In this thesis a force field for divalent metal ions in metal sulfate solutions (i.e. $Mg^{2+}SO_4^{2-}$, $Ca^{2+}SO_4^{2-}$, $Mn^{2+}SO_4^{2-}$, $Fe^{2+}SO_4^{2-}$, $Co^{2+}SO_4^{2-}$, $Ni^{2+}SO_4^{2-}$, $Cu^{2+}SO_4^{2-}$ and $Zn^{2+}SO_4^{2-}$) important in physical and biophysical experiments is produced. Potential of mean force calculations are used to provide ion pair free energy profiles and free energy perturbation calculations are used to calibrate the potential of mean force (PMF) from which association constants for ion pairs can be produced for these metal sulfate solutions. The calibrated free energy profiles result in calculated association constants that are in excellent agreement with available experimental data where available. Consequently the force field has been shown to be accurate for simulations of biophysical and physical systems. Furthermore the method, proposed in this thesis, for calibrating PMFs and calculating detailed association constants from those curves can most likely be used for complex systems that have previously been computationally inaccessible.

Next a detailed account of solvation structures and the nature of ion pair formation mechanisms for important metal sulfates in aqueous media are presented. Radial and spatial distribution functions calculated for several ion pair species reveal that the transition from free ions to contact ion pairs involves the loss of between one to two water molecules from the cation depending on the cation size. This is correlated with the experimental hydration numbers calculated for metal sulfate electrolyte solutions at several concentrations using density and ultrasonic velocity measurements. These experiments reveal a decrease in hydration number with an increase in concentration, which can be attributed to the formation of ion pairs.

A more complex metal system is the industrially important platinum group metal (PGM) chloro-anion one. Their industrial importance relates to the search for *a Green Chemistry Process* for the separation of PGM chloro complexes that have been extracted from the mined ore into an acidic aqueous media. This requires a PGM separation process in water. Here an understanding of the hydration structure about the

PGM chloro-anion complexes and the role that ammonium counter-ions play in disrupting that solvent structure when ammonium PGM salts are formed, is critical in the process design. To this end a solution force field, inclusive of the majority of PGM chloro-anion complexes (i.e. $(Y)_2[PtCl_4]^{2-}$, $(Y)_2[PdCl_4]^{2-}$, $(Y)_2[PtCl_6]^{2-}$, $(Y)_2[PdCl_6]^{2-}$, $(Y)_2[IrCl_6]^{2-}$, $(Y)_2[OsCl_6]^{2-}$, $(Y)_2[RuCl_6]^{2-}$, $(Y)_3[IrCl_6]^{3-}$, $(Y)_3[RhCl_6]^{3-}$ and $(Y)_3[RuCl_6]^{3-}$, where $Y = NH_4^+$) arising in acidic aqueous media, parameterised from experimental and quantum mechanically derived properties, was developed. Nanosecond atomistic molecular dynamics simulations were then performed for the PGM chloro-anion complexes. Analysis of the solvation structure using radial and spatial distribution functions revealed two distinct solvent structures corresponding to the square planar and octahedral species. The formation of ion pairs disrupts the solvent structure where the hydration shells about the bivalent hexachlorometallates are more affected compared with the trivalent hexachlorometallates and these first shell waters in turn are more affected than those in the bivalent tetrachlorometallates.

Finally to inform the design of a separation process transport properties such as diffusion coefficients, ion hydration numbers and water residence times for the PGM chloro-anion complexes were calculated. It is observed that the diffusion rates of PGM chloro-anion complexes are strongly correlated to their ion hydration numbers as calculated by Voronoi tessellation of the simulation cell, such that a larger hydration shell volume results in a slower PGM chloro-anion diffusion rate.

DECLARATION

I declare that the work in this thesis, "*Ion Pairing in Aqueous Metal Sulfates and Platinum Group Metal Ammonium Solutions*" is based on research carried out at the Scientific Computing Research Unit and the Department of Chemistry, at the University of Cape Town, South Africa. No part of this thesis has been submitted elsewhere for any other degree or qualification and is all my own work unless referenced to the contrary in the text.

Richard Paul Matthews Signed by candidate

March 2010

ACKNOWLEDGEMENTS

Supervising a PhD student is a tedious process, especially when the student believes he always knows best. To my supervisor Associate Professor Kevin J. Naidoo, many thanks for your guidance and patience of the last three years. I know I was difficult at times, but thank you for always believing in me and for the many inspirational talks, not only about chemistry but also life.

To Dr Gerhard Venter, thank you for the many hours of discussing the solvation structures and dynamics of metal ions. For the help with CHARMM and Gaussian and for being a good friend throughout the PhD I cannot say how grateful I am.

My wife Jane, a special thank you is required for sticking with me and not letting me give up hope and for all the patience you have had over the writing up period and for the proof reading in these last few months. To my families in Pretoria and Cape Town, thank you for the support and love I have received over the period of this PhD.

Finally, a special thanks to my fellow postgraduate members of the Scientific Computing Research Unit for their thoughts and support during the last three years.

ABBREVIATIONS

Å	Angstrom
AO	Atomic Orbital
CHARMM	Chemistry at Harvard Macromolecular Mechanics
CIP	Contact Ion Pair
DFT	Density Functional Theory
ECP	Effective Core Potential
ESAs	Electronic Structure Approaches
ESP	Electrostatic Surface Potential
FEARCF	Free energy from Adaptive Reaction Coordinate Forces
FEP	Free Energy Perturbation
fs	Femtosecond
GGA	Generalized Gradient Approximation
GTO	Gaussian Type Orbital
HF	Hartree-Fock
LANL	Los Alamos National Laboratory
LDA	Local Density Approximation
LJ	Lennard-Jones
MC	Monte Carlo
MD	Molecular Dynamics
MKS	Merz-Kollman-Singh
MM	Molecular Mechanics
MPPT	Møller-Plesset Perturbation Theory
MSFF	Metal Solution Force Field
NMR	Nuclear Magnetic Resonance
NPT	Isothermal-isobaric Ensemble
ns	Nanosecond
NVT	Canonical Ensemble
PDF	Pair Distribution Function
PGM	Platinum Group Metal
PME	Particle Mesh Ewald

PMF	Potential of Mean Force
ps	Picosecond
QM	Quantum Mechanics
QM/MM	Quantum Mechanics/ Molecular Mechanics
SCF	Self Consistent Field
SDF	Solvent Distribution Function
SSHIP	Solvent Shared Ion Pair
SSIP	Solvent Separated Ion Pair
TI	Thermodynamic Integration
UI	Ultrasonic Interferometry
WHAM	Weighted Histogram Analysis Method
ΔA	Helmholtz Free Energy
ΔG	Gibbs' Free Energy

CONTENTS

LIST OF FIGURES

Figure 8.2 (a) Square planar, (c) bivalent octahedral and (e) trivalent octahedral Metal-oxygen pair distribution functions and (b) square planar, (d) bivalent octahedral and (f) trivalent octahedral chloride-oxygen for PGM chloro-anion complexes.

Figure 8.3. Metal$\cdots NH_4^+$ pair distribution functions $g(r)$ for (a) square planar, (b) bivalent octahedral and (c) trivalent octahedral PGM chloro-anion complexes.

Figure 8.4. SDF plots for the square planar PGM chloro-anion complexes with (c) and (b) without the ammonium counterion densities. The red represents water oxygen densities, blue, the water hydrogen densities and the yellow densities represent the nitrogen of the ammonium counterions. Also shown are the electrostatic potentials of all the square planar PGM chloro-anion complexes mapped onto the same $[PdCl_4]^{2-}$ isodensity surface at an electron density of 0.001. The colour range extends from -0.32 (blue) to -0.27 (red) in units of electron charge.

Figure 8.5. SDF plots for the bivalent octahedral PGM chloro-anion complexes with (c) and (b) without the ammonium counterion densities. The red represents water oxygen densities, blue, the water hydrogen densities and the yellow densities represent the nitrogen of the ammonium counterions. Also shown are the electrostatic potentials of all the bivalent octahedral PGM chloro-anion complexes mapped onto the same $[PtCl_6]^{2-}$ isodensity surface at an electron density of 0.001. The colour range extends from -0.31 (blue) to -0.26 (red) in units of electron charge.

Figure 8.6. SDF plots for the trivalent octahedral PGM chloro-anion complexes with (b) and (a) without the ammonium counterion densities. The red represents water oxygen densities, blue, the water hydrogen densities and the yellow densities represent the nitrogen of the ammonium counterions. Also shown are the electrostatic potentials of all the trivalent octahedral PGM chloro-anion complexes mapped onto the

same $[RuCl_6]^{2-}$ isodensity surface at an electron density of 0.001. The colour range extends from -0.47 (blue) to -0.42 (red) in units of electron charge.

LIST OF TABLES

CHAPTER 1

Liquids and Ion Hydration

1.1 Molecular Association and the Liquid Phase

The strength of molecular association is paramount in describing the macroscopic observables in a chemical system. Examples of this are seen in the recognition of specific nucleotide sequences by DNA-binding proteins governed by amino acid-base interactions [1], the role ion selectivity plays in cellular communication and transport [2, 3], the role CH $\cdots$ π interactions play in crystal packing and in determining clatharate structures [4], the hydrophobic effect and its associated influence on protein folding [5-8] and the enhanced stabilisation of secondary structures by noncovalent forces i.e. hydrogen bonding and metal-ligand interactions and in metallofoldamers upon ion coordination [9]. Furthermore, the competition between solute-solute, solute-solvent and solvent-solvent associations, which determine properties such as solubility and ion pairing, can be observed in the dynamics of hydrated ions [10], the dissolution of hydrogen bonded solvents in organic solvents [11-13] and the dielectric response [14-16] and conductivity of electrolyte solutions [17, 18].

The distinction between solid, liquid and gas states, on the microscopic level, is determined by the interplay between the degree of molecular association and molecular motion. In liquids, forces of attraction (intermolecular forces) between molecules are strong due to short intermolecular distances, while the molecular kinetic energy is sufficiently large to allow for the random tumbling of molecules. This leads to liquids having both the attributes of gases and solids, more specifically the molecular disorder of gases and the structural incompressibility of solids, such that a region within a liquid that is orderly one moment can become random the next and vice versa. The order observed within liquids is generally short-ranged[1] and is best described by pair distribution functions (PDF), from which it is possible to obtain an idea of the magnitude and range of molecular ordering over the total number of atoms, N. The pair distribution function, $g(r_{ij})$, is defined as the probability of finding two atoms, i and j, a distance r_{ij} apart, when compared to a completely random distribution at the same distance, r, and is given as

[1] Dilute gases are without molecular order, whereas solids display a short-range order which persists to larger distances.

$$g(r_{ij}) = \frac{1}{4\pi r_{ij}^2} \frac{dN(r_{ij})}{dr_{ij}} \quad (1.1)$$

1.2 Solutions and Liquid Phase Separation

A solution is defined as the homogenous mixing of one or more solutes into a solvent. Examples of this are seen in the dissolution of liquids within other liquids, i.e. ethanol dissolves in water; the dissolution of solids in solvents, i.e. sucrose molecules in water and iodine in carbon tetrachloride; and the dissolution of ionic solids in water.

The dissolution of ionic solids in aqueous media and the resulting chemical properties of hydrated ions have been used for decades as a means to extract pure metals from metal ore via solvent extraction [19-22]. In hydrometallurgy, solvent extraction is principally a two step process. First, a metal ion is transferred from an aqueous phase (containing several ions) to an organic phase as a metal-ligand (extractant) complex, as shown in Figure 1.1. The second step is where the ion is transferred back to a second aqueous phase to remove impurities, thus arriving at the separation of an ion mixture. However, in practice, the separation of ions can become complex and depend on several mechanisms, i.e. whether the extractant operates on the inner or outer sphere of the metal and how the loading/stripping equilibria are controlled. To convert a metal ion in aqueous media into an extractable complex requires substitution of its waters of hydration with another molecule or ion, i.e. ion pairing, in order to convert a hydrophilic species into a hydrophobic species [20]. Thus metal extraction depends on the chemistry of metal and metal complexes in both aqueous and organic media [21] and on the selectivity of an extractant [20, 21].

Solvent extraction has been used to recover most of the elements in the periodic table, including the alkali metals, alkali earth metals and several transition, rare and precious metals [20, 22]. Used for the separation of platinum group metals, solvent extraction allows for higher selectivity, higher purity and more complete removal of metals over conventional precipitation methods, such as co-precipitation and ion-exchange chromatography [23].

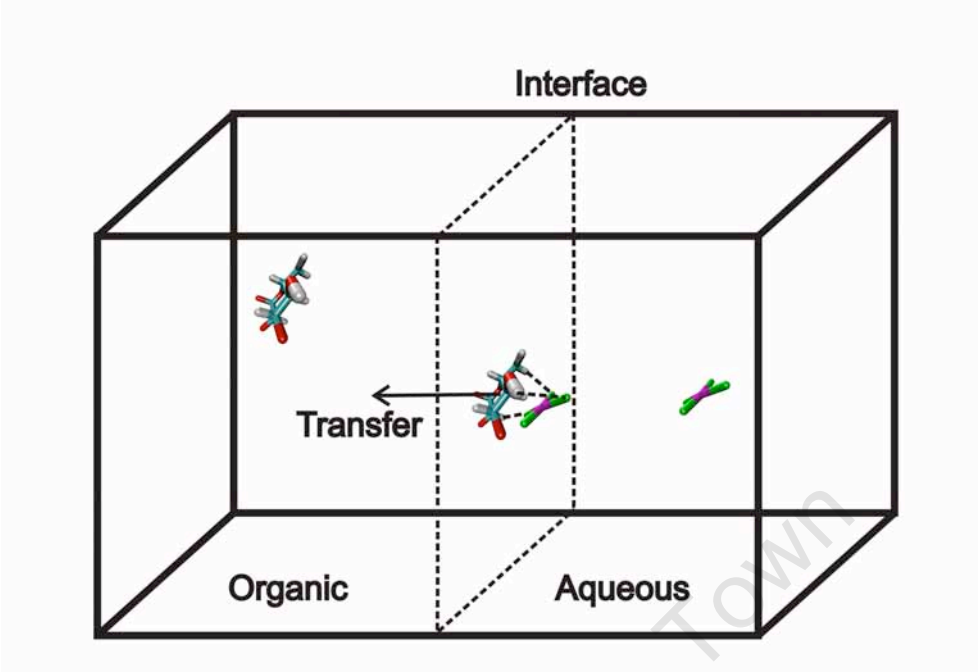

Figure 1.1. Schematic representation of a metal-extractant association, at the organic-aqueous interface and the transfer of the metal-extractant complex to the organic phase. This association is between a metal from the aqueous phase and an extractant from the organic phase.

However, the use of solvent extraction for metal ions raises several environmental concerns, not least of these is the contamination of water and soil, and the oxidation and disposal of unwanted organics, after the metals have been extracted [22]. To counter these effects more efficient separation processes using only water as solvent are required. Ion pairing is believed to be able to play a role in reaching this goal, as the understanding of ion pairing has been used to develop the principle of ion pair chromatography [24, 25]. This is the context in which the phenomenon of ion association and pairing and the effects on the chemistry of ion hydration is studied throughout this thesis.

1.3 Intermolecular Forces [26, 27]

Intermolecular (or van der Waals) forces of attraction give rise to the liquid and solid phases and refer to the weak *electromagnetic interactions* acting at a distance between molecules on the microscopic level [27, 28]. They determine the chemical nature of molecular systems such as the boiling points, vapour pressures and viscosities of liquids, the formation of surface monolayers, micelles and membranes, as well as the transport of ions and molecules across biological membranes [26, 29].

Intermolecular forces are fundamentally electrostatic [2], arising from Coulomb interactions between atoms in molecules [26, 27]. To simplify matters, molecular interactions are described by an intermolecular energy, $U(R)$, rather than an intermolecular force, $F(R)$. $U(R)$ is the difference between the total energy of the particles and the sum of the separate particle energies and $F(R)$ is the negative of the derivative of $U(R)$ with respect to the distance between the particles' centres of mass, R. Typical functions of $U(R)$ and $F(R)$ are shown in Figure 1.2. $U(R)$ for a molecular system can be determined by either *ab initio* or empirical methods, although *ab initio* methods only provide accurate potentials for small to medium sized molecules because of computational expense [30, 31].

$U(R)$ is largely made up of long- and short-range contributions, where long-range interactions act over all values of R and are represented as an inverse power, R^{-n}. The short-range interactions are present only when the electron densities/orbitals overlap, with a distance dependence of the form $\exp(-kR)$, where k is a constant. A summary of the contributions to the interaction energy as well as their pair additivity and sign is given in Table 1.1.

[2] Magnetic interactions also contribute to the intermolecular energy, but are not considered in this work.

Table 1.1. A summary of the long- and short-range contributions to the interaction energy.

Contribution	Pairwise Additive	Sign
Long-range		
Electrostatic	Yes	Positive or negative
Induction	No	Negative
Dispersion	Approximately	Negative
Resonance	No	Positive or negative
Magnetic	Yes	Positive or negative
Short-range		
Exchange	No	Negative
Repulsion	No	Positive
Charge Transfer	No	Negative
Penetration	Yes	Negative
Damping	Approximately	Positive

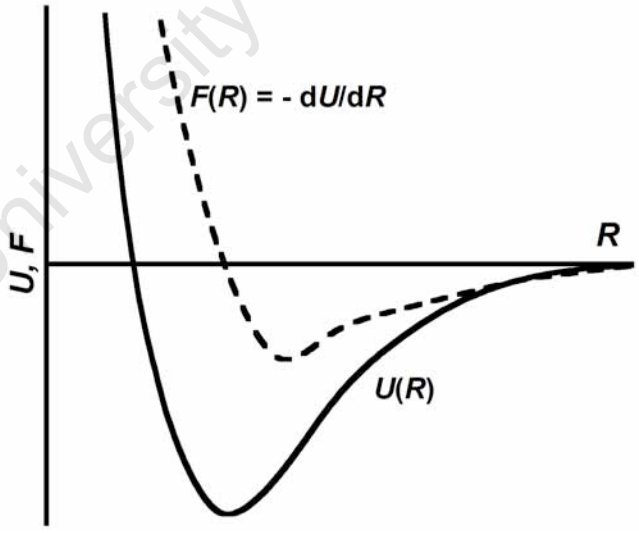

Figure 1.2. The interatomic potential $U(R)$ and force $F(R)$.

1.3.1 Long-Range Interactions

The long-range energies are classified into three types: electrostatic, induction and dispersion. To calculate the electrostatic energy of a chemical system all that is needed is knowledge of the molecular charge distribution. Once determined, the induction and dispersion energies can be calculated based on the behaviour of the same chemical systems electrons under the influence of an external electric field; thus induction and dispersion energies are polarisation dependent.

The electrostatic interaction energy between two molecules is calculated as the sum of the Coulombic interactions between the particles, which can be obtained by summation of the nuclear-nuclear repulsions, the electron-electron repulsions and the electron-nuclear attractions, if the nuclei positions and electron distributions are known.

However, in the large molecular systems now encountered in molecular dynamics simulations this is not feasible [32]. In these situations a mathematical simplification known as the multipole expansion is applied. Following this approach the attractive and repulsive terms are combined, such that the electrostatic energy can be equated to the energy of interaction of the net charges and multipole moments (e.g. monopoles, dipoles and quadrupoles) arising from the non-uniform distribution of electric charge, $\rho(r)$, in a molecular system.

Thus for $\rho(r)$ the potential at point P, at a distance R from the centre of mass of $\rho(r)$, integrated over all phase space is given by

$$V(P) = \frac{1}{4\pi\varepsilon_0}\int \frac{\rho(r)}{|R-r|}\,d\tau \tag{1.2}$$

Assuming $R >> r$ then the expansion can be written as

$$V(P) = \frac{1}{4\pi\varepsilon_0}\sum_{n=0}^{\infty}\frac{1}{R^{(a+b+1)}}\int r^n\, P_n(\cos\theta)\rho(r)\,d\tau \tag{1.3}$$

where P_n(x) are the Legendre polynomials and the angular term cosθ is given by the dot product of the two vectors $\hat{r}$ and $\hat{R}$. The multipole moments arising from the interaction of a pole (e.g. monopole, dipole, quadrupole, etc) of order *a* with a pole of order *b* (where *a* and *b* equal 0 for the charge zeroth moment, 1 for the dipole moment, 2 for the quadrupole moment and so forth, can be obtained from the multipole expansion coefficients. The first three multipoles, monopole, dipole and quadrupole, are given as the first three terms in

$$V(P)=\frac{1}{4\pi\varepsilon_0}\left[\frac{1}{R}\int\rho(r)d\tau+\frac{1}{R^2}\int r\cos\theta\rho d\tau+\frac{1}{R^3}\int r^2\left(\frac{3}{2}\cos^2\theta-\frac{1}{2}\right)\rho d\tau+\ldots\right] \quad (1.4)$$

If generalised, the multipole expansion giving the electrostatic interaction between two molecules, A and B, is only valid when there is negligible overlap of the electron clouds of the two molecules and where the distance between the centres of the two molecules is large compared with the linear dimensions of the two molecules. From the generalisation coefficients corresponding to charge-charge, charge-dipole, dipole-dipole and higher moment interactions are obtained.[3]

Polarisation energies arise from alterations in the electron distribution of molecules, influenced by other molecular electron distributions. The induction energy is described by placing a molecule in an external electric field, F_e. The resulting change in charge distribution is referred to as an induced dipole moment, $\mu_{ind,}$ and is given as

$$_{ind}=\alpha \quad F_e \quad (1.5)$$

where α is the polarisability tensor. The change in energy, E_{ind}, associated with the alteration in charge distribution is subsequently given as

[3] For a full derivation of the multipole expansion and resulting multipole moments the reader is directed to the text *The Theory of Intermolecular Forces* by A. J. Stone.

$$E_{ind} = -\frac{1}{2}\alpha F_e F_m \tag{1.6}$$

where the electric field F_m is derived from the multipole expansion coefficients for the relevant n-pole moments of the molecule interacting with F_e. Therefore, ions or molecules with large dipole moments have large induction energies, whereas nearly spherical molecules with no low-order moments and weak electric fields have small induction energies. This work is primarily concerned with aqueous solutions, where water is described by a dipole moment, μ_w. Introducing a molecule with polarisability α_b in the field of a water dipole moment, the resultant induction energy when averaged over all orientations is given by

$$E_{ind} = \frac{{}^{2}_{w}\alpha_b}{(4\pi\varepsilon_0)^2 R^6} \tag{1.7}$$

Based on the description of induction energies given above, an inert gas which has no permanent moment would be assumed to have zero induction energy. However, if inert gases possess instantaneous moments arising from fluctuations in their electron distributions, these instantaneous moments will induce moments in neighbouring molecules and there will be a resultant energy of interaction between the molecules. This resultant non-zero polarisation energy is called the dispersion energy.[4]

The dispersion energy for dipole-dipole interaction, as in the case of the induction energy is proportional to R^{-6} and is written as

$$E_{disp} = \frac{-C_6}{R^6} \tag{1.8}$$

where the coefficient C_6 can be deduced empirically or by calculation. For spherical molecules C_6 is independent of the relative orientation of the system, whereas for others

[4] The theory of dispersion energy was first derived by F. London, and hence dispersion energies are often referred to as London energies.

C_6 is angle-dependant and by expanding the dispersion energy in R^{-n} one can obtain higher terms arising from the interaction of induced multipoles of order higher than the dipole.

1.3.2 Short-Range Interactions

Short-range energies arise when the electron densities of molecules, either open or closed shell species, interact. Upon overlap, several interactions may occur. These are electrostatic penetration, exchange repulsion, damping and charge transfer. Of these interactions, exchange repulsion is most prominent and is used to describe the repulsive force (energy) associated with the interaction of two closed shell species.[5] This short-range repulsion occurs when the wave functions of two interacting molecules overlap, making the electrons belonging to each respective molecule indistinguishable from each other.

The overlap between the orbitals of two molecules, *A* and *B*, is measured by the overlap integral, integrated over all space and written as

$$S = \int \phi_A \phi_A d\tau \tag{1.9}$$

If *A* and *B* are separated by a significant distance, such that ϕ_A and ϕ_B do not overlap then *S* will become zero. However, if there is overlap then the exchange energy involves the product of two orbital overlap functions such that it is approximately proportional to S^2.

The hydrogen bond is a case where all of the main terms in the intermolecular interaction have a role to play, with the most important contributions coming from electrostatic and repulsion interactions [26]. Hydrogen bonds occur both inter- and intramolecularly [33]. Of special importance are hydrogen bonding liquids, such as water and methanol, which play an important role in both chemistry and biochemistry in

[5] The approach of two open shell species results in an attractive short-range energy, which is the origin of intramolecular energies.

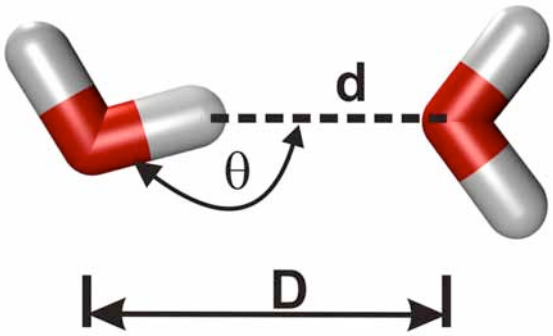

Figure 1.3. The water dimer, the prototypical hydrogen bond. In this figure *d* is the H···O distance, *D* is the O···O distance and θ is the O- H···O angle.

determining macromolecular assemblies and the structure and function of several biomolecules [34-37]. The hydrogen bond is a structure in which the hydrogen atom is partially bonding to two electronegative atoms, of the form A-H···B, where A and B are highly electronegative elements e.g. nitrogen, oxygen or a halogen atom and B possesses a lone pair of electrons.

This results in a charge distribution, $A^{\delta-}$ -$H^{\delta+}$ ···$B^{\delta-}$, where there is a strong electrostatic attraction between H and B. There is also an electrostatic repulsion between A and B which helps to align the hydrogen bond in conjunction with orbital overlap. This is promoted by the electronegativity of A, resulting in an electron density on the H atom which is relatively small, thus creating a weak repulsion between B and H and a shorter distance between A and B. The prototypical hydrogen bond is described by the directional interaction between water molecules and is shown in Figure 1.3.

1.3.3 Model Potentials

Analytical mathematical functions constructed of terms defining contributions to the intermolecular potential, derived from *ab initio* and experimental data, are routinely used to model the interactions for medium to large molecular systems.

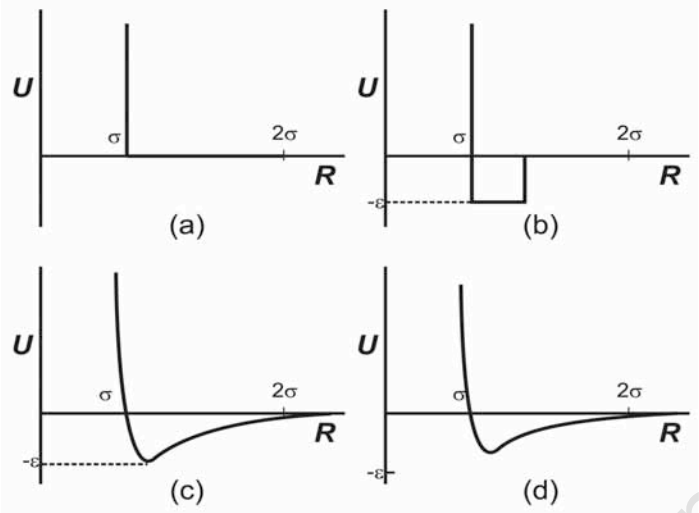

Figure 1.4. A comparison of simple empirical potentials: (a) hard-sphere, (b) square-well, (c) Lennard-Jones and (d) (exp-6).

Several empirical potentials, as shown in Figure 1.4, have been used to model the repulsion and dispersion interactions. Hard-sphere and square-well potentials were used to study fluid properties. However, both of these are discontinuous functions which lead to poor representation of the potential at large distances. The potential which has been the basis of most analytical studies of atomic fluids, due to its low computational expense, and at the same time its close representation of real potentials, is the Lennard-Jones (LJ) potential, written as

$$U_{LJ} = 4\varepsilon\left[\left(\frac{\sigma}{R}\right)^{12} - \left(\frac{\sigma}{R}\right)^{6}\right] \tag{1.10}$$

In the LJ potential, repulsion is represented as an R^{-12} term, and dispersion as an R^{-6} term. U_{LJ} is equal to zero where $R = \infty$ and $R = \sigma$ and has a minimum at $R_{min} = 2^{1/6}\,\sigma$, with $U_{LJ} = -\varepsilon$ at that point, as can be seen in Figure 1.4.

Modelling of polar molecules also requires an electrostatic energy term. Ideally one would like to model this using the full multipole expansion. However, the large computational demand of a distributed-multipole model precludes this and the

electrostatic interaction energy, U_{es}, is more commonly described using atomic point charges. The electrostatic energy between atoms *a* and *b* is given by

$$U_{es} = \sum_{ab} \frac{q_a q_b}{4\pi\varepsilon_0 R_{ab}} \tag{1.11}$$

where q_a and q_b are the atomic charges and R_{ab} is the interatomic distance.

1.4 Liquid Structure: A Look at Water

The most abundant and the most important liquid, in terms of versatility of interactions and resulting chemical processes in solution, is water [38, 39]. The interest in water from a scientific perspective is driven by our need to understand how it sustains life, as well as its fascinating array of properties as both a solvent and a pure substance. Water's complexity is believed to originate from a strong, highly directional hydrogen bonding network, where the distances *d* and *D* and the angle θ (Figure 1.3) contribute to the hydrogen bonding strength, resulting in a local tetrahedral structure around each water atom and an ordered network within the liquid [40-42]. Furthermore, the ability of water to act as both an acceptor, through the negatively charged oxygen atom, and donor through the positively charged hydrogen atoms, results in a highly polar molecule that can make strong electrostatic interactions.

Many empirical models of water routinely used in molecular simulations, e.g. the SPC [43], SPC/E [44], TIP3P/4P [45] models, have invoked some analogy with the solid state structure of ice I_h. Discovered by Bragg in 1921 [46], ice I_h, displays a tetrahedral geometry, where each water molecule has four hydrogen bonded neighbours at a distance of 2.75 Å, with the four neighbours placed at the tetrahedron vertices with a mutual separation of 4.5 Å. This structure is found to persist in the liquid state [47]. However, the hydrogen bonded neighbours are at a larger distance, 2.8-2.9 Å, with an increased coordination number of 4.5-4.7 compared to that of ice I_h which is 4. This increase in coordination number was elicited using both experimental and computational techniques

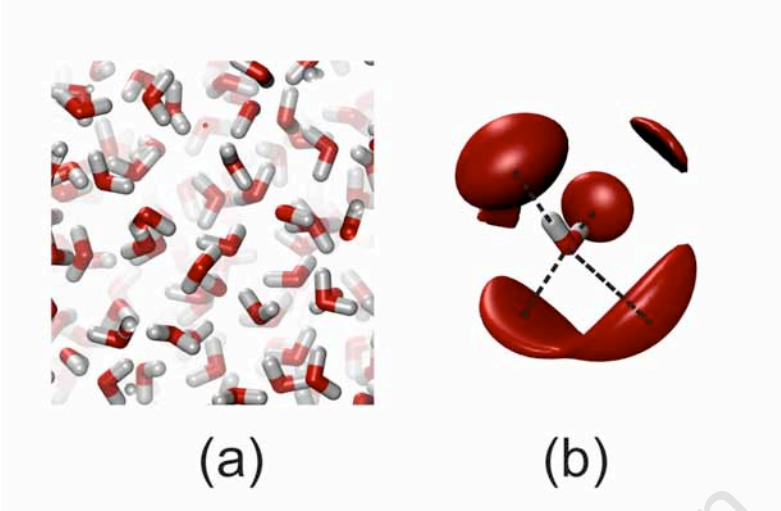

Figure 1.5. The tetrahedral structure of liquid water simulated using the TIP3P water model at 298.15 K and 1 atmosphere, where (a) is a snapshot of the 'random' water structure and (b) shows the time averaged spatial distribution function (using only oxygen atoms) revealing the tetrahedral water structure and interstitially placed waters.

and was concluded to result from water density placed interstitially to the first coordination shell at a distance closer than the second solvation shells [48-51]. Figure 1.5(b) shows a three dimensional probability distribution of water molecules around a central water molecule, revealing the tetrahedral water structure and including the positions of the interstitial water density.

1.5 Solvation and Liquid Polarity

Liquid solvents can be classified as either polar or non-polar. This classification is based on the polarity of the molecules making up a liquid and is a representation of a liquid's ability to dissolve solutes to form solutions, i.e. for ions to dissolve, solvent molecules must orient themselves around the oppositely charged ions in order to shield them

Table 1.2. ε_r of several liquids and their gaseous molecular dipole moments, μ, in Debye units.

	T/K	ε_r	μ/D
CCl_4	298	2.23	0
C_6H_6	298	2.27	0
$C_6H_5NO_2$	298	34.8	4.22
CH_3OH	298	32.6	1.70
HF	200	175	1.82
NH_3	195	25	1.46
H_2O	298	78.4	1.85

from each other. This occurs when the solute-solvent interactions are more favourable than the solute-solute and solvent-solvent interactions.

Solvent polarities are best described by the relative permittivity, ε_r. In Table 1.2, it is seen that solvents with constituent molecules having a permanent dipole moment have relative permittivities an order of magnitude larger than those whose molecules have zero moment. The importance of solvent polarity is shown in calculating the interaction energy, E, between two charges, q_a and q_b, separated by a distance, R, in vacuum (Equation 1.12) and in dielectric medium (Equation 1.13).[6]

$$E = \frac{q_a q_b}{4\pi\varepsilon_0 R} \tag{1.12}$$

$$E = \frac{q_a q_b}{4\pi\varepsilon_0 \varepsilon_r R} \tag{1.13}$$

Thus ion-ion interactions are greatly reduced when in a solvent medium with intermediate or large ε_r values, giving an indication of the degree of solubility of ionic salts, i.e. the higher the energy, the lower the solubility, with these differentiations

[6] ε_0 is the vacuum permittivity which has the value 8.854 x 10^{-12} $J^{-1}C^2m^{-1}$.

routinely finding use in the separation and extraction of ions [52, 53]. ε_r is a macroscopic parameter which allows for treatment of a solvent as a continuous dielectric constant. ε_r has been utilised in the continuum electrostatic models such as that of Debye and Hückel [54]. However, these models are unable to describe accurately simple ion specific behaviours such as their tendency to form contact ion pairs [27] which is a major factor in specific salt solubility, i.e. Hofmeister series, and the specific role of ions in biological systems [55]. This is due to an inability of traditional continuum models to account for the change in ε_r for a solvent when the distance between the solute and solvent molecules decreases.

1.6 Ion Hydration: Aqueous Metal Ions

The hydration of ionic species and the related properties, e.g. the thermodynamics of solvation, hydration structure and ion pairing, has been extensively covered in several monographs [19, 56-61] as well as in published reviews related to the structure of hydrated ions [62], the effect of ions on the structure of water [63], the forces that govern chemical processes and biological structure [55] and the coordination and ligand exchange dynamics of solvated ions [64].

The specific interaction of ions with biomolecules is important, e.g. the activation of brain enzymes brought on by the flow of calcium through ion channels signaling enzyme activation, via complexation with calmodulin [65, 66], the increased transport rate of potassium (over sodium) along the KcsA potassium channel [3, 67, 68], the contraction of muscles via calcium-induced conformational changes [69], the three dimensional structure stabilisation, as well as repair and modification of RNA and DNA by introduction of magnesium ions [70, 71] and the role zinc and iron play in the development of Alzheimer's and Parkinson's disease [72].

In chemistry, the hydration of ions is critical in chemical processes such as anion recognition in both ion-exchange and liquid-liquid extraction [23, 53, 73, 74]. In all of the above examples, the major driving force for ion selectivity is not necessarily ionic size, but rather the structural rearrangement of bulk water hydration spheres and the

thermodynamics of hydration. Thus in order to understand ion selectivity mechanisms, one must first understand ion hydration.

In this thesis the emphasis is on hydrated ions formed by the dissolution of ionic solid lattices. The solubility of ionic solid lattices emanates from the balance between the free energy of ionic solvation (solvent-solute interaction), the lattice free energy (solute-solute interaction) and the solvent free energy (solvent-solvent interaction) [27]. In 1920 the Born model [75] was introduced. This model represents the simplest continuum theory of ionic solvation and allows the ionic free energy of solvation, given as

$$\Delta G^{Born} = \frac{-q^2 e^2}{2R}\left[1 - \frac{1}{\varepsilon_r}\right] \qquad (1.14)$$

to be calculated in terms of the spherical ion radius, *R*, of an ion with charge *qe*, where *e* is the magnitude of the electronic charge. Deficiencies in the Born equation lie firstly in the assumption of a hard-sphere ion, secondly in the treatment of the solvent as a continuous dielectric and thirdly in the assumption that the response of solvent molecules to a solute charge distribution is linear, resulting in the quadratic dependence of ΔG^{Born} on solute charge [27, 76]. This means that the solvation free energy of a cation or anion with equal radii are equal, that smaller ions would have more favourable free energies and that the free energy to transfer an ion to a more polar solvent will be negative [77]. However, this is inconsistent with experimental findings i.e. Grossfield et al. that the chloride anion, although larger than the potassium cation, has a more favourable aqueous solvation energy [77]. Even with improvements over the last several decades, continuum theory intrinsically lacks the ability to account for the structuring of solvents in the regions closest to ions in which solvent molecules are highly structured, relative to solvent molecules further away [77-80]. This may give rise to phenomena such as dielectric saturation which would decrease the solvation free energy [80], or electrostriction which would increase the solvation free energy [19, 78, 81].

In 1933 Bernal and Fowler [82] presented a structural treatment of ion-solvent interactions. They proposed that changes in free energy during solvation be treated electrostatically, i.e. by treating ions as spherically symmetrical fields and waters as

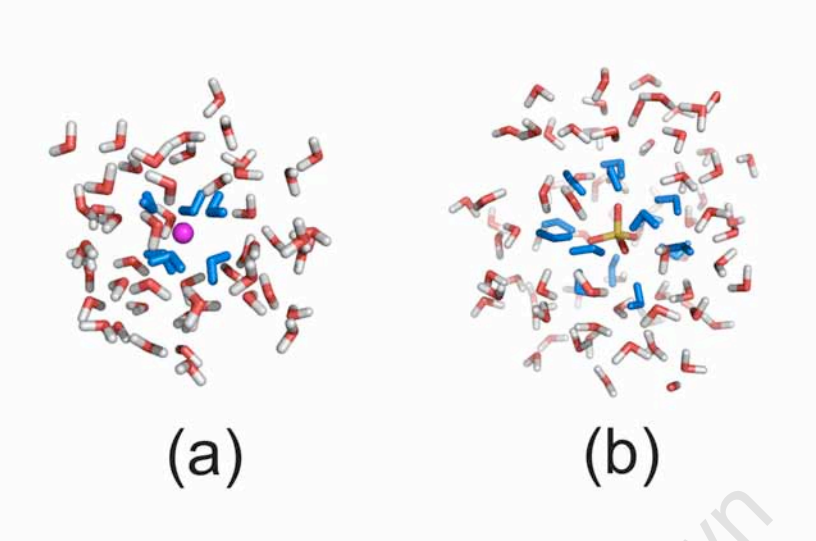

Figure 1.6. The reorientation of water molecules (blue) in direct contact with an ion compared to the 'random' orientation of bulk waters. (a) Shows the negatively charged oxygens of the water molecules pointing towards a positively charged magnesium cation, and (b) shows the positively charged hydrogens of the water molecules pointing towards a negatively charged sulfate anion.

dipole moments, ion-solvent interactions are modelled via ion-dipole interactions, resulting in the reorientation of water molecules within the field of an ion, such that the appropriate charged end is directed towards the ion as shown in Figure 1.6. This provides sufficient energy to break up the 'tetrahedral' water structure observed in the bulk. Furthermore they made allowance for dampening of the ion-solvent interaction energy on waters further from an ion.

The idea of solvent restructuring has since been influenced by the work of Frank and Gurney [83-85], who proposed that solvent around an ion can be divided into several regions, i.e. a primary region where water molecules interact directly with an ion, a secondary region where water molecules may be orientated due to their proximity with the ion and finally the bulk solvent. Furthermore, ions may be described as either 'structure making' or 'structure breaking' [19]. This classification is based on the size of an ion and the water reorientation strength in the primary and secondary regions, e.g.

small ions are considered structure makers, as water molecules are strongly bound to the ion, whereas large ions are generally considered structure breakers due to their 'interference' with the hydrogen-bond network in bulk water. However, very large ions are sometimes considered structure makers because hydrogen bonding between water molecules can be enhanced at the surface of these ions [85]. The structure and dynamics of ion hydration shells, i.e. nearest neighbour distances, coordination numbers and residence times, have been obtained using several experimental measurements and molecular dynamics computations and have been extensively reviewed [62, 63]. However, no consensus has yet been achieved on the best method for studying the structure of hydrated ions. This is because representations of ion hydration structure depend on the experimental technique used. First, different methods do not always measure the same number of solvation shells and second, difficulties arise in data interpretation and assignment of solvation numbers to constituent ions in solution [19, 60, 62]. Computational studies of solvated ions have been carried out using a variety of techniques, e.g. quantum mechanically using both *ab initio* and density functionals, empirical molecular dynamics (MD) and Monte Carlo (MC) methods, as well as hybrid quantum mechanical/molecular mechanics (QM/MM) methods. These studies have been conducted on alkali and alkaline earth metals [86-92], an array of transition metals [64, 87, 88, 90, 93-95] and several mono-valent [96, 97] and multi-valent anions [90, 98-101]. It is advantageous to study ion hydration using computational methods, with or without experimental studies, because they allow for the study of individual ions and the study of more dilute ion solutions [63]. An overview of experimental techniques and the validation of computer simulations are considered in Chapter 4.

So far only ion-solvent interactions have been discussed with relevance to ion hydration. However, recent experimental and computational studies have been conducted with an aim to study the ion-ion interactions with regards to ion pairing. These are presented in the review by Marcus and Hefter [102]. A simplistic view of these ion pairing simulations reveals that structural and energetic factors are prevalent in determining if the ion and counterion will pair, where solvent molecules either reduce or increase the prevalence of pairing and the energetic competition between the solvent and counterion. The concept of ion pairing and relevant examples is discussed in Chapter 2.

1.7 Objectives

The structure and dynamics of ions and ion pairs in solution play an integral part in several biological and chemical processes. Computer simulations allow for greater insight into the ion pairing process and the solvation of charged species in general, as a detailed visualisation of these processes is not obtainable experimentally. However, a comparison of the results obtained from both computational simulations and experimental techniques is required to benchmark the accuracy and correctness of computationally developed methods.

Historically, the calculation of ion pair association constants from computer simulations has been complicated due to the difficulty in validating metal ion force fields for solution simulations. To overcome this requires accurate ion force fields which are to be used in the benchmarking of a potential of mean force (PMF) and free energy perturbation (FEP) method for calculating experimentally consistent association constants. Thus the main objective of this thesis is to develop a method which can be used to calibrate PMFs between ion pairs, so as to obtain accurate ion association constants. To achieve this goal reliable force fields are required. Accordingly parameters for metal ions in several metal sulfate solutions (i.e. $Mg^{2+}SO_4^{2-}$, $Ca^{2+}SO_4^{2-}$, $Mn^{2+}SO_4^{2-}$, $Fe^{2+}SO_4^{2-}$, $Co^{2+}SO_4^{2-}$, $Ni^{2+}SO_4^{2-}$, $Cu^{2+}SO_4^{2-}$ and $Zn^{2+}SO_4^{2-}$) which are important in physical and biophysical experiments are first developed. The calibration method comprising of FEP and PMF calculations is then developed using the above parameters and by testing calculated association constants with experimentally determined association constants.

Further objectives are to understand the solvation structures and the nature of ion pair formation mechanisms for several metal sulfates in aqueous media and to examine the effects of ion pairing on the transport properties of the industrially important platinum group metal (PGM) chloro-anion complexes, with ammonium counterions, (i.e. $(Y)_2[PtCl_4]^{2-}$, $(Y)_2[PdCl_4]^{2-}$, $(Y)_2[PtCl_6]^{2-}$, $(Y)_2[PdCl_6]^{2-}$, $(Y)_2[IrCl_6]^{2-}$, $(Y)_2[OsCl_6]^{2-}$, $(Y)_2[RuCl_6]^{2-}$, $(Y)_3[IrCl_6]^{3-}$, $(Y)_3[RhCl_6]^{3-}$ and $(Y)_3[RuCl_6]^{3-}$, where $Y = NH_4^+$) in aqueous media.

1.8 Thesis Overview

The work contained in this thesis is primarily concerned with the development of a methodology aimed at predicting accurately ion solution association constants, K_as (Chapter 5). The long term objective of this method is the prediction of K_as for PGM chloro-anion species with several counterions and non-charged species. This data is to be used as a tool aiding in the design of PGM separation methods.

At present, this goal cannot be achieved without access to accurate molecular mechanics force fields, as shown in Chapter 5. Therefore the re-parameterisation and parameterisation of several PGM chloro-anion species was conducted (Chapter 8). However, the validity of these anion parameters cannot be proven due to a lack of available experimental data at this present time and as such the results obtained must be viewed within the accuracy of the parameterisation and simulation methods.

Chapter 2 contains an introduction to the partition function and the configurational integral which connects the intermolecular potential of a chemical system to its thermodynamic properties, such as free energy. The chapter then gives a description of the partial association of ions, i.e. ion pairing, and shows how the association constant, K_a, for ion pairing can be calculated from the potential of mean force. The chapter closes with a brief overview of Molecular Mechanics and Molecular Dynamics with an emphasis on simulation methods and considerations used in this thesis.

In Chapter 3 a description of several available free energy methods, including those used in this thesis to calculate and calibrate the potential of mean force (PMF), is given. Chapter 4 details the experimental and computational analysis methods used to determine ion hydration and pairing structures, hydration numbers and transport properties. This includes a detailed description of the ultrasonic interferometry method employed in this thesis to calculate the hydration numbers of several metal sulfate ions in aqueous solution.

Chapter 5 reports the development of a Metal Solution Force Field (MSFF) which incorporates divalent alkaline earth metals, i.e. Magnesium and Calcium, and the divalent first row transition metals, i.e. Cobalt, Copper, Iron, Manganese, Nickel and Zinc. The ion pairing association constants of these ions with a sulfate counterion are studied. The association constants are derived from the PMF, which is calibrated using a free energy

perturbation method. This method of calibrating the PMF is shown to provide association constants that are consistent with experimental values determined from ultrasonic and dielectric relaxation spectroscopy or conductivity measurements.

In Chapter 6 the MSFF ion parameters are used to study the solvation structures and the nature of ion pair formation mechanisms for metal sulfates in aqueous media. The radial and spatial distribution functions, described in Chapter 4, are used to calculate the hydration numbers of each of the ion pairing species, revealing that the transition from free ions to contact ion pairs involves the loss of water molecules, where the number of solvent molecules lost is dependant on the size of the cation. This is correlated with the experimental hydration numbers calculated at several concentrations using density and ultrasonic velocities measurements, as described in Chapter 4.

Chapter 7 presents an overview of the parameterisation methodology and considerations involved in developing a force field to model transition metal complexes. These considerations include the choice of a water model and the use of experimental versus *ab initio* data to fit parameters. The chapter is concluded by giving a brief overview of the quantum chemistry fundamentals and considerations required when using *ab initio* derived data for parameter fitting.

Finally, in Chapter 8 the MSFF is extended to include the industrially important platinum group metal (PGM) chloro-anion complexes. The hydration structure about the PGM chloro-anion complexes and the role ammonium counter-ions plays in disrupting that solvent structure when ammonium PGM chloro-anion contact ion pairs are formed is studied. The solvent structure is studied using radial and spatial distribution functions and transport properties are studied by calculating diffusion coefficients, ion hydration numbers and water residence times, as described in Chapter 4.

1.9 References

1. Luscombe, N.M., Laskowski, R.A., and Thornton, J.M., *Amino acid-base interactions: a three-dimensional analysis of protein-DNA interactions at an atomic level.* Nucleic Acids Res., 2001. **29**(13): p. 2860-2874.
2. Schliwa, M. and Woehlke, G., *Molecular motors.* Nature, 2003. **422**(6933): p. 759-765.
3. Zhou, Y.F., Morais-Cabral, J.H., Kaufman, A., and MacKinnon, R., *Chemistry of ion coordination and hydration revealed by a K+ channel-Fab complex at 2.0 angstrom resolution.* Nature, 2001. **414**(6859): p. 43-48.
4. Suezawa, H., Yoshida, T., Hirota, M., Takahashi, H., Umezawa, Y., Honda, K., Tsuboyama, S., and Nishio, M., *The CH center dot center dot center dot pi interaction as an important factor in the crystal packing and in determining the structure of clathrates.* J. Chem. Soc.-Perkin Trans. 2, 2001(11): p. 2053-2058.
5. Collins, M.D., Hummer, G., Quillin, M.L., Matthews, B.W., and Gruner, S.M., *Cooperative water filling of a nonpolar protein cavity observed by high-pressure crystallography and simulation.* Proc. Natl. Acad. Sci. U. S. A., 2005. **102**(46): p. 16668-16671.
6. Zhou, R.H., Huang, X.H., Margulis, C.J., and Berne, B.J., *Hydrophobic collapse in multidomain protein folding.* Science, 2004. **305**(5690): p. 1605-1609.
7. Young, T., Abel, R., Kim, B., Berne, B.J., and Friesner, R.A., *Motifs for molecular recognition exploiting hydrophobic enclosure in protein-ligand binding.* Proc. Natl. Acad. Sci. U. S. A., 2007. **104**(3): p. 808-813.
8. Pratt, L.R., *Molecular theory of hydrophobic effects: "She is too mean to have her name repeated.".* Annu. Rev. Phys. Chem., 2002. **53**(1): p. 409-436.
9. Maayan, G., *Conformational control in metallofoldamers: Design, synthesis and structural properties.* Eur. J. Org. Chem., 2009. **33**: p. 5699-5710.
10. Benjamin, I., *Structure and Dynamics of Hydrated Ions in a Water-Immiscible Organic Solvent.* J. Phys. Chem. B, 2008. **112**(49): p. 15801-15806.

11. Vaisman, II and Berkowitz, M.L., *Local structural order and molecular associations in water-DMSO mixtures - Molecular-dynamics study.* J. Am. Chem. Soc., 1992. **114**(20): p. 7889-7896.
12. Tummala, N.R. and Striolo, A., *Hydrogen-bond dynamics for water confined in carbon tetrachloride-acetone mixtures.* J. Phys. Chem. B, 2008. **112**(34): p. 10675-10683.
13. Bloch, K. and Lawrence, C.P., *Hydrogen bond lifetimes and clustering of methanol in carbon tetrachloride solutions.* J. Phys. Chem. B. **114**(1): p. 293-297.
14. Akilan, C., Hefter, G., Rohman, N., and Buchner, R., *Ion association and hydration in aqueous solutions of copper(II) sulfate from 5 to 65 degrees C by dielectric spectroscopy.* J. Phys. Chem. B, 2006. **110**(30): p. 14961-14970.
15. Akilan, C., Rohman, N., Hefter, G., and Buchner, R., *Temperature effects on ion association and hydration in $MgSO_4$ by dielectric spectroscopy.* ChemPhysChem, 2006. **7**(11): p. 2319-2330.
16. Atkinson, G. and Petrucci, S., *Ion association of magnesium sulfate in water at 25 degrees.* J. Phys. Chem., 1966. **70**(10): p. 3122-3128.
17. Bester-Rogac, M., Babic, V., Perger, T.M., Neueder, R., and Barthel, J., *Conductometric study of ion association of divalent symmetric electrolytes: I. CoSO4, NiSO4, CuSO4 and ZnSO4 in water.* J. Mol. Liq., 2005. **118**(1-3): p. 111-118.
18. Bester-Rogac, M., *Electrical conductivity of concentrated aqueous solutions of divalent metal sulfates.* J. Chem. Eng. Data, 2008. **53**(6): p. 1355-1359.
19. Marcus, Y., *Ion Solvation*. 1st ed. 1985, New York: John Wiley and Sons Ltd, New York.
20. Tasker, P.A., Tong, C.C., and Westra, A.N., *Co-extraction of cations and anions in base metal recovery.* Coord. Chem. Rev., 2007. **251**(13-14): p. 1868-1877.
21. Ritcey, G.M. and Ashbrook, A.W., *Process Metallurgy, Vol. 1: Solvent Extraction: Principles and Applications to Process Metallurgy, Pt. 1*. 1979: Elsevier.
22. Ritcey, G., *Solvent extraction in hydrometallurgy: Present and future.* Tshingua Science and Technology, 2006. **11**(2): p. 137-152.

23. Bernardis, F.L., Grant, R.A., and Sherrington, D.C., *A review of methods of separation of the platinum-group metals through their chloro-complexes.* React. Funct. Polym., 2005. **65**(3): p. 205-217.
24. Tomlinson, E., Jefferies, T.M., and Riley, C.M., *Ion-pair high-performance liquid-chromatography.* J. Chromatogr., 1978. **159**(3): p. 315-358.
25. Gloor, R. and Johnson, E.L., *Practical aspects of reverse phase ion-pair chromatography.* J. Chromatogr. Sci., 1977. **15**(9): p. 413-423.
26. Stone, A.J. and Editor, *The Theory of Intermolecular Forces.* 1996: Oxford University Press, USA.
27. Murrell, J.N. and Jenkins, A.D., *Properties of Liquids and Solutions: Second Edition*. 1994. 303 pp.
28. Hinchliffe, A., *Chemical Modeling From Atoms To Liquids.* 1999, Chichester, West Sussex: John Wiley & Sons, Ltd.
29. Israelachvili, J.N., *Intermolecular and surface Forces / Jacob N. Israelachvili*. 1991, London ; San Diego :: Academic Press.
30. Leach, A.R., *Molecular Modelling: Principles and Applications.* 1st and 2nd ed. 2001: Longman.
31. Cramer, C.J., *Essentials of Computational Chemistry, 2nd Edition.* 2004: John Wiley & Sons Ltd.
32. Engkvist, O., Astrand, P.O., and Karlstrom, G., *Accurate intermolecular potentials obtained from molecular wave functions: Bridging the gap between quantum chemistry and molecular simulations.* Chem. Rev., 2000. **100**(11): p. 4087-4108.
33. Steiner, T., *The hydrogen bond in the solid state.* Angew. Chem., Int. Ed., 2002. **41**(1): p. 48-76.
34. Pal, S.K., Zhao, L.A., and Zewail, A.H., *Water at DNA surfaces: Ultrafast dynamics in minor groove recognition.* Proc. Natl. Acad. Sci. U. S. A., 2003. **100**(14): p. 8113-8118.
35. Naidoo, K.J. and Chen, J.Y.J., *The role of water in the design of glycosidic linkage flexibility.* Mol. Phys., 2003. **101**(17): p. 2687-2694.

36. Wyttenbach, T. and Bowers, M.T., *Hydration of biomolecules.* Chem. Phys. Lett., 2009. **480**(1-3): p. 1-16.

37. Wang, T., Du, D.G., and Gai, F., *Helix-coil kinetics of two 14-residue peptides.* Chem. Phys. Lett., 2003. **370**(5-6): p. 842-848.

38. Ben-Amotz, D. and Underwood, R., *Unraveling water's entropic mysteries: A unified view of nonpolar, polar, and ionic hydration.* Acc. Chem. Res., 2008. **41**(8): p. 957-967.

39. Franks, F. and Editor, *Water: A Comprehensive Treatise, Vol. 6: Recent Advances*. 1979. 455 pp.

40. Sharp, K.A. and Vanderkooi, J.M., *Water in the half shell: Structure of water, focusing on angular structure and solvation.* Acc. Chem. Res., 2009. **43**(2): p. 231-239.

41. Mason, P.E. and Brady, J.W., *"Tetrahedrality" and the relationship between collective structure and radial distribution functions in liquid water.* J. Phys. Chem. B, 2007. **111**(20): p. 5669-5679.

42. Head-Gordon, T. and Hura, G., *Water structure from scattering experiments and simulation.* Chem. Rev., 2002. **102**(8): p. 2651-2669.

43. Berendsen, H.J.C., Postma, J.P.M., Van Gunsteren, W.F., and Hermans, J., *Interaction Models for Water in Relation to Protein Hydration*, in *Intermolecular Forces*, B. Pullman, Editor. 1981, Reidel Publishing Co.: Dordrecht, Holland. p. 331-342.

44. Berendsen, H.J.C., Grigera, J.R., and Straatsma, T.P., *The missing term in effective pair potentials.* J. Phys. Chem., 1987. **91**(24): p. 6269-6271.

45. Jorgensen, W.L., Chandrasekhar, J., Madura, J.D., Impey, R.W., and Klein, M.L., *Comparison of simple potential functions for simulations liquid water.* J. Chem. Phys., 1983. **79**(2): p. 926-935.

46. Bragg, S.W.H., *The Crystal Structure of Ice.* Proc. Phys. Soc. London, 1921. **34**(1): p. 98.

47. Soper, A.K., *The radial distribution functions of water and ice from 220 to 673 K and at pressures up to 400 MPa.* Chem. Phys., 2000. **258**(2-3): p. 121-137.

48. Kusalik, P.G. and Svishchev, I.M., *The spatial structure in liquid water*. Science, 1994. **265**(5176): p. 1219-1221.
49. Svishchev, I.M. and Kusalik, P.G., *Structure in liquid water - A study of spatial-distribution functions.* J. Chem. Phys., 1993. **99**(4): p. 3049-3058.
50. Svishchev, I.M., Zassetsky, A.Y., and Kusalik, P.G., *Solvation structures in three dimensions.* Chem. Phys., 2000. **258**(2-3): p. 181-186.
51. Soper, A.K., *Probing the structure of water around biological molecules: concepts, constructs and consequences.* Physica B, 2000. **276**: p. 12-16.
52. Moyer, B.A. and Bonnessen, P.V., in *Supramolecular Chemistry of Anions*, A. Bianchi, K. Bowman-James, and E. Garcia-Espana, Editors. 1997, Wiley-VCH, New York.
53. Bell, K.J., Westra, A.N., Warr, R.J., Chartres, J., Ellis, R., Tong, C.C., Blake, A.J., Tasker, P.A., and Schroder, M., *Outer-sphere coordination chemistry: Selective extraction and transport of the [PtCl6](2-) anion.* Angew. Chem., Int. Ed., 2008. **47**(9): p. 1745-1748.
54. Debye, P. and Hückel, E., *The theory of electrolytes. I. Lowering of freezing point and related phenomena* Phys. Z., 1923. **24**: p. 185-206.
55. Collins, K.D., Neilson, G.W., and Enderby, J.E., *Ions in water: Characterizing the forces that control chemical processes and biological structure.* Biophys. Chem., 2007. **128**(2-3): p. 95-104.
56. Conway, B.E., *Hydration in Chemistry and Biophysics.* 1981: Elsevier Scientific Publishing Company.
57. Bockris, J.O.M. and Reddy, A.K.N., *Modern Electrochemistry, Vol. 2A. Ionics.* 2nd ed. 1998: Plenum Press.
58. Marcus, Y., *Ion properties.* 1997, New York: Marcel Dekker, Inc.
59. Nancollas, A.H., *Interactions in Electrolyte Solutions.* 1966: Elsevier ((s.l.)).
60. Burgess, J., *Ions in Solution: Basic Principles of Chemical Interactions.* 1988: Ellis Horwood.
61. Ben-Naim, A., *Water and Aqueous Solutions.* 1974: Plenum Press, New York.
62. Ohtaki, H. and Radnai, T., *Structure and dynamics of hydrated ions.* Chem. Rev., 1993. **93**(3): p. 1157-1204.

63. Marcus, Y., *Effect of ions on the structure of water: Structure making and breaking.* Chem. Rev., 2009. **109**(3): p. 1346-1370.

64. Rode, B.M., Schwenk, C.F., Hofer, T.S., and Randolf, B.R., *Coordination and ligand exchange dynamics of solvated metal ions.* Coord. Chem. Rev., 2005. **249**(24): p. 2993-3006.

65. Lepsik, M. and Field, M.J., *Binding of calcium and other metal ions to the EF-Hand loops of calmodulin studied by quantum chemical calculations and molecular dynamics simulations.* J. Phys. Chem. B, 2007. **111**(33): p. 10012-10022.

66. Lippard, S.J., *The inorganic side of chemical biology.* Nat. Chem. Biol., 2006. **2**(10): p. 504-507.

67. Hille, B., *Ionic Channels of Excitable Membranes.* 2nd ed. 1992: Sinauer Associates.

68. Doyle, D.A., Cabral, J.M., Pfuetzner, R.A., Kuo, A.L., Gulbis, J.M., Cohen, S.L., Chait, B.T., and MacKinnon, R., *The structure of the potassium channel: Molecular basis of K+ conduction and selectivity.* Science, 1998. **280**(5360): p. 69-77.

69. Berridge, M.J., Bootman, M.D., and Lipp, P., *Calcium - a life and death signal.* Nature, 1998. **395**(6703): p. 645-648.

70. Bowen, L.M. and Dupureur, C.M., *Investigation of restriction enzyme cofactor requirements: A relationship between metal ion properties and sequence specificity.* Biochemistry, 2003. **42**(43): p. 12643-12653.

71. Adhikari, S., Toretsky, J.A., Yuan, L.S., and Roy, R., *Magnesium, essential for base excision repair enzymes, inhibits substrate binding of N-methylpurine-DNA glycosylase.* J. Biol. Chem., 2006. **281**(40): p. 29525-29532.

72. Barnham, K.J. and Bush, A.I., *Metals in Alzheimer's and Parkinson's diseases.* Curr. Opin. Chem. Biol., 2008. **12**(2): p. 222-228.

73. Youcef, M.H., Benabdallah, T., Ilikti, H., and Reffas, H., *Equilibrium studies on the synergic liquid-liquid extraction process of copper(II) from sulphate media with mixtures of some bidentate mono-Schiff bases and acyclic polyether non-ionic surfactant in chloroform.* Solvent Extr. Ion Exch., 2008. **26**(5): p. 534-555.

74. Beer, P.D. and Gale, P.A., *Anion recognition and sensing: The state of the art and future perspectives.* Angew. Chem., Int. Ed., 2001. **40**(3): p. 486-516.

75. Born, M., *Volumes and heats of hydration of ions.* Z. Angew. Phys., 1920. **1**: p. 45-48.

76. Babu, C.S. and Lim, C., *Theory of ionic hydration: Insights from molecular dynamics simulations and experiment.* J. Phys. Chem. B, 1999. **103**(37): p. 7958-7968.

77. Grossfield, A., *Dependence of ion hydration on the sign of the ion's charge.* J. Chem. Phys., 2005. **122**(2): p. 024506.

78. Rick, S.W. and Berne, B.J., *The aqueous solvation of water - A comparison of continuum methods with molecular-dynamics.* J. Am. Chem. Soc., 1994. **116**(9): p. 3949-3954.

79. Hummer, G., Pratt, L.R., and Garcia, A.E., *Free energy of ionic hydration.* J. Phys. Chem., 1996. **100**(4): p. 1206-1215.

80. Jayaram, B., Fine, R., Sharp, K., and Honig, B., *Free-energy calculations of ion hydration - An analysis of the Born model in terms of microscopic simulations.* J. Phys. Chem., 1989. **93**(10): p. 4320-4327.

81. Marcus, Y., *Electrostriction, ion solvation, and solvent release on ion pairing.* J. Phys. Chem. B, 2005. **109**(39): p. 18541-18549.

82. Bernal, J.D. and Fowler, R.H., *A Theory of Water and Ionic Solution, with Particular Reference to Hydrogen and Hydroxyl Ions.* J. Chem. Phys., 1933. **1**(8): p. 515-548.

83. Frank, H.S. and Wen, W.-Y., *Structural aspects of ion-solvent interaction in aqueous solutions: A suggested picture of water structure.* Discuss. Faraday Soc., 1957. **24**: p. 133-140.

84. Gurney, R.W., *Ionic Processes in Solution.* 1953: McGraw-Hill Book Co., New York.

85. Impey, R.W., Madden, P.A., and McDonald, I.R., *Hydration and mobility of ions in solution.* J. Phys. Chem., 1983. **87**(25): p. 5071-5083.

86. Bruneval, F., Donadio, D., and Parrinello, M., *Molecular dynamics study of the solvation of calcium carbonate in water.* J. Phys. Chem. B, 2007. **111**: p. 12219-12227.

87. Bock, C.W., Katz, A.K., and Glusker, J.P., *Hydration of zinc ions - a comparison with magnesium and beryllium ions.* J. Am. Chem. Soc., 1995. **117**(13): p. 3754-3763.

88. Bock, C.W., Markham, G.D., Katz, A.K., and Glusker, J.P., *The arrangement of first- and second-shell water molecules around metal ions: effects of charge and size.* Theor. Chem. Acc., 2006. **115**(2-3): p. 100-112.

89. Chaban, G.M., Huo, W.M., and Lee, T.J., *Theoretical study of infrared and Raman spectra of hydrated magnesium sulfate salts.* J. Chem. Phys., 2002. **117**(6): p. 2532-2537.

90. Erras-Hanauer, H., Clark, T., and van Eldik, R., *Molecular orbital and DFT studies on water exchange mechanisms of metal ions.* Coord. Chem. Rev., 2003. **238**: p. 233-253.

91. Azam, S.S., Hofer, T.S., Bhattacharjee, A., Lim, L.H.V., Pribil, A.B., Randolf, B.R., and Rode, B.M., *Beryllium(II): The Strongest Structure-Forming Ion in Water? A QMCF MD Simulation Study.* J. Phys. Chem. B, 2009. **113**(27): p. 9289-9295.

92. Megyes, T., Balint, S., Peter, E., Grosz, T., Bako, I., Krienke, H., and Bellissent-Funel, M.C., *Solution structure of $NaNO_3$ in water: Diffraction and molecular dynamics simulation study.* J. Phys. Chem. B, 2009. **113**(13): p. 4054-4064.

93. Asthagiri, D., Pratt, L.R., Paulaitis, M.E., and Rempe, S.B., *Hydration structure and free energy of biomolecularly specific aqueous dications, including Zn^{2+} and first transition row metals.* J. Am. Chem. Soc., 2004. **126**(4): p. 1285-1289.

94. Obst, S. and Bradaczek, H., *Molecular dynamics simulations of zinc ions in water using CHARMM.* J. Mol. Model., 1997. **3**(6): p. 224-232.

95. Frick, R.J., Hofer, T.S., Pribil, A.B., Randolf, B.R., and Rode, B.M., *Structure and dynamics of the UO_2^{2+} Ion in aqueous solution: An ab initio QMCF MD study.* J. Phys. Chem. A, 2009. **113**(45): p. 12496-12503.

96. Laage, D. and Hynes, J.T., *A molecular jump mechanism of water reorientation.* Science, 2006. **311**(5762): p. 832-835.

97. Patra, M. and Karttunen, M., *Systematic comparison of force fields for microscopic simulations of NaCl in aqueous solutions: Diffusion, free energy of hydration, and structural properties.* J. Comput. Chem., 2004. **25**(5): p. 678-689.

98. Cannon, W.R., Pettitt, B.M., and McCammon, J.A., *Sulfate anion in water - model structural, thermodynamic, and dynamic properties.* J. Phys. Chem., 1994. **98**(24): p. 6225-6230.

99. Lienke, A., Klatt, G., Robinson, D.J., Koch, K.R., and Naidoo, K.J., *Modeling platinum group metal complexes in aqueous solution.* Inorg. Chem., 2001. **40**(10): p. 2352-2357.

100. Mason, P.E., Dempsey, C.E., Neilson, G.W., and Brady, J.W., *Nanometer-scale ion aggregates in aqueous electrolyte solutions: Guanidinium sulfate and guanidinium thiocyanate.* J. Phys. Chem. B, 2005. **109**(50): p. 24185-24196.

101. Naidoo, K.J., Klatt, G., Koch, K.R., and Robinson, D.J., *Geometric hydration shells for anionic platinum group metal chloro complexes.* Inorg. Chem., 2002. **41**(7): p. 1845-1849.

102. Marcus, Y. and Hefter, G., *Ion pairing.* Chem. Rev., 2006. **106**(11): p. 4585-4621.

CHAPTER 2

Ion Solutions and Molecular Simulations

2.1 Introduction

Ions and their formation salts play an integral part in several biological processes, within which they behave as either active participants, as cofactors or as salt buffers. In chemistry, ions affect chemical reaction rates, ion-exchange mechanisms and solvent extraction. In both these cases the metal ions are generally found as hydrated complexes or may be associated with hydrated ions of opposite charge to form ion pairs. The properties of hydrated ions have been studied by examining the effect an ion salt has on water upon dissolution, leading to macroscopic observables. To obtain a fundamental picture of ion hydration at the microscopic level one requires a method that describes ion hydration at the atomic level. Computer simulations allow for this level of observation via statistical mechanics, thus linking the microscopic and macroscopic observables of chemical systems containing ions.

Over the past several decades, computer simulations on molecular liquids and solutions consisting of hundreds to several thousands of atoms and molecules have been carried out. These calculations involve several simulation options, e.g. periodic or spherical boundary conditions, and use statistical mechanics to predict measurable observables, quantities which have proved to be not significantly different from experiment [1]. In the following sub-sections the theory related to the partial association of ion pairs, the statistical mechanics and computational methods used in this thesis are discussed. The statistical mechanics related equations and descriptions given below are derived from *Introduction to Modern Statistical Mechanics* by D. Chandler [2], *Statistical Mechanics* by D. A. McQuarrie [3], *Properties of Liquids and solutions, 2nd Edition* by J. N. Murrell and A. D. Jenkins [4] and the review by Trzesnuak et al. [5].

2.2 The Configurational Integral

A successful theory to describe the liquid state must be able to explain macroscopic properties using a knowledge of the intermolecular potential only [4]. This requires that the relative arrangements of atoms and molecules in the liquid state must be accurately

described. The principles of classical statistical mechanics provide us with such a description.

Thermodynamic functions can be calculated from the sum of a system's intermolecular potential, *U*, using partition functions. This is shown by examining the functional form of the Helmholtz free energy, *A*. For a molecular system at constant volume, *V*, temperature, *T*, and number of particles, *N*, the Helmholtz free energy is given as

$$A = -k_B T \ln Q \tag{2.1}$$

in which k_B is the Boltzmann constant, *T* the temperature and *Q* the canonical partition function. For *N* indistinguishable particles, *Q* is given as

$$Q = \frac{1}{N! h^{sN}} \int \cdots \int e^{-\beta H(p,q)} dp\, dq \tag{2.2}$$

which contains an integral over all coordinates $q \equiv (q_1, q_2, \ldots, q_{sN})$ and conjugate momenta $p \equiv (p_1, p_2, \ldots, p_{sN})$ for the classical energy, $H(p, q)$, and *s* degrees of molecular freedom.

The probability of an individual configurational arrangement having energy $H(p, q)$, is given as

$$P(p,q) = e^{-\beta H(p,q) Q^{-1}} \tag{2.3}$$

It follows that the ensemble average $\langle Q \rangle$ of a quantity $Q(p, r)$ is given as

$$\langle Q \rangle = \int \cdots \int Q(p,q) P(p,q) dp\, dq \tag{2.4}$$

However, the description so far does not take into account the intermolecular potential, $U(q)$. To achieve this, $H(p, q)$ must be written as the sum of internal, $E_{k,A}$, and

translational energies, $E_{trans,A}$, of the molecules and $U(q)$, provided $U(q)$ is independent of the internal state of the molecules, such that

$$H(p,q)=\sum_{A}\left(E_{k,A}+E_{trans,A}\right)+U(q) \tag{2.5}$$

By substituting Equation 2.5 into Equation 2.2 the partition function is given as

$$Q=\left(\frac{q_{\text{int}}q_t}{V}\right)\frac{Z_N}{N!} \tag{2.6}$$

where q_{int} and q_t are the internal and translational partition functions for a single molecule, V is the system volume and Z_N is the classical configurational integral, written as

$$Z_N=\int_V e^{-\beta U(q)}dq \tag{2.7}$$

2.3 Partial Ion Association: Ion Pairing

Ion pairing is described as the association of oppositely charged ions in electrolyte solutions to form distinct physicochemical species. Ion pairs arise when ion-ion interactions become significant with respect to ion-solvent interactions[1], as a result of decreased inter-ion distances which usually occur at high electrolyte concentration and in solvents with low relative permittivities [6-8]. The change in an ion-ion interaction upon pairing results in a change in the ion pair potential energy, which is either raised or lowered relative to its value at infinite dilution (which is zero by definition), depending on whether or not the ions have the same or opposite charges.

[1] The major contribution to ion pair formation is attributed to nondirectional long-range electrostatic forces, usually modelled by Coulomb's law, attenuated by the relative permittivity of the solvent.

Ion pair formation was originally introduced by Bjerrum to account for the behaviour of ionophores in solvents of low dielectric constant [7]. It has since been developed further by several others, namely, Fouss, Justice and Justice, Eigen and Tamm and Barthel [8]. Ion pairs are considered to be formed if two oppositely charged ions are a distance, *r*, apart and $a < r < R$. Where *a*, is the distance of closest approach[2] and *R* is a specified cutoff distance, beyond which the ions are considered 'free'. In addition, upon pairing, ion pairs must exist for a period longer than the time taken for them to diffuse over *r*.

The formation of an ion pair $CA^{(c-a)+}$, in electrolyte solution of concentration *x*, between a cation C^{c+} and an anion A^{a-} can be represented by the ion-pairing equilibrium

$$C^{C+} + A^{a-} \leftrightarrow CA^{(c-a)+} \tag{2.8}$$

and can be quantified in terms of the equilibrium concentration quotient, K_a, or in terms of the standard association constant, K_a^o, at infinite dilution together with a ratio of the activity coefficients, such that

$$K_a = \frac{(1-\alpha)}{\alpha^2 x} = K_a^o \frac{\gamma_{\pm}'^2}{\gamma_{IP}} \tag{2.9}$$

where α and $(1-\alpha)$, obtained experimentally, are the mole fractions of the cation and anion respectively. $\gamma_{\pm}'$ and γ_{IP} are the ionic activity coefficients of the free ions and ion pair [8]. In this work, the ion pairing (association) of several metal sulfate aqueous electrolyte solutions is studied. The 'Eigen mechanism' of ion pairing models these systems best. This is a multistage ion association mechanism developed by the work of Eigen and Tamm, based on the interpretation of sound absorption relaxation processes in electrolyte solutions [9-11]. In this model, ion pairs are defined by the solvent separation of the

[2] The distance of closest approach, *a*, arises from the strong repulsive force originating from the overlap electron densities of the respective ions forming an ion pair.

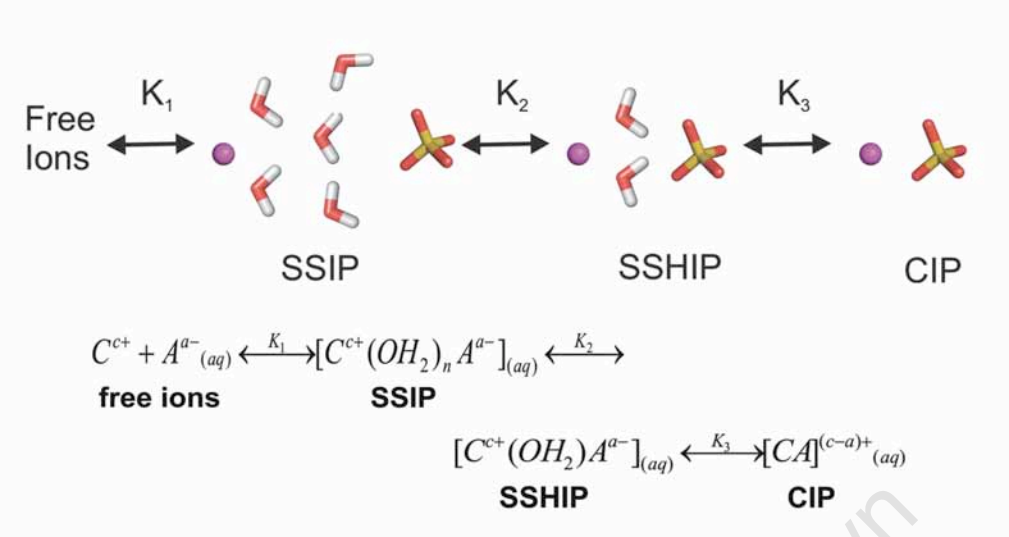

Figure 2.1. Different types of solvated ion pairs and the rate coefficients (K_1, K_2 and K_3) for the formation of each of the ion pairs through solvent loss or gain.

pairing ions and follow a three step mechanism, giving rise to three types of solvated ion pairs, as shown in Figure 2.1. These are the solvent-separated ion pair (SSIP), which has two solvent layers (the primary solvation shells of each of the ions stays intact) between the ions, the solvent-shared ion pair (SSHIP), which has one solvent layer removed between the ions and the contact ion pair (CIP), where no solvent is found between the pairing ions. Conversion from free ions to SSIP occurs rapidly, via diffusion control, whereas conversion from SSIP to CIP is controlled by elimination of solvent molecules and is a slower reaction.[3]

Eigen and Tamm related experimental relaxation times, τ_i, to the short-lived concentration of a relevant ion pair, [IP], relative to the equilibrium ion-paring concentration $[IP]_{eq}$, such that;

$$\frac{d[IP]}{dt} = \frac{\left([IP] - [IP]_{eq}\right)}{\tau_i} \tag{2.10}$$

[3] Ion pairing results in a diminution of the solvent electrostriction around the ions, resulting in a change of the molar volume of the electrolyte.

The reciprocal of τ_i can then be expressed in terms of the forward and backward rate coefficients, K_i, of the ion pairing species, giving a simplified chemical equilibrium as

$$\underset{\textit{free ions}}{A+C} \overset{K_1}{\longleftrightarrow} \underset{\textit{SSIP}}{A\,||\,C} \overset{K_2}{\longleftrightarrow} \underset{\textit{SSHIP}}{A\,|\,C} \overset{K_3}{\longleftrightarrow} \underset{\textit{CIP}}{AC} \tag{2.11}$$

where the association constant for the formation of the ion pairs in Equation 2.11 from the free ions is given as

$$K_a = K_1\left(1 + K_2 + K_2K_3\right) \tag{2.12}$$

2.4 K_a, Work Theory and the Potential of Mean Force

The free energy associated with the formation of an ion pair between two particles at infinite dilution, known as the potential of mean force (PMF), first introduced by Kirkwood in 1935 [12], can be related to K_a through statistical mechanics. To show this a brief description of the link between radial distribution functions and the PMF between two molecules, e.g. ions *A* and *B*, is first required.

This is achieved by considering the reduced configurational distribution function of a system composed of *N* particles in the canonical ensemble. The probability that molecule 1 is in dr_1 at r_1 and molecule 2 is in dr_2 at r_2 independently of the configuration of the remaining N-2 particles is given by

$$P^{(2/N)}\left(r_1, r_2\right) = \int dr_3 \int dr_4 \cdots \int dr_N P\left(r^N\right) \tag{2.13}$$

where $P(r^N)$ is the configurational distribution given in Equation 2.3. The corresponding radial distribution function $g(r_1, r_2)$, gives the probability of finding a pair of particles at a internuclear distance *r* relative to a completely random distribution at the same density and is given as

$$g(r_1, r_2) = g(r) = \frac{V^2 P^{(2/N)}(r_1, r_2)}{N^2} \tag{2.14}$$

The reduced configurational distribution functions are related to the Helmholtz free energy by

$$g(r) = e^{-\beta W(r)} \tag{2.15}$$

where $W(r)$ is the reversible work between molecules 1 and 2, or the potential of mean force, and is written as

$$W(r) = -k_B T \ln g(r) - \ln C \tag{2.16}$$

where C is a constant. Since the process is performed reversibly at constant N, V and T, W(r) is the change in Helmholtz free energy. Thus

$$\Delta A(r) = W(r) = -k_B T \ln g(r) - \ln C \tag{2.17}$$

The link between Equations 2.12 and 2.17 is obtained by calculation of the equilibrium rate, as proposed by Prue [13]. Provided two ions *A* and *B* have spherical geometries, the volume *V* available to *B* to form an ion pair *AB* with *A* is equal to $4\pi r^2 \Delta r$, where Δr is the variation in distance due to the motion of ions. If $N_A V C_{AB}$ is the number of ion pairs[4] in *V* and $N_A V C_A$ is the number of unpaired *A* ions, then the ratio between these numbers is given as

$$\frac{N_A V C_{AB}}{N_A V C_A} = \frac{4\pi r^2 \Delta r N_A V C_B}{V} \tag{2.18}$$

[4] The value N_A is Avagadro's number.

From this the association constant K_a can be obtained, such that

$$K_a = \frac{C_{AB}}{C_A C_B} = 4\pi r^2 \Delta r N_A \tag{2.19}$$

Upon association, K_a can be expressed in terms of the potential of mean force, where

$$K_a = 4\pi N_A \int_0^{r_{max}} r^2 e^{-\beta W(r)} dr = 4\pi N_A \int_0^{r_{max}} r^2 g(r) dr \tag{2.20}$$

where r_{max} is the upper limit of integration.

2.5 Computer Simulations and Statistical Mechanics

2.5.1 Molecular Mechanics

Computational chemistry combined with statistical mechanics allows for the calculation of several properties of a chemical system. However, these calculations are limited by the inability to calculate all possible conformations of a chemical system, thus the complete potential energy surface is unobtainable [14, 15]. To overcome the limitations in sampling phase-spaces, simple mathematical functions are often used to describe the relationship between a chemical system's structure and its potential energy.

Molecular mechanics (MM) or empirical force field calculations, as the approach is often known, is made possible by introducing several assumptions. The most important of these is the Born-Oppenheimer approximation which allows for a system's potential energy to be written as a function of its nuclear coordinates [14]. In addition to these assumptions, parameters developed from experimental data and high level quantum mechanical calculations are included in the mathematical equation to complete the force

field. Finally, the same mathematical equation can be applied to different chemical systems by changing these parameters.

A force field can be interpreted in terms of the intra- and inter-molecular forces within a system and is divided into bonded and non-bonded terms.[5] Energetic penalties are then associated with the deviation of a chemical system from a reference state, as expressed in the parameters. In the molecular modelling program CHARMM [16, 17], the implemented energy function $U\left(\vec{R}\right)$, denoting the potential energy of a chemical system as a function of the positions $\vec{R}$, is given as:

$$\begin{aligned} U\left(\vec{R}\right) = & \sum_{bonds} K_b\left(r - r_o\right)^2 + \sum_{angles} K_\theta\left(\theta - \theta_o\right)^2 + \sum_{torsions} K_\phi\left(1 + \cos\left(n\phi - \delta\right)\right) \\ & + \sum_{impropers} K_\varphi\left(\varphi - \varphi_o\right)^2 + \sum_{Urey-Bradley} K_{UB}\left(r_{1,3} - r_{1,3,o}\right)^2 \\ & + \sum_{electrostatic} \frac{q_i q_j}{4\pi\varepsilon_e r_{ij}} + \sum_{VDW} \varepsilon_{ij}\left[\left(\frac{R_{\min,ij}}{r_{ij}}\right)^{12} - 2\left(\frac{R_{\min,ij}}{r_{ij}}\right)^{6}\right] \end{aligned} \tag{2.21}$$

where K_b, K_θ , K_φ, K_{UB}, and K_ω are the bond, angle, dihedral angle, Urey–Bradley and improper dihedral angle force constants. With b, θ, φ, S, and ω representing the bond length, bond angle, dihedral angle, Urey–Bradley 1,3-distance and improper torsion angle, with the equilibrium values denoted with a subscript zero. Furthermore, the torsion term includes n, which is the periodicity of a torsion, and δ, the phase of the torsion. Non-bonded interactions include the Coulomb and Lennard-Jones (LJ) 6-12 terms. ε is the LJ well depth, $R\min_{,ij}$ is the distance at the LJ minimum, q is the partial atomic charge, ε_e is the effective dielectric constant and r_{ij} is the distance between atoms i and j.

2.5.2 Molecular Dynamics

Computer simulation methods such as molecular dynamics (MD) and Monte Carlo (MC)

[5] The more sophisticated polarisable and class II force fields contain additional terms but still retain the form as shown in Equation 1.

give a detailed insight into the dynamics and molecular interactions of chemical systems, from which structural and thermodynamic properties can be inferred and ultimately compared with experimental measurements.

MD and MC methods allow for lengthy simulations (10ns-100ns) for medium to large systems consisting of 10^3-10^5 atoms, by implementing either empirical energy functions as shown in Equation 2.21 or semi-empirical functions and can be used in the study of conformational fluctuations and solvent interactions. In this work, MD is used exclusively.

MD simulations describe the motion of atoms using Hamiltonian dynamics. The Hamiltonian of a chemical system can be written as a function of time, *t*, such that

$$H\left(p^N, q^N, t\right) = \sum_{i=1}^{N} \frac{p_i^2}{2m_i} + V\left(p^N, q^N, t\right) \tag{2.22}$$

for *N* generalised momenta and coordinates, and where $V(p^N, q^N, t)$ is the potential energy of the system. In MD simulations the potential energy is a function of the position r^N so that

$$H\left(r^N, p^N\right) = \sum_{i=1}^{N} \frac{p_i^2}{2m_i} + V\left(r^N\right) \tag{2.23}$$

where r_i is the three dimensional position of atom *i* and p_i the corresponding momentum. The equations of motion for Hamiltonian dynamics are given by the following differential equations,

$$\vec{p}_i = -\frac{\partial H}{\partial \vec{r}_i} = -\nabla_i V\left(r^N\right) \tag{2.24}$$

$$\vec{r}_i = -\frac{\partial H}{\partial \vec{p}_i} = \frac{p_i}{m_i} \tag{2.25}$$

and by integrating these equations we can calculate the time evolution of a chemical system and its properties.

2.5.2.1 Boundary Conditions

The treatment of boundaries and boundary effects plays an important role in molecular simulations. If treated correctly these methods enable the calculation of the macroscopic properties from a simulation using a relatively small numbers of particles.

Periodic boundary conditions allow for the simulation of the bulk properties of a molecule or solvent without energy fluctuations caused by surface molecule interactions [1, 14]. When using periodic boundary conditions, a system's atoms are enclosed in a regular cell that is space-filling and is usually in the shape of a cube or truncated octahedron. This cell is then replicated using rigid translations to give a periodic array (Figure 2.2a). In a simulation, periodic boundary conditions are imposed as follows: particles' movements within a central cell are replicated in the other cells and when a particle passes the boundary of the central cell, its coordinates are modified so that it reappears on the opposite side of the central cell, with an identical velocity. The overall effect of periodic boundary conditions is the elimination of surface effects, allowing not only for the interaction of any particle with all other particles but also with a replicated image of others but not with itself in an adjacent cell [14].

An alternative method to periodic boundary conditions is the use of stochastic boundary conditions in which a system is divided into three spherical regions. The central region, often called the reaction zone, contains all particles within a given radius, R_1, of the site of interest. Particles within this region are modeled as per the chosen level of theory and using standard molecular dynamics. The second region, the buffer region, uses Langevin dynamics and the third region, the reservoir region, contains all particles outside the reaction and buffer zones. The particles within this region are generally restrained so as to keep them within the shell between R_2 and R_3 (Figure 3.2b) and to maintain a spherical shape. Stochastic boundary conditions are generally employed in the study of macromolecules such as enzymes and cyclodextrins [14]. In this thesis the use of stochastic boundary conditions is limited to the calculation of free energies.

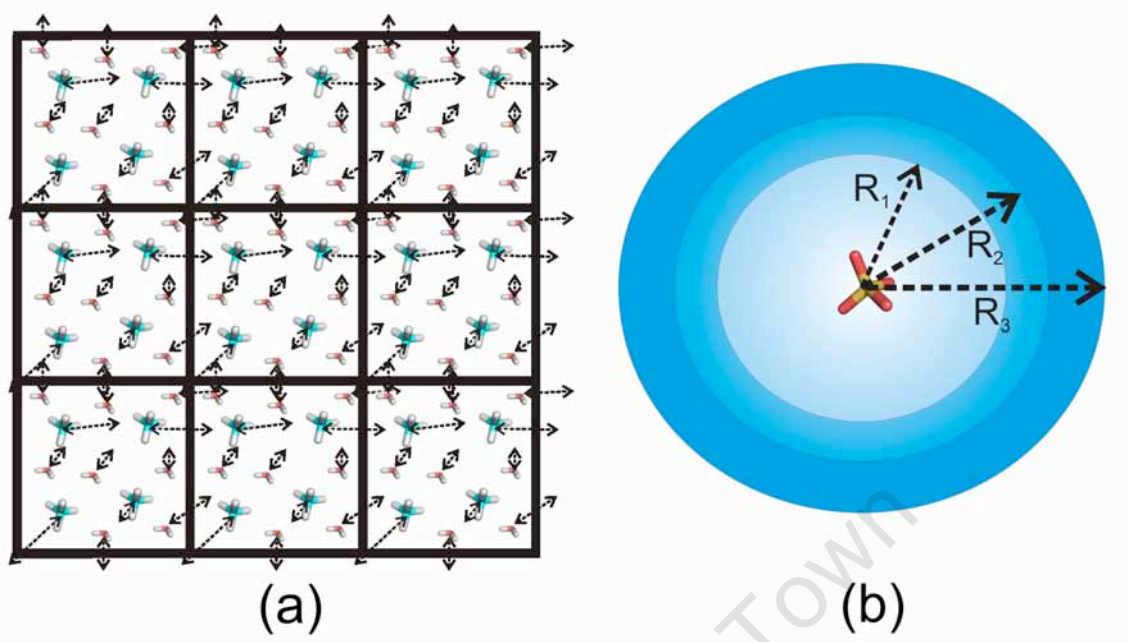

Figure 2.2. Boundary conditions; (a) periodic boundaries in two dimensions and (b) stochastic boundary conditions showing the reaction zone (within radius R_1), the buffer region (shell between R_1 and R_2) and reservoir regions (shell between R_2 and R_3).

2.5.2.2 Truncating the Potential

The computationally expensive part of any molecular dynamics simulation is the calculation of non-bonded interactions. This is as a result of the number of non-bonded terms for a pairwise model which equals N(N-1)/2, where N is the number of atoms. In other words, it is of the order of the square of the number of atoms in the system. Implementation of non-bonded cutoff limits reduces this computational expense. This approach is regarded as a valid assumption because as the van der Waals interaction energies rapidly tend to zero as the distance between atoms increases. When implementing the Lennard-Jones potential, the potential energy at a distance of 2.5 x $R_{min,ij}$ is generally 1% of its value at a distance of $R_{min,ij}$ [1, 14]. However, the non-bonded interactions beyond the cut-off cannot be simply omitted. This would result in a

discontinuity in the potential function at the cut-off distance, creating an artificial increase in the kinetic energy of a system, resulting in fluctuations in the system's temperature [18]. This problem is overcome by applying *shifting* and *switching* functions [1, 19] as implemented in CHARMM.

The shifting function, as the name implies, shifts the whole potential by a constant, υ_c, so that the new shifted potential, υ_s, is zero at the cutoff distance, and is given as

$$\upsilon_s(r_{ij}) = \begin{cases} \upsilon(r_{ij}) - \upsilon_c & r_{ij} \le r_c \\ 0 & r_{ij} > r_c \end{cases} \tag{2.26}$$

However, this method may result in substantial changes in calculated thermodynamic properties and is not generally preferred. An alternative approach is the switching function. This method applies a smoothing polynomial over a relatively small range (between r_{on} and r_{off}) to bring the potential to zero at the cutoff distance r_{off}, and is given as

$$\upsilon_w(r_{ij}) = \begin{cases} \upsilon(r_{ij}) & r_{ij} \le r_{on} \\ \upsilon(r_{ij}) \times \left(\dfrac{\left(r_{off}^2 - r_{ij}^2\right)\left(r_{off}^2 + 2r_{ij}^2 - 3r_{on}^2\right)}{\left(r_{off}^2 - r_{on}^2\right)^3} \right) & r_{on} < r_{ij} < r_{off} \\ 0 & r_{ij} > r_{off} \end{cases} \tag{2.27}$$

In addition to choosing a method to avoid a discontinuous derivative, one also needs to deal with atomic groupings appropriately. Atom-based or group-based cutoffs can be employed. In general, group-based cutoffs are employed as these avoid fluctuations near the cutoff point which result from the long range nature of electrostatic monopole-monopole interactions (which vary as r^{-1}). In group-based methods, each molecule is divided into a collection of connected atoms forming neutral charged groups and interactions occur on a group-based scheme, using the centre of mass of each group to define cutoff distances. This offers better energy conservation for the system modeled, provided that groups are relatively small [19].

2.5.2.3 Long-Range Interactions

In charged systems, more rigorous methods are required to treat the long range charge-charge interactions, which decay as r^{-1} (r^{-n}, where n is the system dimension). The Ewald summation, first devised in 1921 [20] is routinely used, and is accepted as one of the best ways in which to include all effects of long-range forces into simulations. The use of the Ewald method has increased with the development of several efficient N log$N$ methods that calculate the reciprocal space term.

The Smooth Particle Mesh Ewald method (PME) [21, 22] is implemented in CHARMM due to its speed, accuracy, and application to constant pressure systems, which interpolate point charges to grid points using B-spline algorithms, followed by reciprocal space calculation using a three-dimensional fast Fourier transform (3-DFFT) [21]. This is used throughout the work described in this thesis. Alternative methods are the fast Fourier Poisson [23] and Particle-Particle–Mesh [24] Ewald methods.

A brief description of the Ewald summation method is given below. The total charge-charge contribution, V, to the potential energy comprises the following.

1. Interactions within the central box (cube).
2. Interactions of the central box with all the image boxes.
3. Interaction of the image boxes with the surrounding medium.

An expression which incorporates all these interactions is given in Equation 2.28. In this equation the left most series excludes $i = j$ terms for $n = 0$. The number of charges per image box is N, while r_{ij} is the minimum distance between charges q_i and q_j. A box is generally positioned at a cubic lattice point n defined as: (n_xL, n_yL, n_zL), where L is the length of the cube.

$$V = \frac{1}{2}\sum_{|n|=0}^{\infty}\sum_{i=1}^{N}\sum_{j=1}^{N}\frac{q_i q_j}{4\pi\varepsilon_0 \mid r_{ij} + n \mid} \qquad (2.28)$$

This summation is conditionally convergent, as is the sum of all the negative terms in the series. In the Ewald method conditional convergence is overcome by converting the overall summation into two more complicated but rapidly convergent sums. The initial set of charges is surrounded by a Gaussian distribution of equal magnitude but opposite sign (calculated in real space) to which a cancelling set of distributions must be added (calculated in reciprocal space). The functional form of these Gaussian distributions can be modified by altering the parameter α.

The 'real space' summation, as expressed in Equation 2.29, generally converges rapidly and its convergence rate is dependent on the width of the Gaussian distributions. The parameter, α, should therefore be chosen in such a way that the only terms in the series are those for which $|n| = 0$. Equation 2.30 is the complementary error function.

$$V = \frac{1}{2}\sum_{|n|=0}^{\infty}\sum_{i=1}^{N}\sum_{j=1}^{N}\frac{q_i q_j erfc(\alpha\,|\,r_{ij}+n\,|)}{4\pi\varepsilon_0\,|\,r_{ij}+n\,|} \tag{2.29}$$

$$erfc(x) = \frac{2}{\sqrt{\pi}}\int_{x}^{\infty}\exp(-t^2)dt \tag{2.30}$$

A second series of distributions (Equation 2.31) is then added, canceling the first series (the real space summation). This second summation is performed in 'reciprocal space', where the vectors, k, are defined as $k = 2\pi n/L^2$.

$$V = \frac{1}{2}\sum_{k\neq 0}^{\infty}\sum_{i=1}^{N}\sum_{j=1}^{N}\frac{q_i q_j}{4\pi\varepsilon_0}\frac{1}{\pi L^3}\frac{4\pi^2}{k^2}\exp(-\frac{k^2}{4\alpha^2})\cos(k.r_{ij}) \tag{2.31}$$

The real space summation includes the interaction of each Gaussian with itself. This must be subtracted, as shown in Equation 2.32

$$V = -\frac{\alpha}{\sqrt{\pi}} \sum_{k=1}^{N} \frac{q_k^2}{4\pi\varepsilon_0} \tag{2.32}$$

Last, a correction term (Equation 2.33) is needed to account for the medium surrounding the image boxes. This correction is only applicable if the surrounding medium has a permittivity of 1, i.e. a vacuum.

$$V_{correction} = \frac{2\pi}{3L^3} \left| \sum_{i=1}^{N} \frac{q_i}{4\pi\varepsilon_0} \mathbf{r}_i \right|^2 \tag{2.33}$$

The overall Ewald summation energy is thus calculated as the sum of Equations 2.28-2.33.

2.5.3 Ensemble Sampling from Simulations

An ensemble, introduced in Section 2.1 is a collection of points in phase space which conforms to the conditions of a thermodynamic state [14, 25]. This means an ensemble is a collection of all possible systems with identical macroscopic (thermodynamic) states but different microscopic states which allows for comparison between the results from a simulation with those of a physical experiment.

In order to calculate observables and determine macroscopic properties from a simulation, it is necessary to ensure that the simulation is run under the correct thermodynamic conditions, with sufficient sampling. This condition only holds true with assumption of the *ergodic hypothesis*, which states that for a system containing *N* particles, undergoing a stationary random process, the calculated time average, *t*, of a particular property, *A*, is related to the macroscopic observable value, A_{obs}, such that

$$A_{obs} = \iint A(p,q) e^{-\beta H(p,q)} dpdq = \lim_{t\to\infty} \frac{1}{t} \int_0^{\infty} A(p(t), q(t)) dt \tag{2.34}$$

Since the contribution of high energy regions of phase space to ensemble averages is extremely small, they can be ignored. It is therefore important to statistically determine the extent to which phase space has been sampled in a simulation.

The main difficulty in phase space sampling for both MD and MC methods is the existence of high energy barriers which split phase space into disconnected regions. This leads to insufficient sampling of phase space, even with extremely long simulation runs. This problem can be overcome by using non-Boltzmann MD methods, which are discussed in Chapter 3.

In this work the canonical (*NVT*) ensemble is used.[6] The temperature is held constant using a method based on a Nose-Hoover thermostat, whereby a heat bath is coupled to a chemical system. This alters the system Hamiltonian by adding an additional degree of freedom with a coordinate *s*, a corresponding momenta p_s, with mass *Q* [26-28].

Alternatively the volume and temperature can be held constant by altering the velocities of all the particles in order to achieve and maintain a desired temperature. This alteration can be achieved by either scaling the velocities as a factor of the ratio of the actual and desired temperature of the system [14], or by re-assigning velocities according to a Maxwell-Boltzmann distribution. The most important part of velocity re-assignment is the frequency at which the process occurs. A high frequency of velocity re-assignments generally results in artificial behaviour in a dynamics system and may lead to excessive equilibration periods.

[6] The thermodynamic constants, N, P, V, E and T are the number of particles, pressure, volume, energy and temperature respectively.

2.6 References

1. Allen, M.P. and Tildesley, D.J., *Computer Simulations of Liquids*. 1989, Oxford: Clarendon Press.
2. Chandler, D., *Introduction to Modern Statistical Mechanics*. 1987, New York: Oxford University Press.
3. McQuarrie, D.A., *Statistical Mechanics*. 2000, Sausalito, CA: University Science Books.
4. Murrell, J.N. and Jenkins, A.D., *Properties of Liquids and Solutions: Second Edition*. 1994. 303 pp.
5. Trzesniak, D., Kunz, A.P.E., and van Gunsteren, W.F., *A comparison of methods to compute the potential of mean force.* ChemPhysChem, 2007. **8**(1): p. 162-169.
6. Marcus, Y., *Ion Solvation*. 1st ed. 1985: John Wiley and Sons Ltd.
7. Szwarc, M., *Ions and ion pairs.* Acc. Chem. Res., 1969. **2**(3): p. 87-96.
8. Marcus, Y. and Hefter, G., *Ion pairing.* Chem. Rev., 2006. **106**(11): p. 4585-4621.
9. Eigen, M. and Tamm, K., *Schallabsorption in elektrolytlosungen als folge chemischer relaxation.1. Relaxationstheorie der mehstufigen dissoziation.* Z. Elektrochem., 1962. **66**(2): p. 93-107.
10. Eigen, M. and Tamm, K., *Schallabsorption in elektrolytlosungen als folge chemischer relaxation. 2. Messergebenisse und relaxationsmechanismen fur 2-2-wertige elektrolyte.* Z. Elektrochem., 1962. **66**(2): p. 107-121.
11. Petrucci, S., ed. *Ionic Interactions from Fused Solutions to Fused Salts, Vol. 1: Equilibrium and Mass Transport.* Vol. 1. 1971, Academic, New York: New York.
12. Kirkwood, J.G., *Statistical mechanics of fluid mixtures.* J. Chem. Phys., 1935. **3**(5): p. 300-313.
13. Prue, J.E., *Ion pairs and complexes - Free energies enthalpies and entropies.* J. Chem. Educ., 1969. **46**(1): p. 12-+.
14. Leach, A.R., *Molecular Modelling: Principles and Applications.* 1st and 2nd ed. 2001: Longman.
15. Lewars, E., *Computational Chemistry: Introduction to the Theory and Applications of Molecular and Quantum Mechanics.* Vol. Second. 2004: Kluwer Academic Publishers.

16. Brooks, B.R., Bruccoleri, R.E., Olafson, B.D., States, D.J., Swaminathan, S., and Karplus, M., *CHARMM - A program for macromolecular energy, minimization, and dynamics calculations.* J. Comput. Chem., 1983. **4**(2): p. 187-217.

17. Brooks, B.R., Brooks, C.L., Mackerell, A.D., Nilsson, L., Petrella, R.J., Roux, B., Won, Y., Archontis, G., Bartels, C., Boresch, S., Caflisch, A., Caves, L., Cui, Q., Dinner, A.R., Feig, M., Fischer, S., Gao, J., Hodoscek, M., Im, W., Kuczera, K., Lazaridis, T., Ma, J., Ovchinnikov, V., Paci, E., Pastor, R.W., Post, C.B., Pu, J.Z., Schaefer, M., Tidor, B., Venable, R.M., Woodcock, H.L., Wu, X., Yang, W., York, D.M., and Karplus, M., *CHARMM: The biomolecular simulation program.* J. Comput. Chem., 2009. **30**(10): p. 1545-1614.

18. Tasaki, K., McDonald, S., and Brady, J.W., *Observations concerning the treatment of long-range interactions in molecular-dynamics simulations.* J. Comput. Chem., 1993. **14**(3): p. 278-284.

19. Steinbach, P.J. and Brooks, B.R., *New spherical-cutoff methods for long-range forces in macromolecular simulation.* J. Comput. Chem., 1994. **15**(7): p. 667-683.

20. Ewald, P.P., *Die Berechnung optischer und elektrostatischer Gitterpotentiale.* Annalen der Physik, 1921. **369**(3): p. 253-287.

21. Essmann, U., Perera, L., Berkowitz, M.L., Darden, T., Lee, H., and Pedersen, L.G., *A smooth particle mesh Ewald method.* J. Chem. Phys., 1995. **103**(19): p. 8577-8593.

22. Darden, T., York, D., and Pedersen, L., *Particle mesh Ewald - An N.log(N) method for Ewald sums in large systems.* J. Chem. Phys., 1993. **98**(12): p. 10089-10092.

23. York, D. and Yang, W.T., *The fast Fourier-Poisson method for calculating Ewald sums.* J. Chem. Phys., 1994. **101**(4): p. 3298-3300.

24. Hockney, R.W. and Eastwood, J.W., *Computer Simulations Using Particles.* 1981: New York: McGraw-Hill.

25. Frenkel, D. and Smit, B., *Understanding Molecular Simulation From Algorithms to Applications*. Second ed. Computational Science Series. 2002: Elsevier.

26. Lamoureux, G., MacKerell, A.D., and Roux, B., *A simple polarizable model of water based on classical Drude oscillators.* J. Chem. Phys., 2003. **119**(10): p. 5185-5197.

27. Nose, S., *A molecular-dynamics method for simulations in the canonical ensemble.* Mol. Phys., 1984. **52**(2): p. 255-268.

28. Hoover, W.G., *Canonical dynamics - Equilibrium phase-space distributions.* Phys. Rev. A, 1985. **31**(3): p. 1695-1697.

CHAPTER 3

Free Energy Methods

3.1 Introduction

The free energies of molecular systems describe their tendencies to do work (i.e. associate and react), making free energy arguably the most important quantity in thermodynamics [1]. Therefore, accurate prediction of this quantity using molecular theory is important and a seductive goal [2]. Molecular dynamics and Monte Carlo methods are routinely used to implement free energy calculations for several chemical systems. Examples of these are: the solvation of small molecules, including ions in aqueous [3-5] and non-aqueous media [6]; the study of environmental effects on chemical reactions in solutions [7, 8] and enzymes [9, 10], including relative equilibrium and rate constants, along with the enthalpies and entropies associated with chemical reactions. Allowing for in-depth analysis of chemical processes [2].

3.2 Free Energy Methods

The free energy and the partition function (Section 2.1), cannot be directly calculated from either experiment or simulation due to their dependence on measuring of all available configurational space of a chemical system, which is infinite and thus not measurable. However, free energy differences between closely related states can be calculated using both experimental and computational studies. In this thesis the focus is on the calculation of free energy changes using computational methods. Examples of these are the free energy perturbation (FEP) and thermodynamic integration (TI) methods, which relate the free energy difference (i.e. the change in Helmholtz free energy, ΔA, or the change in Gibbs free energy, ΔG) between two states, A and B, to a thermodynamic ensemble average dependant on the potential energy properties of the individual states [11, 12], such as that given in equation 3.4.

FEP and TI methods employ the coupling parameter approach [2] in which the Hamiltonian of each state (A and B) is written as a function of the coupling parameter, λ,

$$H(p,q,\lambda_A) = H_A(p,q) \tag{3.1}$$

$$H(p,q,\lambda_B) = H_B(p,q) \tag{3.2}$$

where the Hamiltonians $H_A(p, q)$ and $H_A(p, q)$ correspond to states A and B and $\lambda_A + \lambda_B = 1$.

It follows that the partition function in the canonical ensemble can be written as a function of λ, given as

$$Q(\lambda) = \frac{1}{h^{3N} N!} \iint e^{-\beta H(p,q,\lambda)} dp\, dq \tag{3.3}$$

Since the Helmholtz free energy, A, depends on, $Q(\lambda)$, it too can be written in terms of λ, such that

$$A(\lambda) = -k_B T \ln Q(\lambda) \tag{3.4}$$

and the calculable change in the Helmholtz free energy, ΔA, can also be written as a function of λ.

3.2.1 Free Energy Perturbation

The free energy perturbation method, predicated by Kirkwood's introduction of the continuous coupling parameter in his integral studies of fluid systems [13] and further developed by Zwanzig [14], treats the change in states as a set of discrete steps. However, representation of the free energy by an analytical function is only valid for simple model systems. To overcome this drawback the Helmholtz free energy differences between related systems A and B, represented by Hamiltonians H_A and H_B, can be written as

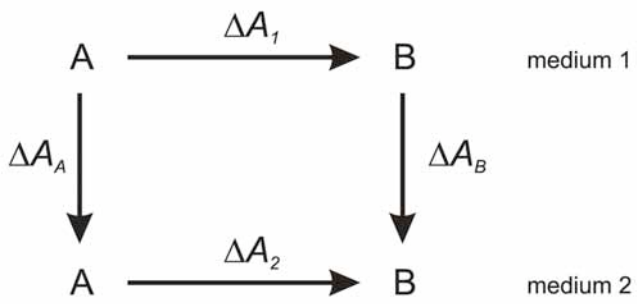

Figure 3.1. A general free energy cycle used to calculate the difference in free energy of converting molecule A to molecule B in different mediums.

$$\Delta A = A_B - A_A = -k_B T \ln\left\langle e^{-\beta(H_B - H_A)} \right\rangle_{\lambda_A} \tag{3.5}$$

where $\langle\ \rangle_{\lambda_A}$ refers to an ensemble average over a system represented by H_A. This can be generalised by writing H_A and H_B as functions of λ, such that λ varies from 0, where $H = H_A$, to 1 where $H = H_B$.

The free energy difference between molecular systems is calculated using a thermodynamic cycle, as shown in Figure 3.1, and a method used to carry out a smooth conversion from an initial to final state. The preferred conversion methods are the single- and dual-topology methods [2, 15]. In this work the dual-topology method is used, whereby the topologies of both the initial and final states co-exist throughout the perturbation, such that

$$H(p,q,\lambda) = \lambda H_B(p,q) + (1-\lambda) H_A(p,q) \tag{3.6}$$

In this method the atom types and internal parameters are never changed. The two sets of atoms interact with the rest of the system but not with each other and their relative contributions to H(p, q, λ) change as λ changes.

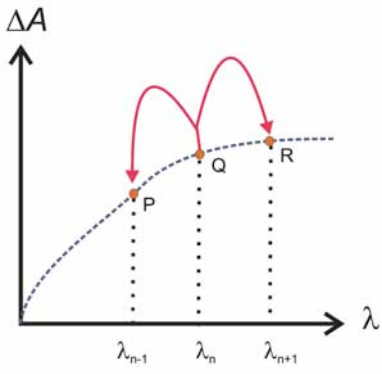

Figure 3.2. Schematic representation of the inner workings of the double-wide sampling method.

The final point to consider in FEP calculations is the data collection method. When a molecular system is perturbed from one state to another data collection is required at each λ point, where λ points are chosen such that the energy difference between the points is less than $2kT$.

In this thesis the double-wide [16] sampling method is employed as opposed to the overlap and double-ended methods [2, 17, 18]. In the double-wide sampling method (Figure 3.2), Q is an intermediate point (where $\lambda = n$) at which a simulation is performed. Q is then used to calculate the average free energy differences $\Delta A_{n\rightarrow n-1}$ for $\lambda_n \rightarrow \lambda_{n-1}$ ($Q \rightarrow P$) and $\Delta A_{n\rightarrow n+1}$ for $\lambda_n \rightarrow \lambda_{n+1}$ ($Q \rightarrow R$). This provides an efficient manner in which to calculate the overall free energy difference, given by

$$\Delta A = \frac{1}{2}\sum_{n=0}^{n-1}\left[\Delta A_{n\rightarrow n-1} + \Delta A_{n\rightarrow n+1}\right] \tag{3.7}$$

and, if need be, allows for the addition of several extra increments in λ.[1] However, increasing the number of λ points does not necessarily improve the calculated free energy difference.

[1] The addition of several increments is possible because free energies are state functions, thus the calculated energies are independent of the path taken between systems *A* and *B*.

3.2.2 Thermodynamic Integration

The alternative to free energy perturbation is thermodynamic integration, where the difference in free energy is calculated by integration of an ensemble average over λ, giving the free energy as

$$\Delta A = \int_{\lambda=0}^{\lambda=1} \left\langle \frac{\partial H(p,q,\lambda)}{\partial \lambda} \right\rangle_{\lambda} d\lambda \tag{3.8}$$

where the Hamiltonian of the initial state is given by $H_{(\lambda=0)}$, and $H_{(\lambda=1)}$ represents the Hamiltonian of the final state.[2] The derivative of the Hamiltonian can be evaluated using equation 3.6, giving

$$\Delta A = \int_0^1 \langle H_B(p,q) - H_A(p,q) \rangle_{\lambda} \, d\lambda \tag{3.9}$$

This is the equation used to calculate the free energy differences states in computational simulations. The numerical evaluation of the change in free energy is carried out using numerical integration of equation 3.9, by setting up several simulations at discrete values of λ between 0 and 1 and calculating the free energy differences.

3.3 The Potential of Mean Force

Free energy perturbation and thermodynamic integration methods obtain free energies as a function of chemical mutations from state *A* to state *B*. The Potential of Mean Force (PMF) (Section 2.3), first introduced by Kirkwood in 1935 [13], allows any reasonably chosen parameter to link states *A* to *B* to be represented as a reaction coordinate, ξ, where

[2] In the alternative to FEP and TI, the *slow growth* method, the Hamiltonian of the system is only changed by an infinitesimally small amount.

$$\xi(q) \equiv \xi(q_1, q_2, \ldots, q_{sN}) \tag{3.10}$$

is a function of the positions of the particles in a system and could represent a distance, angle, a torsional angle or a combination of the mentioned quantities, whereby an n-dimensional energy hypersurface can be described by n-dimensional reaction coordinates [19].

In this thesis the potential of mean force, *W*, is calculated as a function of the distance *r*, where *r* defines the reaction coordinate, between two ions *A* and *B* in a fixed system containing *N* solvent molecules. The reaction coordinate probability $P(r')$, integrated over phase space, is given as

$$P(r') = \frac{\int \cdots \int e^{-\beta H(p,q)} \delta(r' - r(q)) dpdq}{\int \cdots \int e^{-\beta H(p,q)} dpdq} \tag{3.11}$$

From equation (3.11) it follows that in terms of the partition function, the reaction coordinate probability can be written as

$$P(r') = \frac{Q_R(r')}{Q} \tag{3.12}$$

and by substituting equation 3.12 into equation 2.1, the Helmholtz free energy, here defined as the potential of mean force, $W(r')$ is given as

$$W(r') = -k_B T \ln P(r') - kT \ln Q \tag{3.13}$$

The potential of mean force may be obtained using several methods. The simplest of these is the calculation of $W(r')$ from unbiased molecular dynamics simulations. In this method, $W(r')$ between ions *A* and *B*, due to the *N* solvent molecules is obtained from the radial distribution function, $g(r')$, between ions *A* and *B*, as introduced in Section 2.3, such that

$$W(r') = -k_B T \ln g(r') + C \tag{3.14}$$

where

$$g(r') = \frac{P(r')}{4\pi(r')^2} \tag{3.15}$$

and C is a constant that allows the user freedom to choose the energy scale [20-22].

The formulation given in Equation 3.14 is the classical way of computing the potential of mean force via inversion of the radial distribution function from molecular dynamics [1, 23, 24]. However, with reference to electrolyte solutions, this method only works for solutions containing several ion pairing species and is in practice ineffective for dilute electrolyte solutions containing one ion pair [25] or for any system containing energy regions separated by high energy barriers [26].[3]

In order to overcome these barriers, alteration of the potential energy function is required and for this reason several methods have been developed. Potentials of mean force for several systems have been calculated using constraint-biased real space methods which apply holonomic constraints or restraints on reaction coordinates and employ either forces or finite differences of the physical Hamiltonian [26-28]. However, the use of constraint-biased methods requires the introduction of metric tensor corrections in order to deal with quenching of momenta on constrained atoms [29-31] and unlike methods employing Cartesian coordinates, these methods need to compute and apply logarithmic Jacobian corrections [25-27, 31-34]. Alternatively, umbrella-biased simulations have been conducted with a harmonic biasing potential and a multiple window sampling approach along with window matching weighted histogram analysis. Adaptive umbrella sampling methods using non-harmonic and non-local biasing potentials have also been employed.

[3] Barriers greater than $2kT$ are not usually crossed in standard molecular dynamics simulations, thus limiting the sampling of conformational to regions of low energy.

The following sub-sections give a brief description of the adaptive biasing force method, umbrella and adaptive umbrella sampling methods and the Free Energy from Adaptive Reaction Coordinate Forces (FEARCF) method used in this thesis.

3.3.1 Adaptive Biasing Force

The adaptive biasing force method proposed by Darve and Pohorille [34] presents an adaptive way to drive a simulation over free energy barriers, using the thermodynamic integration method. This is achieved by calculating a running average of the force along a reaction coordinate and applying the negative of the force as an external force to the atoms involved in the reaction coordinate. This allows the simulation to proceed in a continuous motion along the reaction coordinate.

The derivative of the free energy, defined by a distance reaction coordinate r is given as

$$\frac{\partial A(r)}{\partial r} = \left\langle -F(r) + \frac{\partial \ln|J|}{\partial r} \middle| r \right\rangle \tag{3.16}$$

where $F(r)$ is the mean force at r and J is the Jacobian. The free energy can be calculated by integrating the negative of the sum in equation 3.16, such that

$$\Delta A(r) = -\int_{r_0}^{r} \left\langle F(r') + \frac{\partial \ln|J|}{\partial r} \right\rangle dr' \tag{3.17}$$

The average force, $F(r\hat{})$, is calculable from molecular dynamics simulations using the finite differences method. However, calculation of the Jacobian correction term is required [33-35].

3.3.2 Umbrella Sampling

Methods employing harmonic restraints or umbrella potentials are free from momentum quenching problems and do not forbid the use of constraints involving restrained atoms. Umbrella sampling, developed by Torrie and Valeau [36], generates non-Boltzmann sampled simulations by adding an external biasing potential focusing the sample on a range r_i-r_0, centered on r_0, given by

$$\omega(r_i; r_0) = \frac{1}{2} k(r_i - r_0)^2 \tag{3.18}$$

This is done in order to enhance the sampling along the reaction coordinate, *r*, and is restricted to the range r_i-r_0 to help improve configurational sampling. The new Hamiltonian is given as

$$H(R) = H(p, r) + \omega(r_i, r_0) \tag{3.19}$$

Computational limitations generally make biasing simulations over the whole range of a reaction coordinates impossible. This is overcome by using the windowing method, which biases different simulations to small overlapping ranges, usually by taking the biasing potential to be the sum of harmonic terms, in the reaction coordinate space. Several simulations are then run, starting in each of the harmonic wells. Ultimately, the harmonic biases are removed and the results are recombined to obtain the potential of mean force.

3.3.3 Adaptive Umbrella Sampling

An alternative biasing potential method regularly employed is the Adaptive Umbrella Sampling method, first described by Mezei [37]. In this method the biasing potential is iteratively adapted based on the probability distributions of the reaction coordinates

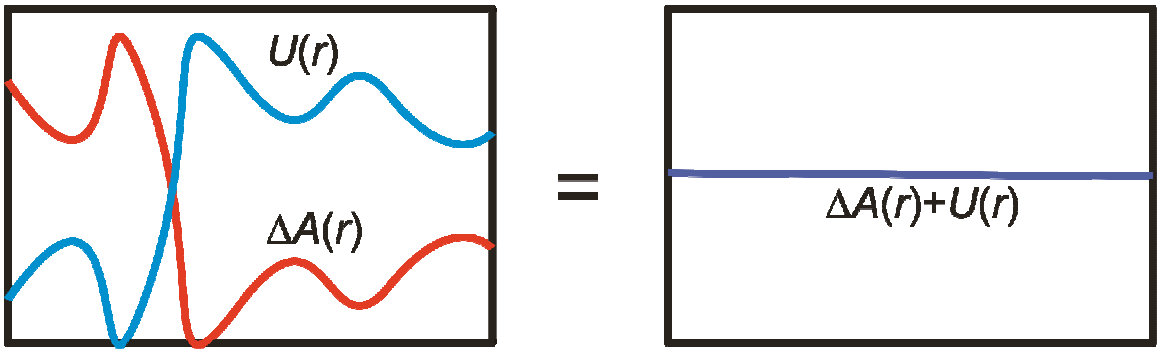

Figure 3.3. Applying the inverse, $U(r)$, of the potential of mean force, $A(r)$, as a biasing potential flattens the energy landscape. This means that there is an equal probability of sampling any location along a reaction coordinate, r.

sampled during previous simulations. Unlike conventional umbrella sampling which only applies a bias to a small region along the reaction coordinate, adaptive umbrella sampling applies a bias along the entirety of r. This biasing potential, $\omega(r)$, is calculated from the probability distributions of previous simulations and is set to zero in the initial simulation. The calculation converges when uniform sampling along r is achieved, at which point the biasing potential is the exact inverse of the potential of mean force, as shown in Figure 3.3.

3.3.3.1 Free Energy from Adaptive Reaction Coordinate Forces

In this work, the potential of mean force for ion pairs is calculated using the FEARCF method, developed by Strumpfer and Naidoo [19], based on the adaptive umbrella sampling method of Mezei, and makes use of histograms to construct probability distributions from which free energy surfaces can be calculated.

To increase the sampling in the high-energy regions of r, an adaptive force, $F(r)$, is applied along the reaction coordinate, r, where r is designated as the vector between the centres of masses of the ions in the ion pairs studied. The force $F(r)$, is shown as

$$F(r) = -\frac{\partial U(r)}{\partial r} \tag{3.20}$$

where $U(r)$ is the inverse of the latest guess of the free energy surface, i.e. $W(r) = -U(r)$. This approach forces the ions into poorly sampled regions of conformational and configurational space over a series of simulations until uniform sampling (or as close as possible) over r is achieved. In this work potential of mean force calculations are started by applying a zero biasing potential in the first simulation. Based on the sampling of the first and subsequent simulations new adaptive biasing forces are calculated and applied to successive simulations (as in the case of adaptive umbrella sampling). This is achieved by applying the weighted histogram method [38, 39], as described below, to arrive at subsequent biasing force estimates.

3.3.3.2 Weighted Histogram Analysis Method

The Weighted Histogram Analysis Method (WHAM) by Kumar *et al.* [38, 39] is a technique whereby biased probability distributions from several simulations are combined using computed weighting factors for each of the probability distribution histograms to obtain the best estimate for the actual unbiased probability distribution, as produced from adaptive umbrella and FEARCF (Section 3.3.3.1) simulations.

For a pair of ions in a system the procedure is as follows: the degree of freedom (the distance, r, between two ions) is divided into k bins; the biased probability distribution for simulation i is sorted into the k bins to give an unnormalised histogram, n_{ij}, based on the values of r sampled during the simulation; after j simulations, the unbiased probability histogram, p_k, is found by iterating the following equations:

$$p_k = \frac{\sum_j n_{j,k}}{\sum_j N_j f_j c_{j,k}} \tag{3.21}$$

and

$$f_j = \frac{1}{\sum_k e^{-\beta U_i(r_k)} p_k} \tag{3.22}$$

with

$$N_j = \sum_k n_{j,k} \,. \tag{3.23}$$

In the above equations, f_j, are the free energy weighting factors, N_j is the total number of configurations stored during the *j*th simulation and $U_j(r_k)$ is the umbrella potential of the *k*th bin in the *j*th simulation.

The convergence criterion is set such that the maximum difference between the weighting factors for each probable histogram is less than a particular tolerance level, i.e. $\left| f_j^{\,i} - f_j^{\,i-1} \right| \leq 0.001$, where $f_j^{\,i}$ and $f_j^{\,i-1}$ are the weighting factors for the *i*th and *i*th minus one simulation.

Once the WHAM algorithm has converged the potential is smoothed for the initial simulations to avoid discontinuous or sudden changes in the umbrella potential and is extrapolated to previously unsampled regions. The extrapolation helps to avoid discontinuities in the calculation of the applied forces, thus directing the new simulation towards unsampled regions along the reaction coordinate.

3.4 Calibration of the Potential of Mean Force

Ion association separation distances for different ion pairs and the relative probability of finding these ion pairs can be derived from a PMF free energy profile. In this work there is a need for the calibration of the PMF curve in order to determine accurately the ion association constants for any ion pairing system. This calibration is to be achieved absolute free energies, which are not determined from PMF profiles, but are calculated using FEP methods (section 3.2.1).

Traditional methods to calibrate PMF profiles have focused on setting the free energy of association to zero at a large distances, i.e. ½ the simulation box length as proposed by Gaurdia [40], such that

$$W(r) = W(r_0) - k_B T \ln P(r) \tag{3.24}$$

where k_B is Boltzmann's constant, T is the temperature and $W(r_0)$ is a constant which should be suitably chosen to obtain $W(r)$ values that are reliable at long separations. $W(r_0)$ is computed from the Coulombic interaction energy at a selected distance

$$W(r_0) = \frac{q_A q_C}{4\pi\kappa\varepsilon_0 r_0} \tag{3.25}$$

in which q_A and q_c are the anion and cation charges, respectively, κ is the dielectric constant, ε_0 is the permittivity of free space and r_0 is the selected anion-cation distance. This process works well for 1:1 charged systems works as $W(r_0) = 0$, when r ~12 Å. However, for 2:2 charged systems, $W(r_0) = 0$, when r ~ 19.5 Å. The increase in r of ~7.5 Å may not seem significant at first, but to model the ion association correctly, this requires a three fold increase in computational time.

The method proposed in this work is shown in Figure 3.4 and is discussed in more detail in Chapter 5.

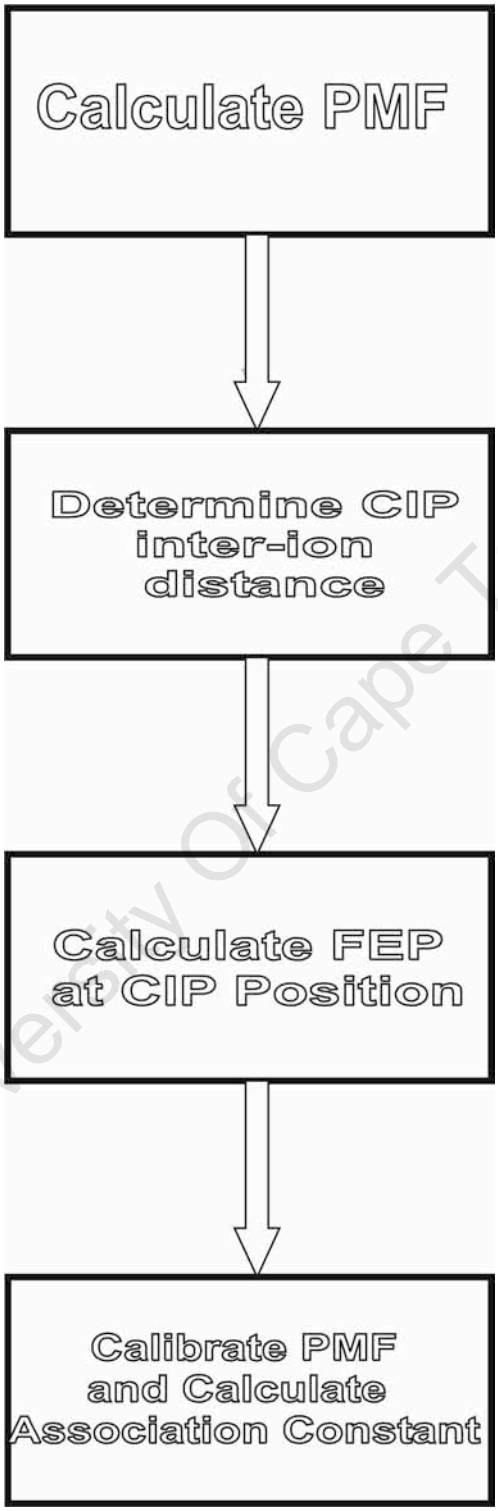

Figure 3.4. A PMF calibration method, as devised in this work.

3.5 References

1. Leach, A.R., *Molecular Modelling: Principles and Applications.* 1st and 2nd ed. 2001: Longman.
2. Kollman, P.A., *Free-energy calculations - Applications to chemical and biochemical phenomena.* Chem. Rev., 1993. **93**(7): p. 2395-2417.
3. Jorgensen, W.L., Blake, J.F., and Buckner, J.K., *Free-energy of TIP4P water and the free-energies of hydration of CH_4 and Cl^- from statistical perturbation-theory.* Chem. Phys., 1989. **129**(2): p. 193-200.
4. Aqvist, J., *Ion water interaction potentials derived from free-energy perturbation simulations.* J. Phys. Chem., 1990. **94**(21): p. 8021-8024.
5. Straatsma, T.P. and Berendsen, H.J.C., *Free-energy of ionic hydration - Analysis of the thermodynamic integration technique to evaluated free-energy differences by molecular-dynamics simulations.* J. Chem. Phys., 1988. **89**(9): p. 5876-5886.
6. Naidoo, K.J., Lopis, A.S., Westra, A.N., Robinson, D.J., and Koch, K.R., *Contact ion pair between Na+ and PtCl62- favored in methanol.* J. Am. Chem. Soc., 2003. **125**(44): p. 13330-13331.
7. Jorgensen, W.L., Buckner, J.K., Huston, S.E., and Rossky, P.J., *Hydration and energetics for $(CH_3)_3CCl$ ion pairs in aqueous-solution.* J. Am. Chem. Soc., 1987. **109**(7): p. 1891-1899.
8. Chorny, I., Dill, K.A., and Jacobson, M.P., *Surfaces affect ion pairing.* J. Phys. Chem. B, 2005. **109**(50): p. 24056-24060.
9. Dudev, T. and Lim, C., *Metal binding affinity and selectivity in metalloproteins: Insights from computational studies.* Ann. Rev. Biophys., 2008. **37**: p. 97-116.
10. Gao, J.L., Ma, S.H., Major, D.T., Nam, K., Pu, J.Z., and Truhlar, D.G., *Mechanisms and free energies of enzymatic reactions.* Chem. Rev., 2006. **106**(8): p. 3188-3209.
11. Beveridge, D.L. and Dicapua, F.M., *Free-energy via molecular simulation - Applications to chemical and biomolecular systems.* Annu. Rev. Biophys. Biophys. Chem., 1989. **18**: p. 431-492.
12. Straatsma, T.P., Zacharias, M., and McCammon, J.A., *Holonomic constraint contributions to the free-energy differences from thermodynamic integration*

molecular-dynamics simulations. Chem. Phys. Lett., 1992. **196**(3-4): p. 297-302.

13. Kirkwood, J.G., *Statistical mechanics of fluid mixtures.* J. Chem. Phys., 1935. **3**(5): p. 300-313.
14. Zwanzig, R.W., *High-temperature equation of state by a perturbation method. I. Nonpolar gases.* J. Chem. Phys., 1954. **22**(8): p. 1420-1426.
15. Axelsen, P.H. and Li, D.H., *Improved convergence in dual-topology free energy calculations through use of harmonic restraints.* J. Comput. Chem., 1998. **19**(11): p. 1278-1283.
16. Jorgensen, W.L. and Ravimohan, C., *Monte-Carlo simulation of differences in free-energies of hydration.* J. Chem. Phys., 1985. **83**(6): p. 3050-3054.
17. Jorgensen, W.L. and Thomas, L.L., *Perspective on free-energy perturbation calculations for chemical equilibria.* J. Chem. Theory Comput., 2008. **4**(6): p. 869-876.
18. Lu, N.D., Kofke, D.A., and Woolf, T.B., *Improving the efficiency and reliability of free energy perturbation calculations using overlap sampling methods.* J. Comput. Chem., 2004. **25**(1): p. 28-39.
19. Strumpfer, J. and Naidoo, K.J., *Computing free energy hypersurfaces for anisotropic intermolecular associations.* J. Comput. Chem., 2010. **31**(2): p. 308-316.
20. Ben-Naim, A., *Water and Aqueous Solutions.* 1974: Plenum Press, New York.
21. Mezei, M. and Ben-Naim, A., *Calculation of the solvent contribution to the potential of mean force between water-molecules in fixed relative orientation in liquid water.* J. Chem. Phys., 1990. **92**(2): p. 1359-1361.
22. Mezei, M. and Beveridge, D.L., *Free energy simulations.* Ann. N. Y. Acad. Sci., 1986. **482**(Comput. Simul. Chem. Biomol. Syst.): p. 1-23.
23. McQuarrie, D.A., *Statistical Mechanics.* 2000, Sausalito, CA: University Science Books.
24. Chandler, D., *Introduction to Modern Statistical Mechanics.* 1987, New York: Oxford University Press.
25. Khavrutskii, I.V., Dzubiella, J., and McCammon, J.A., *Computing accurate potentials of mean force in electrolyte solutions with the generalized gradient-*

augmented harmonic Fourier beads method. J. Chem. Phys., 2008. **128**(4): p. 13.

26. Trzesniak, D., Kunz, A.P.E., and van Gunsteren, W.F., *A comparison of methods to compute the potential of mean force.* ChemPhysChem, 2007. **8**(1): p. 162-169.
27. Berkowitz, M., Karim, O.A., McCammon, J.A., and Rossky, P.J., *Sodium-chloride ion-pair interaction in water - computer simulation.* Chem. Phys. Lett., 1984. **105**(6): p. 577-580.
28. Ghoufi, A. and Malfreyt, P., *Calculations of the potential of mean force from molecular dynamics simulations using different methodologies: an application to the determination of the binding thermodynamic properties of an ion pair.* Mol. Phys., 2006. **104**(22-24): p. 3787-3799.
29. Go, N. and Scheraga, H.A., *Use of classical statistical-mechanics in treatment of polymer-chain conformation.* Macromolecules, 1976. **9**(4): p. 535-542.
30. Fixman, M., *Simulation of polymer dynamics. 1. General theory.* J. Chem. Phys., 1978. **69**(4): p. 1527-1537.
31. Coluzza, I., Sprik, M., and Ciccotti, G., *Constrained reaction coordinate dynamics for systems with constraints.* Mol. Phys., 2003. **101**(18): p. 2885-2894.
32. Carter, E.A., Ciccotti, G., Hynes, J.T., and Kapral, R., *Constrained reaction coordinate dynamics for the simulation of rare events.* Chem. Phys. Lett., 1989. **156**(5): p. 472-477.
33. den Otter, W.K., *Thermodynamic integration of the free energy along a reaction coordinate in Cartesian coordinates.* J. Chem. Phys., 2000. **112**(17): p. 7283-7292.
34. Darve, E. and Pohorille, A., *Calculating free energies using average force.* J. Chem. Phys., 2001. **115**(20): p. 9169-9183.
35. den Otter, W.K. and Briels, W.J., *Free energy from molecular dynamics with multiple constraints.* Mol. Phys., 2000. **98**(12): p. 773-781.
36. Torrie, G.M. and Valleau, J.P., *Monte-Carlo free-energy estimates using non-Boltzmann sampling - Application to subcritical Lennard-Jones fluid.* Chem. Phys. Lett., 1974. **28**(4): p. 578-581.
37. Mezei, M., *Adaptive umbrella sampling - Self-consistent determination of the non-Boltzmann bias.* J. Comput. Phys., 1987. **68**(1): p. 237-248.
38. Kumar, S., Bouzida, D., Swendsen, R.H., Kollman, P.A., and Rosenberg, J.M., *The*

weighted histogram analysis method for free-energy calculations on biomolecules. 1. The method. J. Comput. Chem., 1992. **13**(8): p. 1011-1021.

39. Kumar, S., Payne, P.W., and Vasquez, M., *Method for free-energy calculations using iterative techniques.* J. Comput. Chem., 1996. **17**(10): p. 1269-1275.

40. Guardia, E., Rey, R., and Padro, J.A., Chem. Phys., 1991. **155**: p. 187-195.

CHAPTER 4

Validation of Molecular Simulations

4.1 Introduction

An important feature of computational chemistry is that properties computed from a simulation can be compared directly with measured values from physical experiments, such as thermodynamic compressibility studies or Raman and nuclear magnetic resonance (NMR) spectroscopy. Comparison of experimental measurements and computational calculations allows for the validation and improvement of molecular mechanics models, as well as the interpretation of experimental data in terms of atomic models obtained from simulation. Thus for chemistry in general, the combination of experimental and computational techniques has resulted in an increased understanding of ion hydration structure and dynamics.

Chapters 1 and 2 introduced the importance of ion hydration and pairing in biological and chemical applications, while Chapters 2 and 3 addressed the theoretical aspects of simulating metal ions in aqueous solution. This chapter gives a brief overview of experimental methods used to study ion hydration structures, numbers and pairing. This is followed by a description of ultrasonic interferometry, the experimental method used in this thesis, and how ion hydration numbers can be obtained from isentropic compressibilities. The final section gives a description of the applied computational analytical methods. The methods used to study the solvent structure around an ion, pair and spatial distribution functions are described. This is followed by descriptions of the methods for calculating the dynamic properties of ions in solution. These include correlation functions used to determine, ion self-diffusion coefficients, water and counterion residence times and rotational relaxation rates.

4.2 Experimental Analysis

4.2.1 Solvent Structure and Hydration Numbers

The structuring of water around ions can be studied using several experimental methods. The concept of the structure of hydrated ions is however dependent on the method of

Table 4.1. Several methods used to study ion hydration structures and solvation numbers

Method	Kind of Solvation
1. Static Structure	
Diffraction methods	first and second solvation shells
2. Spectroscopic methods	
UV-VIS spectrometry	primary solvation
NMR	primary solvation
EXAFS	first and second solvation shells
Dielectric Relaxation	primary and some secondary solvation
3.Thermodynamic measurements	
Compressibilities	primary and some secondary solvation
Molar entropies of solvation	primary and some secondary solvation

analysis [1-5]. There are three broad categories of ion hydration structure analysis. Firstly there are static structure analyses, where structural data are obtained from diffraction experiments. Second, ion hydration structure can be described based on the dynamic properties of coordinating water molecules, where data are obtained from spectroscopic measurements (i.e. Raman, nuclear magnetic resonance (NMR), X-ray adsorption fine structure (EXAFS) and dielectric relaxation spectroscopy (DRS)) and third, ion hydration structures can be derived from energetic considerations related to how strongly water molecules coordinate to ions, which can be obtained from Raman spectroscopy, infrared (IR) spectroscopy and thermodynamic studies (i.e. volumetric and compressibility properties of aqueous solutions) [1, 2, 4].

The hydration number S_n, is the number of waters directly associated to an ion and can be determined from all of the above methods for studying ion hydration structure. However, the value obtained for S_n is highly method dependent and large variations occur between them [5, 6]. To quantify the variations in calculated S_n one must understand the 'kind of solvation' studied by each method. In other words, does the experimental method

study only the solvation shells around an ion, or can the method determine the solvent molecules directly associated with an ion which constitutes its primary solvation. Table 4.1 gives a summary of several experimental methods and the kind of solvation studied.

In this work, ion hydration (solvation) numbers are estimated from thermodynamic properties of aqueous metal sulfate solutions. These properties are derived from density and sound velocities, using ultrasonic interferometry which is discussed in section 4.3.

4.2.2 Ion Pairing Association Constants

The determination of ion pairing, as with ion hydration numbers, can be performed using several experimental methods and has been covered in the review by Marcus and Hefter [7]. In this work, computational studies on ion pairing are concentrated on metal sulfate 2:2 electrolyte solutions. To validate the computationally determined results (association constants) a source of experimental data is required.

In the past several decades ion pairing of aqueous metal sulfate solutions has been studied using a multitude of experimental techniques, i.e. ultrasonic relaxation spectroscopy (URS) [8-12], DRS [13-17], Raman spectroscopy [18] and conductometric studies [19-21]. Ion pairing of strong electrolyte solutions has recently been determined using infrared spectroscopy [22], Raman spectroscopy [23] and pulsed field gradient spin-echo (PGSE) NMR methods [24, 25]. However, spectroscopic techniques do not always provide dependable association constants, as they cannot reliably detect solvent separated (SSIP) and solvent shared ion pairs (SSHIP) [16, 26]. Systems containing SSIP and SSHIP are best studied using DRS and URS, which can detect all ion-pair types, or traditional thermodynamic methods (i.e. conductivity), which detect the overall association [26].

4.3 Ultrasonic Interferometry

Ultrasonic Interferometry (UI) is a simple and direct method used to determine the ultrasonic velocity in liquids, with a high degree of accuracy. UI is based on interference of sound propagation in a medium. UI presents several advantages as far as accuracy and reproducibility for sound velocity measurements is concerned. The method is based on the determination of the differences between the reference and perturbed signals, rather than the measurement of absolute values [27, 28]. The observed differences are responsible for destructive or constructive interference between signals, which is measured with high precision using a simple experimental setup.

Several thermodynamic properties (i.e. including molar volumes, expansibilities and isentropic compressibilities) of aqueous electrolyte solutions can be estimated directly from the measurement of ultrasonic velocity and density [29, 30], assuming there is no loss in solution volume and no change in adiabatic nature of the system.

4.3.1 The Ultrasonic Interferometer

The velocity of the ultrasonic waves traveling through an aqueous electrolyte solution is measured using a multi frequency ultrasonic interferometer with a single crystal and variable path type as shown in Figure 4.1. The apparatus consists of two parts; a high frequency generator, and a measuring cell.

The high frequency generator, which is provided with a direct current, consists of a crystal controlled oscillator in the form of a modified circuit, operating in the megacycle range. It is designed to excite the transducer (quartz crystal fixed at the bottom of the measuring cell) to produce ultrasonic waves at the crystals resonant frequency in a solution. There are two controls, one for the initial adjustment of the micrometer and the other for the purpose of controlling the current sensitivity. The measuring cell is a cylindrical metal container placed vertically on a heavy metal base and serves as a coupler between the quartz crystal and the high frequency generator. The measuring cell is a double-walled cell which holds the solution and allows for water circulation (in the wall around the solution) from a thermostatically regulated water bath, to maintain

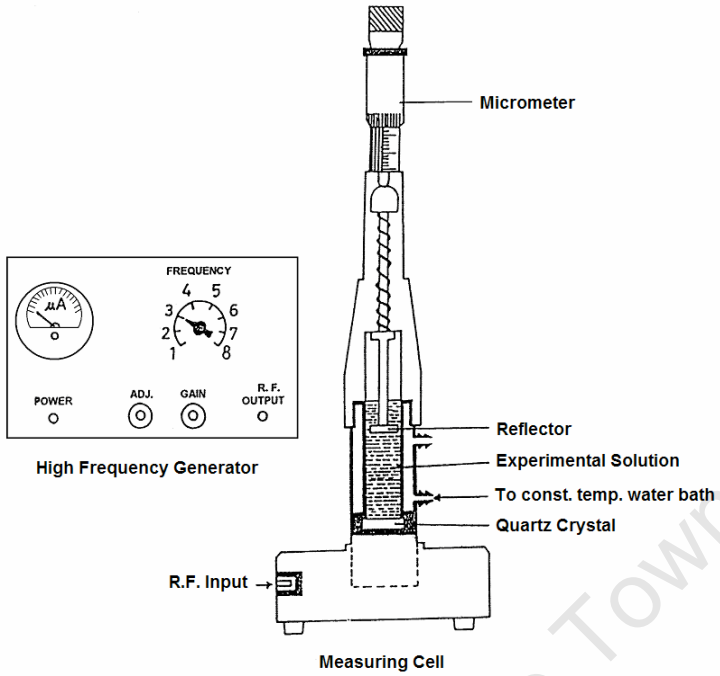

Figure 4.1. The ultrasonic interferometer instrument used for the experimental section of this work.

constant temperature with an accuracy of ± 0.1 ^{o}C. A quartz crystal transducer is fixed at the bottom of the cell and a movable metallic reflecting plate is controlled by a micrometer screw.[1]

An ultrasonic wave is formed when a high frequency generator excites a quartz crystal transducer, which also acts as a detecting transducer. The resulting ultrasonic wave travels through a solution toward a movable reflecting metallic plate. Moving the reflective plate towards and away from the vibrating crystal, results in a change in amplitude and phase. The reflector can be made to pass through successive positions of maxima and minima of the ultrasonic wave. When the distance, between the movable metallic plate and the quartz crystal, is an exact multiple of the ultrasonic wavelength, standing waves are formed. The resulting change in amplitude and phase of the vibrating crystal gives rise to piezoelectricity, allowing a current to be measured. The ultrasonic

[1] The metal plate is kept parallel to the quartz transducer at all times.

propagation produces an electrical reaction on the oscillator of the quartz crystal and the anode current of the generator is a maximum when standing waves are formed.

If the distance between the reflector plate and the crystal is increased or decreased, and the variation is a multiple of half of the wavelength ($\lambda/2$), the anode current is also at a maximum.

4.3.2 Ultrasonic Velocity Measurements

Measurements of the ultrasonic velocity traveling through a solution, is based primarily on finding the wavelength (λ) of the ultrasonic wave in the solution. When a multiple of half the wavelength is achieved, a maximum in the observed current is obtained. Determination of the wavelength and subsequent knowledge of the frequency, allows the velocity to be calculated using the relation

$$u = v\lambda \tag{4.1}$$

where u is the ultrasonic speed, v is the frequency and λ is the wavelength.

The wavelength is calculated as

$$d = \frac{(n-1)\lambda}{2} \tag{4.2}$$

where d is the total distance moved by the micrometer screw, for a maximum or minimum deflection, and n is number of maxima or minima of anode current for a distance d. The ultrasonic velocity can thus be calculated using

$$u = \frac{2vd}{n} \tag{4.3}$$

4.3.3 Isentropic Compressibility and Hydration Numbers

Isentropic compressibility, β, depends on the compressible volume of solvent molecules around an ion. This volume is sensitive to the intermolecular interactions in electrolyte solutions. The relationship between isentropic compressibility and ultrasonic velocity is given by the Newton-Laplace equation

$$\beta = \left(\rho u^2\right)^{-1} \tag{4.4}$$

where ρ is the density of a solution.

The hydration number of a solute is determined from β using the expression

$$n_h = \frac{n_w}{n_s}\left(1 - \frac{\beta}{\beta_w}\right) \tag{4.5}$$

where β_w is the isentropic compressibility of pure water, and n_w and n_s are the number of moles of water and solute, respectively. Equation 4.5 implicitly assumes that: 1) n_h is the number of water molecules in the primary solvation shell of a solute (i.e. metal salt), and 2) these water molecules are trapped so tightly around metal ions that they are considered as incompressible due to electrostriction [6].

4.4 Computational Analysis

4.4.1 Solvent Structural Analysis

The most practical means of describing the structure of a chemical system, particularly ions in solution, is the pair distribution function (PDF), $g_{\alpha\beta}(r)$. The isotropic probability density via site-site pair distribution functions is defined as

$$g_{\alpha\beta}(r) = \frac{V}{N_\alpha N_\beta} \left\langle \sum_{i=1}^{N_\alpha} \sum_{j=1}^{N_\beta} \delta\left(r - r_{\alpha_i \beta_j}\right) \right\rangle \tag{4.6}$$

where $r_{\alpha_i \beta_j}$ is the distance between the atomic sites α and β on the molecules *i* and *j*. N_α and N_β are the total number of α and β atoms in the volume *V* and the angular brackets denote an ensemble average. $g_{\alpha\beta}(r)$ relates the probability of finding a pair of atoms, α and β, at a distance *r* apart and is normalised by the probability of all the atoms being evenly distributed in a chemical system at the same density [31, 32].

$g_{\alpha\beta}(r)$ calculated between metal ions and solvent atoms, such as the Mg-O and Mg-H $g_{\alpha\beta}(r)$ for the hydration of magnesium, can be compared directly to $g_{\alpha\beta}(r)$ obtained from X-ray and neutron diffraction experiments [1, 2], with favourable comparisons validating a force field model. The main drawback of $g_{\alpha\beta}(r)$ is their limited ability in ion hydration structure analysis, because $g_{\alpha\beta}(r)$ only provide information about the number of solvent neighbours around an ion, determined by integration under the first peak of a calculated $g_{\alpha\beta}(r)$, and the respective solvent-ion distances, without giving the mutual orientation of molecules in a solvation shell.

To construct molecular detailed configurations of the first solvation shells of metal ions, three-dimensional solvent probability density distributions are calculated for solvated ions. These distributions are known as the spatial distribution functions (SDFs). This is achieved by removing the rotational and translational diffusion of a selected ion for each frame in a molecular dynamics (MD) trajectory. The ion in each stored coordinate set is re-oriented to a best least squares fit with a reference coordinate set, and a coordinate transformation is then applied to all the atoms in the system. The complete MD trajectory for each data set is then used to analyse the solvent structure. Furthermore the statistical independence of each frame is maintained by separating the frames by at least 0.5 ps from each other.

Solvent sites are used to calculate the probability densities on a grid using a Gaussian distribution function

$$G(r) = \left(\frac{a}{\pi}\right)^{\frac{3}{2}} \exp\left(-ar^2\right) \tag{4.7}$$

centered on each solvent site to represent accurately the distribution of the sites across the mesh. The densities of the sites are distributed over neighbouring bins such that 90% of the binned density for a molecular site is within its site radius, *r*. This is determined by appropriate selection of the constant, *a*, for each site. The densities in each box are then summed for all the selected frames from a dynamics run and a final solvent density matrix is normalised using Equation 4.8 such that the density of bulk solvent corresponds to a value of 1, while 50% above bulk density corresponds to a value of 1.5, etc.

$$\overline{\rho}(x_i, y_i, z_i) = \rho(x_i, y_i, z_i) \frac{n_{xbin} n_{ybin} n_{zbin}}{n_{molecular\,site} n_{frames}} \tag{4.8}$$

In Equation 4.8, n_{xbin}, n_{ybin} and n_{zbin} are the number of divisions in the *x*, *y* and *z* directions in a simulation box while $n_{molecularsite}$ and n_{frames} represent the number of selected atoms in each frame and the number of frames respectively. The non-normalised density for each grid point (x_i,y_j,z_k) is given as $\rho(x_i,y_j,z_k)$.

4.4.2 Time-dependent Properties

Time-dependent properties such as molecular rotational times, solvent residence times and ion self-diffusion coefficients can be extracted from MD trajectories. This is achieved through the calculation of correlation functions, which provide a numerical quantification of the strength of correlation of any property in the simulation, at any time. These correlation functions can be linked to experimental measurements through statistical mechanics [32]. In general, an autocorrelation function, $C(t)$, for a time-dependent variable, $A(t)$, sampled at equal time intervals of τ, is given by

$$C(t) = \lim_{T \to \infty} \int_0^T A(t+\tau)A(\tau)d\tau \tag{4.9}$$

This equation is more commonly written in an ensemble average form

$$C(t) = \langle A(0)A(t) \rangle \tag{4.10}$$

The decay of a time series to zero indicates how quickly the properties become uncorrelated. This decay is usually assumed to be exponential, with the general form $A\exp(-t/\tau)$, where τ is the correlation time [32].

4.4.2.1 Solvent Residence Times and Dynamic Hydration Numbers

The time that a water molecule spends in the first solvation shell, of an ion, before diffusing back into the bulk solution, is known as its residence time. Several procedures have been suggested to calculate residence times from MD simulations [33]. In this thesis the residence time as defined by Impey et al. [34] is used.

In this method, the residence time is calculated from a number correlation function, similar to a time correlation function, except that the dynamical variable has a value of either 0 or 1. The correlation time, τ, calculated from the time correlation function is the (average) residence time that a water molecule will spend in the first solvation shell. A spherical cutoff is used in the calculation and is chosen such that it slightly beyond the distance of the first solvation shell from the centre of the ion.

The residence time for a water molecule, α, is obtained by calculating Equation 4.11, where $P_\alpha(t_n, t, t^*)$ is the probability of finding α within the first solvation shell of an ion at times t_n and $t + t_n$. $P_\alpha = 1$ if α is within the first solvation shell of an ion and does not leave that solvation shell for any period longer than t^*, otherwise $P_\alpha = 0$. It then follows that $n_{ion}(t)$, which is characteristic of the ion, is expressed as

$$n_{ion}(t) = \frac{1}{N_t}\sum_{n=1}^{N_t}\sum_{\alpha} P_{\alpha}(t_n, t, t*) \tag{4.11}$$

The above correlation function decays as $\exp(-t/\tau^{S}_{ion})$ over time, giving τ^{S}_{ion} as the resultant residence time. From this and a subsequent calculation of a bulk residence time, τ^{S}_{Bulk}, from a pure solvent simulation, one is able to define a dynamic hydration number, n_h, for any particular ion, given as

$$n_h = n_{coor} \exp\left(- \tau^{S}_{Bulk} \Big/ - \tau^{S}_{ion} \right) \tag{4.12}$$

where the coordination number, n_{coor}, is calculated from the pair distribution function.

4.4.2.2 Ion Self-Diffusion Coefficients

Time correlation functions are not only useful for analysing conformational events; they can also be used to calculate transport properties such as diffusion. The mobility of ions in solution is an indication of their degree of solvation [5]. However, ion-self diffusion coefficients calculated from MD trajectories can only be of semi-quantitative significance, as these are generally calculated for one ion and are not a true reflection of what happens in real solutions, as the statistical uncertainties in the calculations may be in error by as much as 50% [34]. The statistical error may be limited by ensuring that MD simulations are run for a sufficient length (at least 10 ns), sufficient for the Ergodic assumption to hold.

In this thesis ion self-diffusion coefficients are calculated from the average of the mean square displacement, of the respective ions, using the Einstein relation [32, 34]

$$D = \lim_{t\to\infty} \frac{1}{6t} \left\langle \left| r_i(t) - r_i(0) \right|^2 \right\rangle \tag{4.13}$$

where $r_i(t)$ is the molecular position i at time t and $r_i(0)$ is the initial position, with < > denoting an ensemble average. Calculated ion-self diffusion coefficients can be compared directly to diffusion coefficients determined from pulsed field gradient spin echo (PGSE) NMR techniques. This technique has been used to study diffusion of sodium hexachloroplatinate aqueous and methanol solutions [35], and has recently been shown to give a qualitative estimate to ion pairing in electrolyte solutions using the difference in diffusion coefficients between cations and anions [24, 25].

4.5 References

1. Ohtaki, H. and Radnai, T., *Structure and dynamics of hydrated ions.* Chem. Rev., 1993. **93**(3): p. 1157-1204.
2. Marcus, Y., *Effect of ions on the structure of water: Structure making and breaking.* Chem. Rev., 2009. **109**(3): p. 1346-1370.
3. Marcus, Y., *Ion Solvation.* 1st ed. 1985: John Wiley and Sons Ltd.
4. Bockris, J.O.M. and Reddy, A.K.N., *Modern Electrochemistry, Vol. 2A. Ionics.* 2nd ed. 1998: Plenum Press.
5. Burgess, J., *Ions in Solution: Basic Principles of Chemical Interactions.* 1988: Ellis Horwood.
6. Marcus, Y., *Electrostriction, ion solvation, and solvent release on ion pairing.* J. Phys. Chem. B, 2005. **109**(39): p. 18541-18549.
7. Marcus, Y. and Hefter, G., *Ion pairing.* Chem. Rev., 2006. **106**(11): p. 4585-4621.
8. Larson, J.W., *Thermodynamics of divalent metal sulfate dissociation and structure of solvated metal sulfate ion pair.* J. Phys. Chem., 1970. **74**(18): p. 3392-3396.
9. Eigen, M. and Tamm, K., *Schallabsorption in elektrolytlosungen als folge chemischer relaxation.1. Relaxationstheorie der mehstufigen dissoziation.* Z. Elektrochem., 1962. **66**(2): p. 93-107.
10. Eigen, M. and Tamm, K., *Schallabsorption in elektrolytlosungen als folge chemischer relaxation. 2. Messergebenisse und relaxationsmechanismen fur 2-2-wertige elektrolyte.* Z. Elektrochem., 1962. **66**(2): p. 107-121.
11. Atkinson, G. and Petrucci, S., *Ion association of magnesium sulfate in water at 25 degrees.* J. Phys. Chem., 1966. **70**(10): p. 3122-3128.
12. Bhatti, S.S. and Lark, B.S., *Ultrasonic studies of association constants and reaction volumes of $MnSO_4$ and $CoSO_4$ in aqueous-solutions at 298.15 K.* Acustica, 1981. **48**(1): p. 64-68.
13. Akilan, C., Hefter, G., Rohman, N., and Buchner, R., *Ion association and hydration in aqueous solutions of copper(II) sulfate from 5 to 65 degrees C by dielectric spectroscopy.* J. Phys. Chem. B, 2006. **110**(30): p. 14961-14970.

14. Akilan, C., Rohman, N., Hefter, G., and Buchner, R., *Temperature effects on ion association and hydration in $MgSO_4$ by dielectric spectroscopy.* ChemPhysChem, 2006. **7**(11): p. 2319-2330.
15. Buchner, R. and Barthel, J., *Dielectric Relaxation in Solutions.* Annual Reports on the Progess of Chemistry, Section C, Physical Chemistry, 1994. **91**: p. 71-106.
16. Buchner, R., Chen, T., and Hefter, G., *Complexity in "simple" electrolyte solutions: Ion pairing in MgSO4(aq).* J. Phys. Chem. B, 2004. **108**(7): p. 2365-2375.
17. Chen, T., Hefter, G., and Buchner, R., *Ion association and hydration in aqueous solutions of nickel(II) and cobalt(II) sulfate.* J. Solution Chem., 2005. **34**(9): p. 1045-1066.
18. Rudolph, W.W., Irmer, G., and Hefter, G.T., *Raman spectroscopic investigation of speciation in MgSO4(aq).* Phys. Chem. Chem. Phys., 2003. **5**(23): p. 5253-5261.
19. Pethybridge, A.D. and Taba, S.S., *Precise conductimetricstudies on aqueous-solutions of 2-2 electrolytes. 3. Detailed study of the individual electrolytes.* J. Chem. Soc. Faraday T., 1982. **78**: p. 1331-1344.
20. Bester-Rogac, M., Babic, V., Perger, T.M., Neueder, R., and Barthel, J., *Conductometric study of ion association of divalent symmetric electrolytes: I. CoSO4, NiSO4, CuSO4 and ZnSO4 in water.* J. Mol. Liq., 2005. **118**(1-3): p. 111-118.
21. Bester-Rogac, M., *Electrical conductivity of concentrated aqueous solutions of divalent metal sulfates.* J. Chem. Eng. Data, 2008. **53**(6): p. 1355-1359.
22. Max, J.J. and Chapados, C., *Infrared spectroscopy of aqueous ionic salt mixtures at low concentrations: Ion pairing in water.* J. Chem. Phys., 2007. **127**(11): p. 10.
23. Xu, M., Larentzos, J.P., Roshdy, M., Criscenti, L.J., and Allen, H.C., *Aqueous divalent metal-nitrate interactions: hydration versus ion pairing.* Phys. Chem. Chem. Phys., 2008. **10**(32): p. 4793-4801.
24. Pregosin, P.S., *Ion pairing using PGSE diffusion methods.* Prog. Nucl. Magn. Reson. Spectrosc., 2006. **49**(3-4): p. 261-288.

25. Pregosin, P.S., *NMR spectroscopy and ion pairing: Measuring and understanding how ions interact.* Pure Appl. Chem., 2009. **81**(4): p. 615-633.
26. Hefter, G., *When spectroscopy fails: The measurement of ion pairing.* Pure Appl. Chem., 2006. **78**(8): p. 1571-1586.
27. Batra, N.K., Delsanto, P.P., Romano, A., and Scalerandi, M., in *The Wiley Encyclopedia of Electrical and Electronics Engineering*. 1999, Wiley.
28. Fortunko, C.M., Peterson, G.L., Chick, B.B., Renken, M.C., and Preis, A.L., *Absolute measurements of elastic-wave phase and group velocities in lossy materials.* Rev. Sci. Instrum., 1992. **63**(6): p. 3477-3486.
29. Wawer, J., Krakowiak, J., and Grzybkowski, W., *Apparent molar volumes, expansibilities, and isentropic compressibilities of selected electrolytes in methanol.* J. Chem. Thermodyn., 2008. **40**(8): p. 1193-1199.
30. Apelblat, A., Manzurola, E., and Orekhova, Z., *Thermodynamic Properties of Aqueous Electrolyte Solutions. Volumetric and Compressibility Studies in 0.1 mol.kg(-1), 0.5 mol.kg(-1), and 1.0 mol.kg(-1) Sodium Carbonate and Sodium Sulfate Solutions at Temperatures from 278.15 K to 323.15 K.* J. Chem. Eng. Data, 2009. **54**(9): p. 2550-2561.
31. Leach, A.R., *Molecular Modelling: Principles and Applications.* 1st and 2nd ed. 2001: Longman.
32. Allen, M.P. and Tildesley, D.J., *Computer Simulations of Liquids.* 1989, Oxford: Clarendon Press.
33. Laage, D. and Hynes, J.T., *On the residence time for water in a solute hydration shell: Application to aqueous halide solutions.* J. Phys. Chem. B, 2008. **112**(26): p. 7697-7701.
34. Impey, R.W., Madden, P.A., and McDonald, I.R., *Hydration and mobility of ions in solution.* J. Phys. Chem., 1983. **87**(25): p. 5071-5083.
35. Nama, D., Kumar, P.G.A., and Pregosin, P.S., *Pt-195, H-1 and P-31 PGSE diffusion studies on platinum complexes.* Magn. Reson. Chem., 2005. **43**(3): p. 246-250.

CHAPTER 5

Ion Association of Metal Solutions from Free Energy Simulations

5.1 Introduction

Ions and their formation salts play an integral part in several biological processes, where in they behave as either active participants; as cofactors or as salt buffers (Section 1.7). Divalent metal ions such as the alkaline earth metals, Mg and Ca; and the divalent transition metals, Fe, Cu, Mn and Zn have been shown to play extensive roles in aiding the structural stability of proteins, or in the regulation of enzymatic reactions, in which they act as metal cores for metalloproteins and metalloenzymes [1, 2]. Metal ions such as Ca play important roles in activating brain enzymes by flowing through ion channels signaling enzyme activation via complexation with calmodulin and through EF-hand motifs [1, 3]; in the contraction of muscles via Ca-induced conformational change and in mammalian fertilization [4]. Furthermore, Mg is a common cofactor used in the synthesis, repair and modification of RNA and DNA [5] while Zn and Fe play central roles in the development of Alzheimer's and Parkinson's disease [6]. In chemistry ion association affects chemical reaction rates, ion-exchange mechanisms and solvent extraction. The latter is widely used in hydrometallurgical processes of which platinum group metal (PGM) extraction and transport [7, 8], as well as base metal extraction are commercially important examples [9].

In both chemical and biological processes the metal ions investigated are generally hydrated [2, 10] and may associate with hydrated ions of opposite charge to form ion pairs [11]. Ion pair formation in electrolyte solutions is generally low but occurs more frequently with an increase in salt concentration [11], increases in solvent temperature [12] and by making use of solvents with low dielectric constants [11, 13].

Metal sulfate ion pairs in 2:2 electrolyte solutions have been under investigation for several decades using a multitude of experimental techniques [12, 14-16]. However, the number of computational studies is limited [17, 18]. The majority of these studies have adopted the Eigen and Tamm three-step association mechanism based on their results for $MgSO_4$. There it was proposed that strongly hydrated ions associate via a three-step process in which the initial free hydrated ions (C and A, for cation and anion) initially form solvent separated ion pairs (SSIP or 2SIP), followed by solvent-shared ion pairs (SSHIP or SIP) and followed by contact ion pairs (CIP). This process is believed to

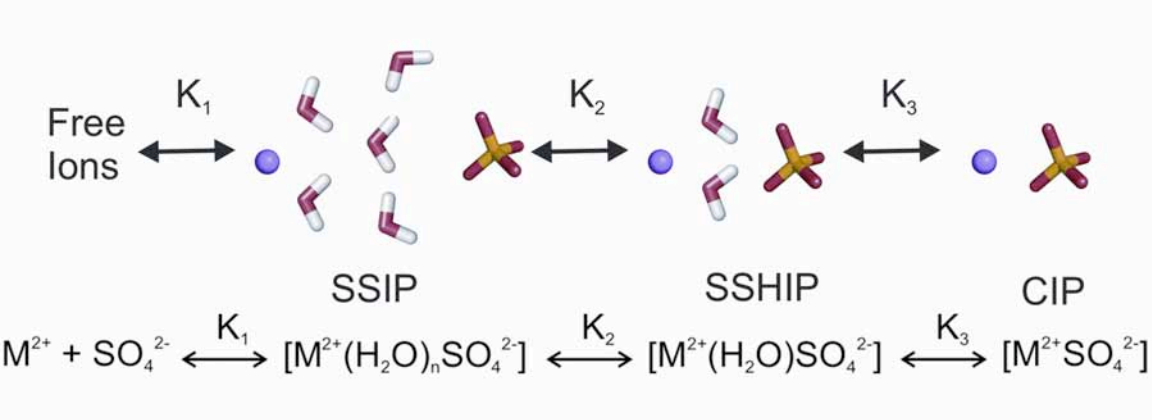

Figure 5.1. Three step ion pairing mechanism

proceed via a stepwise release of several water molecules around the respective ions in steps one and two (outer-sphere coordination), terminating in step three in a complex formation (inner-sphere complexation) via ligand exchange [19], as shown in Figure 5.1.

A convincing measure of the accuracy of computer simulations occurs when experimental observables are matched without the introduction of empirical correction parameters. In the case of ion solutions, experiments have produced association constants for several divalent metal sulfate systems such as $MgSO_4$, $MnSO_4$, $CoSO_4$, $NiSO_4$, and $CuSO_4$. However, there have been difficulties in measuring the individual K_i association constants for several other species (e.g., $CaSO_4$ and $FeSO_4$) and only the overall K_a values have been obtained for all the metal sulfate systems. No previous calculations of association constants from molecular computer simulations for these divalent metal sulfate systems have been reported despite the critical importance of these properties. This is partly because the derivation of association constants from distribution functions or free energy profiles is complicated since these functions provide relative information about the CIP, SSHIP and SIP configurations. In this chapter, a procedure to arrive at force field parameters for divalent metal sulfate (i.e. Mg^{2+}-SO_4^{2-}, Ca^{2+}-SO_4^{2-}, Mn^{2+}-SO_4^{2-}, Fe^{2+}-SO_4^{2-}, Co^{2+}-SO_4^{2-}, Ni^{2+}-SO_4^{2-}, Cu^{2+}-SO_4^{2-} and Zn^{2+}-SO_4^{2-}) solution simulations that are of physical and biophysical importance is presented. The association constants for $M^{2+}\cdots SO_4^{2-}$ ion pairing species are calculated from potential of mean force calculations. In doing so the force field and the method determining the association

constants from free energy profiles are shown to be valid for solution simulations and reliable for the study of ion pairing in computer simulations.

5.2 Computational Methods

All aqueous solution simulations presented here used the TIP3P[20] water model as implemented in CHARMM [21-23]. The sulfate ion used in all metal sulfate solutions was modeled using the literature potentials of Cannon et al. (sulfate and oxygen atom charges: S, 2.4; O,-1.1; S, R_{min}=1.99237, ε = 0.25; O, R_{min}=1.76788, ε = 0.25) [24, 25]. The metal Mg^{2+} ion was modeled using three previously published and commonly used parameter sets, with an additional one developed here. The published parameters are taken from 1) the CHARMM27 protein force field [23], 2) the Aqvist force field [26], and 3) the recently developed force field by Babu and Lim [27]. Ab initio calculations were performed using the Gaussian03 program [28]. Minimum interaction energies and geometries of hydrated Mg^{2+}-$(H_2O)_n$ ion species (n = 1-6) were determined by optimising the intermolecular distance at MP2/6-311++G(3d, 3p) level while constraining the water at the TIP3P internal geometry, as done for previous CHARMM parameterisations [29]. The interaction energies were calculated as the difference between the complex and the monomers. Basis set superposition error was accounted for via the inclusion of the counterpoise correction [30].

Molecular dynamics (MD) simulations were performed in the canonical ensemble *NVT* using the CHARMM program [21, 22]. Potential of mean force (PMF) simulations consisted of 2 ions and 1020 water molecules in cubic boxes of sides 33.98 Å in length, employing periodic boundary conditions. Equations of motion were integrated using the Velocity-Verlet2 (vv2) integrator with a time step of 1 fs [31], and the temperature was maintained at 298.15 K using a method based on the Nose-Hoover thermostat with τ = 0.1 [31]. Electrostatic interactions were calculated using the particle-mesh Ewald (PME) method [32, 33] with a 16.0 Å real space cutoff while the Lennard-Jones interactions were truncated using an atom-based switching function applied between 14.0 and 16.0 Å.

Free energy perturbation (FEP) calculations were performed on single ions and contact ion pairs (CIP) ions that were placed at the centre of a 24.3 Å water sphere

initially containing 1941 TIP3P water molecules. Overlapping waters within 2.5 Å of the ions were deleted, and a spherical boundary force consistent with a water density of 1.0 g.cm^{-3} was applied to the droplet surface. The Verlet integrator with a time step of 1 fs was used and the temperature was kept at 298.15 K using a Nose-Hoover thermostat. Cutoffs using an atom-based switching function between 14.00 and 16.00 Å, for both electrostatic and van der Waal interactions were used.

The Lorentz–Berthelot [34] combining rules where ε_{ij} values are based on the geometric mean of ε_i and ε_j and $R_{min,\mathrm{ij}}$ values are based on the arithmetic mean of $R_{min,i}$ and $R_{min,j}$, as follows:

$$\varepsilon_{ij} = \sqrt{\varepsilon_i \varepsilon_j} \tag{5.1a}$$

$$R_{\min,ij} = \left(R_{\min,ii} + R_{\min,jj}\right)/2 = R_{\min,i} + R_{\min,j} \tag{5.1b}$$

The PMFs for metal and sulfate ions (i.e. Mg^{2+}-SO_4^{2-}, Ca^{2+}-SO_4^{2-}, Mn^{2+}-SO_4^{2-}, Fe^{2+}-SO_4^{2-}, Co^{2+}-SO_4^{2-}, Ni^{2+}-SO_4^{2-}, Cu^{2+}-SO_4^{2-} and Zn^{2+}-SO_4^{2-}) were calculated using the FEARCF method (Section 3.3.3.1) [35].

The FEARCF method is designed to calculate free energy surfaces in multiple dimensions from probability distributions and histograms of the reaction coordinates. The reaction coordinate space is a discretized *n*-dimensional grid in which the sampling frequency for a bin site is recorded for each simulation. The case of ion pair association is the simplest implementation requiring only a one-dimensional grid. The population of this grid represents a running tally of the probability density for the distance between the ions, derived from the history of simulations to that point. It is used as input for a cubic-spline interpolation from which the reaction coordinate biasing forces are calculated. These forces are applied to all atoms used in the reaction coordinate definition to bias the next simulation's reaction coordinate trajectory away from previously sample areas. In this case, we consider the center of mass for the sulfate anion, which is located on the sulfur atom, and the forces are applied to the sulfur and oxygen atoms that make up the sulfate anion. The entire reaction coordinate space is equally sampled when the biasing forces are derived from the true PMF. The forces are applied on Cartesian coordinates, and therefore, the PMF does not need logarithmic Jacobian corrections.36 We calculate

the effect of the perturbing forces generated from the reaction biasing potential $U(\xi)$. The free energy of association between two ions requires only one independent reaction coordinate ($\xi=r$). Adding $U(\xi)$ to the unbiased Hamiltonian changes the system Hamiltonian H_0

$$H(\xi) = H_0 + U(\zeta) \tag{5.2}$$

The biased Hamiltonian $H(\xi)$ is then used in the simulation instead of H_0 and so generates a biased probability distribution of sampled coordinates $P'(\xi)$. This $P'(\xi)$ can then be converted to an unbiased probability distribution by accounting for the biasing potential as follows:

$$P'(\zeta) = CP(\zeta)\exp\left[\frac{U(\zeta)}{k_B T}\right] \tag{5.3}$$

where C is the normalization constant, kB is Boltzmann's constant, and T is the temperature of the system. The PMF for a calculated unbiased probability distribution is then

$$W(\zeta) = -k_B T \log P(\zeta) \tag{5.4}$$

The force arising from the treatment of the molecules as effective rigid bodies ensures that during the simulation, the atoms within each molecule do not move apart and deform the molecules because of differing accelerations that arise from the biasing potential. Consequently, when the resultant acceleration for these molecules is calculated as a whole, the forces on the atoms are determined such that the atoms experience the same resultant acceleration. The translational force arises from a reaction coordinate, which is defined as a distance between two points, $P1$ (metal atom) and $P2$ (center of mass sulfate ion). A positive force in this case should increase the distance, and a negative decreases it by applying equal but opposite forces to the points that define the molecules. The force

arising from the biasing potential for the reaction coordinate $\xi = |r\hat{}| = r$ (i.e., the distance between $P1$ and $P2$) is $F(r) = \nabla W|r$, which results in accelerations $a_{P1} = -F/M_{P1}$ and $a_{P2} = -F/M_{P2}$ on each molecule or ion. Here $MP1$ and $MP2$ are the masses of the metal ion at $P1$ and sulfate anion at $P2$, respectively, and the vector $r\hat{}$ connects $P1$ on molecule 1 and $P2$ on molecule 2. The accelerations, a_{P1} and a_{P2}, are then spread equally among the atoms of sulfate anion and the metal atom, such that the kth atom of the sulfate at $P2$ experiences a force

$$f_k(\zeta) = \frac{F(\zeta)}{M} m_k \tag{5.5}$$

where m_k is the mass of atom k. The Cartesian force arising from the derivative of the potential with respect to r is then applied to the atoms of the molecules as

$$f_{1,k}^{r} = -\frac{\partial U}{\partial r}\frac{m_k}{\sum_{i=1}^{N_1} m_i}(-\hat{r}), \quad f_{2,k}^{r} = -\frac{\partial U}{\partial r}\frac{m_k}{\sum_{i=1}^{N_2} m_i}(\hat{r}) \tag{5.6}$$

with $\mathbf{f}2,k(\xi)$ being the force on atom k of the sulfate molecular ion and $\mathbf{f}1(\xi)$ being the force on the metal ion atom. The biasing forces were calculated from the iteratively developing reaction coordinate free energy profile. The initial free energy profile guess is zero and is successively adapted on the basis of the sampling histogram of the preceding biased simulations. PMF calculations were conducted by placing the metal ion at the center of a water box and the sulfate ion an arbitrary distance from the metal ion. Several short (0.8 ns) simultaneous simulations were conducted at 298.15 K to develop the profile. These were then increased to longer run times (3 ns) using bins 0.125 Å in length, with an ion separation distance of up to 16.0 Å. The iterations were continued until a sampling ratio of at least 1:30 was obtained for the lowest energy to highest-energy regions. A more detailed description of the FEARCF method has been previously presented [35].

5.2.1 Metal Ion Parameterisation

Metal ions and their solution interactions are governed by the non-bonded terms within the CHARMM force field. This is generally of the form

$$U\left(\vec{R}\right)=\sum_{nonbonds}\left\{\varepsilon_{ij}\left[\left(\frac{R_{\min,ij}}{r_{ij}}\right)^{12}-2\left(\frac{R_{\min,ij}}{r_{ij}}\right)^{6}\right]+\frac{q_i q_j}{4\pi D r_{ij}}\right\} \qquad (5.7)$$

and includes the Coulomb and Lennard-Jones (LJ) 6-12 terms. In these terms ε is the LJ well depth, $R_{min,ij}$ is the distance at the LJ minimum, q is the partial atomic charge, D is the effective dielectric constant and r_{ij} is the distance between atoms i and j.

In the derivation of the M^{2+} parameters there is no need to adjust the Coulomb term, as the metal charge is fixed at +2.0 throughout all testing and simulations.This leaves only the Lennard-Jones 6-12 term requiring parameterization, which is achieved by adjusting the inter-atomic dispersion-attraction and repulsive potentials, or ε_{ij} and $R_{min,ij}$ for each pair of distinct atoms. In this work the LJ parameters are initially derived from quantum mechanical calculations and refined until FEP calculated absolute free energies of hydration are reproduced. These LJ parameters are then used to determined association constants from the $M^{2+}\ldots SO_4^{2-}$ PMF profiles.

To get an initial estimate of the van der Waals behaviour of the metal ions we adjusted the Lennard-Jones r_{min} and ε values by fitting the molecular mechanics interaction energy for Mg^{2+}-$(H_2O)_n$, (n=1, …6) to that of the optimized MP2/6-311++G(3d, 3p) values for the same systems. These values were refined using FEP calculations benchmarked against experimental values. Since there is an abundant amount of solution experimental data for Mg^{2+} and $MgSO_4$ we used this metal and the corresponding salt to calibrate all our divalent metal sulfates.

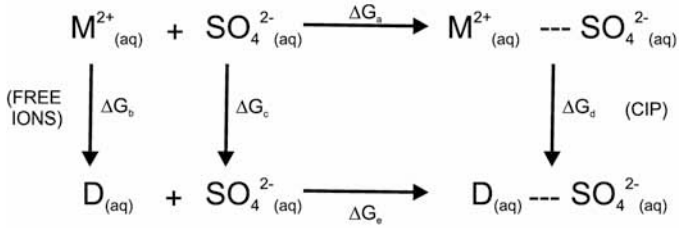

Scheme 5.1. Free energy perturbation cycle used in the calculation of the absolute free energy upon Ion Pairing for the MSO_4 systems

The solvated Mg^{2+} ion solution was minimised for 1000 steps using steepest descent, followed by 100 ps of equilibration at a mean temperature of 298.15 K. To calculate the hydration free energies of the ion, a two stage perturbation approach was used. In the first stage, the charge of the ion was removed in water, and in the second stage, the van der Waals potentials were removed. Both the charge and van der Waals potentials removal was done using 40 windows between the unperturbed ($\lambda = 0$) and perturbed ($\lambda = 1$) states, with each window being sampled for 100ps. The FEP simulations were iteratively performed by adjusting the LJ parameters for the Mg^{2+} ion until the free energy of hydration of -437.4 kcal.mol^{-1} which matches experimentally reported values [36] was produced.

Next the free energy of association of a single Mg^{2+} and a single SO_4^{2-} ion was calculated as illustrate in Scheme 5.1. This was done by initially constraining the two ions (in vacuum) at a distance corresponding to the contact ion pair minima (as seen in the PMF profile). This CIP neutral species was placed at the centre of a 24.3 Å water sphere and the Mg^{2+} ion was perturbed to a dummy atom as above, with the constraint still in place. Reverse perturbations were performed from configurations independent of the forward perturbation runs. The free energies for the forward and reverse runs were then averaged and the free energy of hydration of the metal ion was subtracted from this to obtain the absolute free energy of the $MgSO_4$ electrolyte species.

Lennard-Jones parameters of the divalent metal ions Ca^{2+}, Mn^{2+}, Co^{2+}, Ni^{2+}, Cu^{2+} and Zn^{2+} were derived from a series of FEP calculations where these ions were perturbed from Mg^{2+} to calculate their free energies of hydration. The FEP calculations were repeated following an adjustment of the Lennard-Jones parameters until the free energies

Table 5.1. MSFF parameter set shown with the calculated differences in hydration free energies relative to $Mg^{2+}$and the corresponding experimental hydration free energies values as taken from reference [36].

Ion	ε	$R_{min}/2$ / Å	$\Delta G_{Expt.}$ / kcal.mol^{-1}	$\Delta\Delta G_{Expt.}$ / kcal.mol^{-1}	$\Delta\Delta G_{Calc.}$ / kcal.mol^{-1}
Mg^{2+}	0.020	1.0358	437.4	0.0	0.0
Ca^{2+}	0.030	1.521	359.7	77.7	77.7
Mn^{2+}	0.030	1.134	420.7	16.7	17.0
Fe^{2+}	0.030	0.983	439.8	-2.4	-2.3
Co^{2+}	0.030	0.798	457.7	-20.3	-19.8
Ni^{2+}	0.030	0.738	473.2	-35.8	-35.6
Cu^{2+}	0.030	0.762	480.4	-43.0	-41.8
Zn^{2+}	0.030	0.750	467.3	-29.9	-29.2

of hydration matched values reported from experiments. These metal parameters will produce experimentally consistent results when using the TIP3P water model and may do so for other water models but this should be confirmed. This parameter set is referred to as the *Metal Solution Force Field* (MSFF). These are listed along with their differences in free energies of hydration relative to Mg^{2+} in Table 5.1.

5.2.2 Calibrating Ion Association Free Energy Curves

The PMF has previously been used to determine ion pair species in dilute electrolyte solutions for NaCl under ambient [37] and supercritical conditions [38, 39]; high temperature aqueous H_3O^+/Cl^- solutions [40, 41] and a $Na^+/[PtCl_6]^{2-}$ system [42-44]. PMF calculations have also been used to determine ion pair thermodynamic properties for $CaSO_4$ [17] and $(CH_3)_3CCl$ [45]. As with structural data extracted from molecular dynamics simulations, PMF calculations are dependant on the parameters used in the simulation [46, 47]. While ion association separation distances for CIP, SSHIP and SIP ion pairs and the relative probability of occurrence for these ion pairs may be derived from the free energy curve, absolute free energies cannot be determined from a PMF profile without calibrating the curve.

The procedure of calibration is problematic, as unlike the interaction of a pair of neutral species; it cannot be assumed that at relatively large ion separations (i.e., greater than 15 Å) the interaction between the two ions is zero in the presence of the solvent. Therefore, setting the free energy of association to zero at a large distance such as ½ the simulation box length may not yield experimentally consistent values. Developing a reliable means of calibration is critical if PMFs are to be used to predict absolute solution properties such as overall and individual ion association equilibrium constants. Previously Jorgensen calibrated PMFs using FEP calculations and from that derived absolute free energies for methane dimers [48]. However, while in that study the results were compared to predictions from the integral equation theory of Pratt and Chandler [49] no experimental observables for solution properties such as association constants were calculated from the calibrated PMF.

The PMF could be adjusted by calculating its value at a specific point $W(r_0)$ using the solvent dielectric constant, as proposed by Gaurdia [37] so that

$$W(r) = W(r_0) - k_B T \ln P(r) \tag{5.8}$$

where k_B is Boltzmann's constant, T is the temperature and $W(r_0)$ is a constant which should be suitably chosen to obtain $W(r)$ values that are reliable at long separations. $W(r_0)$ may be computed from the Coulombic interaction energy at a selected distance

$$W(r_0) = \frac{q_A q_C}{4\pi\kappa\varepsilon_0 r_0} \tag{5.9}$$

in which q_A and q_c are the anion and cation charges, respectively, κ is the dielectric constant, ε_0 is the permittivity of free space and r_0 is the selected anion-cation distance (in this work r_0 was selected to be 12Å). This calculation should be done using the computational dielectric constant, κ_{comp} corresponding to the solvent model used [37]. Calculating K_a values that match those measured in an experiment is an important measure of the accuracy of a simulation and the model used. Since the choice of κ has an

Table 5.2. Results from Mg^{2+} hydration FEP cycle where ΔG_a, ΔG_b and ΔG_d are the respective free energies from the FEP cycle shown in Scheme 5.1.

	Mg^{2+}		
Parameter Set	**ΔG_a / kcal.mol^{-1}**	**ΔG_b / kcal.mol^{-1}**	**ΔG_d / kcal.mol^{-1}**
Aqvist	-3.35	-456.9	-453.55
Babu	-2.85	-451.7	-448.15
Roux	-1.28	-458.9	-457.62
MSFF	-1.19	-437.4	-436.21

exponential effect on computed K_a values, this method of calculating $W(r_0)$ is not reliable. Using the MSFF the absolute free energies for the CIP of M^{2+} (M = Mg^{2+}, Ca^{2+}, Mn^{2+}, Fe^{2+}, Co^{2+}, Ni^{2+}, Cu^{2+} and Zn^{2+}) and SO_4^{2-} are calculated from FEPs of the CIP as shown in Scheme 5.1 and by removing the contribution of the absolute free energy of hydration for each ion as listed in Table 5.1. These absolute free energies compare well with experimental values (Table 5.2) for the ion pairing hydration energies. Although these have been measured for the combined individual CIP, SSHIP and SIP species. Using these calculated absolute free energy values at the CIP position and by adjusting the CIP PMF to that value results in the effective calibration of the PMF for the case of the MSFF.

5.2.3 Calculating K_a from PMF Profiles

In principle, association constants, K_a, can be calculated from radial distribution functions of anions (A) and cations (C), $g_{AC}^{\infty}(r)$, where at infinite dilution the relation is

$$K_a = 4\pi R \int_{r_0}^{r} g_{AC}^{\infty}(r) r^2 dr \qquad (5.10)$$

and integration is performed over the region containing all ion pairing species and free ions. R is the conversion factor from Å^3 molecule^{-1} to dm^3 mol^{-1} (viz., R = 6.0221×10^{-4}

dm^3 mol^{-1} $Å^{-3}$ molecule). However, a direct determination of $g_{AC}^{\infty}(r)$ or an equivalent probability distribution function, $P(r)$ is computationally impractical because it involves infinite dilution and, added to this, the inability of conventional molecular dynamics simulations to sample high-energy barrier regions (greater than $2kT$) frequently, resulting in lengthy simulations.

Instead of the above approach, the PMF where the reaction coordinate is the distance r between the cation and anion can be used. However, if $W(r_0)$ is computed correctly and included in the PMF, then K_a may be expressed in terms of the $W(r)$ as,

$$K_a = 4\pi R \int_{r_0}^{r} \exp\left[\frac{-W(r)}{k_B T}\right] r^2 dr \qquad (5.11)$$

here the value r in the definite integration is identical to that in Equation 5.10, but the PMF curve has a maximum in this position, rather than the minimum in the $g_{AC}^{\infty}(r)$ curve. This representation leads to the calculation of the overall equilibrium constants of ion association. However, by choosing integration limits that are specific for CIP, 2SIP and SIP configurations, equilibrium rate constants K_1, K_2 and K_3 can be calculated as

$$K_1 = \frac{[SSIP]}{[A][C]} = \frac{\int_{r_2}^{r_3} \exp\left[\frac{-w(r)}{k_B T}\right] r^2 dr}{\int_{r_3}^{r_n} \exp\left[\frac{-w(r)}{k_B T}\right] r^2 dr} \qquad (5.12a)$$

$$K_2 = \frac{[SSHIP]}{[SSIP]} = \frac{\int_{r_1}^{r_2} \exp\left[\frac{-w(r)}{k_B T}\right] r^2 dr}{\int_{r_2}^{r_3} \exp\left[\frac{-w(r)}{k_B T}\right] r^2 dr} \qquad (5.12b)$$

Table 5.3. $M^{2+}\ldots SO_4^{2-}$ FEP cycle results for the MSFF ion parameters. Where ΔG_a, ΔG_b and ΔG_d are the respective free energies from the FEP cycle shown in Scheme1.

Ion	ΔG_a / kcal.mol^{-1}	ΔG_b / kcal.mol^{-1}	ΔG_d / kcal.mol^{-1}
Mg^{2+}	-1.19	-437.40	-436.21
Ca^{2+}	-2.98	-359.70	-356.72
Mn^{2+}	-3.67	-420.40	-416.73
Fe^{2+}	-1.56	-439.70	-438.14
Co^{2+}	-2.76	-457.20	-454.44
Ni^{2+}	-1.80	-473.00	-471.20
Cu^{2+}	-1.79	-479.20	-477.42
Zn^{2+}	-0.56	-466.60	-466.04

$$K_3 = \frac{[CIP]}{[SSHIP]} = \frac{\int_{r_0}^{r_1} \exp\left[\frac{-w(r)}{k_B T}\right] r^2 dr}{\int_{r_1}^{r_2} \exp\left[\frac{-w(r)}{k_B T}\right] r^2 dr} \qquad (5.12c)$$

In these equations the individual ion pair species are integrated over specific regions, for example the CIP is integrated from r_0 to r_1, where r_0 and r_1 are the positions of the first and second maxima of $W(r)$, or the boundaries of the free energy well corresponding to the CIP species.

The PMF may be calibrated using the absolute free energy of the CIP calculated from FEP as described in 5.2.2 above. In Figure 5.2 procedural steps for calibrating the $MgSO_4$ PMF using the absolute CIP value from FEP calculations are illustrated. Listed in Table 5.2 are the absolute CIP values for $MgSO_4$ calculated using several metal parameter sets, while in Table 5.3 the values calculated for the other metal sulfate systems are shown for comparison. The maximum favorable free energy (PMF local minima) CIP point on PMF curves were shifted to match the FEP calculated CIP free energy of association. Following this, the overall association constants and individual CIP, 2SIP and SIP association constants were calculated for $Mg^{2+}\ldots SO_4^{2-}$.

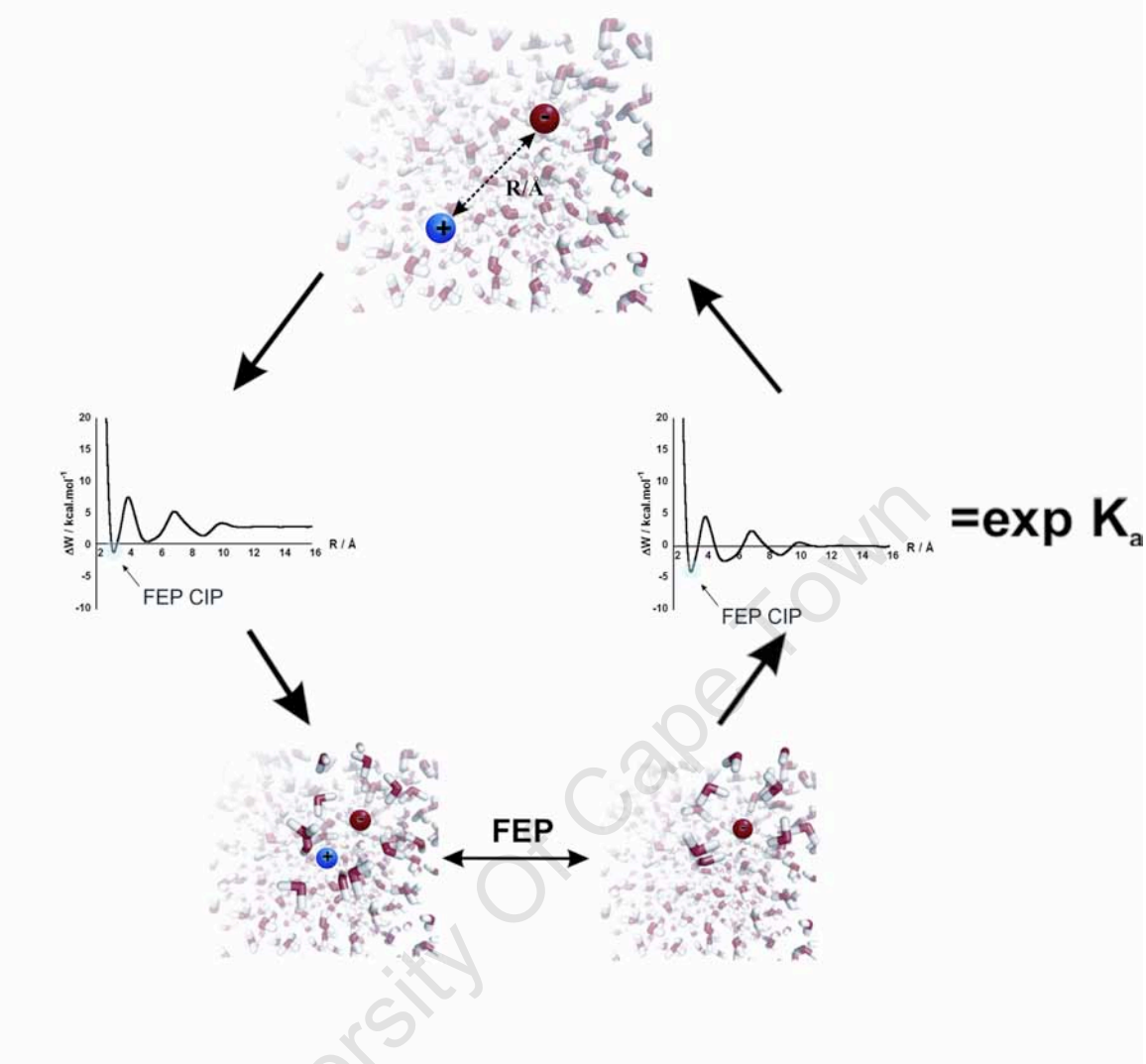

Figure 5.2. Summary of the FEP CIP method used to calibrate PMF profiles.

Using Mg^{2+}…SO_4^{2-} a comparison of the association constants calculated from, (a) the ½ box length, (b) Guardia's $W(r_0)$ and the (c) FEP CIP method of PMF calibration are reported along with the experimentally measured values in Table 5.4. The ½ box length and the Gaurdia method both give an underestimation of 20% of the overall metal sulfate association constant while the FEP method produces a K_a = 167.64 which is in good agreement with experiment. The FEP CIP calibration is equally impressive in the reproduction of individual association constants as they compare with experimental values for SSIP (K_1 = 56.36), SSHIP (K_2 = 1.94) and CIP (K_3 = 0.02). The ½ box length

Table 5.4. Association constants (molar scale) calculated from MSFF for $MgSO_4$ CIP, SSHIP and SIP configurations using different PMF calibration procedures.

	$MgSO_4$			
	K_a	K_1	K_2	K_3
1/2 Box Length	199.03	86.1	1.28	0.03
Guardia Correction	180.31	62.3	1.85	0.03
FEP calibration	167.64	56.36	1.94	0.02
Expt. [12, 14]	164.94	50.00	1.96	0.02

and Guardia's method perform poorly; for example, K_1 is overestimated by 135% and 70% by each of these computational techniques respectively.

Transferability of metal ion parameters is not often considered when simulating solution properties or metal containing proteins. The performance of the MSFF parameters is evaluated here in relation to metal parameters currently used for ionic solution simulations. The overall K_as and individual association constants are compared for each of the ion pair configurations (K_1, K_2 and K_3) produced from FEP CIP calibrated PMFs using the Mg^{2+} parameters of Aqvist, Babu and Lim, CHARMM and MSFF in combination with the Canon et al SO_4^{2-} anion parameters.

The PMFs were calibrated using the specific FEP CIP absolute values produced for that force field (Figure 5.3). An analysis of the PMFs in Figure 5.4 reveals that all the PMFs show clearly defined CIP, SSHIP and SSIP regions, with the CIP minima ranging from 3.375-3.750 Å for Mg through to Ca. All the MSO_4 systems have a SSHIP broad region around 4-6Å that is broken into two minima (these corresponding to different sulfate ion orientations relative to the metal centers). The SSIP regions are similarly broad ranging from 7-10Å, which reflects increase in ion separation to the 'free ion' configuration. The transition barrier from the SSHIP to CIP regions is significantly larger (i.e. 3-12 kcal.mol^{-1}) compared with the barriers separating the other configurations. This is the energy required to remove a water layer between the ions resulting in a CIP. This energy

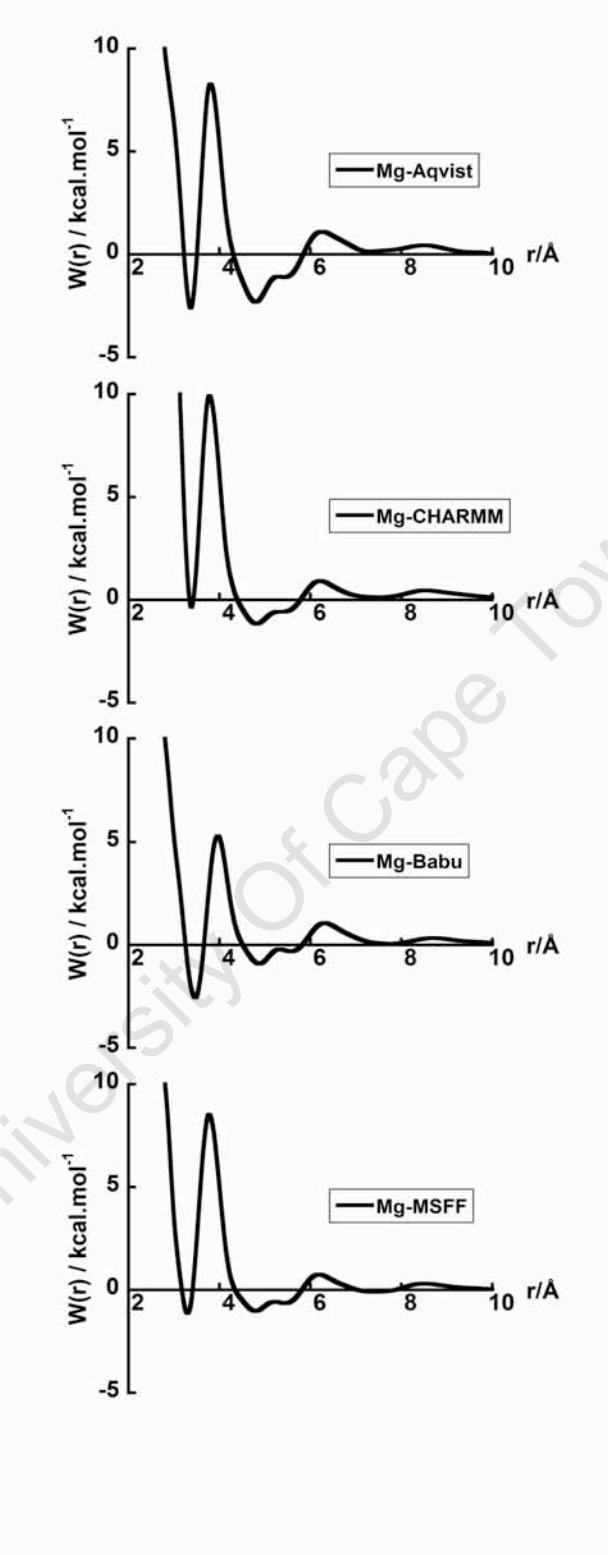

Figure 5.3. Comparison of FEP CIP calibrated PMF profiles of $MgSO_4$ using several parameter sets.

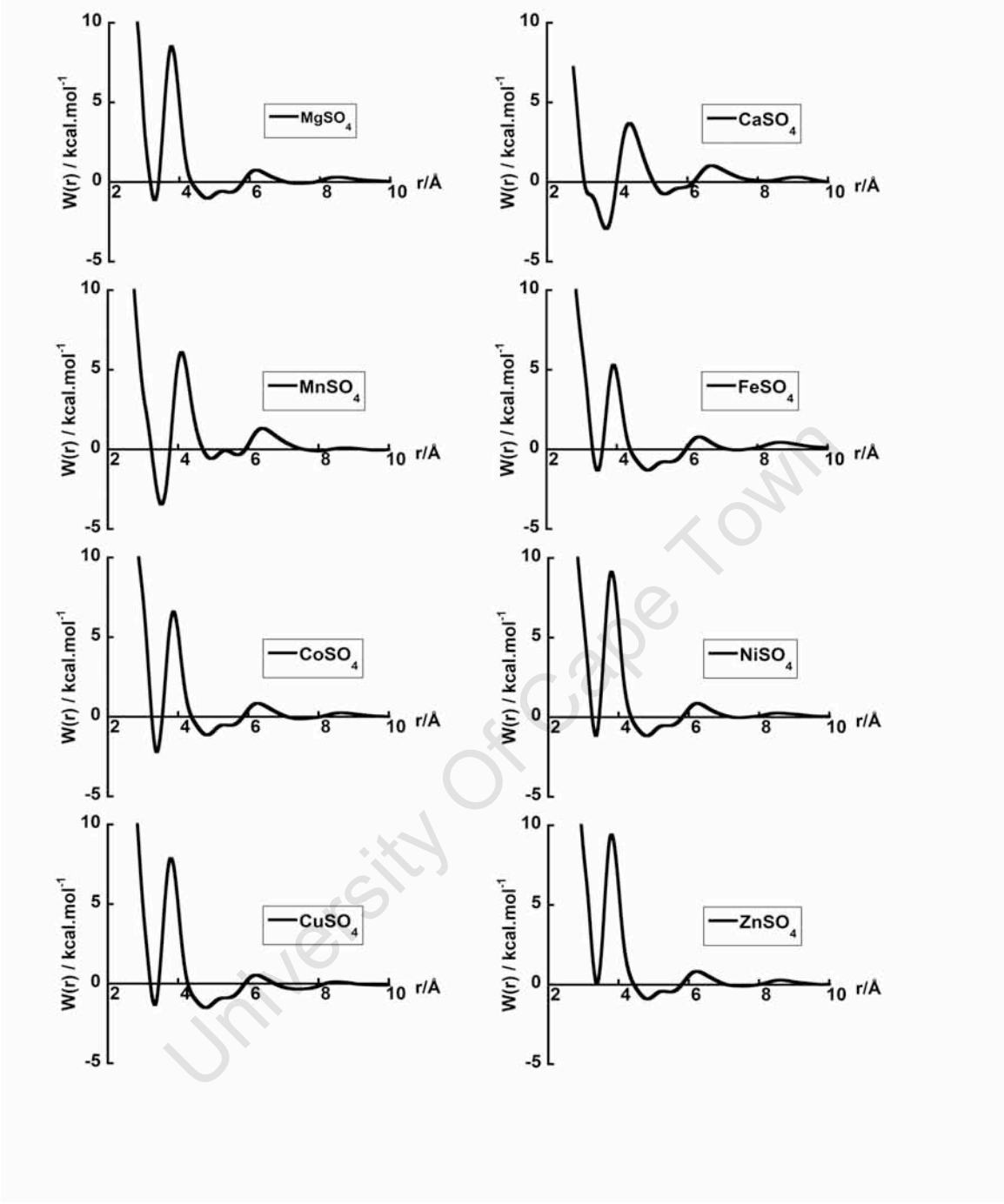

Figure 5.4. FEP CIP calibrated PMF profiles of M^{2+}-SO_4^{2-} systems using the MSFF parameters.

Table 5.5. A comparison of association constants (molar scale) calculated for $MgSO_4$ using the FEP CIP PMF calibration method for published parameter sets and the MSFF.

	$MgSO_4$			
	K_a	K_1	K_2	K_3
Aqvist	140.83	48.33	1.86	0.03
Babu	138.33	11.67	8.57	0.27
CHARMM	143.27	52.21	1.71	0.02
MSFF	167.64	56.36	1.94	0.02
Expt. [14]	164.94	50.00	1.96	0.02

increases with a decrease in the metal ions radius (i.e., an increased charge density). Furthermore, it was observed that the CIP is favored over the SSHIP region but as the charge density increases this preference changes to the SSHIP being favored over CIP. Finally in the $CaSO_4$ PMF, an inflection point occurs within the CIP, this corresponds to the loss of a second water molecule, which results from a change in orientation of Ca^{2+} relative to SO_4^{2-}. The Mg^{2+}-SO_4^{2-} association constants calculated from the calibrated Aqvist, Babu and Lim, CHARMM and MSFF PMFs are listed in Table 5.5. All the force fields other than the MSFF one underestimate K_a. The individual K_i(i=1,2,3) values produced from the Aqvist, Babu and Lim and CHARMM force fields are not within the experimental error estimation, unlike the values produced from the MSFF.

A set of K_as for the complete set of MSFF metal ion parameters that include the metal sulfates; $Ca^{2+}…SO_4^{2-}$, $Mn^{2+}…SO_4^{2-}$, $Fe^{2+}…SO_4^{2-}$, $Co^{2+}…SO_4^{2-}$, $Ni^{2+}…SO_4^{2-}$, $Cu^{2+}…SO_4^{2-}$ and $Zn^{2+}…SO_4^{2-}$ are presented in Table 5.6. The CIP is favoured in every system, followed by the SSHIP and then the SSIP. All the ions (to varying degrees) show two minima within the SSHIP region separated by barriers with differing heights. These minima correspond to the reorientation (rotation and removal) of the waters between the ions, when the ions exchange between the SSIP to SSHIP regions. All the ions, except Mn have a definitive SSIP region. The lack of a clearly defined SSIP region suggests that $Mn^{2+}…SO_4^{2-}$ ion configuration is governed by a two and not a three step ion association

Table 5.6. Association constants (molar scale) for $M^{2+}\ldots SO_4^{2-}$ ion pairs (M= Mg^{2+}, Ca^{2+}, Mn^{2+}, Fe^{2+}, Co^{2+}, Ni^{2+}, $Cu^{2+}$and Zn^{2+}) calculated from FEP CIP calibrated PMFs using the MSFF metal ion parameters compared with available experimental values.

	Sim.				Expt.				
	K_a	**K_1**	**K_2**	**K_3**	**K_a**	**K_1**	**K_2**	**K_3**	**Ref.**
Mg^{2+}	167.64	56.36	1.94	0.02	164.94	50.00	1.96	0.02	[16]
Ca^{2+}	220.83	43.23	1.78	1.31	207.5	-	-	-	[50]
Mn^{2+}	165.81	53.41	0.45	3.21	139	52.63	0.37	3.52	[51]
Fe^{2+}	184.45	51.19	1.43	0.82	158	-	-	-	[52]
Co^{2+}	289.61	54.22	2.54	0.71	328	52.63	2.69	0.88	[51, 53]*
Ni^{2+}	203.33	61.43	1.32	0.75	194.7	54.00	1.9	0.3	[53]
Cu^{2+}	183.36	58.21	1.72	0.25	190.8	54.00	1.95	0.3	[12]*
Zn^{2+}	201.77	51.27	1.96	0.49	199	-	-	-	[14]

*The values for Ni and Cu are not explicitly reported in the publications reference, we have calculated the values from the respective plots for K_i.

mechanism. This observation is consistent with an earlier suggestion by Jackopin and Yeager [54]. The transition barrier going from the SSHIP to CIP ranges between ~4.5-11.1 kcal.mol^{-1} for Ca through to Mg, whereas going from CIP to SSHIP the barrier ranges from ~6.8-11.4 kcal.mol^{-1}. Interestingly, there is little difference (0.4 to 2.2 kcal.mol^{-1}) between the free energies of the SSHIP and CIP pairs.

5.3 Conclusions

In this Chapter, the van der Waals molecular mechanics parameters for a series of divalent metals commonly used in biological and materials aqueous solution simulations were calculated. The Mg^{2+} ion was used to benchmark the ion hydration free energy from a creation/annihilation FEP calculation in water. Using this value the magnesium Lennard-Jones parameters were refined using the contact ion pair free energy value as a reference to ultrasonically measured one. This allowed for the calculation of a parameter set for other divalent ions resulting in the MSFF. Using this parameter set along with FEP CIP PMF calibration method it is shown that for $MgSO_4$, $MnSO_4$, $CoSO_4$, $NiSO_4$, and $CuSO_4$ the overall, CIP, SSHIP and SIP association constants are in excellent agreement with experimentally measured ones. Moreover, accurate association constants for $CaSO_4$, $FeSO_4$, and $ZnSO_4$ were predicted. The MSFF force field along with the FEP CIP PMF calibration method produces very accurate solution behaviour thus allowing the extent of CIP, SSHIP and SIP to be predicted using biased computer simulations. This degree of accuracy may make the MSFF useful in calculating free energy differences in biophysical systems such as divalent metal containing proteins.

5.4 References

1. Lippard, S.J., *The inorganic side of chemical biology.* Nat. Chem. Biol., 2006. **2**(10): p. 504-507.
2. Dudev, T. and Lim, C., *Metal binding affinity and selectivity in metalloproteins: Insights from computational studies.* Ann. Rev. Biophys., 2008. **37**: p. 97-116.
3. Lepsik, M. and Field, M.J., *Binding of calcium and other metal ions to the EF-Hand loops of calmodulin studied by quantum chemical calculations and molecular dynamics simulations.* J. Phys. Chem. B, 2007. **111**(33): p. 10012-10022.
4. Berridge, M.J., Bootman, M.D., and Lipp, P., *Calcium - a life and death signal.* Nature, 1998. **395**(6703): p. 645-648.
5. Bowen, L.M. and Dupureur, C.M., *Investigation of restriction enzyme cofactor requirements: A relationship between metal ion properties and sequence specificity.* Biochemistry, 2003. **42**(43): p. 12643-12653.
6. Barnham, K.J. and Bush, A.I., *Metals in Alzheimer's and Parkinson's diseases.* Curr. Opin. Chem. Biol., 2008. **12**(2): p. 222-228.
7. Bernardis, F.L., Grant, R.A., and Sherrington, D.C., *A review of methods of separation of the platinum-group metals through their chloro-complexes.* React. Funct. Polym., 2005. **65**(3): p. 205-217.
8. Bell, K.J., Westra, A.N., Warr, R.J., Chartres, J., Ellis, R., Tong, C.C., Blake, A.J., Tasker, P.A., and Schroder, M., *Outer-sphere coordination chemistry: Selective extraction and transport of the [PtCl6](2-) anion.* Angew. Chem., Int. Ed., 2008. **47**(9): p. 1745-1748.
9. Youcef, M.H., Benabdallah, T., Ilikti, H., and Reffas, H., *Equilibrium studies on the synergic liquid-liquid extraction process of copper(II) from sulphate media with mixtures of some bidentate mono-Schiff bases and acyclic polyether non-ionic surfactant in chloroform.* Solvent Extr. Ion Exch., 2008. **26**(5): p. 534-555.
10. Richens, D., *The Chemistry of Aqua Ions.* 2004: John Wiley & Sons Ltd, New York.

11. Marcus, Y., *Ion Solvation*. 1st ed. 1985, New York: John Wiley and Sons Ltd, New York.
12. Akilan, C., Hefter, G., Rohman, N., and Buchner, R., *Ion association and hydration in aqueous solutions of copper(II) sulfate from 5 to 65 degrees C by dielectric spectroscopy*. J. Phys. Chem. B, 2006. **110**(30): p. 14961-14970.
13. Moyer, B.A. and Bonnessen, P.V., in *Supramolecular Chemistry of Anions*, A. Bianchi, K. Bowman-James, and E. Garcia-Espana, Editors. 1997, Wiley-VCH, New York.
14. Akilan, C., Rohman, N., Hefter, G., and Buchner, R., *Temperature effects on ion association and hydration in $MgSO_4$ by dielectric spectroscopy*. ChemPhysChem, 2006. **7**(11): p. 2319-2330.
15. Larson, J.W., *Thermodynamics of divalent metal sulfate dissociation and structure of solvated metal sulfate ion pair*. J. Phys. Chem., 1970. **74**(18): p. 3392-3396.
16. Atkinson, G. and Petrucci, S., *Ion association of magnesium sulfate in water at 25 degrees*. J. Phys. Chem., 1966. **70**(10): p. 3122-3128.
17. Ghoufi, A. and Malfreyt, P., *Calculations of the potential of mean force from molecular dynamics simulations using different methodologies: an application to the determination of the binding thermodynamic properties of an ion pair*. Mol. Phys., 2006. **104**(22-24): p. 3787-3799.
18. Chaban, G.M., Huo, W.M., and Lee, T.J., *Theoretical study of infrared and Raman spectra of hydrated magnesium sulfate salts*. J. Chem. Phys., 2002. **117**(6): p. 2532-2537.
19. Petrucci, S., ed. *Ionic Interactions from Fused Solutions to Fused Salts, Vol. 1: Equilibrium and Mass Transport*. Vol. 1. 1971, Academic, New York: New York.
20. Jorgensen, W.L., Chandrasekhar, J., Madura, J.D., Impey, R.W., and Klein, M.L., *Comparison of simple potential functions for simulations liquid water*. J. Chem. Phys., 1983. **79**(2): p. 926-935.
21. Brooks, B.R., Bruccoleri, R.E., Olafson, B.D., States, D.J., Swaminathan, S., and Karplus, M., *CHARMM - A program for macromolecular energy, minimization, and dynamics calculations*. J. Comput. Chem., 1983. **4**(2): p. 187-217.

22. Brooks, B.R., Brooks, C.L., Mackerell, A.D., Nilsson, L., Petrella, R.J., Roux, B., Won, Y., Archontis, G., Bartels, C., Boresch, S., Caflisch, A., Caves, L., Cui, Q., Dinner, A.R., Feig, M., Fischer, S., Gao, J., Hodoscek, M., Im, W., Kuczera, K., Lazaridis, T., Ma, J., Ovchinnikov, V., Paci, E., Pastor, R.W., Post, C.B., Pu, J.Z., Schaefer, M., Tidor, B., Venable, R.M., Woodcock, H.L., Wu, X., Yang, W., York, D.M., and Karplus, M., *CHARMM: The biomolecular simulation program.* J. Comput. Chem., 2009. **30**(10): p. 1545-1614.

23. MacKerell, A.D., Bashford, D., Bellott, M., Dunbrack, R.L., Evanseck, J.D., Field, M.J., Fischer, S., Gao, J., Guo, H., Ha, S., Joseph-McCarthy, D., Kuchnir, L., Kuczera, K., Lau, F.T.K., Mattos, C., Michnick, S., Ngo, T., Nguyen, D.T., Prodhom, B., Reiher, W.E., Roux, B., Schlenkrich, M., Smith, J.C., Stote, R., Straub, J., Watanabe, M., Wiorkiewicz-Kuczera, J., Yin, D., and Karplus, M., *All-atom empirical potential for molecular modeling and dynamics studies of proteins.* J. Phys. Chem. B, 1998. **102**(18): p. 3586-3616.

24. Cannon, W.R., Pettitt, B.M., and McCammon, J.A., *Sulfate anion in water - model structural, thermodynamic, and dynamic properties.* J. Phys. Chem., 1994. **98**(24): p. 6225-6230.

25. Mason, P.E., Dempsey, C.E., Neilson, G.W., and Brady, J.W., *Nanometer-scale ion aggregates in aqueous electrolyte solutions: Guanidinium sulfate and guanidinium thiocyanate.* J. Phys. Chem. B, 2005. **109**(50): p. 24185-24196.

26. Aqvist, J., *Ion water interaction potentials derived from free-energy perturbation simulations.* J. Phys. Chem., 1990. **94**(21): p. 8021-8024.

27. Babu, C.S. and Lim, C., *Empirical force fields for biologically active divalent metal cations in water.* J. Phys. Chem. A, 2006. **110**(2): p. 691-699.

28. Frisch, M.J., et al., *Gaussian 03, Revision C.02.* 2003.

29. Chen, I.J., Yin, D.X., and MacKerell, A.D., *Combined ab initio/empirical approach for optimization of Lennard-Jones parameters for polar-neutral compounds.* J. Comput. Chem., 2002. **23**(2): p. 199-213.

30. Boys, S.F. and Bernardi, F., *Calculation of small molecular interactions by differences of seperate total energies - Some procedures wiht reduced errors.* Mol. Phys., 1970. **19**(4): p. 553-&.

31. Lamoureux, G. and Roux, B., *Modeling induced polarization with classical Drude oscillators: Theory and molecular dynamics simulation algorithm.* The Journal of Chemical Physics, 2003. **119**(6): p. 3025-3039.

32. York, D.M., Darden, T.A., and Pedersen, L.G., *The effect of long-range electrostatic interactions in simulations of macromolecular crystals: A comparison of the Ewald and truncated list methods.* J. Chem. Phys., 1993. **99**(10): p. 8345-8348.

33. Essmann, U., Perera, L., Berkowitz, M.L., Darden, T., Lee, H., and Pedersen, L.G., *A smooth particle mesh Ewald method.* J. Chem. Phys., 1995. **103**(19): p. 8577-8593.

34. Allen, M.P. and Tildesley, D.J., *Computer Simulations of Liquids.* 1989, Oxford: Clarendon Press.

35. Strumpfer, J. and Naidoo, K.J., *Computing free energy hypersurfaces for anisotropic intermolecular associations.* J. Comput. Chem., 2010. **31**(2): p. 308-316.

36. Marcus, Y., *Ion properties.* 1997, New York: Marcel Dekker, Inc.

37. Guardia, E., Rey, R., and Padro, J.A., Chem. Phys., 1991. **155**: p. 187-195.

38. Chialvo, A.A., Cummings, P.T., Cochran, H.D., Simonson, J.M., and Mesmer, R.E., J. Chem. Phys., 1995. **103**: p. 9379-9387.

39. Gao, J., *Simulation of the Na^+Cl^- ion pair in supercritical water.* J. Phys. Chem., 1994. **98**(24): p. 6049-6053.

40. Chialvo, A.A., Cummings, P.T., and Simonson, J.M., J. Chem. Phys., 2000. **113**: p. 8093-8100.

41. Chialvo, A.A., Ho, P.C., Palmer, D.A., Gruszkiewicz, M.S., Cummings, P.T., and Simonson, J.M., J. Phys. Chem. B, 2002. **106**: p. 2047-2053.

42. Lienke, A., Klatt, G., Robinson, D.J., Koch, K.R., and Naidoo, K.J., *Modeling platinum group metal complexes in aqueous solution.* Inorg. Chem., 2001. **40**(10): p. 2352-2357.

43. Naidoo, K.J., Lopis, A.S., Westra, A.N., Robinson, D.J., and Koch, K.R., *Contact ion pair between Na+ and PtCl62- favored in methanol.* J. Am. Chem. Soc., 2003. **125**(44): p. 13330-13331.

44. Naidoo, K.J., Klatt, G., Koch, K.R., and Robinson, D.J., *Geometric hydration shells for anionic platinum group metal chloro complexes.* Inorg. Chem., 2002. **41**(7): p. 1845-1849.

45. Jorgensen, W.L., Buckner, J.K., Huston, S.E., and Rossky, P.J., *Hydration and energetics for $(CH_3)_3CCl$ ion pairs in aqueous-solution.* J. Am. Chem. Soc., 1987. **109**(7): p. 1891-1899.

46. Patra, M. and Karttunen, M., *Systematic comparison of force fields for microscopic simulations of NaCl in aqueous solutions: Diffusion, free energy of hydration, and structural properties.* J. Comput. Chem., 2004. **25**(5): p. 678-689.

47. Gavryushov, S. and Linse, P., *Effective interaction potentials for alkali and alkaline earth metal ions in SPC/E water and prediction of mean ion activity coefficients.* J. Phys. Chem. B, 2006. **110**(22): p. 10878-10887.

48. Jorgensen, W.L., Buckner, K., Boudon, S., and Tirado-Rives, J., *Efficient computation of absolute free energies of binding by computer simulations. Application to the methane dimer in water.* J. Chem. Phys., 1988. **89**(6): p. 3742-3746.

49. Pratt, L.R. and Chandler, D., J. Chem. Phys., 1977. **67**: p. 3683.

50. Bester-Rogac, M., *Electrical conductivity of concentrated aqueous solutions of divalent metal sulfates.* J. Chem. Eng. Data, 2008. **53**(6): p. 1355-1359.

51. Bhatti, S.S. and Lark, B.S., *Ultrasonic studies of association constants and reaction volumes of $MnSO_4$ and $CoSO_4$ in aqueous-solutions at 298.15 K.* Acustica, 1981. **48**(1): p. 64-68.

52. Izatt, R.M., Eatough, D., and Christen, J., J. Chem. Soc. A - Inorg. Phys. Theor, 1969: p. 45.

53. Chen, T., Hefter, G., and Buchner, R., *Ion association and hydration in aqueous solutions of nickel(II) and cobalt(II) sulfate.* J. Solution Chem., 2005. **34**(9): p. 1045-1066.

54. Jackopin, L.G. and Yeager, E., *Ultrasonic relaxation in manganese sulfate solutions.* J. Phys. Chem., 1970. **74**(21): p. 3766-&.

CHAPTER 6

Experimental and Computational Study of Hydrated Metal Sulfates

6.1 Introduction

In both chemistry and biology these metal ions are generally solvated and can associate with oppositely charged solvated ions to form complexes and ion pairs [1]. In aqueous media, the formation of ion paired species in dilute electrolyte solutions of alkali earth metal sulfates is limited due to the shielding of the small metal ions by water, via strong ion-solvent interactions, primarily resulting from solvent polarization and the high charge-to-size ratios (electrostatics) of the ions [2-5].

Ion solvation has been extensively studied using both computational and experimental methods. Recent studies related to ion solvation have focused on several aspects including ion hydration structure, mobilities of hydrated ions, reorientation of water molecules closely associated with ions and ligand/water exchange mechanisms [6-12]. All of these studies have lead to a greater understanding of ion solvation and association. Experimentally ion solvation and pairing studies of several metal sulfate 2:2 electrolyte solutions [13-19] have revealed a three-step mechanism whereby strongly hydrated ions associate via a stepwise release of several water molecules around the respective ions in steps one and two (outer-sphere coordination), terminating at step three in a complex formation (inner-sphere complexation) via ligand exchange [20], as shown in Scheme 6.1. Where C and A are the cation and anion, SSIP is the solvent separated ion pairs, SSHIP is the solvent-shared ion pairs and CIP is the contact ion pairs and the association constant, K_a, is consequently given as

$$K_a = K_1\left(1 + K_2 + K_2K_3\right) \tag{6.1}$$

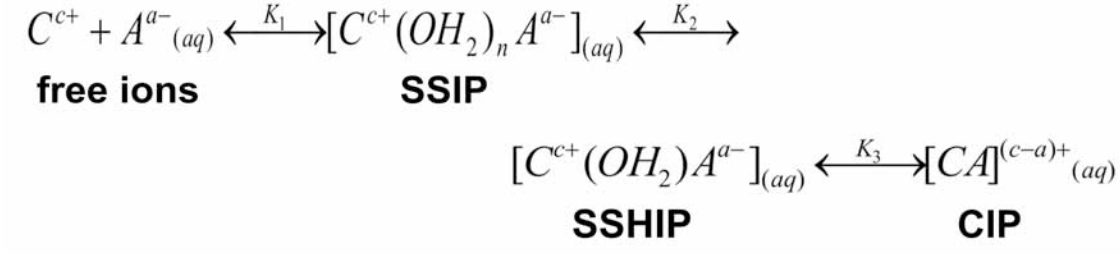

Scheme 6.1. Three step mechanism of ion association

In this chapter the hydration structures for metal sulfate electrolyte solutions using the metal solution force field (MSFF) parameters derived in Chapter 5, are determined from molecular dynamics simulations. Hydration numbers for the $MgSO_4$, $CoSO_4$, $NiSO_4$ and $ZnSO_4$ salt solutions have been determined from density and ultrasonic velocity studies and are compared to hydration numbers obtained from molecular dynamics simulations.

6.2 Thermo-acoustic Analysis

6.2.1 Experimental

Thermodynamic properties (i.e. including molar volumes, expansibilities and isentropic compressibilities) of aqueous electrolyte solutions can be estimated directly from the measurement of ultrasonic velocity and density [21, 22], assuming there is no loss in solution volume and no change in adiabatic nature of the system. In this Chapter, experimental studies of several metal sulfate solutions (i.e. $MgSO_4 \cdot 7H_2O$, $CoSO_4$, $NiSO_4 \cdot 6H_2O$ and $ZnSO_4 \cdot 7H_2O$) which have been performed using ultrasonic interferometery (UI) are described. The total hydration number of ionic salts can then be determined using Pasynski's equation, given as

$$n_h = \frac{n_w}{n_s}\left(1 - \frac{\beta}{\beta_w}\right) \tag{6.2}$$

where β (obtained from the Newton-Laplace Equation as given in Chapter 4, Equation 4.4) and β_w are the isentropic compressibilities of a metal sulfate solution and of pure water and n_w and n_s are the number of moles of water and solute, respectively.

Equation 6.2 holds true if it is assumed that, n_h is the number of water molecules of the first solvent layer surrounding the solute and these water molecules are trapped so tightly that they can be considered as incompressible [7].

6.2.2 Materials and Methods

All chemicals ($MgSO_4 \cdot 7H_2O$, $CoSO_4$, $NiSO_4 \cdot 6H_2O$ and $ZnSO_4 \cdot 7H_2O$) used were obtained from Anglo-Platinum Pty Ltd SA. The salt solutions were prepared by weight using an Afcoset-ER-120A scale with a precision of ± 0.01 mg to weigh the salts, which were dissolved in doubly Millipore water. Salt solution compositions are given in molarity ($mol.dm^{-3}$) throughout the chapter. Density determinations were carried out at 298.15 K using an Anton Paar digital Model DMA 35 with a precision of ± 0.01 $g.cm^{-3}$.

Ultrasound measurements were performed at 298.15 K using an ultrasonic interferometer Model M-81G operating at 3 MHz, after calibration with Millipore water at 298.15 K. This model consists of a double-walled measuring cell which holds the solution and allows for water circulation (in the wall around the solution) from a thermostatically regulated Huber water bath, with a CC1 compatible control, to maintain constant temperature with an accuracy of ± 0.1 K, as described in Section 4.3.

6.3 Molecular Dynamics Simulations

Molecular dynamics (MD) simulations of the aqueous metal sulfate (i.e. $Mg^{2+}SO_4^{2-}$, $Ca^{2+}SO_4^{2-}$, $Mn^{2+}SO_4^{2-}$, $Fe^{2+}SO_4^{2-}$, $Co^{2+}SO_4^{2-}$, $Ni^{2+}SO_4^{2-}$, $Cu^{2+}SO_4^{2-}$ and $Zn^{2+}SO_4^{2-}$) where started using either the CIP (r ~ 3.5 Å) or the free ion (r ~ 10.0 Å) orientations, by taking the distance, r, the starting distance between the ions from the PMF plots in Chapter 5 (Figure 5.4). The metal ions are modeled using the MSFF parameters derived in Chapter 5, the sulfate ions are taken from the literature potentials of Cannon et al. (sulfate and oxygen atom charges: S, 2.4; O,-1.1) [23, 24] and the CHARMM variant of the TIP3P water model [25, 26] was used to model the solvent.

Molecular dynamics simulations were performed in the canonical (NVT) ensemble using the CHARMM program [27, 28]. Simulations consisted of 2 ions (one M^{2+} ion and one SO_4^{2-}) ion and either 503 (free ion simulation) or 504 (CIP simulation) water molecules in cubic boxes of sides 24.86 Å in length, employing periodic boundary conditions and were run for 20 ns. Equations of motion were integrated using the

Velocity-Verlet2 (vv2) integrator with a time step of 1 fs [29]. The temperature was maintained at 298.15 K using a method based on the Nose-Hoover thermostat with τ = 0.1 [29]. Electrostatic interactions were calculated using the particle-mesh Ewald (PME) method [30, 31] with a 12.0 Å real space cutoff while the Lennard-Jones interactions were truncated using an atom-based switching function applied between 10.0 and 12.0 Å. The SHAKE algorithm [32] was employed to restrain all bond parameters containing hydrogen atoms.

6.4 Results and Discussion

6.4.1 Experimental Hydration Numbers

The densities ρ and ultrasonic velocity υ of the aqueous solutions of $MgSO_4 \cdot 7H_2O$, $CoSO_4$, $NiSO_4 \cdot 6H_2O$ and $ZnSO_4 \cdot 7H_2O$ measured as a function of the molar concentration over the range 0.05 – 0.25 mol.dm^{-3} at 298.15 K are presented in Table 6.1. These data were subsequently used to calculate the isentropic compressibilities of the salt solutions as shown in Figure 6.1(a), using the Newton-Laplace formula. From these plots it is seen that a linear dependence exists for each of the aqueous salt solution at 298.15 K, such that the compressibility gradually decreases with an increasing concentration of salt.

In general, a decreasing compressibility of an ionic solution is attributed to an increased number of solvent molecules, which are attracted to the electric field of the ions [4]. While solvent molecules become incompressible in a strong electric field (electrostriction), an increase in the salt (ion) concentration should result in more solvent molecules participating in incompressible solvation shells effectively lowering the isentropic compressibility. However, competition for positions within the first hydration sphere of metal ions between sulfate ions and water molecules resulting in ion pair formation would lower the effective charge density of the metal ions, making them less electrostrictive with respect to their surroundings. Thus, the ion pairing process would cause an increase in the observed compressibility of the solution at increased concentration. Thus the degree of ion pairing involved in aqueous metal sulfate salt

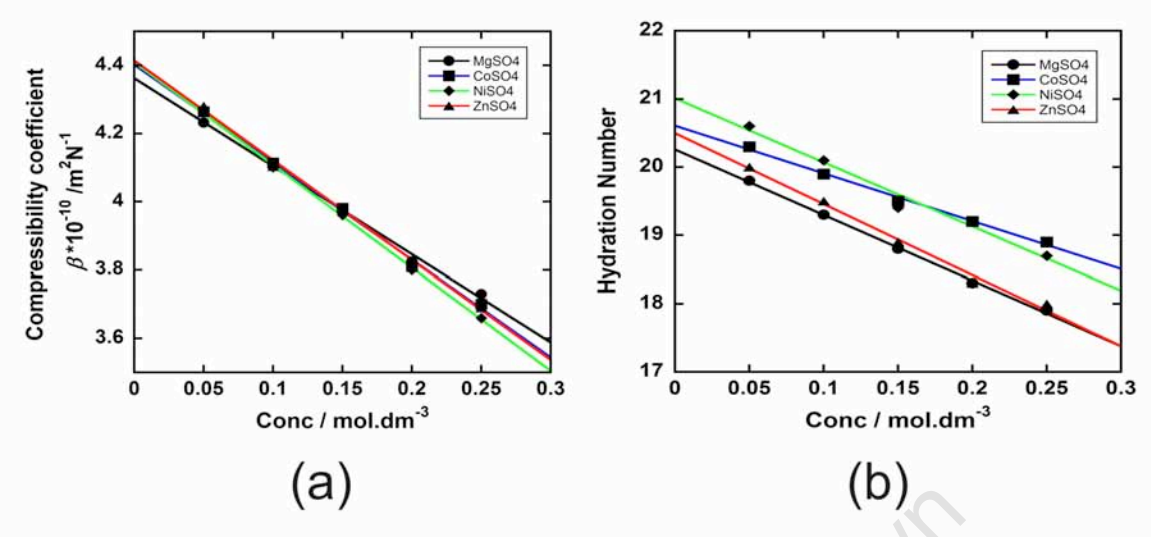

Figure 6.1. (a) Isentropic compressibility and (b) Hydration number vs. salt concentration in water.

solutions must be known in order to fully understand the dynamics of the hydration of these systems.

The combination of the isentropic compressibilities of the salt solutions and the compressibility of water (calculated at $4.42*10^{-10}$ m^2N^{-1}) allows for the calculation of hydration numbers, N_h, and associated differences in hydration number, ΔN_h, for the aqueous $MgSO_4 \cdot 7H_2O$, $CoSO_4$, $NiSO_4 \cdot 6H_2O$ and $ZnSO_4 \cdot 7H_2O$ solutions at 298.15 K, using the Pasynski method (Equation 6.2).[1] The solvation numbers as a function of concentration are given in Table 6.2 and are graphically shown in Figure 6.1(b).

From Figure 6.2(b) and Table 6.2, there is a linear relationship between the calculated solvation numbers, N_h, and the concentration within the range used for this work. In order to compare these results to the computationally derived hydration data, the hydration number at infinite dilution (concentration = 0) is calculated by extrapolation of the linear fit (y = ax + b) to C=0. Table 6.3 contains solvation numbers calculated in this manner, along with the associated coefficients and the coefficient errors. The coefficient errors are

[1] The Pasynski method yields solvation numbers that have errors increasing rapidly with decreasing salt concentration.

Table 6.1. Densities (in units $g.cm^{-3}$) and ultrasonic velocities (in units $m.s^{-1}$) of aqueous $MgSO_4 \cdot 7H_2O$, $CoSO_4$, $NiSO_4 \cdot 6H_2O$ and $ZnSO_4 \cdot 7H_2O$ solutions at 298.15 K.

	MgSO4		**CoSO4**		**NiSO4**		**ZnSO4**	
Concentration ($mol.dm^{-3}$)	ρ	v	ρ	v	ρ	v	ρ	v
0.05	1003	1536	1004	1537	1004	1534	1003	1538
0.10	1004	1560	1008	1558	1009	1557	1009	1561
0.15	1006	1593	1013	1589	1014	1592	1016	1597
0.20	1009	1611	1018	1604	1019	1601	1019	1608
0.25	1015	1632	1023	1631	1025	1634	1024	1636

Table 6.2. Hydration numbers, N_h, and associated differences in hydration number, ΔN_h, obtained for aqueous $MgSO_4 \cdot 7H_2O$, $CoSO_4$, $NiSO_4 \cdot 6H_2O$ and $ZnSO_4 \cdot 7H_2O$ solutions at 298.15 K, as a function of concentration.

	$MgSO_4$		**$CoSO_4$**		**$NiSO_4$**		**$ZnSO_4$**	
Concentration ($mol.dm^{-3}$)	**N_h**	**ΔN_h**	**N_h**	**ΔN_h**	**N_h**	**ΔN_h**	**N_h**	**ΔN_h**
0.05	19.8	5.8	20.3	4.4	20.6	4.7	20.0	4.4
0.10	19.3	4.7	19.9	3.9	20.1	4.3	19.5	4.2
0.15	18.8	3.8	19.5	3.7	19.4	3.5	18.9	3.8
0.20	18.3	3.0	19.2	3.2	19.2	3.4	18.3	3.4
0.25	17.9	3.1	18.9	3.0	18.7	2.9	18.0	2.8

Table 6.3. Parameters obtained from the linear fit (y = ax + b) of the metal sulfate solutions to obtain the hydration number at infinite dilution, N_{h0}.

Salt	a	Error in a	b	Error in b	R	N_h	N_h[a]
$MgSO_4$	-9.6	0.2309	20.26	0.0383	0.99913	20.3	21.6
$CoSO_4$	-7.0	0.3055	20.61	0.0507	0.99716	20.6	23.3
$NiSO_4$	-9.4	0.2000	21.01	0.0332	0.99865	21.0	24.5
$ZnSO_4$	-10.4	0.2309	20.50	0.3830	0.99486	20.5	22.0

a. N_h values obtained from the work of Marcus.

factors associated with fitting a straight line to data points (obtained at several concentrations), within the plotting facility kaleidograph."

The trend in the solvation numbers obtained in this work matches that obtained by Marcus [33], i.e. the hydration number trend from lowest to highest is, $MgSO_4$ < $ZnSO_4$ < $CoSO_4$ < $NiSO_4$. However, the differences in hydration number for this work are 30 – 50 % smaller. Furthermore, 1.7 – 2.5 (system dependent) water molecules are shown to be released when comparing the hydration number at infinite dilution at 0.25 mol.dm^{-3}. These differences suggest the presence of ion pairing at this low concentration and compare favourably with the change in solvation numbers calculated by Marcus (2.5 - 4.1 water molecules) based on volume changes upon ion pairing.

6.4.2 Solvent Structuring from Simulation

Solvent structures of the CIP and free ion metal sulfates from the molecular dynamics simulations were analysed using the isotropic probability density via site-site pair distribution functions (PDFs),

$$g_{\alpha,\beta}(r) = \frac{V}{N_\alpha N_\beta}\left\langle \sum_{i=1}^{N_\alpha}\sum_{j=1}^{N_\beta}\delta\left(r - r_{\alpha_i\beta_j}\right)\right\rangle \tag{6.3}$$

where $r_{\alpha_i\beta_j}$ is the distance between the atomic sites α and β on the molecules *i* and *j* respectively, N_α and N_β are the total number of α and β atoms in the volume *V* and the angular brackets denote the ensemble average. Furthermore, three-dimensional water probability density matrices are constructed in order to obtain the detailed anisotropic molecular associations of the first solvation shells for several of the metal sulfate species in the CIP and free ion configurations. This was done by removing the rotational and translational diffusion of the salt complex (i.e. the solute), for each frame in the trajectories. The solute in each stored coordinate set was then reoriented to the best least squares fit with a reference coordinate set. A coordinate transformation was then applied to all the atoms in the system. The complete MD trajectory for each metal sulfate solution simulation was used to analyse the solvent structure. Furthermore, the statistical independence of each frame was maintained by an imposed separation of at least 0.5 ps from each other. The solvent sites were used to calculate the probability densities on a grid with a mesh size of 0.5 Å. A Gaussian distribution function,

$$G(r) = \left(\frac{a}{\pi}\right)^{\frac{3}{2}}\exp\left(-ar^2\right) \tag{6.4}$$

centered on each solvent site is used to represent accurately the distribution of the sites across the mesh. The densities of the sites are distributed over neighboring bins such that 90% of the binned density for a molecular site is within its site radius (van der Waals

radius). This parameter is determined by appropriate selection of the constant *a* for each site. The densities in each box were summed for all the selected frames from the dynamics run. The final solvent density matrix was normalised using equation 6.5 so that the density of bulk solvent corresponds to a value of 1, while 50% above bulk density corresponds to a value of 1.5, etc.

$$\overline{\rho}(x_i, y_i, z_i) = \rho(x_i, y_i, z_i)\frac{n_{xbin} n_{ybin} n_{zbin}}{n_{molecular\,site} n_{frames}} \tag{6.5}$$

Here n_{xbin}, n_{ybin} and n_{zbin} are the number of divisions in the *x*, *y* and z directions in the simulation box while $n_{molecularsite}$ and n_{frames} represent the number of oxygen atoms in each frame and the number of frames respectively. The non-normalized density for grid point (x_i,y_j,z_k) is given as $\rho(x_i,y_j,z_k)$. SDFs for the first solvation shells are calculated at 50% above bulk.

The number of solvent molecules within the first hydration shell of the metal sulfate complexes is calculated by integrating the first peaks of the metal-O(w) and sulfur-(w) PDFs for each salt solution. This results in the running integration numbers $n_{\alpha\beta}(r)$, defined in equation 6.6, where ρ_0 is the number density of the atoms of type β.

$$n_{\alpha\beta}(r) = 4\pi\rho_0 \int_0^r g_{\alpha\beta}(r')r'^2 dr \tag{6.6}$$

The number of correlated atoms $n_{\alpha\beta}(r)$ for the first peaks are the ensemble averaged number of waters found in the first solvation shell.

The PDFs, i.e. metal-O(w), metal-H(w), sulfur-O(w) and sulfur-H(w) along with their corresponding running integration numbers for the CIP simulations are shown in Figures 6.2 and 6.3, while the PDFs for the free ion simulations are given in Appendix A. The characteristic values for the PDFs for the salt solutions are presented in Tables 6.4 (metal) and 6.5 (sulfate). $CaSO_4$ and $MnSO_4$ do not have any value for free ions as they associate forming a contact ion pair within the equilibration simulation, and do not become unassociated throughout the 20ns production simulation. This association is explained by

the low free energy barriers for these systems described by the potentials of mean force in Chapter 5.

6.4.2.1 Metal-Water Pair Distribution Functions

Examination of the metal-O(w) metal-H(w) PDFs for both the CIP and free ion simulations reveals no significant differences in the overall profiles for all the metal sulfate solutions, with the metal-O(w) first maxima positions ranging from 1.93 - 2.01 Å and a second maxima in the region of 4.1 - 4.2 Å. Similarly, the metal-H(w) first maxima vary from 2.9 - 3.1 Å. Upon formation of the CIP the position of the first peaks (first solvation shell) of the metal-O(w) either increase, i.e. the Mg^{2+}-O intermolecular distance is 1.93 Å for the free ion and 1.97 Å in the CIP, or they remain the same.

The metal-O(w) peak heights give an indication of the degree of association between the metal ion and water molecules [34, 35]. From the free ion simulations, the $g(r)$ values are observed to range between 21.65 for $CuSO_4$ to 23.76 for $NiSO_4$. With the formation of the CIP these values are reduced by ~20-40%, i.e. 15.17 for $CuSO_4$ and 14.51 for $NiSO_4$. This reduction in the metal-O(w) peak heights reveals that upon ion pairing

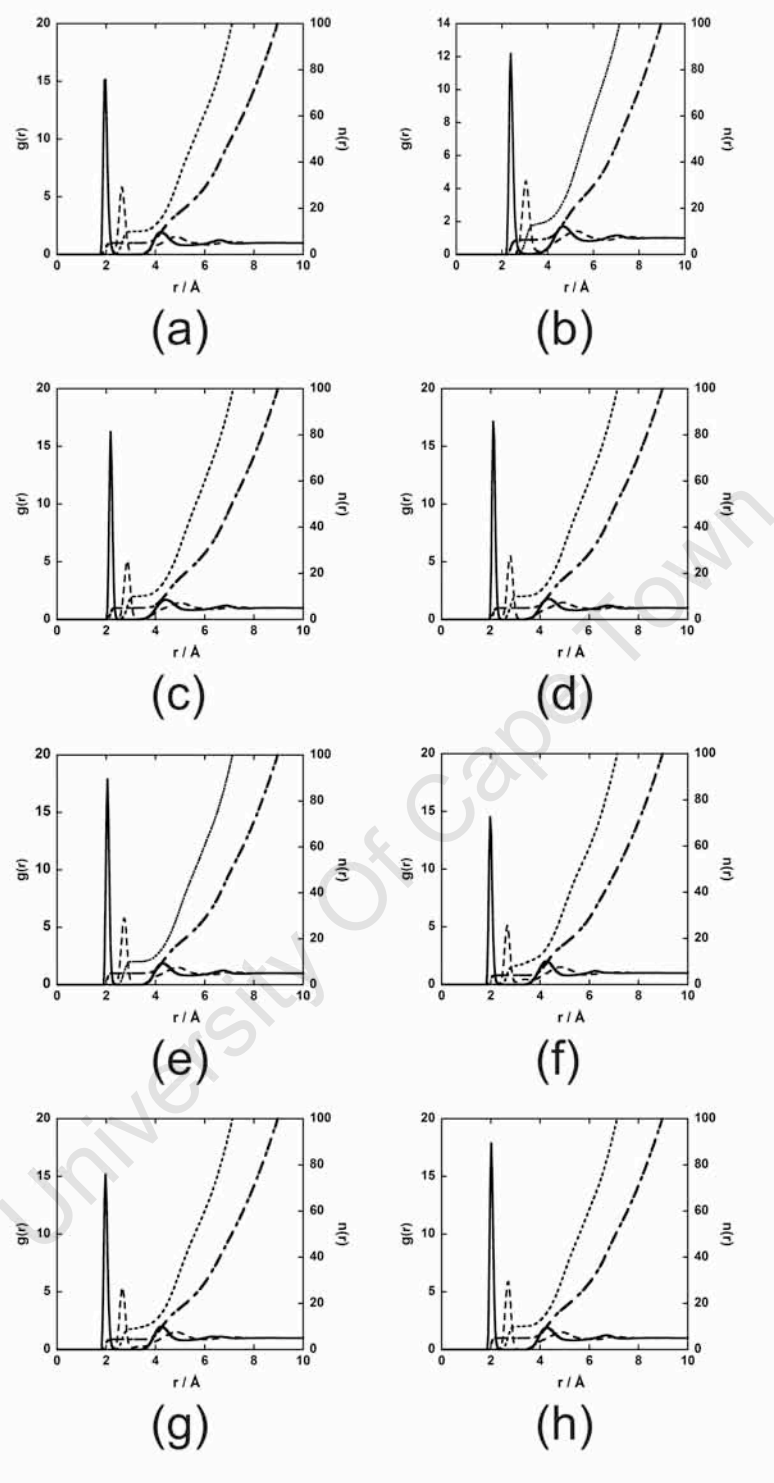

Figure 6.2. Metal-oxygen (solid line) and metal-hydrogen (dashed) pair distribution functions along with their corresponding plots of $n(r)$ for (a) $MgSO_4$, (b) $CaSO_4$, (c) $MnSO_4$, (d) $FeSO_4$, (e) $CoSO_4$, (f) $NiSO_4$, (g) $CuSO_4$ and (h) $ZnSO_4$ from the CIP simulation.

Table 6.4. Characteristic values for the pair distribution functions for the metal ion of the aqueous salt solutions for both the CIP and free ion simulations to the water oxygen g(M^{2+}-O). Δn is the difference between $n(r)$ for the free ion simulations and the CIP simulation.

	CIP			Free Ions			
	r_{M1} / Å	$g(r)$	$n(r)$ / # of waters	r_{M1} / Å	$g(r)$	$n(r)$ / # of waters	Δn
MgSO4	1.97	15.15	5.00	1.93	22.58	6.00	1.00
CaSO4	2.38	12.18	6.35	-	-	-	-
MnSO4	2.18	16.25	5.00	-	-	-	-
FeSO4	2.09	17.14	5.00	2.09	22.31	6.00	1.00
CoSO4	2.05	17.88	5.00	2.01	22.79	6.00	1.00
NiSO4	1.97	14.51	4.00	1.97	23.76	6.00	2.00
CuSO4	1.97	15.17	4.41	1.93	21.65	6.00	1.59
ZnSO4	2.01	17.87	5.00	2.01	23.00	6.00	1.00

the metal-water association strength is reduced. This results from the reduction in the metal ion charges due to the formation of neutral metal sulfate complexes.

Another feature upon CIP formation is the reduction of the number of waters found in the first solvation shell of the metal ions given in Table 6.4. On average 1 water molecule is released upon ion pairing; however, the difference for $CuSO_4$ is ~1.6 water whereas $NiSO_4$ releases 2 water molecules upon CIP formation. This suggests either a greater reduction in effective charge of these ions, which is unlikely for a simple molecular mechanics force field model, or that $CuSO_4$ and $NiSO_4$ have different ion pairing structures compared to the other metal sulfate systems. This topic is discussed further in Section 6.4.2.3.

Table 6.5. Characteristic values for the pair distribution functions for the sulfate ion of the aqueous salt solutions for both the CIP and free ion simulations. These data are calculated from the sulfur of the sulfate to the water oxygen. Δn is the difference between n(*r*) for the free ion simulations and the CIP simulation.

	CIP			Free Ions			
	r_{M1} / Å	*g*(*r*)	*n*(*r*) / # of waters	r_{M1} / Å	*g*(*r*)	*n*(*r*) / # of waters	Δ*n*
MgSO4	3.87	4.14	15.39	3.75	3.77	14.53	-0.86
CaSO4	3.75	3.19	15.57	-	-	-	-
MnSO4	3.79	3.09	16.60	-	-	-	-
FeSO4	3.79	3.19	16.06	3.75	3.75	14.33	-1.73
CoSO4	3.87	3.42	15.74	3.75	3.77	14.48	-1.26
NiSO4	3.83	2.60	14.68	3.75	3.76	14.49	-0.19
CuSO4	3.83	3.11	14.86	3.75	3.75	14.48	-0.38
ZnSO4	3.87	3.62	15.58	3.75	3.77	14.49	-1.09

6.4.2.2 Sulfate-Water Pair Distribution Functions

The structuring of water molecules around the sulfate ions for the metal sulfate systems is represented by the sulfur-O(w) and sulfur-H(w) PDF profiles for both the CIP and free ion simulations. As with the metal-O(w) PDFs, the sulfur-O(w) and sulfur-H(w) reveal similar profiles, except for $NiSO_4$, as shown in Figure 6.3(f). This change in the $NiSO_4$ profile corresponds with the idea above that the solvent structuring of the $NiSO_4$ CIP is different to that of the other metal sulfate systems.

The data summarised in Table 6.5 reveals that upon ion pairing the first maxima of the sulfur-O(w) PDF shifts to the right from ~3.75 Å to a range of 3.75-3.87 Å depending on the metal counterion, while the heights of the maxima decrease, except for $MgSO_4$ which increases, indicating a stronger association with water upon ion pairing.

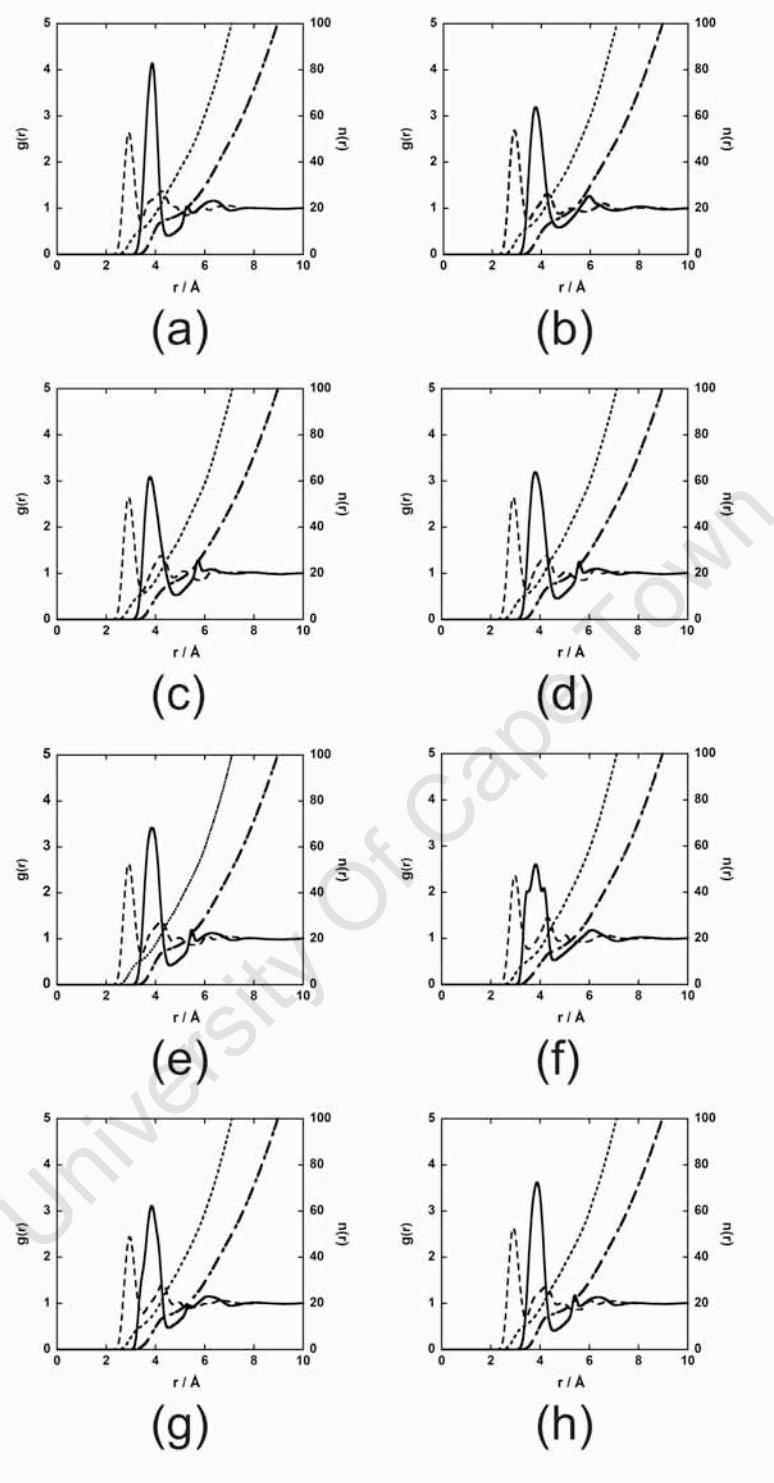

Figure 6.3. Sulfur-oxygen (solid line) and sulfur-hydrogen (dashed) pair distribution functions along with their corresponding plots of $n(r)$ for (a) $MgSO_4$, (b) $CaSO_4$, (c) $MnSO_4$, (d) $FeSO_4$, (e) $CoSO_4$, (f) $NiSO_4$, (g) $CuSO_4$ and (h) $ZnSO_4$ from the CIP simulation.

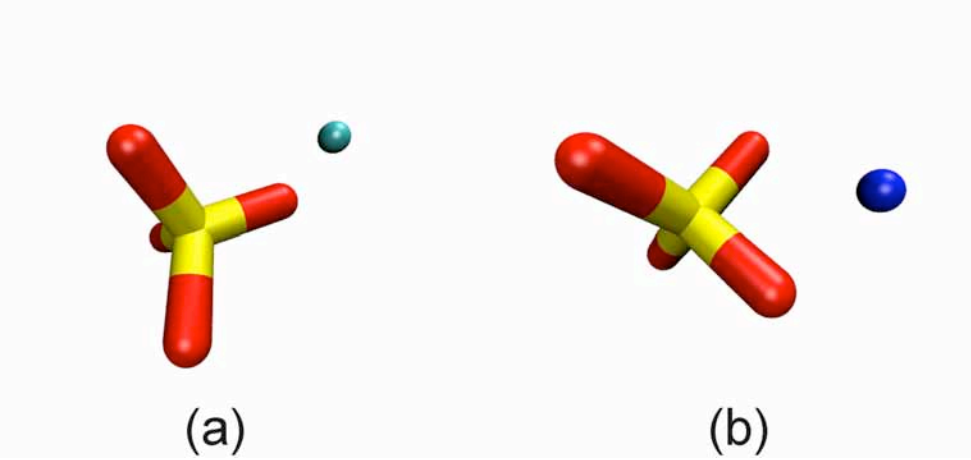

Figure 6.4. The average configuration of metal ions, relative to the associated sulfate ion for (a) $CoSO_4$ and (b) $NiSO_4$, from the CIP molecular dynamics simulations.

Interestingly, upon ion pairing the number of water molecules closely associated with the sulfate ions increases by ~1-2 waters, compared to the loss of waters experienced by the metal ions.

6.4.2.3 Three-Dimensional Picture of Metal Sulfate Hydration

The relative orientations of the metal and sulfate ions are important in determining their overall solvated structure. From the MD simulations it is found that $MgSO_4$, $CaSO_4$, $MnSO_4$, $FeSO_4$, $CoSO_4$ and $ZnSO_4$ have the same relative intermolecular orientations with the metal ion forming a uni-dentate association with the sulfate ion for the duration of the simulations, as shown in Figure 6.4(a). For $NiSO_4$, the metal ion is found to predominantly favour a bidentate association with the sulfate ion (Figure 6.4(b)), while in the case of $CuSO_4$ the metal ion is observed to move relative to the sulfate ion forming both the uni-dentate and bidentate structures.

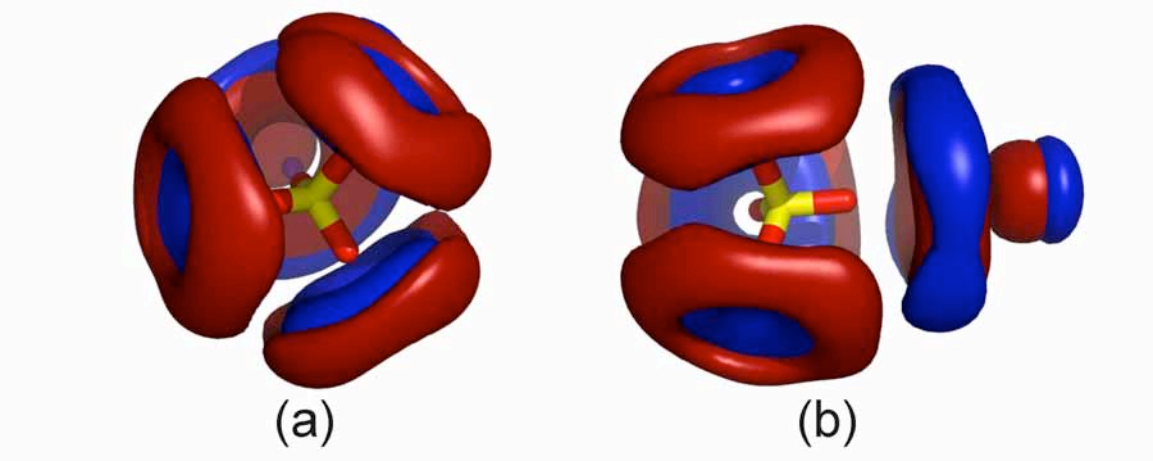

Figure 6.5. The average solvent structure of $MgSO_4$ obtained from the CIP simulation, represented by the three-dimensional water probability densities. The water oxygen density is coloured red and the water hydrogen density is coloured blue.

The same relative orientations of the metal and sulfate ions for $MgSO_4$, $CaSO_4$, $MnSO_4$, $FeSO_4$, $CoSO_4$ and $ZnSO_4$ are confirmed in the three-dimensional water probability distributions. This is observed by obtaining the same three-dimensional solvent structuring, as shown in Figure 6.5, with minimal differences in the respective probability densities for each of the metal sulfate systems. For all of the above complexes, the SDFs reveal four *doughnut* like water rings perpendicular to the sulfate oxygens with the metal ion sitting inside one of the rings (Figure 6.4(a)). Each of the oxygen probability density rings contains four maximum density points indicating four water molecules per sulfate oxygen. Water probability density is also observed by the metal ions coordinated at 180° relative to the sulfate oxygen associated with the metal ions and has one density maximum. The sum of the maximum density points reveal that on average 17 water molecules sit within the first solvation shell of the $MgSO_4$, $CaSO_4$, $MnSO_4$, $FeSO_4$, $CoSO_4$ and $ZnSO_4$ CIP complexes.

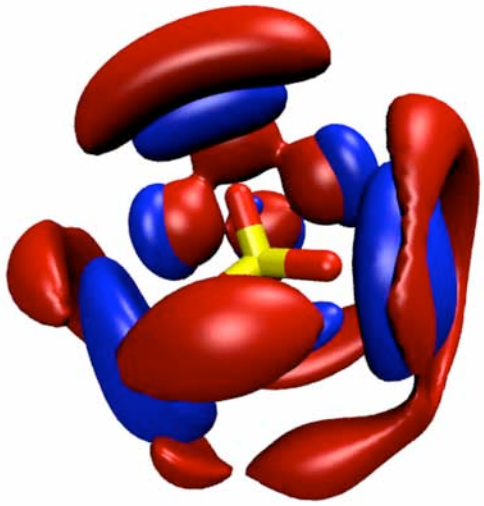

Figure 6.6. The average solvent structure of $NiSO_4$ obtained from the CIP simulation, represented by the three-dimensional water probability densities. The water oxygen density is coloured red and the water hydrogen density is coloured blue.

The probability density ring containing the metal ion has a different relative orientation of the oxygen and hydrogen probability densities relative to the other three rings on the sulfate ion. This re-orientation is indicated by the oxygen density being closest to the metal ion relative to the hydrogen density, compared to the three oxygen density rings around the sulfate ion which have the hydrogen density closest to the sulfate.

The loss of 2 water molecules by the Ni^{2+} ion observed from the metal-O(w) PDF and the observed differences in its associated sulfate-O(w) PDF can be explained by the orientation of the nickel ion relative to the sulfate ion (Figure 6.4(b)) and by the $NiSO_4$ SDF, shown in Figure 6.6. From the $NiSO_4$ SDF it is observed that the *doughnut* density probabilities are partially destroyed by the formation of the bidentate $NiSO_4$ complex. Furthermore, the nickel ion is coordinated with four water molecules, rather than the five coordinated waters observed for $MgSO_4$, $CaSO_4$, $MnSO_4$, $FeSO_4$, $CoSO_4$ and $ZnSO_4$ CIP complexes, as seen from the metal-O(w) PDF.

6.4.3 The Effect of Residence Time on Hydration Numbers

The average number of water molecules closely associated with the metal and sulfate ions (in the first hydration shell) were obtained in Section 6.4.2.1 by calculating $n(r)$ for each of the respective metals and corresponding sulfates, from the CIP and free ion simulations. To obtain a dynamic number of water molecules within the first hydration shell of a chemical species requires the calculation of the dynamic hydration number. The dynamic hydration number, n_{dyn}, for any particular ion is defined via the following expression,

$$n_{dyn} = n_h \exp\left(-\tau^S_{Bulk} \Big/ -\tau^S_{ion} \right) \tag{6.7}$$

where n_h is the coordination number (obtained from the running integration number $n(r)$), τ^S_{Bulk} is the mean residence time of bulk water (calculated to be 4.55ps for TIP3P) and τ^s_{ion} is the residence time of water associated with a particular ion. In this work the residence times are calculated using the definition of Impey et al. The metal and sulfate residence times, t_{res} were calculated by introducing a probability function $P_\alpha(t,t_n,t^*)$, where $P_\alpha = 1$ if solvent molecule α is within the first solvation shell of the ion at time t and t_n, and does not leave the solvation shell for any period longer than t^*; otherwise $P_\alpha = 0$. It then follows that t_{res}, which is characteristic of the ion, is expressed as

$$t_{res} = \frac{1}{N_t} \sum_{n=1}^{N_t} \sum_{\alpha} P_\alpha(t, t_n, t^*) \tag{6.8}$$

The above correlation function decays as $\exp(-t/\tau^s_{ion})$ over a particular time frame, giving τ^s_{ion}. The residence times of water molecules in the first hydration shells for the metal ions were calculated to be of infinite length, indicating that the waters coordinated to the metal ions do not leave the first hydration shell during the full length (20 ns) of the molecular dynamics simulations.

Table 6.6. The effect of ion pairing on sulfate water residence times, t_{res}, and a summary of the PDF running integration numbers, n(r) and dynamic hydration numbers, n_{dyn}. Δn is calculated as the difference between n_{dyn} from the free ion simulations and n_{dyn} from the CIP simulations.

	CIP			Free Ions			
	***n*(*r*) / # of waters**	***t*$_{res}$ / *ps***	***n*$_{dyn}$/ # of waters**	***n*(*r*) / # of waters**	***t*$_{res}$ / *ps***	***n*$_{dyn}$/ # of waters**	**Δ*n***
$MgSO_4$	15.39	18.3	12.3	14.53	19.1	11.4	-0.4
$CaSO_4$	15.57	15.8	11.7	-	-	-	-
$MnSO_4$	16.60	16.4	12.6	-	-	-	-
$FeSO_4$	16.06	16.1	12.1	14.33	18.2	11.2	-0.9
$CoSO_4$	15.74	16.6	11.7	14.48	17.4	11.1	-0.7
$NiSO_4$	14.68	15.3	10.9	14.49	16.9	11.1	0.2
$CuSO_4$	14.86	16.3	11.2	14.48	17.1	11.1	-0.1
$ZnSO_4$	15.58	17.3	12.0	14.49	18.1	11.3	-0.7

The residence times for the sulfate ions from both the free ion (16.9 – 19.1 ps) and CIP (15.8 – 18.3 ps) are of the same order. The decrease observed for the CIP sulfate ions indicates that the substitution of water molecules around the sulfate oxygen atoms by a metal ion increases the effective charge of the sulfate, allowing waters to be displaced more easily. The dynamic hydration numbers for both the free ion and CIP simulations are observed to be 3-4 lower than those obtained from the PDFs

6.4.4 Comparison of Experimental and Computational Hydration Numbers

A summary of the computational (from PDFs and n_{dyn}), experimental hydration numbers and their corresponding differences in hydration numbers are reported in Table 6.7. Analysis of the $n(r)$ and n_{dyn} from the free ion simulations reveals that the total number of water molecules surrounding the ions is effectively identical for the set of metal sulfates

Table 6.7. Summary of the hydration and difference in hydration numbers from experimental and computational studies.

	CIP		Free Ions						
	***n*(*r*) / # of waters**	**n_{dyn}/ # of waters**	***n*(*r*) / # of waters**	**n_{dyn}/ # of waters**	**N_h/ # of waters**	**N_h^a/ # of waters**	**Δn**	**$\Delta n_{(tres)}$**	**Δn^a**
$MgSO_4$	20.4	17.3	20.5	17.4	20.3	21.6	0.1	0.1	2.5
$CaSO_4$	21.9	20.0	-	-		20.2	-	-	4.0
$MnSO_4$	21.6	17.6	-	-		20.8	-	-	2.5
$FeSO_4$	21.1	17.1	20.3	17.2		-	-0.8	0.1	-
$CoSO_4$	20.7	16.7	20.5	17.1	20.6	23.3	-0.2	0.4	3.8
$NiSO_4$	18.7	15.0	20.5	17.1	21.0	24.5	1.8	2.1	4.1
$CuSO_4$	19.3	15.7	20.5	17.1		23.9	1.2	1.4	3.9
$ZnSO_4$	20.6	17.0	20.5	17.3	20.5	22.0	-0.1	0.3	3.5

a. N_h and Δn values obtained from the work of Marcus.

studied. In the case of the CIP simulations the $n(r)$ (18.7 – 21.9 water molecules) and n_{dyn} (15.7 – 20.0 water molecules) values vary. These differences observed in $n(r)$ and n_{dyn} result from the relative orientations of the metal ions with regards to the sulfate anion (M-O or M-2O, where M = metal and O = sulfate oxygen) and the effect the ion pairing has on the water residence times for each metal sulfate CIP.

The trend in hydration numbers obtained from ultrasonic interferometry, $MgSO_4$ < $ZnSO_4$ < $CoSO_4$ < $NiSO_4$ is not observed in the hydration numbers obtained from the molecular dynamics simulations, $NiSO_4$ < $MgSO_4$ < $ZnSO_4$ < $CoSO_4$. However, the trend in the calculated difference in dynamic hydration numbers, $MgSO_4$ < $ZnSO_4$ < $CoSO_4$ < $NiSO_4$ is the same as that obtained from experiment.

6.5 Conclusions

The formation of CIPs from free ions proceeds via a two step intermediate pathway. Molecular dynamic simulations carried out on several metal sulfates ($Mg^{2+}SO_4^{2-}$, $Ca^{2+}SO_4^{2-}$, $Mn^{2+}SO_4^{2-}$, $Fe^{2+}SO_4^{2-}$, $Co^{2+}SO_4^{2-}$, $Ni^{2+}SO_4^{2-}$, $Cu^{2+}SO_4^{2-}$ and $Zn^{2+}SO_4^{2-}$) reveal that the transition from free ions to SSHIP proceeds without the release of water molecules from the first solvation shells of either dissociated metal or sulfate ions, while the formation of a CIP species requires the loss of between 1 -2 water molecules from the metal ion. Furthermore the trend in hydration numbers observed from ultrasonic interferometry experiments was not seen in the molecular dynamics simulations, but the trend in the calculated difference in dynamic hydration numbers was.

This suggests that molecular dynamics simulations run at the molecular mechanics level of theory are insufficient with regards to obtaining quantitative data about ion pairing, but can give qualitative data.

6.6 References

1. Marcus, Y. and Hefter, G., *Ion pairing.* Chem. Rev., 2006. **106**(11): p. 4585-4621.
2. Marcus, Y., *Ion Solvation*. 1st ed. 1985, New York: John Wiley and Sons Ltd, New York.
3. Richens, D., *The Chemistry of Aqua Ions.* 2004: John Wiley & Sons Ltd, New York.
4. Bockris, J.O.M. and Reddy, A.K.N., *Modern Electrochemistry, Vol. 2A. Ionics.* 2nd ed. 1998: Plenum Press.
5. Burgess, J., *Ions in Solution: Basic Principles of Chemical Interactions.* 1988: Ellis Horwood.
6. Laage, D. and Hynes, J.T., *A molecular jump mechanism of water reorientation.* Science, 2006. **311**(5762): p. 832-835.
7. Impey, R.W., Madden, P.A., and McDonald, I.R., *Hydration and mobility of ions in solution.* J. Phys. Chem., 1983. **87**(25): p. 5071-5083.
8. Rode, B.M., Schwenk, C.F., Hofer, T.S., and Randolf, B.R., *Coordination and ligand exchange dynamics of solvated metal ions.* Coord. Chem. Rev., 2005. **249**(24): p. 2993-3006.
9. Bock, C.W., Markham, G.D., Katz, A.K., and Glusker, J.P., *The arrangement of first- and second-shell water molecules around metal ions: effects of charge and size.* Theor. Chem. Acc., 2006. **115**(2-3): p. 100-112.
10. Naidoo, K.J., Klatt, G., Koch, K.R., and Robinson, D.J., *Geometric hydration shells for anionic platinum group metal chloro complexes.* Inorg. Chem., 2002. **41**(7): p. 1845-1849.
11. Yu, H.B., Noskov, S.Y., and Roux, B., *Hydration number, topological control, and ion selectivity.* J. Phys. Chem. B, 2009. **113**(25): p. 8725-8730.
12. Erras-Hanauer, H., Clark, T., and van Eldik, R., *Molecular orbital and DFT studies on water exchange mechanisms of metal ions.* Coord. Chem. Rev., 2003. **238**: p. 233-253.
13. Akilan, C., Hefter, G., Rohman, N., and Buchner, R., *Ion association and hydration in aqueous solutions of copper(II) sulfate from 5 to 65 degrees C by dielectric spectroscopy.* J. Phys. Chem. B, 2006. **110**(30): p. 14961-14970.

14. Akilan, C., Rohman, N., Hefter, G., and Buchner, R., *Temperature effects on ion association and hydration in $MgSO_4$ by dielectric spectroscopy.* ChemPhysChem, 2006. **7**(11): p. 2319-2330.

15. Eigen, M. and Tamm, K., *Schallabsorption in elektrolytlosungen als folge chemischer relaxation.1. Relaxationstheorie der mehrstufigen dissoziation.* Z. Elektrochem., 1962. **66**(2): p. 93-107.

16. Eigen, M. and Tamm, K., *Schallabsorption in elektrolytlosungen als folge chemischer relaxation. 2. Messergebenisse und relaxationsmechanismen fur 2-2-wertige elektrolyte.* Z. Elektrochem., 1962. **66**(2): p. 107-121.

17. Atkinson, G. and Petrucci, S., *Ion association of magnesium sulfate in water at 25 degrees.* J. Phys. Chem., 1966. **70**(10): p. 3122-3128.

18. Chen, T., Hefter, G., and Buchner, R., *Ion association and hydration in aqueous solutions of nickel(II) and cobalt(II) sulfate.* J. Solution Chem., 2005. **34**(9): p. 1045-1066.

19. Hefter, G., *When spectroscopy fails: The measurement of ion pairing.* Pure Appl. Chem., 2006. **78**(8): p. 1571-1586.

20. Petrucci, S., ed. *Ionic Interactions from Fused Solutions to Fused Salts, Vol. 1: Equilibrium and Mass Transport.* Vol. 1. 1971, Academic, New York: New York.

21. Wawer, J., Krakowiak, J., and Grzybkowski, W., *Apparent molar volumes, expansibilities, and isentropic compressibilities of selected electrolytes in methanol.* J. Chem. Thermodyn., 2008. **40**(8): p. 1193-1199.

22. Apelblat, A., Manzurola, E., and Orekhova, Z., *Thermodynamic Properties of Aqueous Electrolyte Solutions. Volumetric and Compressibility Studies in 0.1 mol.kg(-1), 0.5 mol.kg(-1), and 1.0 mol.kg(-1) Sodium Carbonate and Sodium Sulfate Solutions at Temperatures from 278.15 K to 323.15 K.* J. Chem. Eng. Data, 2009. **54**(9): p. 2550-2561.

23. Cannon, W.R., Pettitt, B.M., and McCammon, J.A., *Sulfate anion in water - model structural, thermodynamic, and dynamic properties.* J. Phys. Chem., 1994. **98**(24): p. 6225-6230.

24. Mason, P.E., Dempsey, C.E., Neilson, G.W., and Brady, J.W., *Nanometer-scale ion aggregates in aqueous electrolyte solutions: Guanidinium sulfate and guanidinium thiocyanate.* J. Phys. Chem. B, 2005. **109**(50): p. 24185-24196.

25. Jorgensen, W.L., Chandrasekhar, J., Madura, J.D., Impey, R.W., and Klein, M.L., *Comparison of simple potential functions for simulations liquid water.* J. Chem. Phys., 1983. **79**(2): p. 926-935.

26. MacKerell, A.D., Bashford, D., Bellott, M., Dunbrack, R.L., Evanseck, J.D., Field, M.J., Fischer, S., Gao, J., Guo, H., Ha, S., Joseph-McCarthy, D., Kuchnir, L., Kuczera, K., Lau, F.T.K., Mattos, C., Michnick, S., Ngo, T., Nguyen, D.T., Prodhom, B., Reiher, W.E., Roux, B., Schlenkrich, M., Smith, J.C., Stote, R., Straub, J., Watanabe, M., Wiorkiewicz-Kuczera, J., Yin, D., and Karplus, M., *All-atom empirical potential for molecular modeling and dynamics studies of proteins.* J. Phys. Chem. B, 1998. **102**(18): p. 3586-3616.

27. Brooks, B.R., Bruccoleri, R.E., Olafson, B.D., States, D.J., Swaminathan, S., and Karplus, M., *CHARMM - A program for macromolecular energy, minimization, and dynamics calculations.* J. Comput. Chem., 1983. **4**(2): p. 187-217.

28. Brooks, B.R., Brooks, C.L., Mackerell, A.D., Nilsson, L., Petrella, R.J., Roux, B., Won, Y., Archontis, G., Bartels, C., Boresch, S., Caflisch, A., Caves, L., Cui, Q., Dinner, A.R., Feig, M., Fischer, S., Gao, J., Hodoscek, M., Im, W., Kuczera, K., Lazaridis, T., Ma, J., Ovchinnikov, V., Paci, E., Pastor, R.W., Post, C.B., Pu, J.Z., Schaefer, M., Tidor, B., Venable, R.M., Woodcock, H.L., Wu, X., Yang, W., York, D.M., and Karplus, M., *CHARMM: The biomolecular simulation program.* J. Comput. Chem., 2009. **30**(10): p. 1545-1614.

29. Lamoureux, G. and Roux, B., *Modeling induced polarization with classical Drude oscillators: Theory and molecular dynamics simulation algorithm.* The Journal of Chemical Physics, 2003. **119**(6): p. 3025-3039.

30. York, D.M., Darden, T.A., and Pedersen, L.G., *The effect of long-range electrostatic interactions in simulations of macromolecular crystals: A comparison of the Ewald and truncated list methods.* J. Chem. Phys., 1993. **99**(10): p. 8345-8348.

31. Essmann, U., Perera, L., Berkowitz, M.L., Darden, T., Lee, H., and Pedersen, L.G., *A smooth particle mesh Ewald method.* J. Chem. Phys., 1995. **103**(19): p. 8577-8593.

32. Van Gunsteren, W.F., *Algorithms for macromolecular dynamics and constraint dynamics.* Mol. Phys., 1977. **34**: p. 1311-1327.

33. Marcus, Y., *Electrostriction, ion solvation, and solvent release on ion pairing.* J. Phys. Chem. B, 2005. **109**(39): p. 18541-18549.

34. Khavrutskii, I.V., Dzubiella, J., and McCammon, J.A., *Computing accurate potentials of mean force in electrolyte solutions with the generalized gradient-augmented harmonic Fourier beads method.* J. Chem. Phys., 2008. **128**(4): p. 13.

35. Trzesniak, D., Kunz, A.P.E., and van Gunsteren, W.F., *A comparison of methods to compute the potential of mean force.* ChemPhysChem, 2007. **8**(1): p. 162-169.

CHAPTER 7

Force Field Parameterisation and Electronic Structure Approaches

7.1 Introduction

Choosing a mathematical function to represent a chemical system is generally straight forward. However selecting an appropriate parameter set or performing the parameterisation for new parameters is not [1]. Extensive studies of biological systems over several decades have lead to well established and reliable CHARMM [2] and AMBER [3-6] biological force fields, which include suitable alkali and alkaline earth metals. Within the CHARMM modelling package very little attention has been placed on purely inorganic chemical systems, i.e. coordination metal systems or ion-ion association studies. This has resulted in a lack of coordination type d-block metal force fields.[1]

In order to reproduce accurately both structural and thermodynamic properties for transition metal containing systems in the condensed phase one almost always needs to parameterise for each system. This arises from the limited transferability of parameters between solvent models and modelling packages [7-9]. In Chapter 8 a force field for Platinum Group Metals (PGM) chloro-anion complexes is formulated and tested in aqueous condensed phase. In the subsections below, points to consider prior to and during parameterisation are discussed. These include: selection of a water model for studies in the condensed phase, target experimental or *ab initio* data and some of the theory behind the Electronic Structure Approaches (ESAs) applied to obtain target data.

7.2 Selecting a Water Model

Water models chosen for molecular dynamics simulations must be accurate and must simultaneously allow for time-efficient simulations [10]. Empirical aqueous condensed phase simulations raise several major problems, namely, (a) the ability of the model to reproduce experimental results, such as the collective structure of liquid water resulting from the extensive hydrogen bonding capacity of the individual molecules [11] and (b), more importantly, the number of water molecules to be simulated. The latter is of most

[1] CHARMM contains a limited number of transition metal parameters. The us of these parameters is generally limited to biological applications.

concern as the calculation of the water-water interactions generally dominates the computational cost of any simulation. In the past implicit water models were used to speed up simulations. However, in the last two decades the increase in computational capacity has resulted in most molecular dynamics (MD) simulations being carried out with explicit models, allowing for the calculation of both explicit solvent-solvent and solvent-solute interactions.

MD simulations of biological systems are generally run using one of several explicit water models. These include the SPC [12], SPC/E [13] and TIP3P/4P [14] which are either simple three- or four-site models and make use of effective pairwise potentials with no explicit three body terms or polarisation effects, allowing for minimal computational time. The main limitation of these models is their original parameterisation for use at room temperature (~298.15K) [15], effectively rendering them inadequate in their representation of water, over a large array of temperatures and phases. This inherent deficiency has prompted the development of more sophisticated water models, such as the fixed charge TIP5P [16] and several polarisable water models [17-21], parameterised over a range of temperatures. These models have been able to accurately reproduce experimental results such as (but not limited to) water dimer energies, density, heat capacity constant and pair distribution functions, but at additional computational cost, making them less popular when simulating medium to large sized chemical systems.

Another consideration in choosing a suitable water model is the method of treating the long range interactions in molecular dynamics simulations. Parameterisation of many of the water models was carried out using truncated Coulomb interactions. The norm in recent times is to treat the long range interactions using Ewald summation methods. This has several consequences. Such consequences include thermodynamic and kinetic property changes in simulated systems, e.g. lower densities and greater diffusion constants, when using these models in simulations with Ewald summation. As such, alterations have been made to several three-, four- and five-site models [15, 22, 23] to correct for these deviations.

7.3 Target Data for Parameterisation

The overall objective of force field parameterisation is to develop a predictive model that reproduces experimental measurements to as high a degree as possible [24]. There is no one correct way of achieving this goal; several systematic parameterisation procedures have been devised. In this work, parameterisation is carried out using an adaptation of the procedure proposed by Chen et al. [25]. In this procedure the first step is the choice of chemical systems one wishes to study, i.e. hydrated first row transition metals. This is followed by the collection and choice of experimental and/or *ab initio* data, with which parameters are to be fitted against. This data includes structural data, vibrational frequencies and interaction energies. Data collection is followed by an initial construction and parameter stage, at which point molecular topologies and parameters are generated from either existing crystal structures, *ab initio* generated structures or via analogy with respect to existing parameter sets. This is followed by several iterations of bonded and non-bonded parameterisation, condensed phase simulations and calculations of differences between calculated and target data, until selected convergence criteria are achieved.

The most important of the above steps is the choice of target data which is to be used in the parameterisation procedure. Below is a brief overview of important target data used in the development of a force field.

7.3.1 Chemical Structure and Electrostatic Interactions

Metal-ligand bond lengths and angles are known to be sensitive to the crystal environment [26]. This effect is quite pronounced and exceeds the accuracy by which a structure can be determined using X-ray and neutron diffraction. Alternatively chemical structures can be obtained from high level electronic structure approaches (ESAs). In recent years, improvement in accuracy of calculations allows for the provision of reliable chemical structures. However, the choice of functional and basis set is of paramount importance [27, 28] as several studies have shown that reproducing accurate geometries

is not straightforward[2]. Therefore, if experimental chemical structures are available for inorganic complexes, these should be used rather than those obtained from ESAs. To overcome the inaccuracies obtained in experimental chemical structures an extensive structure search is required, followed by sorting and analysis, so as to determine the best overall structure for a particular species, i.e. $[PtCl_6]^{2-}$.

In the formulation of charged PGM chloro-anion complexes, electrostatic effects are critical. To model electrostatic interactions in CHARMM using a Coulomb interaction (Section 2.5.1) requires determination of partial atomic charges. As there is no experimental method that can do this, ESAs are routinely applied. Methods devised for this purpose include Mulliken Analysis, Löwdin population Analysis and Natural Population Analysis (NPA). In recent years partial charges have been derived from the *electrostatic potential* (ESP) from electronic structure calculations. This is because the ESP is the most reproducible property from which partial atomic charges are derived and that can be used in modelling molecule–molecule interactions at short to long range, as in molecular mechanics simulations. ESP charge-fitting schemes involve the determination of atomic partial charges q_n. When applied as a monopole expansion the ESP is calculated according to

$$V_{ESP}(r) = \sum_{n}^{nuclei} \frac{q_n}{|r - r_n|} \tag{7.1}$$

ESP algorithms select a large number of points spaced evenly on a cubic grid surrounding the van der Waals surface of the molecule. To ensure rotational invariance, a reasonable density of points is required. The two algorithms in widest use are CHelpG [30] and the Merz-Singh-Kollman scheme [31, 32], which is sometimes slightly less robust than CHelpG, but usually gives very similar results.

[2] For transition metal systems, HF theory is known to underestimate bond lengths. Whereas, MP2 overestimates bond distances in closed-shell transition metal systems. These errors are exaggerated when determining geometries for the corresponding open-shell systems, leading to the use of DFT as the standard for the prediction of transition metal molecular structures.29. Koch, W. and Holthausen, M.C., *A Chemist's Guide to Density Functional Theory, 2nd Edition*. 2001: Wiley-VCH.

7.3.2 Spectroscopy and Parameterisation

Vibrational spectroscopy (Infra-Red and Raman) is of importance in many areas of chemical research. Force constants derived from normal coordinate analyses have formed the basis of many molecular mechanic force fields. Determining bond, angle and improper-torsional force constants for a specific group of inorganic complexes such as the PGM chloro-anion complexes requires normal modes for each of the species. If these are not available, ESAs can be used for the calculation of harmonic frequencies.

Frequencies calculated at the Hartree Fock (HF) level in combination with small to medium sized basis sets, commonly show a systematic 10 % overestimation [27, 29], which can be traced back to the missing electron correlation, basis set deficiencies and the neglect of anharmonicity. These deviations are in most cases uniform, and can be improved by applying a simple empirical scaling factor, where the scale factors are usually transferable within the same class of compounds. Similarly, DFT has been shown to give systematic errors (of a lesser degree) which require scaling [33, 34].

7.3.3 Complex-Water Interaction Energies

Chemical structure and vibrational fitting are important starting points in force field parameterisation. However, more important is the accurate calculation of the interaction energies of a chemical species with its surrounding environment, i.e. for a solvated ion this is the energy associated with ion-solvent interaction. The hydration free energy of an ion is generally used as an overall target. To obtain this, initial estimation several iterations of parameterisation (charge fitting) are required. The interaction energy/energies between the target molecule, in specific orientation(s), and one or several waters, in multiple orientations, are routinely chosen to be the initial estimates.

Electronic structure approaches are generally used to obtain these mono- and multi-hydrated species, as little or no experimental data are available. These multi-species interactions and energies are then reproduced with the chosen molecular mechanics model through modification of the partial charges initially obtained from ESP charge-fitting schemes.

7.4 Electronic Structure Approaches

The discussion on ESAs below is primarily limited to application considerations with limited theory and equations. For a full theoretical development of quantum chemistry the reader is referred to the texts of Atilla Szabo and Neil S. Ostland, *Modern Quantum Chemistry: Introduction to Advanced Electronic Structure Theory* [35], Wolfram Koch and Max C. Holthausen, *A Chemist's Guide to Density Functional Theory* [29] and Christopher J. Cramer, *Essentials of Computational Chemistry Theories and Models* [24].

7.4.1 Fundamental Aspects of Quantum Mechanics

Several electronic structure theory methods are used to solve the time-independent non-relativistic form of the electronic Schrödinger equation. This is made possible via the Born-Oppenheimer approximation[3], resulting in the electronic Schrödinger equation being written as

$$\hat{H}_{elec}(r,R)\Psi_{elec}(r,R) = E_{elec}(R)\Psi_{elec}(r,R) \tag{7.2}$$

where $\hat{H}_{elec}$ is the electronic Hamiltonian operator dependant on the electronic coordinates, r, and parametrically on the nuclear coordinates, R. Ψ_{elec} is the electronic wavefunction with eigenvalues E_{elec}.

The electronic Hamiltonian (in atomic units) describing the motion of N electrons in the field of M nuclei is

$$\hat{H}_{elec} = -\frac{1}{2}\sum_{i=1}^{N}\nabla_i^2 - \sum_{i=1}^{N}\sum_{A=1}^{M}\frac{Z_A}{r_{iA}} + \sum_{A>B}\frac{Z_A Z_B}{R_{AB}} + \sum_{i>j}\frac{1}{r_{ij}} \tag{7.3}$$

[3] The Born-Oppenheimer approximation stems from the fact that the ratio of nucleus to electron mass is greater than 1800/1. Thus electrons move at a much greater velocity compared to nuclei, so the nuclei may be considered to be stationery

and is composed of several terms representing the energies of nuclear-electron attractions, nuclear-nuclear repulsions, and electron-electron repulsions which overall give the electronic kinetic energy of a chemical system.

$\hat{H}_{elec}$ can be simplified by assembling operators based on their electron indices. As such, the one-electron operators *h(i)* can be defined as

$$h(i) = -\frac{1}{2}\nabla_i^2 - \sum_A \frac{Z_A}{r_{iA}} \tag{7.4}$$

and if the nuclear-nuclear repulsion term $\sum_{A>B} \frac{Z_A Z_B}{R_{AB}}$, is represented by V_{nn}, then $\hat{H}_{elec}$ can be written in terms of one and two-electron operators:

$$\hat{H}_{elec} = \sum_i h(i) + \sum_{i>j} \frac{1}{r_{ij}} + V_{nn} \tag{7.5}$$

This is made possible by the fact that V_{nn} is a constant term for fixed nuclei-nuclei distances and can be added at the end of the calculation without altering the eigenfunctions.

By solving Equation 7.5 we obtain E_{elec}. If calculated over all possible nuclear coordinates E_{elec} gives rise to a Potential Energy Surface (PES), which is the potential energy 'felt' by the nuclei. Thus from the determination of E_{elec}, Ψ_{elec} and their derivatives, several molecular properties, such as (but not restricted to) transition state geometries, vibrational spectra and electrostatic potentials may be obtained.

7.4.2 *Ab* Initio versus Density Functional Theory

7.4.2.1 Hartree Fock Theory

HF theory is an approximate theory in which the many electron problem is replaced with a one electron problem. This is achieved by making use of the self-consistent-field (SCF)

method, in which every electron in a chemical system 'feels' an average coulomb repulsion resulting from the sum presence of all the other electrons.

Considering an *N*-electron wavefunction $\Psi(x_1, x_2, x_3, ..., x_N)$ that depends on coordinates $x_1, x_2, x_3, ..., x_N$ of electrons *1,2,3 … N*, and where $x_i = (r_i, \omega)$ is represented by the spatial (r_i) and spin ($\omega = \alpha \text{ or } \beta$) coordinates of the *i-th* electron. In HF theory, this wavefunction is expressed as a Slater determinant, which is a generalization of the Hartree Product,

$$\Psi_{HF} = \frac{1}{\sqrt{N!}} \begin{vmatrix} \chi_1(x_1) & \chi_2(x_1) & \chi_3(x_1) & \cdots & \chi_N(x_1) \\ \chi_1(x_2) & \chi_2(x_2) & \chi_3(x_2) & \cdots & \chi_N(x_3) \\ \vdots & \vdots & \vdots & \ddots & \vdots \\ \chi_1(x_N) & \chi_2(x_N) & \chi_3(x_N) & \cdots & \chi_N(x_3) \end{vmatrix} \tag{7.6}$$

where $\chi_i(x_j)$ means that electron x_j is associated with orbital χ_i.

The Slater determinant expression of the wavefunction conforms to two main quantum mechanics postulates. First is the indistinguishability of electrons, where it can be seen, that each and every electron is associated with all the orbitals in the wavefunction. Secondly, it satisfies the antisymmetry principle, which states that the wavefunction should be antisymmetric under the interchange of any two electrons. Therefore, if we interchange the labels x_1, and x_2 above, two rows of the determinant are then interchanged, resulting in a change of sign for the *N*-electron wavefunction $\Psi(x_1, x_2, x_{3...} x_N)$.

The variational principle is used to generate systematic solutions to the electronic Schrödinger equation, which allows the best Slater determinant (the one yielding the lowest energy) to be found. It states that an approximate wavefunction (i.e. the HF wavefunction) will produce an energy that is larger than the true energy. For normalised wavefunctions, the electronic energy is calculated as the expectation value of the Hamiltonian operator:

$$E_{elec} = \left\langle \Psi \middle| \hat{H}_{elec} \middle| \Psi \right\rangle \tag{7.7}$$

The HF energy can be written as the sum of one- and two-electron integrals and the nuclear repulsion energy, V_M, as:

$$E_{HF} = \sum_{i=1}^{N} \langle \chi_i | h(i) | \chi_i \rangle + \frac{1}{2} \sum_{ij}^{N} \left(J_{ij} - K_{ij} \right) + V_M \tag{7.8}$$

where the first summation is constructed of one-electron integrals

$$\langle \chi_i | h(i) | \chi_i \rangle = \int dx_1 \chi_i^*(x_1) h(r_1) \chi_i(x_1) \tag{7.9}$$

and the second summation is constructed of the two-electron coulomb ***J*** and the exchange ***K*** integrals.

$$J_{ij} = \int dx_1 dx_2 \chi_i^*(x_1) \chi_j^*(x_2) \frac{1}{r_{12}} \chi_i(x_1) \chi_j(x_2) \tag{7.10}$$

$$K_{ij} = \int dx_1 dx_2 \chi_i^*(x_1) \chi_j^*(x_2) \frac{1}{r_{12}} \chi_i(x_1) \chi_j(x_2) \tag{7.11}$$

In general, the majority of chemical systems studied contain an even number of electrons which are all paired to give an overall singlet. These are referred to as closed-shell systems. Chemical compounds, such as water, methanol and other ground state species in organic or inorganic chemistry fall within this class. In these systems the HF solution is usually characterised by having doubly occupied spatial orbitals. If the double occupancy criterion is imposed the result is the restricted HF approximation.

Alternatively, chemical systems containing an odd number of electrons, such as certain charged anions and cations, or chemical systems with an even number of electrons where not all of the electrons occupy the pair-wise spatial orbital, are referred to as open-shell systems. Within the HF approximation there are two possible ways to treat open-shell systems. This is achieved by either keeping as close to the RHF picture, as possible

and doubly occupying all spatial orbitals, with the only exception being the explicitly singly occupied ones. Or complete abandonment of the notion of doubly occupied spatial orbitals and allow each spin orbital to have its own spatial part. The former is the restricted open-shell HF scheme (ROHF) while the latter is the much more popular unrestricted HF variant (UHF).

The more frequently used method is the UHF theory developed by Pople and Nesbet [36]. In UHF α and β orbitals do not share the same effective potential but experience different potentials, V^{α}_{HF} and V^{β}_{HF}. As a consequence, the α- and β-orbitals differ in their spatial characteristics and have different orbital energies. The major advantage of the UHF scheme is application of simpler equations compared to those of ROHF. However, the UHF scheme always deals with single-determinant wavefunctions and the major disadvantage of the UHF technique is that unlike the RHF and ROHF wavefunctions, a UHF Slater determinant is no longer an eigenfunction of the total spin operator, $\hat{S}^2$.

7.4.2.2 Møller-Plesset Perturbation Theory

The main failure of HF theory is the inadequate manner in which electron correlation is represented. The SCF method leads to the neglect of the effect neighbouring electrons have on instantaneous positions. In reality, electrons try to avoid close contact with one another by optimally distributing themselves within the region around a nucleus. This optimal distribution results in lower energies. To counter this problem of electron correlation representation several methods are employed such as Møller-Plesset Perturbation Theory (MPPT), Configuration Interaction (CI) and Coupled Clusters (CC) [24, 35].

An important characteristic of MPPT is its size-extensivity, where the energy of a system AB computed at infinite separation will be equal to the sum of the energies of the two individually computed fragments. However, energies computed using perturbation theory methods are not variational, i.e. they do not constitute upper limits to the true energy of the system. The MPPT method based upon Rayleigh-Schrödinger perturbation theory is one of the more popular electron correlation methods. In this method the

unperturbed electronic Hamiltonian $\hat{H}^0$ is defined as the sum of one-electron Fock operators:

$$\hat{H}^0 = \sum_{i=1}^{N} f(x_i) \tag{7.12}$$

and the zeroth-order energy is given as

$$E^{(0)} = \left\langle \Psi_{HF} \middle| \hat{H}^0 \middle| \Psi_{HF} \right\rangle \tag{7.13}$$

The perturbation in MPPT is thus the difference between the sum of the Fock operators and the true electronic Hamiltonian, such that

$$\hat{H}' = \hat{H} - \hat{H}^0 = \hat{H} - \sum_{i=1}^{N} f(x_i) \tag{7.14}$$

where the first-order energy correction $E^{(1)}$ is given by the expectation value of the perturbation using the HF wavefunction

$$E^{(1)} = \left\langle \Psi_{HF} \middle| \hat{H}' \middle| \Psi_{HF} \right\rangle \tag{7.15}$$

Adding the zeroth-order energy $E^{(0)}$ to $E^{(1)}$ gives

$$\begin{aligned} E^{(0)} + E^{(1)} &= \left\langle \Psi_{HF} \middle| \hat{H}^0 \middle| \Psi_{HF} \right\rangle + \left\langle \Psi_{HF} \middle| \hat{H}' \middle| \Psi_{HF} \right\rangle \\ &= \left\langle \Psi_{HF} \middle| \hat{H}^0 + \hat{H}' \middle| \Psi_{HF} \right\rangle = \left\langle \Psi_{HF} \middle| \hat{H} \middle| \Psi_{HF} \right\rangle \end{aligned} \tag{7.16}$$

but, from this it can be seen that $\left\langle \Psi_{HF} \middle| \hat{H} \middle| \Psi_{HF} \right\rangle$ is just the HF energy, thus the sum of the zeroth-order energy and the first-order energy correction is

$$E^{(0)} + E^{(1)} = E_{HF} \tag{7.17}$$

In order to improve on the HF energy a second-order energy correction needs to be evaluated. This correction is known as the MP2 energy correction [24, 35]. With the application of Bruillion's Theorem and the Condon Slater rules, it turns out that only doubly excited determinants contribute to the MP2 energy correction, such that,

$$E^{(2)} = \sum_{ij}^{occupied} \sum_{ab}^{virtual} \frac{\left\langle \Psi_{HF} \middle| \hat{H}' \middle| \Psi_{ij}^{ab} \right\rangle \left\langle \Psi_{ij}^{ab} \middle| \hat{H}' \middle| \Psi_{HF} \right\rangle}{\varepsilon_i + \varepsilon_j - \varepsilon_a - \varepsilon_b} \tag{7.18}$$

where Ψ_{ij}^{ab} represents a doubly-excited determinant differing from the reference HF determinant Ψ_{HF} by the replacement of spinorbitals χ_i and χ_j with virtual spinorbitals χ_a and χ_b, respectively. Also, the energies ε_i, ε_j, ε_a, and ε_b represent the orbital energies associated with spinorbitals χ_i, χ_j, χ_a, and χ_b, respectively.

The MP2 method scales with basis set size as K^5 due to the integral transformation from the atomic orbital to the molecular orbital (MO) basis where the MP2 energies is computed scales as K^5. Due to their relatively moderate computational cost, MP2 methods are widely used in the calculations of the correlation energy [24, 35].

7.4.2.3 Density Functional Theory

Density Functional Theory (DFT) provides an alternative means of introducing electron correlation to a single-determinant wavefunction and is based on the principle that the energy of any chemical system can be expressed as a functional of the electron density, ρ [24, 29].

The first attempt to use the electron density rather than the wavefunction was developed by Thomas and Fermi. This method was based on a quantum statistical model of electrons which takes only the kinetic energy into account and treats the nuclear-electron and electron-electron contributions in a classical manner. However, the main development in DFT was the work published by Hohenberg and Kohn, in 1964 [24, 29].

They proposed that the energy and all other electronic properties of the electronic ground state of any chemical system can be calculated from the systems charge density, $\rho(r)$. In this approach Hohenberg and Kohn showed that the ground state energy, $E_0[\rho]$, is given as

$$E_0[\rho] = F_{HK}[\rho] + \int \rho(r)V(r)dr \tag{7.19}$$

where the first term $F_{HK}[\rho]$ is a functional based on a chemical systems independent parts of the ground state energy (the kinetic energy and electron-electron repulsion), and the second term represents the energy resulting from the external potential $V(r)$. However, the Hohenberg and Kohn theorem has two main drawbacks [29, 37]. First, it does not define the form of $F_{HK}[\rho]$, and secondly, it does not show how the exact charge density can be calculated. These drawbacks were addressed by Kohn and Sham (KS) [29, 38], who proposed that the kinetic energy is computed via one electron functions, and the remainder is combined with the non-classical contributions to the electron-electron contributions.

In the KS method, a non-interacting reference system of N particles whose ground state is a single Slater determinant Θ_S (i.e. one electron function)[4] given as

$$\Theta_S = \frac{1}{\sqrt{N!}}\begin{vmatrix} \varphi_1(\vec{x}_1) & \varphi_2(\vec{x}_1) & \cdots & \varphi_N(\vec{x}_1) \\ \varphi_1(\vec{x}_2) & \varphi_2(\vec{x}_2) & & \varphi_N(\vec{x}_2) \\ \vdots & \vdots & & \vdots \\ \varphi_1(\vec{x}_N) & \varphi_2(\vec{x}_N) & \cdots & \varphi_N(\vec{x}_N) \end{vmatrix} \tag{7.20}$$

and whose density, ρ_S, equals that of a real interacting chemical systems density, ρ_0.

The spin orbitals are determined by

$$\hat{f}^{KS}\varphi_i = \varepsilon_i\varphi_i \tag{7.21}$$

[4] The HF Slater determinant Ψ_{HF} and spin orbitals χ are replaced with Θ_S and φ (KS spin orbitals) in the KS Slater determinant to indicate they are not related quantities.

with the one-electron KS operator $\hat{f}^{KS}$ defined as

$$\hat{f}^{KS} = -\frac{1}{2}\nabla^2 + V_S(\vec{r}) \tag{7.22}$$

At this point, the kinetic energy, T_S, of a non-interacting reference system is determined as

$$T_S = -\frac{1}{2}\sum_i^N \left\langle \varphi_i \middle| \nabla^2 \middle| \varphi_i \right\rangle \tag{7.23}$$

and in order to account for the difference in the non-interacting and true kinetic energies, KS separated the functional $F_{KS}[\rho]$, such that;

$$F_{KS}[\rho(\vec{r})] = T_S[\rho(\vec{r})] + J[\rho(\vec{r})] + E_{XC}[\rho(\vec{r})] \tag{7.24}$$

This formulation includes the exchange-correlation energy, $E_{XC}[\rho]$, as the sum of the difference in the kinetic energies, $T_C[\rho]$, and the non-classical electrostatic contribution.

$$E_{XC}[\rho] = T_C[\rho] + E_{ncl}[\rho] \tag{7.25}$$

The energy of an interacting, real system is given as

$$\begin{aligned} E[\rho(\vec{r})] &= T_S[\rho] + E_{XC}[\rho] + E_{Ne}[\rho] \\ &= -\frac{1}{2}\sum_i^N \left\langle \varphi_i \middle| \nabla^2 \middle| \varphi_i \right\rangle + \frac{1}{2}\sum_i^N \sum_j^N \iint |\varphi_i(\vec{r}_1)|^2 \frac{1}{r_{12}} |\varphi_j(\vec{r}_2)|^2 d\vec{r}_1 d\vec{r}_2 \\ &+ E_{XC}[\rho(\vec{r})] - \sum_i^N \int \sum_A^M \frac{Z_a}{r_{1A}} |\varphi_j(\vec{r}_1)|^2 d\vec{r}_1 \end{aligned} \tag{7.26}$$

and by taking into account the variational principle, the resulting equations are

$$\left(-\frac{1}{2}\nabla^2 + V_{eff}(\vec{r}_1)\right)\varphi_i = \varepsilon_i \varphi_i \tag{7.27}$$

Comparison of equation 7.24 with the one-particle equations for a non-interacting reference system, we see that

$$V_S(\vec{r}) \equiv V_{eff}(\vec{r}) = \int \frac{\rho(\vec{r}_2)}{r_{12}} d\vec{r}_2 + V_{XC}(\vec{r}_1) - \sum_A^M \frac{Z_A}{r_{1A}} \tag{7.28}$$

However, since the exact V_{XC} is not known an approximation for the exchange-correlation potential is introduced. Thus, V_{XC} is defined as the functional of E_{XC} with respect to ρ, such that

$$V_{XC} \equiv \frac{\delta E_{XC}}{\delta \rho} \tag{7.29}$$

and using this V_S can be determined and subsequently the one electron equations to obtain the KS orbitals which leads to the exact ground state density can be solved, such that

$$\rho_S(\vec{r}) = \sum_i^N \sum_S |\varphi_i(\vec{r}, s)|^2 = \rho_0(\vec{r}) \tag{7.30}$$

and the exact ground state energy given by equation 7.23 provided the exact functionals are known. However, in practice approximations for the unknown functional E_{XC} are used.

7.4.2.3.1 Pure and Hybrid Functionals

The selection of the exchange-correlation functional is the key point in DFT. This can sometimes appear to be a daunting task due to the wide choice of exchange functionals and their correlation counterparts that can be combined in any way.

There are basically two families of pure density functionals: those based on the Local Density Approximation (LDA) or those that include gradient corrections, i.e. the Generalized Gradient Approximation (GGA) [29]. Added to these is the more popular HF/DFT hybrid functionals.

The LDA model is based on a hypothetical uniform electron gas in which electrons move on a positive background charge distribution resulting in a total ensemble that is electrically neutral. Furthermore, the E_{XC} can be expressed as a function of E_{XC} per particle, $\varepsilon_{XC}(\rho)$, and the single-particle density $\rho(r)$. Thus the LDA can be written as

$$E_{XC}^{LDA} = \int \rho(r)\varepsilon_{XC}[\rho(r)]dr \tag{7.31}$$

provided $\rho^{\alpha}(r) \neq \rho^{\beta}(r)$.

$\varepsilon_{XC}[\rho(r)]$ can be divided into two parts representing the exchange and correlation contributions,

$$\varepsilon_{XC}[\rho(r)] = \varepsilon_X[\rho(r)] + \varepsilon_C[\rho(r)] \tag{7.32}$$

The exchange part $\varepsilon_X[\rho(r)]$,[5] is shown to be

$$E_X^{LDA} = -C_X \int \rho(r)^{4/3} dr \tag{7.33}$$

and on this basis several authors have derived analytical expressions for $\varepsilon_C[\rho(r)]$, based on interpolation schemes.

The most widely used correlation functionals are those developed by Vosko, Wilk, and Nusair (VWN) [39] and Perdew and Wang [40]. LDA models are known to reproduce accurate molecular bonding, but fall short in the calculation of binding energies, which are usually overestimated.

The GGA model introduces additional functionals (corrections) to the LDAs. These corrections consider the gradient of the charge density, $\nabla\rho(r)$, such that

[5] Shown by Bloch, Dirac and Slater is proportional to $\rho^{1/3}$.

$$E_{XC}^{GGA}[\rho] = \int F(\rho, \nabla\rho) dr \tag{7.34}$$

As with the LDA model the exchange-correlation energy from the GGA model can be split so that the exchange part is rewritten as

$$E_X^{GGA} = E_X^{LDA} - \sum_\sigma \int F(s_\sigma) \rho_\sigma^{4/3}(r) dr \tag{7.35}$$

where F is the reduced density gradient for spin σ. Several formulations have been put forward for F (see reference 2 for details) resulting in a multitude of exchange functionals. If these are then combined with the several correlation functionals (which in principle is possible) we could end up with hundreds of GGA exchange-correlation functionals. However, only a few combinations are generally in use. The exchange part is generally chosen to be Becke's functional [41]. This is then combined with either Perdew's 1986 correlation functional (P86) [42], or the functional of Lee, Yang and Parr (LYP) [43] resulting in the popular BP86 and BLYP GGAs.

The hybrid functionals method is based on the work of Becke, in which he suggested mixing the 'exact' HF exchange with DFT exchange and correlation energies. In this method semi-empirical weighting factors assigned to the functional components are obtained from a fit to established experimental values. The most used functional of this type is the 3-parameter functional due to Becke (B3), which incorporates non-local corrections, given as

$$E_{XC} = 0.2E_X^{HF} + 0.8E_X^{LDA} + 0.72E_X^B + 1.0E_C^{LDA} + 0.81E_C^{NL} \tag{7.36}$$

The implementation of this functional allows for different gradient-corrected functionals to be used for E_C^{NL}, i.e. the B3LYP and B3P86.

7.4.3 Basis Set Selection

A basis set is a mathematical description of the linear combination of basis functions. When combined these give an approximation of the total electronic wavefunction describing a chemical system. A basis set is chosen such that calculated wavefunctions approach the HF limit in an efficient manner. Three points are crucial when making a basis set choice.

First, the number of two-electron integrals increases as N^4 where N is the number of basis functions. Therefore, it is computationally attractive to minimise the number of basis functions. Secondly, a larger basis set whose greater number of integrals can be evaluated faster than a smaller basis sets is most advantageous. And thirdly, the basis functions must be chosen to have a form that is chemically useful. Meaning that functions should cover sufficiently large regions of space where the electron probability density is large, and minimal amplitudes where the probability density is at a minimum.

7.4.3.1 Gaussian Basis Functions

In this work, Gaussian basis functions (atomic orbitals (AOs)) that are centered on the atoms of a molecule and are called Gaussian-type orbitals (GTOs), introduced by S. F. Boys in 1950 [44] are used. The general form of a normalised primitive GTO in atom-centred Cartesian coordinates is

$$\phi(x,y,z;\alpha,i,j,k)=\left(\frac{2\alpha}{\pi}\right)^{\frac{3}{4}}\left[\frac{(8\alpha)^{i+j+k}\,i!\,j!\,k!}{(2i)!(2j)!(2k)!}\right]^{\frac{1}{2}}x^i y^j z^k e^{-\alpha\left(x^2+y^2+z^2\right)} \qquad (7.37)$$

where α is an exponent controlling the width of the GTO, and i, j, and k are non-negative integers whose sum $L = i + j + k$ is referred to as the angular momentum. This angular momentum dictates the 'shape' of GTO used, i.e. $L = 0$ refers to a GTO with spherical symmetry (s-type GTO), whereas $L = 1$ and $L = 2$, refers to p- and d-type GTOs and so forth.

Several GTOs are usually combined to provide better approximations of different orbitals in atomic and nuclear environments. A basis function defined as a linear combination of primitive Gaussians is referred to as a contracted basis function or contracted Gaussian-type orbital (CGTO) and is written as,

$$\varphi(x,y,z;\{\alpha\},i,j,k)=\sum_{a=1}^{M}c_a\phi(x,y,z;\alpha_a,i,j,k) \tag{7.38}$$

where M is the number of Gaussians used in the linear combination and the coefficients c are chosen to optimise the shape of the basis function sum and to ensure normalisation.

7.4.3.2 Basis Set Notation

A 'single-ζ' or minimal basis set, such as the STO-3G basis set, is a basis that uses one contracted Gaussian function to represent each atomic orbital of each atom. This type of basis set would contain one function for H and He, and five basis functions for atoms from Li to Ne (one for *1s*, one for *2s*, and three for the *2p*-orbitals), etc.

The initial step in improving a minimal basis set is to increase its flexibility by 'decontracting' it. This is achieved by constructing several basis functions for each AO, i.e. increasing the number of basis functions per atom. A basis set with two functions for each AO is called a 'double-ζ' basis. By decontracting further a 'triple- ζ' basis is obtained, and the addition of more functions leads to the creation of higher multiple-ζ basis sets. Examples of such basis sets are the 'correlation-consistent polarized Core and Valence (Double/Triple/Quadruple) Zeta' or cc-pVXZ (X = D, T, Q and 5) sets of Dunning et al [45].

A further improvement is to add flexibility in the valence basis functions. This has lead to the development of 'split-valence' or 'valence-multiple-ζ' basis sets. An example of this is the split-valence double-zeta basis set which uses one contracted function for each inner AO and two contracted functions for each valence AO. In this work the Pople split-valence basis sets are used. Examples of these basis sets are the popular 6-31G and 6-311G, where their nomenclature is a guide to the contraction scheme. The first number

indicates the number of primitives used in the contracted core functions. The numbers after the hyphen indicate the number of primitives used in the valence functions – if there are two such numbers, a valence-double-ζ basis is indicated and three numbers indicate a valence-triple-ζ set.

To remove the limitation of an orbital's shape, a polarised basis set adds orbitals with angular momentum beyond that which is required for a description of the ground state of each atom [24]. This addition allows for the study of molecules containing heavy atoms, by distorting the orbital shapes, by mixing orbitals with higher valence shell symmetry. Polarisation functions, as with split-valence functions, are readily added to Gaussian-type orbitals and can yield greater accuracy with calculations on charged systems. Examples of basis sets containing polarisation are the 6-311G (d) and 6-311G (d, p), which have added d and p functions, respectively.

Diffuse functions introduce oversized s- and p-type functions, allowing orbitals to occupy a larger region of space. The introduction of diffuse functions allows for added accuracy in the study of systems [24], in which the electrons are relatively far from the nucleus, e.g. molecules that contain lone pairs or molecular systems that contain negative charges (anions). In the Pople basis sets diffuse functions are indicated by a '+' in the basis set name, whereas, the Dunning family of cc-pVXZ basis sets, diffuse functions on all atoms are indicated by prefixing with *aug*.

7.4.3.3 Effective Core Potentials

If the chemical system being studied contains elements heavier than krypton, as in the case of the Platinum Group Metals (PGMs), one could use analytical functions referred to as (relativistic) effective core potentials ((R)ECPs), also called pseudopotentials, to model the energetically 'buried' and mainly chemically inert core electrons [24, 29].

For an ECP to be effective it is required not only to represent correctly Coulomb repulsion effects, but also to follow Pauli's principle. Moreover, if the potentials have been fitted to atomic calculations explicitly incorporating relativistic effects, these are called relativistic. A popular pseudopotential and the one used in this work is the LANL2 ECP, which is one of many developed by Hay and Wadt at the Los Alamos National

Laboratory (LANL) [46-48]. Other pseudopotentials include those developed by Dolg [49] and Stevens et al [50].

7.5 References

1. Joung, I.S. and Cheatham, T.E., *Determination of alkali and halide monovalent ion parameters for use in explicitly solvated biomolecular simulations.* J. Phys. Chem. B, 2008. 112(30): p. 9020-9041.
2. MacKerell, A.D., Bashford, D., Bellott, M., Dunbrack, R.L., Evanseck, J.D., Field, M.J., Fischer, S., Gao, J., Guo, H., Ha, S., Joseph-McCarthy, D., Kuchnir, L., Kuczera, K., Lau, F.T.K., Mattos, C., Michnick, S., Ngo, T., Nguyen, D.T., Prodhom, B., Reiher, W.E., Roux, B., Schlenkrich, M., Smith, J.C., Stote, R., Straub, J., Watanabe, M., Wiorkiewicz-Kuczera, J., Yin, D., and Karplus, M., *All-atom empirical potential for molecular modeling and dynamics studies of proteins.* J. Phys. Chem. B, 1998. 102(18): p. 3586-3616.
3. Wang, J.M., Cieplak, P., and Kollman, P.A., *How well does a restrained electrostatic potential (RESP) model perform in calculating conformational energies of organic and biological molecules?* J. Comput. Chem., 2000. 21(12): p. 1049-1074.
4. Cornell, W.D., Cieplak, P., Bayly, C.I., Gould, I.R., Merz, K.M., Ferguson, D.M., Spellmeyer, D.C., Fox, T., Caldwell, J.W., and Kollman, P.A., *A 2nd generation force-field for the simulation of proteins, nucleic-acids, and organic-molecules.* J. Am. Chem. Soc., 1995. 117(19): p. 5179-5197.
5. Cheatham, T.E., Cieplak, P., and Kollman, P.A., *A modified version of the Cornell et al. force field with improved sugar pucker phases and helical repeat.* J. Biomol. Struct. Dyn., 1999. 16(4): p. 845-862.
6. Hornak, V., Abel, R., Okur, A., Strockbine, B., Roitberg, A., and Simmerling, C., *Comparison of multiple amber force fields and development of improved protein backbone parameters.* Proteins, 2006. 65(3): p. 712-725.
7. Jensen, K.P. and Jorgensen, W.L., *Halide, ammonium, and alkali metal ion parameters for modeling aqueous solutions.* J. Chem. Theory Comput., 2006. 2(6): p. 1499-1509.

8. Patra, M. and Karttunen, M., *Systematic comparison of force fields for microscopic simulations of NaCl in aqueous solutions: Diffusion, free energy of hydration, and structural properties.* J. Comput. Chem., 2004. 25(5): p. 678-689.
9. Gavryushov, S. and Linse, P., *Effective interaction potentials for alkali and alkaline earth metal ions in SPC/E water and prediction of mean ion activity coefficients.* J. Phys. Chem. B, 2006. 110(22): p. 10878-10887.
10. Allen, M.P. and Tildesley, D.J., *Computer Simulations of Liquids.* 1989, Oxford: Clarendon Press.
11. Mason, P.E. and Brady, J.W., *"Tetrahedrality" and the relationship between collective structure and radial distribution functions in liquid water.* J. Phys. Chem. B, 2007. 111(20): p. 5669-5679.
12. Berendsen, H.J.C., Postma, J.P.M., Van Gunsteren, W.F., and Hermans, J., *Interaction Models for Water in Relation to Protein Hydration,* in *Intermolecular Forces,* B. Pullman, Editor. 1981, Reidel Publishing Co.: Dordrecht, Holland. p. 331-342.
13. Berendsen, H.J.C., Grigera, J.R., and Straatsma, T.P., *The missing term in effective pair potentials.* J. Phys. Chem., 1987. 91(24): p. 6269-6271.
14. Jorgensen, W.L., Chandrasekhar, J., Madura, J.D., Impey, R.W., and Klein, M.L., *Comparison of simple potential functions for simulations liquid water.* J. Chem. Phys., 1983. 79(2): p. 926-935.
15. Horn, H.W., Swope, W.C., Pitera, J.W., Madura, J.D., Dick, T.J., Hura, G.L., and Head-Gordon, T., *Development of an improved four-site water model for biomolecular simulations: TIP4P-Ew.* J. Chem. Phys., 2004. 120(20): p. 9665-9678.
16. Mahoney, M.W. and Jorgensen, W.L., *A five-site model for liquid water and the reproduction of the density anomaly by rigid, nonpolarizable potential functions.* J. Chem. Phys., 2000. 112(20): p. 8910-8922.
17. Dang, L.X. and Chang, T.M., *Molecular dynamics study of water clusters, liquid, and liquid-vapor interface of water with many-body potentials.* J. Chem. Phys., 1997. 106(19): p. 8149-8159.

18. Svishchev, I.M., Kusalik, P.G., Wang, J., and Boyd, R.J., *Polarizable point-charge model for water: Results under normal and extreme conditions.* J. Chem. Phys., 1996. 105(11): p. 4742-4750.

19. Rick, S.W., Stuart, S.J., and Berne, B.J., *Dynamical fluctuating charge force-fields - Application to liquid water.* J. Chem. Phys., 1994. 101(7): p. 6141-6156.

20. Dang, L.X., *The nonadditive intermolecular potential for water revised.* J. Chem. Phys., 1992. 97(4): p. 2659-2660.

21. Lamoureux, G., MacKerell, A.D., and Roux, B., *A simple polarizable model of water based on classical Drude oscillators.* J. Chem. Phys., 2003. 119(10): p. 5185-5197.

22. Rick, S.W., *A reoptimization of the five-site water potential (TIP5P) for use with Ewald sums.* J. Chem. Phys., 2004. 120(13): p. 6085-6093.

23. Price, D.J. and Brooks, C.L., *A modified TIP3P water potential for simulation with Ewald summation.* J. Chem. Phys., 2004. 121(20): p. 10096-10103.

24. Cramer, C.J., *Essentials of Computational Chemistry, 2nd Edition.* 2004: John Wiley & Sons Ltd.

25. Chen, I.J., Yin, D.X., and MacKerell, A.D., *Combined ab initio/empirical approach for optimization of Lennard-Jones parameters for polar-neutral compounds.* J. Comput. Chem., 2002. 23(2): p. 199-213.

26. Martin, A. and Orpen, A.G., *Structural systematics .6. Apparent flexibility of metal complexes in crystals.* J. Am. Chem. Soc., 1996. 118(6): p. 1464-1470.

27. Neese, F., *Prediction of molecular properties and molecular spectroscopy with density functional theory: From fundamental theory to exchange-coupling.* Coord. Chem. Rev., 2009. 253(5-6): p. 526-563.

28. Comba, P. and Kerscher, M., *Computation of structures and properties of transition metal compounds.* Coord. Chem. Rev., 2009. 253(5-6): p. 564-574.

29. Koch, W. and Holthausen, M.C., *A Chemist's Guide to Density Functional Theory, 2nd Edition.* 2001: Wiley-VCH.

30. Breneman, C.M. and Wiberg, K.B., *Determining atom-centered monopoles from molecular electrostatic potentials - The need for high sampling density in formamide conformational-analysis.* J. Comput. Chem., 1990. 11(3): p. 361-373.

31. Singh, U.C. and Kollman, P.A., *An approach to computing electrostatic charges for molecules.* J. Comput. Chem., 1984. 5(2): p. 129-145.

32. Besler, B.H., Merz, K.M., and Kollman, P.A., *Atomic charges derived from semiempirical methods.* J. Comput. Chem., 1990. 11(4): p. 431-439.

33. Waller, M.P. and Buhl, M., *Vibrational corrections to geometries of transition metal complexes from density functional theory.* J. Comput. Chem., 2007. 28(9): p. 1531-1537.

34. Lienke, A., Klatt, G., Robinson, D.J., Koch, K.R., and Naidoo, K.J., *Modeling platinum group metal complexes in aqueous solution.* Inorg. Chem., 2001. 40(10): p. 2352-2357.

35. Szabo, A. and Ostlund, N.S., *Modern Quantum Chemistry: Introduction to Advanced Electronic Structure Theory. 1st Ed. Revised*. 1989: New York: McGraw-Hill.

36. Pople, J.A. and Nesbet, R.K., *Self-consistent orbitals for radicals.* J. Chem. Phys., 1954. 22(3): p. 571-572.

37. Hohenberg, P. and Kohn, W., *Inhomogeneous Gas.* Phys. Rev. B, 1964. 136(3B): p. B864-&.

38. Kohn, W. and Sham, L.J., *Self-Consistent Equations Including Exchange and Correlation Effects.* Phys. Rev., 1965. 140(4A): p. 1133-&.

39. Vosko, S.H., Wilk, L., and Nusair, M., *Accurate spin-dependent electron liquid correlation energies for local spin-density calculations - A critical analysis.* Can. J. Phys., 1980. 58(8): p. 1200-1211.

40. Perdew, J.P. and Wang, Y., *Accurate and simple analytic representation of the electron-gas correlation-energy.* Phys. Rev. B, 1992. 45(23): p. 13244-13249.

41. Becke, A.D., *Density-functional thermochemistry .3. The role of exact exchange.* J. Chem. Phys., 1993. 98(7): p. 5648-5652.

42. Perdew, J.P., *Density-functional approximation for the correlation-energy of the inhomogeneous electron-gas.* Phys. Rev. B, 1986. 33(12): p. 8822-8824.

43. Lee, C.T., Yang, W.T., and Parr, R.G., *Development of the Colle-Salvetti correlation-energy formula into a functional of the electron-density.* Phys. Rev. B, 1988. 37(2): p. 785-789.

44. Boys, S.F., *Electronic wave functions. I. A general method of calculation for the stationary states of any molecular system.* Proc. Roy. Soc. London Ser. A, 1950. 200(1063): p. 542-554.

45. Woon, D.E. and Dunning, T.H., *Gaussian-basis sets for use in correlated molecular calculations. 5. Core-valence basis-sets for boron through neon.* J. Chem. Phys., 1995. 103(11): p. 4572-4585.

46. Hay, P.J. and Wadt, W.R., *Ab initio effective core potentials for molecular calculations - potentials for K to Au including the outermost core orbitals.* J. Chem. Phys., 1985. 82(1): p. 299-310.

47. Hay, P.J. and Wadt, W.R., *Ab initio effective core potentials for molecular calculations - potentials for the transition-metal atoms Sc to Hg.* J. Chem. Phys., 1985. 82(1): p. 270-283.

48. Wadt, W.R. and Hay, P.J., *Ab initio effective core potentials for molecular calculations - Potentials for main group elements Na to Bi.* J. Chem. Phys., 1985. **82**(1): p. 284-298.

49. Dolg, M., *Fully relativistic pseudopotentials for alkaline atoms: Dirac-Hartree-Fock and configuration interaction calculations of alkaline monohydrides.* Theor. Chim. Acta, 1996. **93**(3): p. 141-156.

50. Stevens, W.J., Krauss, M., Basch, H., and Jasien, P.G., *Relativistic compact effective potentials and efficient, shared-exponent basis-sets for the 3rd-row, 4th-row, and 5th-row atoms.* Can. J. Chem.-Rev. Can. Chim., 1992. **70**(2): p. 612-630.

CHAPTER 8

Modelling of Platinum Group Metals in Aqueous Solution

8.1 Introduction

The importance of platinum group metals (PGMs) in industrial processes and technological advances, combined with their naturally low abundance, necessitates an effective separation of PGM chloro complexes from aqueous chloride solutions [1]. Several chemical properties of the PGMs have been identified as important in contributing toward their separation [1]. The properties routinely used as discriminators in large-scale separation and refinement are the favourable characteristics of their anionic chloro-complexes, in aqueous chloride media, along with the oxidative distillation of Ru and Os that are used in their large-scale separation and refinement [1]. In the past separation of the PGMs has been achieved through selective precipitation and a combination of chromatography, ion-exchange mechanisms and solvent extraction [1, 2]. In recent times the trend has been towards selective extraction of PGMs using either solvent extraction, incorporating inner- or outer-sphere coordination chemistry, e.g. Bell et al. have shown that up to 98% Pt can be selectively extract from aqueous media into chloroform via outer-sphere coordination of tris(2-aminoethyl)amine-based urea and amide receptors [3], or using solid-phase such as anion-exchange resins (e.g. Amberlite IRA 400), and ion-exchange chromatography [1].

The major challenge in the separation of anions is selective recognition, which is dependant on several properties. These are the ionic size, charge, geometry and hydration free energy (which is related to an anions ability to form hydrogen bonds with water molecules). Furthermore, the confined pH range in which many anions exist limits anion recognition processes [3, 4].

The role of solvent effects in anion selectivity is very important because (anion) receptors continually compete with solvent molecules in order to bind to anions. Thus, a more detailed understanding of the nature of hydration and ion pairing/speciation properties of the PGM chloro-anion complexes is required. Solvation effects are represented in classical condensed phase simulations by the strong electrostatic (Coulomb) and the weaker dispersion (van der Waal terms) interactions [5]. Accurate ion-solvent and solvent-solvent interactions are imperative in obtaining force fields that can be used for

Table 8.1. Series of PGM chloro-anions parameterised in this work.

Hexa-chloro anions		Tetra-chloro anions
Bivalent	**Trivalent**	
$[PtCl_6]^{2-}$	$[IrCl_6]^{3-}$	$[PtCl_4]^{2-}$
$[PdCl_6]^{2-}$	$[RuCl_6]^{3-}$	$[PdCl_4]^{2-}$
$[OsCl_6]^{2-}$	$[RhCl_6]^{3-}$	
$[IrCl_6]^{2-}$		
$[RuCl_6]^{2-}$		

free energy simulations [6, 7]. These features, along with accurate anion geometries, are paramount for accurate ion representation in computer simulations used for anion recognition and ion pairing.

Force field parameters for bi- and trivalent octahedral ($[PtCl_6]^{2-}$ and $[RhCl_6]^{3-}$) and square planar ($[PdCl_4]^{2-}$ and $[PtCl_4]^{2-}$) PGM chloro-anion complexes have previously be presented [8, 9]. The parameters were used to study the condensed phase properties and ionic hydration structures [9]. Furthermore, the force field was used to study the ion pairing process of $[PtCl_6]^{2-}\cdots Na^{+}$ in methanol [10]. In this Chapter the Metal Solution Force Field (MSFF) derived in Chapter 5 was expanded by including a subset of PGM chloro-anion complexes found in aqueous acidic media, as presented in Table 8.1. Parameterisation of the force field was achieved by predicting, and where possible reproducing, experimental geometries, vibrational frequencies and monohydrated anion interaction energies. The parameter set was tested by conducting condensed phase simulations in water. From these simulations the ionic hydration structures of the anions were analysed from radial and spatial distribution functions. Analysis was expanded to include the dynamic hydration numbers [11] of the anionic complexes and the anion self-diffusion coefficients, residence times and rotational relaxation times. The work was concluded by examining the effect of the anion size and charge, as well as the effect the ammonium counterions have on the aforementioned properties.

8.2 Computational Details

8.2.1 DFT Calculations

Density functional theory (DFT) calculations were performed using the Gaussian03 program [12]. Geometries, harmonic potentials and relative point charges for the PGM chloro-anions were calculated using the SVWN [13, 14] functional. This functional was chosen as the percentage difference between calculated and experimental geometries and vibrational frequencies were the smallest for a large subset of the parameterised complexes, when compared to other functionals, (i.e. the hybrid B3LYP [15-17] and GGA BP86 [15, 18] functionals) in combination with the LanL2DZ [19-21] effective core potential (ECP) for the metal centres and using the 6-31+G(2d) basis set for the chloride ligands. The choice of a functional and basis set to calculate structural and vibrational data for force field parameterisation is validated by the accuracy of the computed results [22, 23]. Geometries calculated using this combination showed excellent agreement with experimental M-Cl bond lengths compared to bond lengths that are calculated using the hybrid B3LYP functional. A previously derived correction factor for the vibrational frequencies, addition of a constant of 27 cm^{-1} [8] (rather than the use of the more familiar multiplication factor) was found to produce good agreement between calculated and experimental vibrational frequencies. This spanned the full vibrational analysis of the $[PtCl_6]^{2-}$ and $[IrCl_6]^{2-}$ anions with potassium counterions [24] and an incomplete vibrational analysis for the $[PdCl_4]^{2-}$, $[PdCl_6]^{2-}$, $[IrCl_6]^{3-}$ and $[RhCl_6]^{3-}$ anions [25]. The constant (27 cm^{-1}) was added to the computed frequencies resulting in them being mostly within 10 cm^{-1} of the experimental ones.

The B3LYP functional, with the LanL2DZ basis for the metal centers, with a 6-311++G(2d,2p) basis set used for all other atoms, was used to calculate several monohydrated PGM anion interaction energies. For the octahedral species the water was placed with one of the hydrogen atoms a) pointing to the face created by three chlorides, b) bisecting two chlorides and c) pointing directly at one chloride. For the square planar species orientations b and c were used. In all the interaction energies calculations, the waters were constrained at the TIP3P geometry [26, 27].

8.2.2 MM/MD Computational Details

The CHARMM program was used for all molecular mechanics calculations and molecular dynamics simulations [28, 29]. Octahedral and square planar geometries were maintained using the electrostatic repulsion of the chloride-chloride non-bonded interactions. This was achieved by making use of 1, 3 non-bonded interaction terms for the forces acting between ligand atoms and the exclusion of valence angle bending terms from the potential energy expression [8]. The present force field is thus represented by the following energy expression,

$$E_{tot} = \sum_{bonds} K_b (r - r_o)^2 + \sum_{impropers} K_\omega (\omega - \omega_o)^2 + \sum_{electrostatic} \frac{q_i q_j}{4\pi\varepsilon_e r_{ij}} + \sum_{VDW} \varepsilon_{ij} \left[\left(\frac{R_{\min,ij}}{r_{ij}} \right)^{12} - 2 \left(\frac{R_{\min,ij}}{r_{ij}} \right)^{6} \right] \quad (8.1)$$

where K_b and K_ω are the bond and improper dihedral angle force constants; r and r_0 are the bond and equilibrium lengths, and ω and ω_0 are the improper and equilibrium torsion angles. Non-bonded interactions were expressed via the Coulomb and Lennard-Jones (LJ) 6-12 terms, where ε is the LJ well depth, $R_{\min,ij}$ is the distance at the LJ minimum, q_i and q_j are the atomic partial charges of atoms i and j, r_{ij} is the distance between atoms i and j and ε_e is the effective dielectric constant. The improper dihedral is only used for the square-planar complexes; this is to prevent the unwanted tetrahedral geometry.

To maintain metal-ligand bond lengths and vibrational frequencies that are consistent with experimental (or ab initio) values, the position of the reference r_0 value and force constant k_i will vary on the basis of the strength of the repulsive forces of the interacting ligands. This is due to the inclusion of the 1, 3 nonbonded interactions, consequently r_0 and k_i no longer have their usual relation to experiment. In this force field the equilibrium bond lengths were determined by the sum of the harmonic bond potentials and the inter-ligand interaction potentials.

Condensed phase simulations of the PGM-chloro anion complexes with the appropriate number of ammonium counterions, to neutralise the charge, were

conducted using the CHARMM variant of the TIP3P water model [26, 27] in a cubic box of length 33.9772 Å for 10 ns using periodic boundary conditions. All simulations were run in the canonical ensemble (NVT) and trajectories were integrated using the Velocity-Verlet2 integrator [30] and a 1 fs time step. The temperature was maintained at 298.15 K using a the TPCONTROL method based on the Nose-Hoover thermostat with τ set to 0.1 [30]. Electrostatic interactions were calculated using particle-mesh Ewald (PME) [31, 32] with a 16.0 Å real space cutoff while the Lennard-Jones interactions were truncated using an atom-based switching function applied between 14.0 and 16.0 Å.

8.3 Force Field Parameterisation

8.3.1 Electrostatic and van der Waals Parameters

The final parameter set is given in Table 8.2. The van der Waals parameters were taken directly from the previous study [8]. These values; R_{min} = 1.70 and ε = -0.200 for the metal centers and R_{min} = 2.03 and ε = -0.240 for the chloride ligands; were used throughout the series of PGM chloro-anion species, in order to add a degree of transferability to the series parameters and to minimise the parameterisation process. This approach was chosen since the non-bonded energies in the force field are the sum of the VdW and LJ terms and by setting one as a constant, the other can be parameterised more effectively. In support of this, it has been independently shown that for simple alkali metal cations and halide anions the free energy of hydration can be accurately calculated by using several combinations of R_{min} and ε [33]. Relative point charges were calculated from the quantum mechanically produced electrostatic potential (ESP) according to the CHELPG fitting scheme of Breneman and Wiberg [34]. Optimised point charges were obtained by taking the CHELPG values and fitting the DFT and force field PGM chloro-anion water interaction energies, to obtain best fit charges, as reported in Table 8.2. In general, the CHELPG point charges gave the best initial results, compared to the Merz-Kollman-Singh [35, 36] and CHELP [37] schemes when calculating the MM anion-water interaction energies. Point charges calculated from CHELPG, MKS and CHELP schemes

Table 8.2. Summary of PGM-chloro anion complex force field.

	$[PtCl_4]^{2-}$	$[PdCl_4]^{2-}$	$[PtCl_6]^{2-}$	$[PdCl_6]^{2-}$	$[IrCl_6]^{2-}$	$[RuCl_6]^{2-}$	$[OsCl_6]^{2-}$	$[IrCl_6]^{3-}$	$[RuCl_6]^{3-}$	$[RhCl_6]^{3-}$
R_0	2.167	2.135	2.080	2.075	2.095	2.085	2.116	1.788	1.798	1.800
k_b	108.0	95.0	108.0	98.0	108.0	98.0	108.0	70.0	70.0	75.0
k_w	59.0	54.0	---	---	---	---	---	---	---	---
q(M)	0.128	0.328	1.168	0.718	1.078	1.048	1.132	1.728	1.884	1.776
q(Cl)	-0.532	-0.582	-0.528	-0.453	-0.513	-0.508	-0.522	-0.788	-0.814	-0.796
ε(Cl)	-0.240	-0.240	-0.240	-0.240	-0.240	-0.240	-0.240	-0.240	-0.240	-0.240
$R_{min/2}$(Cl)	2.030	2.030	2.030	2.030	2.030	2.030	2.030	2.030	2.030	2.030
ε(M)	-0.200	-0.200	-0.200	-0.200	-0.200	-0.200	-0.200	-0.200	-0.200	-0.200
$R_{min/2}$(M)	1.700	1.700	1.700	1.700	1.700	1.700	1.700	1.700	1.700	1.700

Table 8.3. PGM-Metal charges derived from DFT using the SVWN functional and several ESP methods.

Anion	MKS	CHELPG	CHELP
$[PtCl_4]^{2-}$	0.1086	0.2474	0.6222
$[PdCl_4]^{2-}$	0.2593	0.3783	0.7033
$[PtCl_6]^{2-}$	0.2043	0.7502	1.4505
$[PdCl_6]^{2-}$	0.0465	0.7165	1.4393
$[IrCl_6]^{2-}$	0.4818	0.9569	1.5373
$[RuCl_6]^{2-}$	0.7734	1.1651	1.5898
$[OsCl_6]^{2-}$	0.6764	1.1291	1.5869
$[IrCl_6]^{3-}$	1.3987	1.9403	2.1392
$[RuCl_6]^{3-}$	1.6981	2.0388	2.1526
$[RhCl_6]^{3-}$	1.4890	1.9831	2.1499

using the SVWN functional, for the respective metal centers are reported in Table 8.3.

A summary of the molecular mechanics and DFT (B3LYP) hybrid functional monohydrated anion interactions and distances is reported in Table 8.4. A comparison of the DFT and MM energies for the monohydrated anion-water systems reveals a very good fit, with the MM interaction energies generally within 1.5 kcal.mol^{-1} of the corresponding QM values. There are differences in the MM and DFT distances, with the QM distances consistently 0.3-0.4 Å greater in length. A better fit can be achieved by altering the van der Waal parameters. But this in turn leads to poor M-Cl bond lengths and a poor reproduction of the Met-O and Cl-O radial distribution functions in the condensed phase simulations.

8.3.2 Optimisation of Geometries and Force Constants

Square planar symmetry was used for the tetra-chloro anions and octahedral symmetry for the closed-shell hexa-chloro anions. The open-shell complexes, $[RuCl_6]^{3-}$ and $[IrCl_6]^{2-}$, exhibited small distortions in M-Cl bond lengths in the axial positions. However, these

Table 8.4. Summary of the monohydrated PGM chloro-anion interaction energies, calculated using MM and DFT in orientations A, B and C. N.A implies that the calculations did not converge.

	A				B				C			
	MM		QM		MM		QM		MM		QM	
Anion	**r / Å**	**E / kcal.mol^{-1}**	**r / Å**	**E / kcal.mol^{-1}**	**r / Å**	**E / kcal.mol^{-1}**	**r / Å**	**E / kcal.mol^{-1}**	**r / Å**	**E / kcal.mol^{-1}**	**r / Å**	**E / kcal.mol^{-1}**
$[PtCl_4]^{2-}$					3.49	-12.060	3.88	-11.106	4.40	-11.142	4.66	-10.564
$[PdCl_4]^{2-}$					3.50	-11.999	3.87	-10.999	4.39	-11.498	4.56	-10.939
$[PtCl_6]^{2-}$	3.36	-9.969	3.66	-9.419	3.55	-10.492	N.A	N.A	4.44	-9.957	4.70	-8.752
$[PdCl_6]^{2-}$	3.29	-10.667	3.65	-9.606	3.52	-10.832	3.80	-10.521	4.45	-9.627	4.71	-8.540
$[IrCl_6]^{2-}$	3.35	-10.068	3.64	-8.597	3.55	-10.532	3.89	-9.792	4.46	-9.854	4.70	-8.803
$[RuCl_6]^{2-}$	3.35	-10.077	3.63	-8.755	3.55	-10.526	3.80	-9.884	4.45	-9.840	4.66	-5.287
$[OsCl_6]^{2-}$	3.37	-9.909	3.63	-8.843	3.55	-10.528	N.A	N.A	4.46	-9.889	4.70	-8.958
$[IrCl_6]^{3-}$	3.34	-14.342	3.61	-14.434	3.49	-15.465	3.76	-15.941	4.38	-15.372	N.A	N.A
$[RuCl_6]^{3-}$	3.37	-13.951	3.64	-13.546	3.51	-15.220	3.79	-15.122	4.40	-15.462	4.68	-14.364
$[RhCl_6]^{3-}$	3.39	-14.344	3.63	-13.933	3.49	-15.487	3.78	-15.369	4.37	-15.442	4.67	-14.822

distortions where only evident in the fourth decimal place and are averaged out in the force field resulting in an expected octahedral geometry.

Table 8.5 gives the M-Cl bond lengths calculated using both the SVWN and B3LYP functionals and their respective percentage difference when compared to average M-Cl bond lengths determined from several crystallographic structures obtained from the Cambridge Structural Database (CSD) [38]. A summary of the average crystallographic M-Cl bond lengths can be found in Table 8.5. Comparisons of the DFT calculated M-Cl bond lengths to crystallographic data reveal that the M-Cl bond lengths calculated using the SVWN functionals are all within 1.5% (~0.03 Å) of the experimental data while the B3LYP results are within 5.9% (~0.14 Å).

Calculating intramolecular distances to an accuracy of 0.03 Å is an excellent result given the accuracy commonly achieved from DFT calculations. However, this level of accuracy exceeds of the experimental structural geometry scatter among the PGM chloro-anion complexes. The crystallographic M-Cl bond lengths were therefore used as a reliable target for the parameterization of these simple metal complexes. Structures were selected from the CSD such that the average M-Cl distance was at least within two standard deviations of the total sample average of bond lengths from all CSD PGM chloro-anion structures.

MM vibrational frequencies were calculated using the VIBRAN module in CHARMM. The MM reference bond lengths (r_o) and stretching constants (k_i) were varied under the constraint that the experimentally observed M-Cl bond lengths are reproduced. The final values for these are summarised in Table 8.2. Since the 1, 3 non-bonded interaction terms are used the variation in the magnitudes of the atomic charges should have a strong influence on the vibrational frequencies calculated from a MM normal-mode analysis. However, as previous work showed manipulating the charges does not enhance the quality of the frequency calculation [8]. Since experimental frequencies exist for a limited number of PGM chloro species, parameters were chosen that gave MM wavenumbers which compared well to those obtained from DFT calculations. A summary of calculated and experimental wave numbers is given in Table 8.6. The overall agreement between the MM wavenumbers with those from either experiment or DFT calculations is good for the majority of complexes.

Table 8.5. Summary of M-Cl bond lengths in Å for SVWN, B3LYP and MM calculated values compared to Crystallographic average.

Anion	Averaged M-Cl bond length (Xtal)	Averaged M-Cl bond length (SVWN)	Percentage difference Xtal vs. SVWN (%)	Averaged M-Cl bond length (B3LYP)	Percentage difference Xtal vs. B3LYP (%)	Averaged M-Cl bond length (MM)	Percentage difference Xtal vs. MM (%)
$[PtCl_6]^{2-}$	2.318	2.346	1.19	2.412	4.07	2.319	0.04
$[PdCl_6]^{2-}$	2.309	2.334	1.08	2.412	4.45	2.309	0.00
$[OsCl_6]^{2-}$	2.338	2.339	0.03	2.407	2.95	2.338	0.00
$[IrCl_6]^{2-}$	2.323	2.336	0.54	2.403	3.46	2.324	0.04
$[RuCl_6]^{2-}$	2.329	2.335	0.27	2.407	3.37	2.329	0.00
$[IrCl_6]^{3-}$	2.357	2.383	1.12	2.480	5.22	2.357	0.00
$[RuCl_6]^{3-}$	2.375	2.397	0.94	2.508	5.59	2.375	0.00
$[RhCl_6]^{3-}$	2.349	2.381	1.38	2.486	5.83	2.349	0.00
$[PtCl_4]^{2-}$	2.304	2.325	0.92	2.411	4.62	2.304	0.00
$[PdCl_4]^{2-}$	2.307	2.327	0.85	2.424	5.08	2.307	0.00

Table 8.6. Summary of calculated vibrational frequencies compared to DFT and experimental frequencies. All values are given in units of wavenumbers.

	Frequency	MM	DFT	Experimental
$[PtCl_4]^{2-}$	E_u	332	335	
	A_{1g}	324	319	
	B_{1g}	263	316	
	E_u	188	173	
	A_{2u}	147	152	
	B_{2g}	181	165	
	B_{2u}	108	104	
$[PdCl_4]^{2-}$	E_u	341	332	337
	A_{1g}	311	308	309
	B_{1g}	246	280	284
	E_u	158	173	
	A_{2u}	206	166	
	B_{2g}	189	167	
	B_{2u}	101	95	
$[PtCl_6]^{2-}$	A_{1g}	361	349	346
	T_{1u}	347	337	346
	E_g	287	325	325
	T_{1u}	180	184	183
	T_{2g}	168	159	164
	T_{2u}	116	150	147
$[PdCl_6]^{2-}$	A_{1g}	361	329	330
	T_{1u}	354	358	361
	E_g	276	306	
	T_{1u}	185	192	
	T_{2g}	181	160	
	T_{2u}	117	145	
$[IrCl_6]^{2-}$	A_{1g}	359	330	350

	T_{1u}	347	357	330
	E_g	287	295	310
	T_{1u}	177	188	177
	T_{2g}	166	168	166
	T_{2u}	114	145	143
$[RuCl_6]^{2-}$	A_{1g}	361	341	
	T_{1u}	347	332	
	E_g	274	270	
	T_{1u}	182	193	
	T_{2g}	174	174	
	T_{2u}	112	124	
$[OsCl_6]^{2-}$	A_{1g}	353	359	
	T_{1u}	344	322	
	E_g	285	280	
	T_{1u}	170	189	
	T_{2g}	162	169	
	T_{2u}	109	132	
$[IrCl_6]^{3-}$	A_{1g}	322	316	330
	T_{1u}	291	299	296
	E_g	235	288	
	T_{1u}	181	179	
	T_{2g}	180	153	
	T_{2u}	112	146	
$[RuCl_6]^{3-}$	A_{1g}	317	276	
	T_{1u}	313	291	
	E_g	233	233	
	T_{1u}	198	178	
	T_{2g}	175	151	
	T_{2u}	108	133	
$[RhCl_6]^{3-}$	A_{1g}	331	296	302-308
	T_{1u}	324	302	312

E_g	243	274
T_{1u}	205	180
T_{2g}	184	155
T_{2u}	114	141

8.4 PGM Chloro-anions Condensed Phase Simulations

The diffusion (mobilities) of ions in solution is primarily governed by the size and charge of the ions. In aqueous solutions the lifetime of the ion hydration sphere is governed by the energetic interaction and orientation of water molecules with the ions [9, 10]. This is the so-called *dynamic hydration volume* that gives an accurate measure of the hydrated ion size, which in turn can be related to the hydrodynamic friction of an ion [39]. A second important interaction is that between the anion and the counterions. The cationic counterions could lower the effective charge on the anion and disrupt the solvent structure around it with intermittent weak ion-water interaction energies. In the section below we examine the dynamic hydration volume and its relationship with the relative diffusion rates of the PGM chloro-anion complexes. We aim to understand the construction of the hydration volume and how it stems from the attraction between the ion and water interactions strengths and from the competing anion and cation interaction strengths. Using these fundamental interactions the solvent structure about the PGM anion and the disruption of that solvent structure by the ammonium counterions is explained.

8.4.1 Ensemble Averaged Ion-Solvent and Ion-Ion Interaction Energy

The ensemble averaged ion-solvent interaction energy between a molecule *i* and the surrounding molecules *j* was calculated, so arriving at a *pseudo-solvation shell free energy W(r)* profile, from the total Coulomb interaction ($Q_t(r_{\alpha\beta})$: second last term in equation 8.2) and the total van der Waals interaction ($vdw_t(r_{\alpha\beta})$: last term in equation 8.2)

between a specific molecule (α) that is the so called *solute* and its surrounding solvent molecules (j) that are a distance $r_{\alpha\beta} = |r_\alpha - r_\beta|$ apart,

$$W(r) \approx \langle V(r) \rangle = \frac{1}{N_t} \sum_{t=1}^{N_t} \sum_{j \neq \alpha}^{N} \delta(r - r_{\alpha\beta}) [Q_t(r) + vdW_t(r)] \qquad (8.2)$$

This calculation was performed over the first 5 ns of the trajectory and was done for the total number of frames N_t recorded along that trajectory. In a frame at time t and bin value $r_{\alpha\beta}$ the complete box of solvent molecules (N) was evaluated to create the set of molecules (β_r) that comprise solvent molecules that are separated a distance $r_{\alpha\beta}$ from the *selected atom* of the solute α. Evaluating the solvent interaction energy in this way, where the angular and configurational entropy is included, results in an approximate free energy of solvation. The method is fast and can be done post equilibrium dynamics simulations. It yields qualitatively good estimates of the solute solvent interaction free energy but it is not a rigorous free energy method that can be used for systems with limited configurations and high energy barriers. In the case of simple solutions the configurational sampling is excellent as each solvent molecule contributes to the solute-solvent configurational ensemble. However, for aqueous electrolyte MD simulations the solute solvent interactions are interfered with by the slow convergence to equilibrium between the completely separated ions, the contact, solvent shared and solvent separated ion pairs. This method was chosen, in favor of force-based biased PMF calculations [10], to obtain a simple measure of the water PGM energetics. For all the PGM chloro-anion solutions (the metal complexes are the solute α) the pseudo free energy of solvation was calculated as a function of the separation distance, $r_{M...O}$, between the PGM chloro-anions and the oxygens on each of the solvent molecules in the set β_r. The analysis was done over 5 ns of the simulation for bin sizes of 0.1 Å in the separation range 3.0 to 10.0 Å.

Plots of the pseudo $W(r)$ for the PGM chloro-anion complexes are shown in Figure 8.1. The square planar complexes reveal two minima at approximately 4.2 Å and 6.8 Å and it is clearly seen that for the square planar species, $[PdCl_4]^{2-}$ associates more strongly with water than $[PtCl_4]^{2-}$ does. The bivalent and trivalent octahedral complexes too reveal

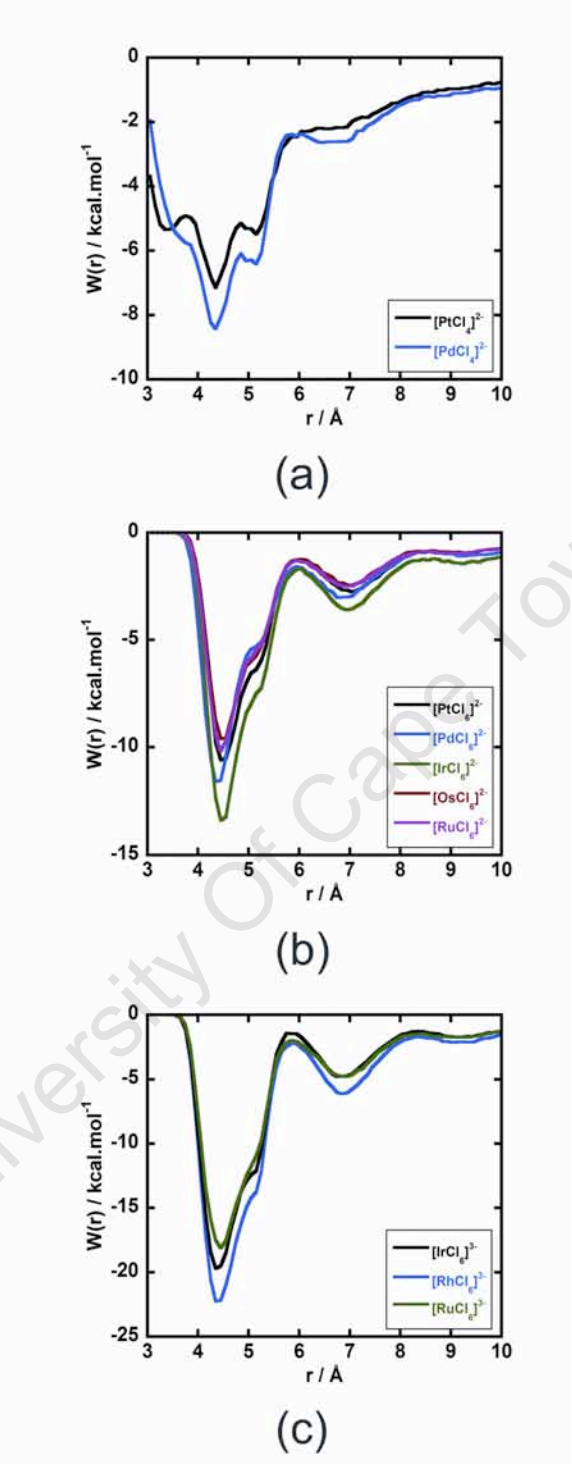

Figure 8.1. Psuedo solvation free energies $W(r)$ for (a) square planar, (b) bivalent octahedral and (c) trivalent octahedral PGM chloro-anion complexes.

double minima ranging at around 4.35-4.5 Å and 6.8-6.9 Å, with a deviation at the end of the first solvation shell minima approximately at 5.2 Å indicating a secondary solvation shell. The strength of association for the bivalent octahedral species with water in decreasing order is $[IrCl_6]^{2-} > [PdCl_6]^{2-} > [PtCl_6]^{2-} > [RuCl_6]^{2-} > [OsCl_6]^{2-}$, while for the trivalent octahedral species $[RhCl_6]^{3-} > [IrCl_6]^{3-} > [RuCl_6]^{3-}$. These orderings are a result of the approximate enthalpic and entropic interaction between water and the PGM chloro-anion complexes. It may be surmised that the fundamental energetic drive for these interactions match the point charges on the chloride atoms as listed in Table 8.2. However, this reasoning is incomplete as there is a disrupting effect of the counterion that disturbs the solvent structures of the octahedral complexes more than they do for the square planar complexes; consequently the ordering does not strictly follow the electrostatic trend.

8.4.2 Solvent and Ion Pairing Structure

Solvent structures of the PGM chloro-anion-water complexes were analyzed using the isotropic probability density via site-site pair distribution functions (PDFs),

$$g_{\alpha,\beta}(r) = \frac{V}{N_\alpha N_\beta} \left\langle \sum_{i=1}^{N_\alpha} \sum_{j=1}^{N_\beta} \delta\left(r - r_{\alpha_i \beta_j}\right) \right\rangle \tag{8.3}$$

where $r_{\alpha_i \beta_j}$ is the distance between the atomic sites α and β on the molecules i and j respectively, N_α and N_β are the total number of α and β atoms in the volume V and the angular brackets denote the ensemble average. To construct the detailed anisotropic molecular associations of the first solvation shells the three-dimensional water probability density matrices for all ten PGM chloro-anion complexes under consideration were calculated. The spatial distribution functions (SDFs) with and without counterion density are determined. This was done by removing the rotational and translational diffusion of a selected metal complex molecule (i.e., the *solute*), for each frame in the trajectories. The solute in each stored coordinate set was then reoriented to the best least squares fit with a

reference coordinate set. A coordinate transformation was then applied to all the atoms in the system. The complete MD trajectory for each PGM solution simulation was used to analyze the solvent structure. Furthermore, the statistical independence of each frame was maintained by separating them by at least 0.5 ps from each other. The solvent sites were used to calculate the probability densities on a grid with a mesh size of 0.5 Å. A Gaussian distribution function,

$$G(r) = \left(\frac{a}{\pi}\right)^{\frac{3}{2}} \exp\left(-ar^2\right) \tag{8.4}$$

centered on each solvent site to accurately represent the distribution of the sites across the mesh. The densities of the sites are distributed over neighbouring bins such that 90% of the binned density for a molecular site is within its site radius (van der Waals radius or methyl group radius built from the atomic van der Waals radii). This is determined by appropriate selection of the constant *a* for each site. The densities in each box were summed for all the selected frames from the dynamics run. The final solvent density matrix was normalised using equation 8.5 so that the density of bulk solvent corresponds to a value of 1, while 50% above bulk density corresponds to a value of 1.5, etc.

$$\overline{\rho}(x_i, y_i, z_i) = \rho(x_i, y_i, z_i) \frac{n_{xbin} n_{ybin} n_{zbin}}{n_{molecular\ site} n_{frames}} \tag{8.5}$$

Here n_{xbin}, n_{ybin} and n_{zbin} are the number of divisions in the *x*, *y* and *z* directions in the simulation box while $n_{molecularsite}$ and n_{frames} represent the number of oxygen atoms in each frame and the number of frames respectively. The non-normalised density for grid point (x_i,y_j,z_k) is given as $\rho(x_i,y_j,z_k)$. SDFs for the first solvation shells are calculated at 50% above bulk.

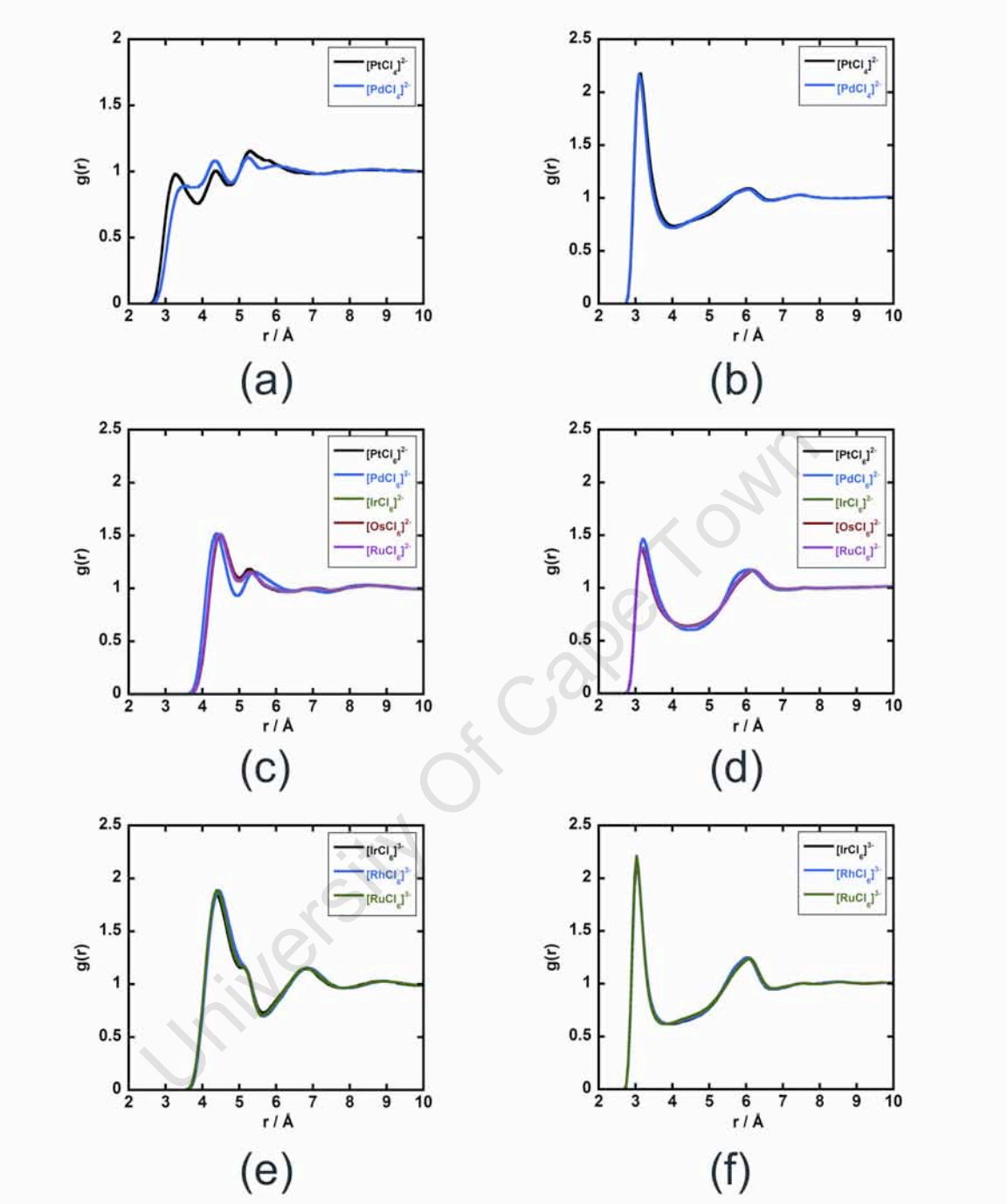

Figure 8.2 (a) Square planar, (c) bivalent octahedral and (e) trivalent octahedral Metal-oxygen pair distribution functions and (b) square planar, (d) bivalent octahedral and (f) trivalent octahedral chloride-oxygen for PGM chloro-anion complexes.

The two square planar complexes have previously been discussed [9] and only the most important features are highlighted here. The metal-O(w) PDFs, shown in Figure 8.2a, indicate several closely spaced peaks from 3 to 6 Å. These are attributed to two solvation shells, since the second shell emerges when the SDF probabilities are varied from 50% to 75% above bulk solvent density (see Ref. 10). The first peak, which is much less pronounced for the $[PdCl_4]^{2-}$ complex, is due to the rectangular elongation of the first solvation shell leading to different Pt/Pd-O(w) distances above and in the molecular plane. The effect of the ammonium counterions on the square planar complex's solvation structure is examined using the SDFs showing the ammonium probability densities as shown in Figure 8.4b and the percentage ion pairing given in Table 8.7. Considering both these observations it appears that the $[PdCl_4]^{2-}$ complex ion pair formation competes with water positions in the first solvation shell positions, whereas ion pairing for the $[PtCl_4]^{2-}$ complex competes with waters in the first and second solvation shells. The metal-$N(NH_4^+)$ PDFs (Figure 8.3) lead to the observation that in the $[PdCl_4]^{2-}$ solution at least one ion pair forms in a definite first shell symmetry position while in the $[PtCl_4]^{2-}$ solution more diffuse ion pairing occurs shared between first and second solvation shells. This results in a disrupted second solvation shell (Figure 8.4 b and c) and correlates well with the greater amount of negative (i.e., more blue) charge available for cation binding in the $[PtCl_4]^{2-}$ electrostatic surface potential (ESP) than that in the $[PtCl_4]^{2-}$ ESP (Figure 8.4 a). The ESPs were generated by first calculating an isodensity surface for $[PdCl_4]^{2-}$ using Gaussian. We generated potentials for both of the square planar complexes based on our molecular mechanic charges using an in-house program (based on the Merz-Kollman ESP approach). The potentials were plotted on the $[PdCl_4]^{2-}$ isodensity surface with contour ranges from -0.32 to -0.27 in units of electron charge. The $[PdCl_6]^{2-}$ complex is slightly smaller (45.9 $Å^3$ vs. 46.1 $Å^3$ for $[IrCl_6]^{2-}$) than $[IrCl_6]^{2-}$, $[PtCl_6]^{2-}$, $[RuCl_6]^{2-}$ or $[OsCl_6]^{2-}$ and therefore has a higher charge density as can be seen from its ESP compared with the other four bivalent complexes (Figure 8.5 a). The ESPs for the bivalent octahedral complexes were generated in the same way as was applied to the square planar complexes. We plotted the potentials on the $[PtCl_6]^{2-}$ isodensity surface with contour ranges from -0.31 to -0.26 in units of electron charge. The hydration shell that forms around this complex is well defined as seen from the SDF (Figure 8.5 b) where only the

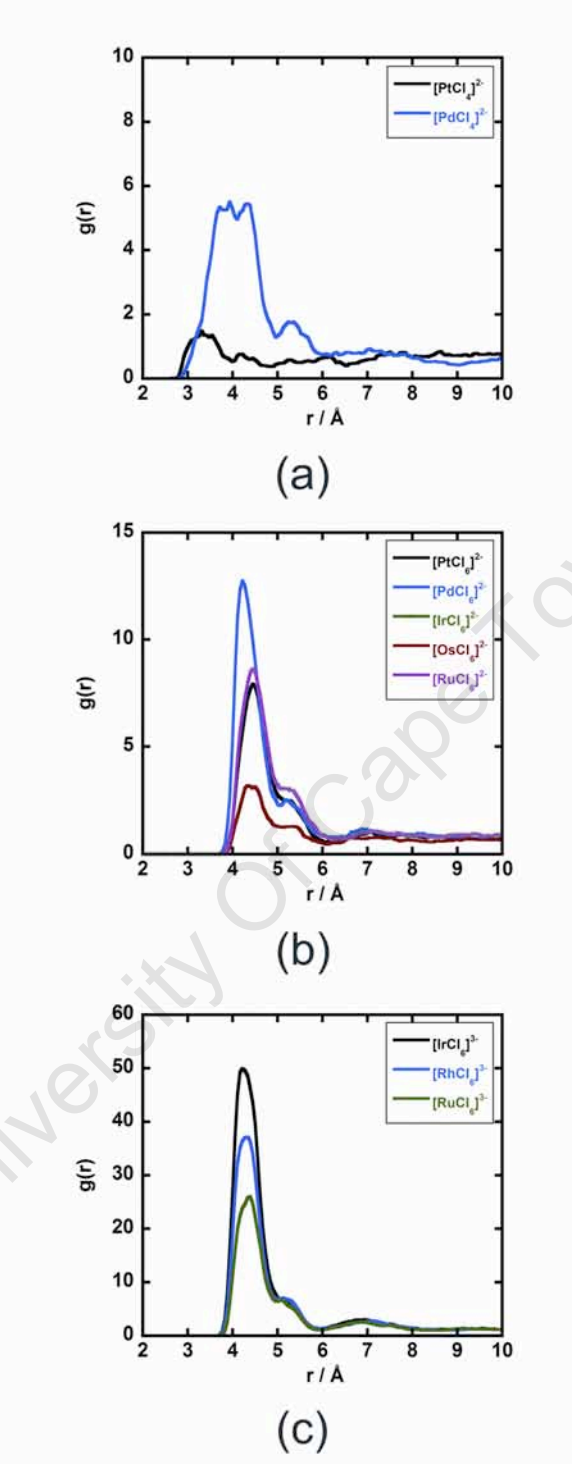

Figure 8.3. Metal···NH_4^+ pair distribution functions $g(r)$ for (a) square planar, (b) bivalent octahedral and (c) trivalent octahedral PGM chloro-anion complexes.

Table 8.7. The percentage occurrence of finding one or several ammonium counterions within 5.5 Å the PGM chloro-anion complexes and the minimum interaction energy at the most favourable interaction distance (~4.5 Å). The distance for determining ion pairing is taken from the metal centre to the centre of mass of the ammonium counterions.

	Number of Counterions and there %				
Anion	**0**	**1**	**2**	**3**	**W(r) (kcal.mol^{-1})**
$[PtCl_4]^{2-}$	89.0	11	0.0	----	-0.25
$[PdCl_4]^{2-}$	85.0	12.9	2.1	----	-1.48
$[PdCl_6]^{2-}$	82.6	17.3	0.1	----	-2.67
$[PtCl_6]^{2-}$	88.0	11.9	0.1	----	-2.75
$[IrCl_6]^{2-}$	81.4	17.8	0.8	----	-1.79
$[OsCl_6]^{2-}$	88.8	10.8	0.4	----	-0.93
$[RuCl_6]^{2-}$	86.1	13.8	0.1	----	-1.83
$[RhCl_6]^{3-}$	45.0	41.5	13.5	0.1	-9.19
$[RuCl_6]^{3-}$	54.5	41.6	3.9	0.0	-7.60
$[IrCl_6]^{3-}$	49.9	43.1	7.0	0.0	-9.81

first hydration shell emerges at 50% above bulk probability density. This is supported by the separation between the first and second metal-O(w) pair probability peaks (Figure 8.2 c), where the relative position of the first hydration shell peak (~4.4 Å compared to the other four which are at ~4.5 Å) implies that the solvent has moved closer to the complex.

This movement is due to the confined space around the smaller $[PdCl_6]^{2-}$ complex which restricts the build up of the proposed second solvation sites (see Ref 8) and limits the influence of the ammonium counterions. The DFT interaction energy data (Table 8.4) does indeed indicate that the Pd complex has the strongest interaction with water in the positions that the solvation shell is localised (and that the shifts (to the right) of the first peaks of the other metal-O(w) PDFs, corresponds to weaker interaction energies). The counterions of the bivalent octahedral complexes compete for positions with waters in the first solvation sphere (Figure 8.5 c) for the high charge density species (highest to lowest charge density

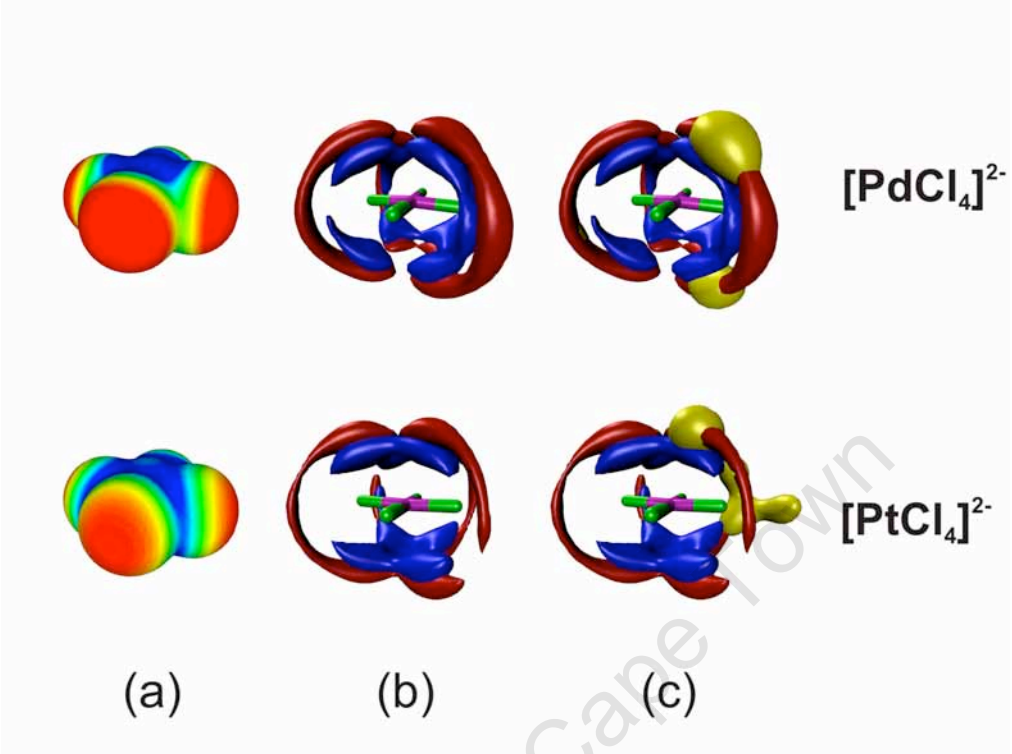

Figure 8.4. SDF plots for the square planar PGM chloro-anion complexes with (c) and (b) without the ammonium counterion densities. The red represents water oxygen densities, blue, the water hydrogen densities and the yellow densities represent the nitrogen of the ammonium counterions. Also shown are the electrostatic potentials of all the square planar PGM chloro-anion complexes mapped onto the same $[PdCl_4]^{2-}$ isodensity surface at an electron density of 0.001. The colour range extends from -0.32 (blue) to -0.27 (red) in units of electron charge.

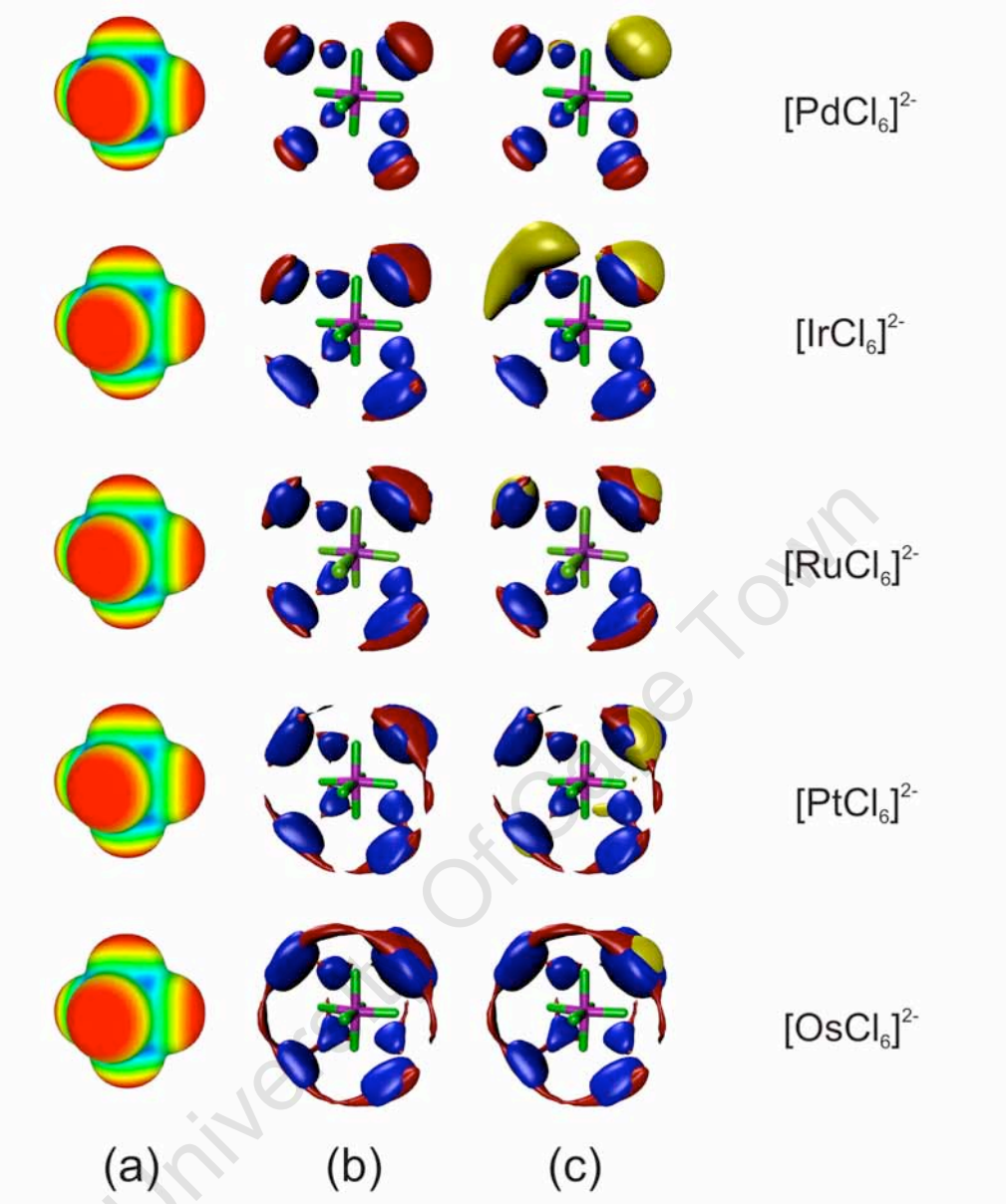

Figure 8.5. SDF plots for the bivalent octahedral PGM chloro-anion complexes with (c) and (b) without the ammonium counterion densities. The red represents water oxygen densities, blue, the water hydrogen densities and the yellow densities represent the nitrogen of the ammonium counterions. Also shown are the electrostatic potentials of all the bivalent octahedral PGM chloro-anion complexes mapped onto the same $[PtCl_6]^{2-}$ isodensity surface at an electron density of 0.001. The colour range extends from -0.31 (blue) to -0.26 (red) in units of electron charge.

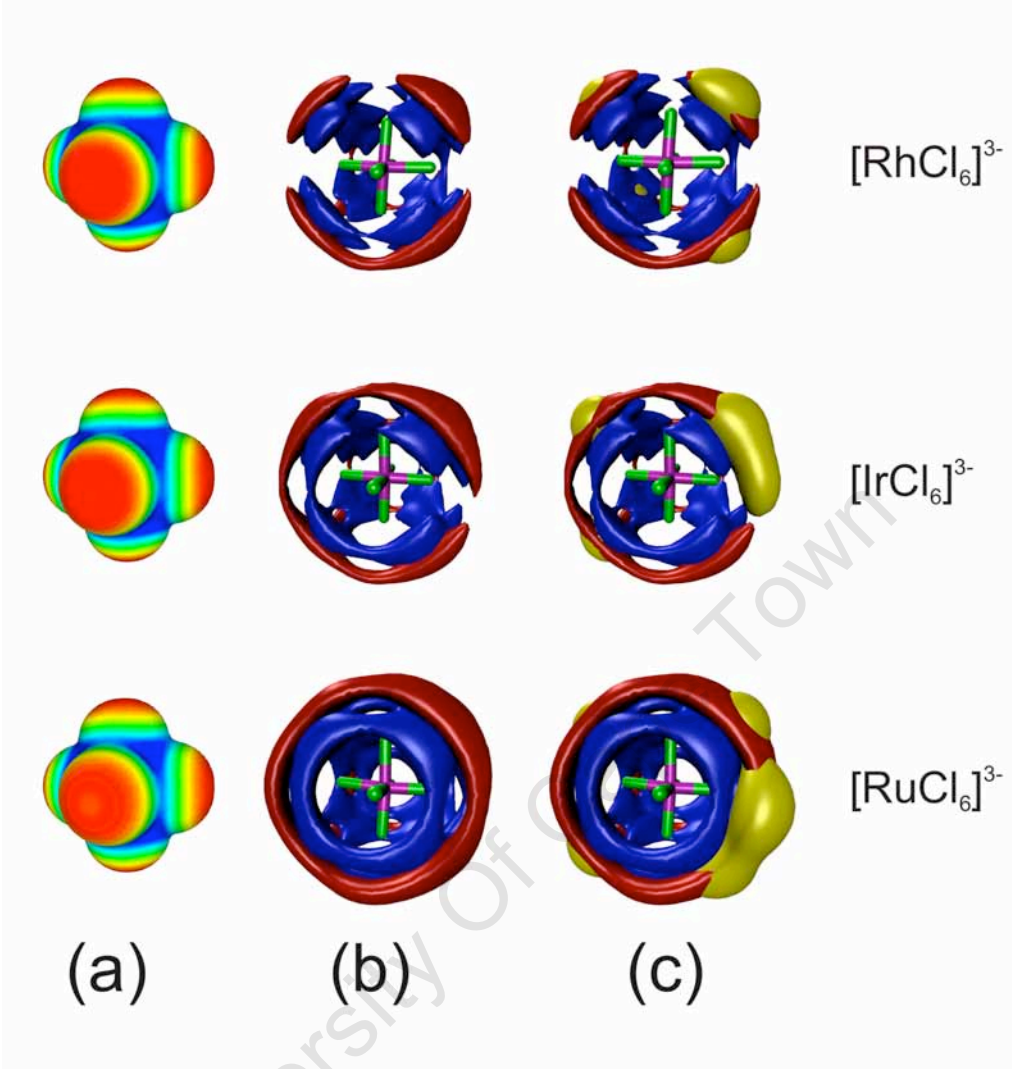

Figure 8.6. SDF plots for the trivalent octahedral PGM chloro-anion complexes with (b) and (a) without the ammonium counterion densities. The red represents water oxygen densities, blue, the water hydrogen densities and the yellow densities represent the nitrogen of the ammonium counterions. Also shown are the electrostatic potentials of all the trivalent octahedral PGM chloro-anion complexes mapped onto the same $[RuCl_6]^{2-}$ isodensity surface at an electron density of 0.001. The colour range extends from -0.47 (blue) to -0.42 (red) in units of electron charge.

shown from top to bottom of Figure a). They occupy these positions 11-18 % of the 10ns simulation time, effectively increasing the overall charge on the complex to -1. As the charge density becomes lower (with increasing complex size) the second solvation shell appears (Figure 8.5 b). The positioning of the ammonium counterions become less localised in the faces of the anions as the size of the metal complexes increase.

The first and second solvation shells that appear at ~4.5 Å and ~5.5 Å respectively in the metal-O(w) PDFs for the bivalent complexes (Figure 8.2 c) merge into one large solvation shell. This is evident from the single broad probability peaks that show up in the metal-O(w) PDFs (Figure 8.2 e) for the trivalent $[RhCl_6]^{3-}$, $[IrCl_6]^{3-}$ and $[RuCl_6]^{3-}$ complexes. This phenomenon of solvent restructuring about highly charged species has been observed and studied extensively for cations [40]. As with the bivalent species the hydration sphere is observed to become more radially extensive (Figure 8.6b seen from top to bottom) as the charge density decreases (Figure 8.6a shown from top to bottom). Unlike the bivalent octahedral complexes, the trivalent octahedral complexes have water densities for all three complexes in both the first and second solvation sites. Once again the counterions of the complex with the highest charge density i.e., $[RhCl_6]^{3-}$, compete for positions with waters in the first solvation sphere positions (top structure in Figure 8.6 c). As with the bivalent octahedral complexes, the extent of hydration sphere disruption correlates with an increase in ion pairing and an increase in the water interaction energies at the solvation sites.

8.4.3 Ensemble Averaged Ion-Solvent and Ion-Ion Interaction Energy

To calculate the volumes of the hydration spheres about the metal complexes Voronoi Polyhedra (VP) were constructed for each solvent molecule from its center of mass in each frame of a trajectory using Finney's procedure, resulting in a space filled tessellation. VPs are defined as neighbours if they share a common face in the Voronoi construction for a solvent in a periodically replicated box. Voronoi analysis is a purely geometrical approach and is not restricted to solvent atoms within a solvent's first solvation sphere. Voronoi analysis is used here to describe the volume of the first hydration spheres of the PGM chloro-anion complexes, with and without counterions. VP

gives the following details; V_k is the volume of the polyhedra of the kth solvent molecule and indicates the solvents space, while the reciprocal is a measure of the local density around a molecule. The number of faces of a VP corresponds to the number of neighbouring solvent molecules, while the area of each face reveals the distance to the nearest neighbour. The VP asphericity parameter, η refers to the shape and quantifies how the shape differs from a perfect sphere, where η = 1. The area of the kth face A_k is defined as

$$A_k = \frac{1}{2}\sum_{j=2}^{n_k^i - 1} \left| \left(r_j^{(k)} - r_1^{(k)} \right) \times \left(r_{j+1}^{(k)} - r_1^{(k)} \right) \right| \tag{8.6}$$

where n_k is the number of vertices pertaining to the kth face, $r_1^{(k)}$, $r_j^{(k)}$ and $r_{j+1}^{(k)}$ are the vectors of the first, jth and j + 1 vertex of the kth vertex respectively. The total volume of a Voronoi analysis , V is calculated as

$$V = \frac{1}{6}\sum_{k=1}^{N_f} \sum_{j=2}^{n_v^{(k)} - 1} \left| \vec{r}_1^{(k)} \times \vec{r}_j^{(k)} \cdot \vec{r}_{j+1}^{(k)} \right| \tag{8.7}$$

In Figure 8.7 the calculated hydration volumes of the PGM chloro-anions are plotted against various dynamic properties of the metal complexes.

8.4.4 Dynamic Hydration Numbers and Residence Times

The number of solvent molecules within the first hydration shell of the PGM chloro-anion complexes can be calculated by integrating the first peaks of the metal-O(w) PDFs. This results in the running integration numbers $n_{\alpha\beta}(r)$, defined in equation 8.8, where ρ_0 is the number density of the atoms of type β.

$$n_{\alpha\beta}(r) = 4\pi\rho_0 \int_0^r g_{\alpha\beta}(r') r'^2 dr \tag{8.8}$$

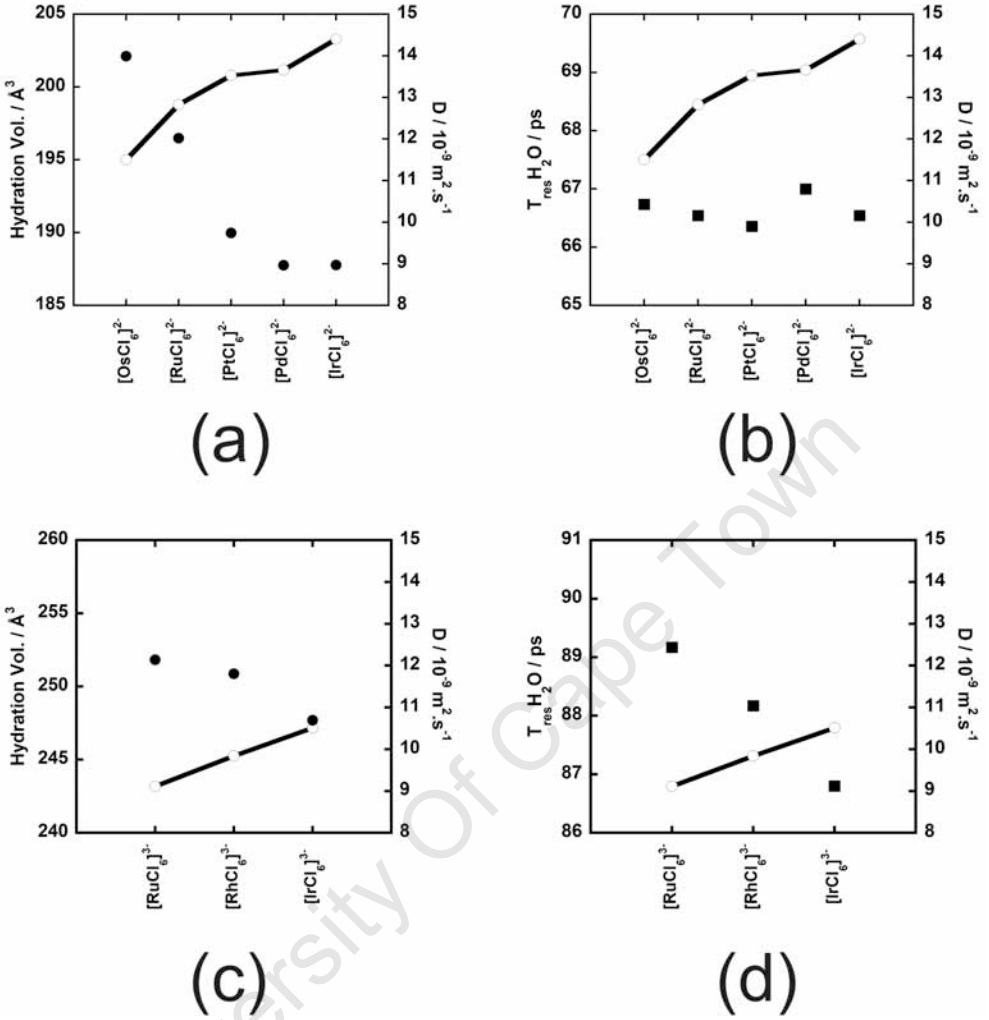

Figure 8.7. Plots of diffusion (○) and hydration volumes (●) and the diffusion (○) and water residence times (■) for the bivalent (a, b) and trivalent (c, d) octahedral PGM chloro-anion complexes.

The number of correlated atoms $n_{\alpha\beta}(r)$ for the first peaks are the ensemble averaged number of waters found in the first solvation shell and are from here on collectively referred to as the coordination number, n_h, that are listed in Table 8.8. On average 9-10 water molecules are within the first solvation shell of the square planar complexes, while the first solvation shell of the octahedral species have 9-12 water molecules. These numbers are 2-4 water molecules more than those previously reported [8]. The increase in hydration numbers appears correlated to the formation of ion pairs that lower the effective complex charge causing a disruption in the solvation shell. Previously Koneshan et al. [39] observed that the residence time of water in the first solvation shell increased on neutralising I^-. This suggests the formation of a solvent cage around the large uncharged ion species which partially breaks up on charging [39]. The dynamic hydration number, n_{dyn}, for each ion is calculated using the definition,

$$n_{dyn} = n_h \exp\left(-\tau^S_{Bulk} \Big/ -\tau^S_{ion} \right) \tag{8.9}$$

where n_h is the coordination number, τ^S_{Bulk} is the mean residence time of bulk water (calculated to be 4.55ps for TIP3P) and τ^s_{ion} is the residence time of water associated with a particular ion.

The residence times of water molecules in the first hydration shells for all the PGM chloro-anion complexes and the corresponding dynamic hydration numbers are given in Table 8.8. Several procedures have been suggested to determine the residence times from MD simulations. In this work we use the definition proposed by Impey et al. [11]. The PGM chloro-anion residence time, $n_{ion}(\mathbf{t})$ is calculated by introducing a probability function $P_\alpha(t,t_n,t^*)$, where $P_\alpha = 1$ if solvent molecule α is within the first solvation shell of the ion at time t and t_n, and does not leave the solvation shell for any period longer than t^*; otherwise $P_\alpha = 0$. It then follows that $n_{ion}(t)$, which is characteristic of the ion, is expressed as

$$n_{ion}(t) = \frac{1}{N_t} \sum_{n=1}^{N_t} \sum_{\alpha} P_\alpha(t, t_n, t^*) \tag{8.10}$$

Table 8.8. Summary of Coordination number (n_h), residence time (t_{res}) and the dynamic hydration number (n_{dyn}), which is calculated using a t_{bulk} for the solvent of 4.55 ps.

Anion	n_h/ # of waters	t_{res} / ps	n_{dyn}
$[PtCl_4]^{2-}$	9.95	81.37	9.41
$[PdCl_4]^{2-}$	10.57	82.91	10.01
$[PtCl_6]^{2-}$	10.81	66.36	10.10
$[PdCl_6]^{2-}$	9.75	66.99	9.11
$[IrCl_6]^{2-}$	10.80	66.54	10.09
$[RuCl_6]^{2-}$	10.65	66.54	9.95
$[OsCl_6]^{2-}$	10.78	66.73	10.07
$[IrCl_6]^{3-}$	10.93	86.80	10.37
$[RuCl_6]^{3-}$	11.93	89.17	11.33
$[RhCl_6]^{3-}$	11.93	88.17	11.33

The above correlation function decays as $\exp(-t/\tau^{s}_{ion})$ over a particular time frame, giving τ^{s}_{ion}. The calculated residence times and subsequent dynamic hydration numbers are presented in Table 8.8 and show that the dynamic hydration numbers on average reflect 0.5-0.7 water molecules less than the corresponding coordination numbers. The residence times reveal that the smaller square planar and the trivalent octahedral (t_{res} = 81-90 ps) species have a longer lasting metal-water association, compared with the bivalent octahedral complexes (t_{res} = 66-67 ps). The residence times, the coordination numbers and the corresponding dynamic hydration times are dependant on the occurrence of ion pairs. The effect of ion pairing is to lower the charge on the metal complex. By removing the ion pairs, the residence times for the PGM chloro-anion complexes are found to increase by as much as 25 %, while the corresponding hydration numbers decrease. This increase in residence times is due to the increase in ion complex charge density upon the loss of contact ion pairing with NH_4^+ causing the surrounding waters to more closely bind

to the anionic complex which leads to an increase in the water density of the first hydration sphere.

8.4.5 Hydration Volumes and PGM Chloro-anion Self-diffusion

The mobility of ions in solution is an indication of their degree of solvation [41]. Molecular dynamics diffusion coefficients can only be of semi-quantitative significance since the statistical uncertainties in the calculations may be in error by as much as 50% [11]. Furthermore, previous diffusion calculations for alkali and halide ions have been seen to be water model dependant, with ions in TIP3P water diffusing faster than in the same ions do in TIP4P$_{EW}$, SPC and SPC/e water models. This is due to the inherent TIP3P diffusion rate that is much larger than the experimentally calculated value [7, 39].

Here the anion self-diffusion coefficients are calculated from the average of the mean square displacement of the respective anions using the Einstein relation [11, 42]:

$$D = \lim_{t\to\infty} \frac{1}{6t} \left\langle \left| r_i(t) - r_i(0) \right|^2 \right\rangle \tag{8.11}$$

where $r_i(t)$ is the molecular position i at time t and $r_i(0)$ is the initial position, with the < > bracket denoting and ensemble average. The diffusion times calculated for the PGM chloro-anion species, along with the corresponding force field charges of the individual chloride ions are presented in Table 8.9. At present, experimental diffusion constants only exist for the $[PtCl_6]^{2-}$ $(Na^+)_2$ complex (7.13 X 10^{-9} m^2 s^{-1}) and $[PtCl_6]^{2-}$ $(H_3O^+)_2$ (7.00 X 10^{-9} m^2 s^{-1}) counter ions [43]. While the calculated diffusion rate for $[PtCl_6]^{2-}$ $(NH_4^+)_2$ of 13.57 X 10^{-9} m^2 s^{-1} is substantially higher, the experimental values do fall within the calculated standard deviation (see Table A.2. in Appendix A). Setting this aside, the diffusion rates for the PGM complexes are listed in Table 8.9 and are used for analyses of the qualitative differences between the PGM chloro-anion solutions.

Using the Voronoi tessellation a hydration volume for $[PtCl_4]^2$ of 54.8 Å^3 was calculated along with a diffusion rate of 15.6 X 10^{-9} m^2 s^{-1}. Compared with $[PdCl_4]^{2-}$ which has an effective volume of 61.2 Å^3 and a diffusion rate of 13.17 X 10^{-9} m^2 s^{-1} it

appears that the diffusion of the square planar complexes increases with an decrease in their effective hydration volume. The effective hydration volume is calculated for the first and second solvation shell including the effects of ion pairing for the octahedral PGM chloro-anion complexes and shown in Figure 8.7. The diffusion rates increase as the effective hydration volumes decrease (Figure 8.7 a and c). This inverse correlation between diffusion rates and water residence times is repeated (Figure 8.7 b and d) by both bivalent and trivalent octahedral complexes. However, the general observation that a decrease in hydration volume results in an increase in diffusion is not seen in the case of $[PdCl_6]^{2-}$, which diffuses slower than $[IrCl_6]^{2-}$. This is because $[IrCl_6]^{2-}$ has a higher percentage of ion pairing that disrupts its hydration sphere and results in a faster diffusing ion paired complex.

8.4.6 Reorientational Relaxation Times

The dynamic interaction of the solute with its environment is influenced not only by its linear motion (characterised by diffusion coefficients) but also by its rotational motion. This degree of freedom is analysed using the reorientational relaxation times. The time correlation function of an *l*-rank Legendre polynomial is taken from the rotation of each solvent molecule *i* about its reference vector. The final time correlation function (TCF) is an average over *N* separate functions,

$$C_l(t) = \frac{1}{N}\sum_{i=1}^{N}\left\langle P\left[\cos\theta_i(t)\right]\right\rangle \tag{8.12}$$

The noise normally observed for a TCF derived from single particles is removed by sampling over *N* particles, thus improving the statistical probability. The reorientational relaxation times were calculated by determining an exponential fit to the TCFs of the form

$$T(t) = N\exp(-t/\tau) \tag{8.13}$$

Table 8.9. Summary electrostatic surfaces and corresponding transport properties of the PGM chloro-anion complexes

Anion	Contour slice of the electrostatic surface	Electrostatic Dimension / Å	t_{res} H_2O / ps	t_{res} NH_4^+ / ps	t_{rot} v1 / ps	Interaction Energy / kcal.mol^{-1}	D / 10^{-9} m^2.s^{-1}
$[PtCl_4]^{2-}$	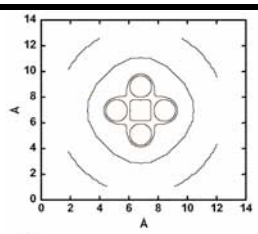	3.2	81.4	13.4	20.8	-7.2	15.6
$[PdCl_4]^{2-}$	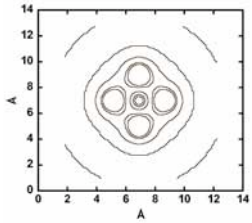	3.3	82.9	14.9	18.1	-8.4	13.2
$[PtCl_6]^{2-}$	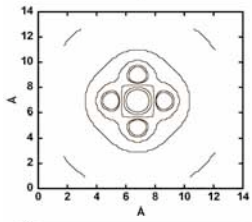	3.6	66.4	19.9	16.1	-10.6	13.6
$[PdCl_6]^{2-}$	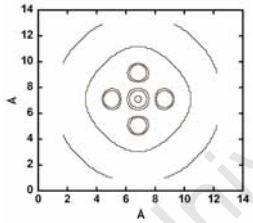	3.5	67.0	20.3	16.9	-11.6	13.7
$[IrCl_6]^{2-}$	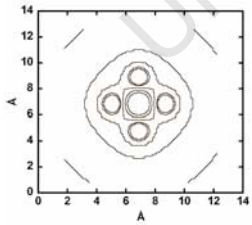	3.6	66.5	16.9	16.8	-13.4	14.4
$[OsCl_6]^{2-}$	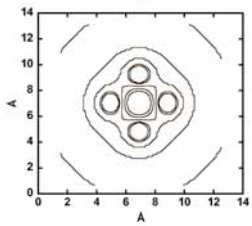	3.6	66.7	14.1	16.9	-9.6	11.5

$[RuCl_6]^{2-}$	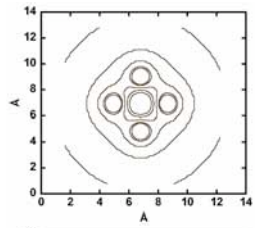	3.5	66.5	17.4	16.8	-10.2	12.8
$[IrCl_6]^{3-}$	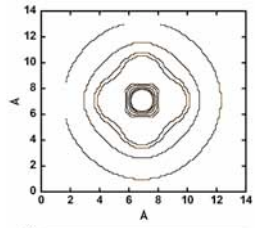	3.9	86.8	61.2	26.7	-19.7	10.5
$[RuCl_6]^{3-}$	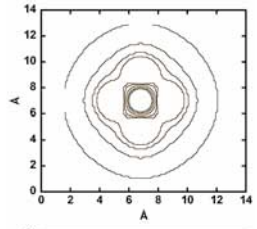	3.8	89.2	45.6	26.9	-18.1	9.1
$[RhCl_6]^{3-}$	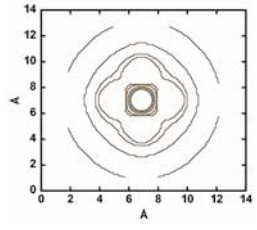	3.8	88.2	67.7	26.8	-22.2	9.8

where τ is the characteristic time and $N = 1$.

By setting the reference vector parallel to the bond axis, the anisotropic effects from and tumbling about the M-Cl bond can be determined. The overall correlation time, $\tau_{c,l,}$ for the l-rank spherical harmonic is a function of θ (which is the angle between a reference vector and the vector through the bond axis) and the correlation times, $\tau_{l,m}$, of the normalized time autocorrelation function of the spherical harmonic $Y_{l,m}(\theta, \varphi)$. The relaxation times calculated by fitting the TCF curves with exponentials as described above, are given in Table 8.7. The reorientational relaxation times predicted by our model indicate that the overall relaxation of the PGM chloro-anion complexes is correlated to the degree of solvation, i.e. the anions with the largest number of solvent molecules around them relax the slowest. This trend is, however, not seen for the square planar complexes, where $[PtCl_4]^{2-}$ relaxes more slowly than $[PdCl_4]^{2-}$ although it has approximately one more water molecule in its hydration sphere (Table 8.8). This

difference is attributed to the extensive association the ammonium counterions have with $[PtCl_4]^{2-}$, (18 %) in the outer solvation shells, where they form a solvent shared ion pair (SSHIP), as well as in the inner shell CIP (Figure 8.4c) which hinder the rotation of the anion. This is compared with the SSHIP that the ammonium counterions form with $[PdCl_4]^{2-}$ 11 % of the time.

8.5 Conclusions

The MSFF is expanded to better understand the association of water and commonly used counter ions such as $[NH_4]^+$ with platinum group metal chloro anions. The diffusion rates of the bivalent metal chloro anions are found to be in the order $[IrCl_6]^{2-} > [PdCl_6]^{2-} > [PtCl_6]^{2-} > [RuCl_6]^{2-} > [OsCl_6]^{2-}$, while for the trivalent octahedral species the trend is $[IrCl_6]^{3-} > [RhCl_6]^{3-} > [RuCl_6]^{3-}$. The strength of PGM complex to water association for bivalent octahedral species in decreasing order is $[IrCl_6]^{2-} > [PdCl_6]^{2-} > [PtCl_6]^{2-} > [RuCl_6]^{2-} > [OsCl_6]^{2-}$, while for the trivalent octahedral species $[RhCl_6]^{3-} > [IrCl_6]^{3-} > [RuCl_6]^{3-}$.

It follows that the link of the diffusion rate pattern with the electrostatic surface or the comparative strength of association of the metal complex with water is only complete for both bivalent and trivalent cases. In particular, it is found that the break in the latter trend compared with the trend in the diffusion rates may be due to the high charge density of $[RhCl_6]^{3-}$, thus emphasising the competitive association the ammonium counter ions have with waters for positions in the first solvation sphere. This is not the case for the other two trivalent metals that have a lower charge density and diffuse ion pairing. The effect of the solvent and counter ion associations with the metal species is summed up in the effective hydration volume that was calculated using a Voronoi tessellation. The hydration volume trend from biggest to smallest for the bivalent species is $[OsCl_6]^{2-} > [RuCl_6]^{2-} > [PtCl_6]^{2-} > [IrCl_6]^{2-} \sim [PdCl_6]^{2-}$, and $[RuCl_6]^{3-} > [RhCl_6]^{3-} > [IrCl_6]^{3-}$ for the trivalent octahedral species. The hydration volume trend is therefore the exact inverse of the trend in diffusion rate for the metal complexes.

8.6 References

1. Bernardis, F.L., Grant, R.A., and Sherrington, D.C., *A review of methods of separation of the platinum-group metals through their chloro-complexes.* React. Funct. Polym., 2005. **65**(3): p. 205-217.
2. Moyer, B.A. and Bonnessen, P.V., in *Supramolecular Chemistry of Anions,* A. Bianchi, K. Bowman-James, and E. Garcia-Espana, Editors. 1997, Wiley-VCH, New York.
3. Bell, K.J., Westra, A.N., Warr, R.J., Chartres, J., Ellis, R., Tong, C.C., Blake, A.J., Tasker, P.A., and Schroder, M., *Outer-sphere coordination chemistry: Selective extraction and transport of the [PtCl6](2-) anion.* Angew. Chem., Int. Ed., 2008. **47**(9): p. 1745-1748.
4. Beer, P.D. and Gale, P.A., *Anion recognition and sensing: The state of the art and future perspectives.* Angew. Chem., Int. Ed., 2001. **40**(3): p. 486-516.
5. Jensen, K.P. and Jorgensen, W.L., *Halide, ammonium, and alkali metal ion parameters for modeling aqueous solutions.* J. Chem. Theory Comput., 2006. **2**(6): p. 1499-1509.
6. Aqvist, J., *Ion water interaction potentials derived from free-energy perturbation simulations.* J. Phys. Chem., 1990. **94**(21): p. 8021-8024.
7. Joung, I.S. and Cheatham, T.E., *Molecular dynamics simulations of the dynamic and energetic properties of alkali and halide ions using water-model-specific ion parameters.* J. Phys. Chem. B, 2009. **113**(40): p. 13279-13290.
8. Lienke, A., Klatt, G., Robinson, D.J., Koch, K.R., and Naidoo, K.J., *Modeling platinum group metal complexes in aqueous solution.* Inorg. Chem., 2001. **40**(10): p. 2352-2357.
9. Naidoo, K.J., Klatt, G., Koch, K.R., and Robinson, D.J., *Geometric hydration shells for anionic platinum group metal chloro complexes.* Inorg. Chem., 2002. **41**(7): p. 1845-1849.
10. Naidoo, K.J., Lopis, A.S., Westra, A.N., Robinson, D.J., and Koch, K.R., *Contact ion pair between Na+ and PtCl62- favored in methanol.* J. Am. Chem. Soc., 2003. **125**(44): p. 13330-13331.

11. Impey, R.W., Madden, P.A., and McDonald, I.R., *Hydration and mobility of ions in solution.* J. Phys. Chem., 1983. **87**(25): p. 5071-5083.

12. Frisch, M.J., Trucks, G.W., Schlegel, H.B., Scuseria, G.E., Robb, M.A., Cheeseman, J.R., Montgomery, J.A., Vreven, T., Kudin, K.N., Burant, J.C., Millam, J.M., Iyengar, S.S., Tomasi, J., Barone, V., Mennucci, B., Cossi, M., Scalmani, G., Rega, N., Petersson, G.A., Nakatsuji, H., Hada, M., Ehara, M., Toyota, K., Fukuda, R., Hasegawa, J., Ishida, M., Nakajima, T., Honda, Y., Kitao, O., Nakai, H., Klene, M., Li, X., Knox, J.E., Hratchian, H.P., Cross, J.B., Bakken, V., Adamo, C., Jaramillo, J., Gomperts, R., Stratmann, R.E., Yazyev, O., Austin, A.J., Cammi, R., Pomelli, C., Ochterski, J.W., Ayala, P.Y., Morokuma, K., Voth, G.A., Salvador, P., Dannenberg, J.J., Zakrzewski, V.G., Dapprich, S., Daniels, A.D., Strain, M.C., Farkas, O., Malick, D.K., Rabuck, A.D., Raghavachari, K., Foresman, J.B., Ortiz, J.V., Cui, Q., Baboul, A.G., Clifford, S., Cioslowski, J., Stefanov, B.B., Liu, G., Liashenko, A., Piskorz, P., Komaromi, I., Martin, R.L., Fox, D.J., Keith, T., Laham, A., Peng, C.Y., Nanayakkara, A., Challacombe, M., Gill, P.M.W., Johnson, B., Chen, W., Wong, M.W., Gonzalez, C., and Pople, J.A., *Gaussian 03, Revision C.02.* 2003.

13. Vosko, S.H., Wilk, L., and Nusair, M., *Accurate spin-dependent electron liquid correlation energies for local spin-density calculations - A critical analysis.* Can. J. Phys., 1980. **58**(8): p. 1200-1211.

14. Slater, J.C., *Quantum Theory of Molecules and Solids.* Vol. 4. 1974, New York: McGraw-Hill.

15. Becke, A.D., *Density-functional thermochemistry .3. The role of exact exchange.* J. Chem. Phys., 1993. **98**(7): p. 5648-5652.

16. Lee, C.T., Yang, W.T., and Parr, R.G., *Development of the Colle-Salvetti correlation-energy formula into a functional of the electron-density.* Phys. Rev. B, 1988. **37**(2): p. 785-789.

17. Stephens, P.J., Devlin, F.J., Chabalowski, C.F., and Frisch, M.J., *Ab-initio calculation of the vibrational absorption and circular-dichroism spectra using density-functional force-fields.* J. Phys. Chem., 1994. **98**(45): p. 11623-11627.

18. Perdew, J.P., *Density-functional approximation for the correlation-energy of the inhomogeneous electron-gas.* Phys. Rev. B, 1986. **33**(12): p. 8822-8824.
19. Hay, P.J. and Wadt, W.R., *Ab initio effective core potentials for molecular calculations - potentials for K to Au including the outermost core orbitals.* J. Chem. Phys., 1985. **82**(1): p. 299-310.
20. Hay, P.J. and Wadt, W.R., *Ab initio effective core potentials for molecular calculations - potentials for the transition-metal atoms Sc to Hg.* J. Chem. Phys., 1985. **82**(1): p. 270-283.
21. Wadt, W.R. and Hay, P.J., *Ab initio effective core potentials for molecular calculations - Potentials for main group elements Na to Bi.* J. Chem. Phys., 1985. **82**(1): p. 284-298.
22. Neese, F., *Prediction of molecular properties and molecular spectroscopy with density functional theory: From fundamental theory to exchange-coupling.* Coord. Chem. Rev., 2009. **253**(5-6): p. 526-563.
23. Comba, P. and Kerscher, M., *Computation of structures and properties of transition metal compounds.* Coord. Chem. Rev., 2009. **253**(5-6): p. 564-574.
24. Parker, S.F. and Forsyth, J.B., *K2MCl6 (M = Pt, Ir) - location of the silent modes and forcefields.* J. Chem. Soc.-Faraday Trans., 1998. **94**(8): p. 1111-1114.
25. Cotton, S.A., *Chemistry of Precious Metals.* 1997: Chapman and Hall: London.
26. Jorgensen, W.L., Chandrasekhar, J., Madura, J.D., Impey, R.W., and Klein, M.L., *Comparison of simple potential functions for simulations liquid water.* J. Chem. Phys., 1983. **79**(2): p. 926-935.
27. MacKerell, A.D., Bashford, D., Bellott, M., Dunbrack, R.L., Evanseck, J.D., Field, M.J., Fischer, S., Gao, J., Guo, H., Ha, S., Joseph-McCarthy, D., Kuchnir, L., Kuczera, K., Lau, F.T.K., Mattos, C., Michnick, S., Ngo, T., Nguyen, D.T., Prodhom, B., Reiher, W.E., Roux, B., Schlenkrich, M., Smith, J.C., Stote, R., Straub, J., Watanabe, M., Wiorkiewicz-Kuczera, J., Yin, D., and Karplus, M., *All-atom empirical potential for molecular modeling and dynamics studies of proteins.* J. Phys. Chem. B, 1998. **102**(18): p. 3586-3616.

28. Brooks, B.R., Bruccoleri, R.E., Olafson, B.D., States, D.J., Swaminathan, S., and Karplus, M., *CHARMM - A program for macromolecular energy, minimization, and dynamics calculations.* J. Comput. Chem., 1983. **4**(2): p. 187-217.

29. Brooks, B.R., Brooks, C.L., Mackerell, A.D., Nilsson, L., Petrella, R.J., Roux, B., Won, Y., Archontis, G., Bartels, C., Boresch, S., Caflisch, A., Caves, L., Cui, Q., Dinner, A.R., Feig, M., Fischer, S., Gao, J., Hodoscek, M., Im, W., Kuczera, K., Lazaridis, T., Ma, J., Ovchinnikov, V., Paci, E., Pastor, R.W., Post, C.B., Pu, J.Z., Schaefer, M., Tidor, B., Venable, R.M., Woodcock, H.L., Wu, X., Yang, W., York, D.M., and Karplus, M., *CHARMM: The biomolecular simulation program.* J. Comput. Chem., 2009. **30**(10): p. 1545-1614.

30. Lamoureux, G. and Roux, B., *Modeling induced polarization with classical Drude oscillators: Theory and molecular dynamics simulation algorithm.* The Journal of Chemical Physics, 2003. **119**(6): p. 3025-3039.

31. York, D.M., Darden, T.A., and Pedersen, L.G., *The effect of long-range electrostatic interactions in simulations of macromolecular crystals: A comparison of the Ewald and truncated list methods.* J. Chem. Phys., 1993. **99**(10): p. 8345-8348.

32. Essmann, U., Perera, L., Berkowitz, M.L., Darden, T., Lee, H., and Pedersen, L.G., *A smooth particle mesh Ewald method.* J. Chem. Phys., 1995. **103**(19): p. 8577-8593.

33. Joung, I.S. and Cheatham, T.E., *Determination of alkali and halide monovalent ion parameters for use in explicitly solvated biomolecular simulations.* J. Phys. Chem. B, 2008. **112**(30): p. 9020-9041.

34. Breneman, C.M. and Wiberg, K.B., *Determining atom-centered monopoles from molecular electrostatic potentials - The need for high sampling density in formamide conformational-analysis.* J. Comput. Chem., 1990. **11**(3): p. 361-373.

35. Besler, B.H., Merz, K.M., and Kollman, P.A., *Atomic charges derived from semiempirical methods.* J. Comput. Chem., 1990. **11**(4): p. 431-439.

36. Singh, U.C. and Kollman, P.A., *An approach to computing electrostatic charges for molecules.* J. Comput. Chem., 1984. **5**(2): p. 129-145.

37. Chirlian, L.E. and Francl, M.M., *Atomic charges derived from electrostatic potentials - A detailed study.* J. Comput. Chem., 1987. **8**(6): p. 894-905.

38. Allen, F.H. and Kennard, O., *The Cambridge database of molecular-structures.* Perspectives in Computing, 1983. **3**(3): p. 28-43.

39. Koneshan, S., Rasaiah, J.C., Lynden-Bell, R.M., and Lee, S.H., *Solvent structure, dynamics, and ion mobility in aqueous solutions at 25 degrees C.* J. Phys. Chem. B, 1998. **102**(21): p. 4193-4204.

40. Collins, K.D., Neilson, G.W., and Enderby, J.E., *Ions in water: Characterizing the forces that control chemical processes and biological structure.* Biophys. Chem., 2007. **128**(2-3): p. 95-104.

41. Burgess, J., *Ions in Solution: Basic Principles of Chemical Interactions.* 1988: Ellis Horwood.

42. Allen, M.P. and Tildesley, D.J., *Computer Simulations of Liquids.* 1989, Oxford: Clarendon Press.

43. Nama, D., Kumar, P.G.A., and Pregosin, P.S., *Pt-195, H-1 and P-31 PGSE diffusion studies on platinum complexes.* Magn. Reson. Chem., 2005. **43**(3): p. 246-250.

APPENDIX A

Table A1. Difference in average binding energies for Mg-nH2O (n = 1-6)configurations from MM and *ab initio* calculations.

# Waters	Structure	MSFF		MP2/311++g(3d, 3p)	
		E / kcal.mol^{-1}	Δ E / kcal.mol^{-1}	E / kcal.mol^{-1}	Δ E / kcal.mol^{-1}
1	C_{2v}	-71.8		-76.4	
2	D_{2d}	-141.6	-69.8	-147.6	-71.2
3	D_3	-193.4	-51.8	-200.7	-53.1
4	S_4	-236.3	-42.9	-245.1	-44.4
5	C_{2v}	-263.1	-26.8	-274.4	-29.3
6	D_3	-286.5	-23.4	-299.7	-25.3

Table A2. The diffusion, standard deviations and percentage error in the calculated diffusion, determined from the PGM solution simulations.

Anion	D / 10^{-9}m^2.s^{-1}	Std deviation in D / 10^{-9}m^2.s^{-1}	% Error in D
$[PtCl_4]^{2-}$	15.6	8.8	56.4
$[PdCl_4]^{2-}$	13.2	4.6	34.8
$[PdCl_6]^{2-}$	13.7	7.2	52.4
$[PtCl_6]^{2-}$	13.5	6.9	49.3
$[IrCl_6]^{2-}$	14.4	7.6	53.0
$[OsCl_6]^{2-}$	11.5	6.6	52.4
$[RuCl_6]^{2-}$	12.8	5.4	41.9
$[RhCl_6]^{3-}$	9.1	5.9	65.1
$[RuCl_6]^{3-}$	9.8	4.4	44.5
$[IrCl_6]^{3-}$	10.5	2.6	24.7

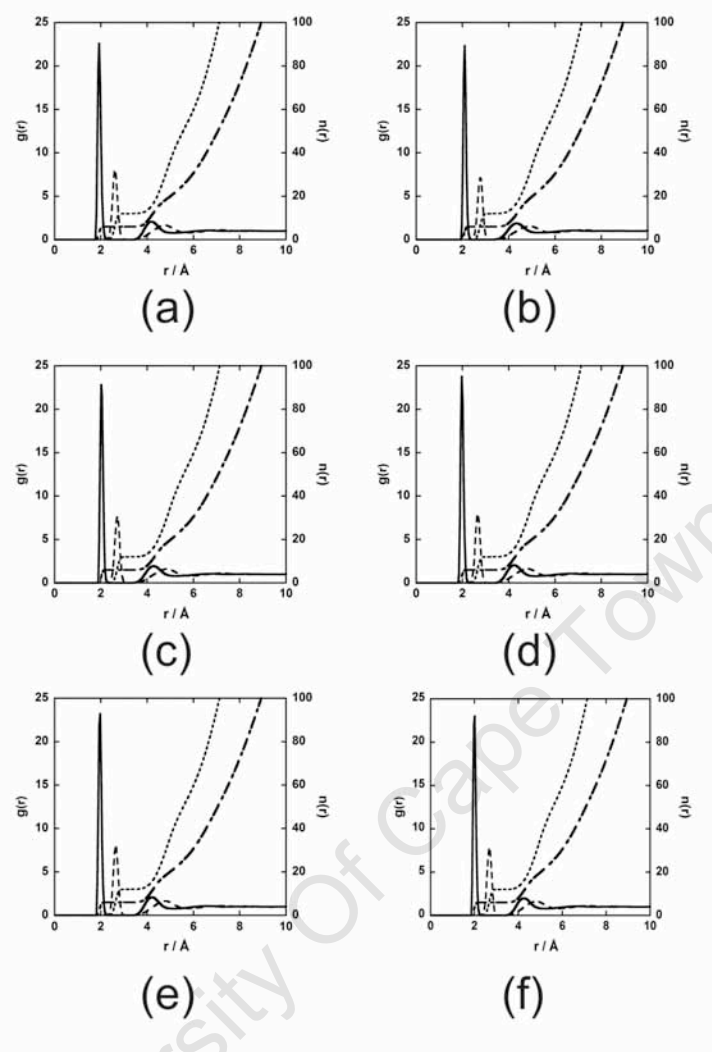

Figure A.1. Metal-oxygen (solid line) and metal-hydrogen (dashed) pair distribution functions along with their corresponding plots of $n(r)$ for (a) $MgSO_4$, (b) $FeSO_4$, (c) $CoSO_4$, (d) $NiSO_4$, (e) $CuSO_4$ and (f) $ZnSO_4$ from the CIP simulation.

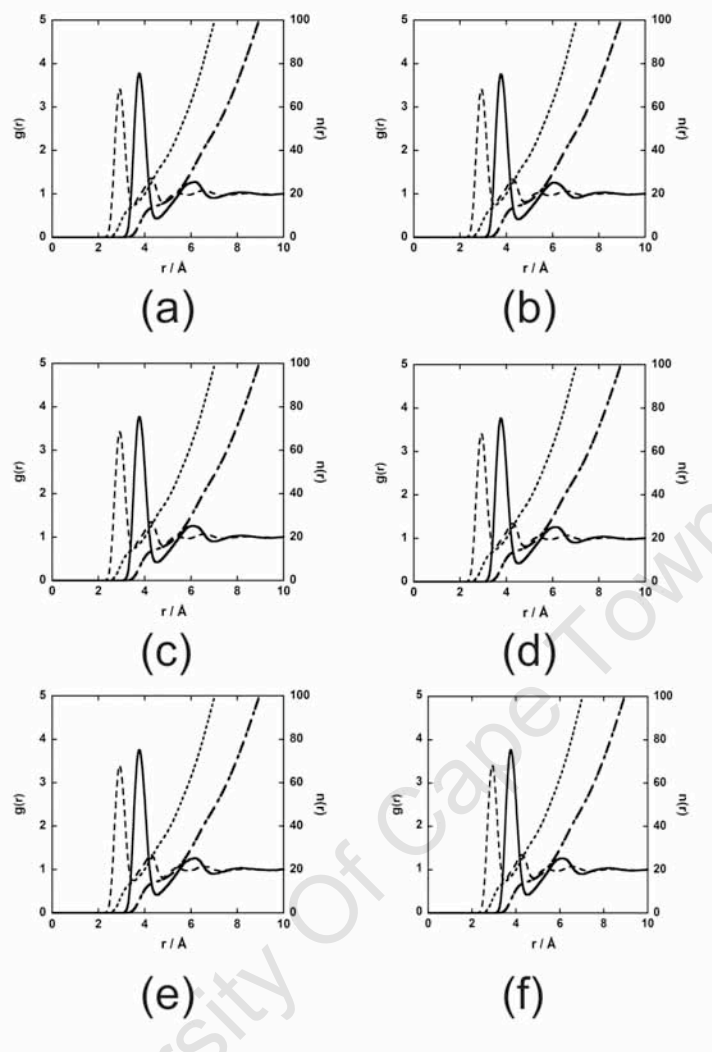

Figure A.2. Sulfur-oxygen (solid line) and sulfur-hydrogen (dashed) pair distribution functions along with their corresponding plots of $n(r)$ for (a) $MgSO_4$, (b) $FeSO_4$, (c) $CoSO_4$, (d) $NiSO_4$, (e) $CuSO_4$ and (f) $ZnSO_4$ from the CIP simulation.